EAST ANTARCTIC LANDFAST SEA-ICE DISTRIBUTION AND VARIABILITY

by

Alexander Donald Fraser, B.Sc.-B.Comp., B.Sc. Hons

Submitted in fulfilment of the requirements
for the Degree of Doctor of Philosophy

Institute for Marine and Antarctic Studies
University of Tasmania
May, 2011

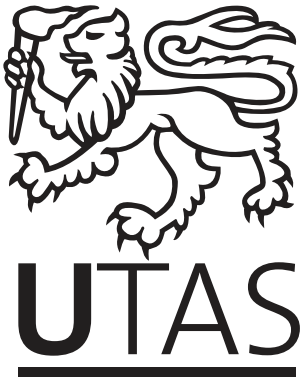

I declare that this thesis contains no material which has been accepted for a degree or diploma by the University or any other institution, except by way of background information and duly acknowledged in the thesis, and that, to the best of my knowledge and belief, this thesis contains no material previously published or written by another person, except where due acknowledgement is made in the text of the thesis, nor does the thesis contain any material that infringes copyright.

Signed: _____
Alexander Donald Fraser

Date: _____

Signed: _____
Alexander Donald Fraser

Date: _____

ABSTRACT

Landfast sea ice (sea ice which is held fast to the coast or grounded icebergs, also known as fast ice) is a pre-eminent feature of the Antarctic coastal zone, where it forms an important interface between the ice sheet and pack ice/ocean to exert a major influence on high-latitude atmosphere-ocean interaction and biological processes. It is highly vulnerable to climate variability and change, given that its formation and breakup are intimately associated with oceanic and atmospheric forcing, yet is not currently represented in global climate models or coupled atmosphere-ocean-ice models. Fast ice forms a key breeding habitat for a number of iconic species, including Weddell seals and Emperor penguins, and plays a crucial role in the breeding success and foraging behaviour of Adélie penguins. Recent work further suggests that fast ice may stabilize floating glacier tongues and ice shelves, to affect iceberg calving and ultimately the mass balance of the ice sheet plus the drift rates of icebergs. Moreover, fast ice has a major impact on the logistics of the resupply of Antarctic bases.

While Antarctic sea ice extent and variability has been the focus of considerable recent research, fast-ice extent and variability are currently poorly understood. This is in large part due to the difficulty associated with discriminating fast ice from pack ice on a large scale in satellite data. "Snapshot" analyses are unable to discriminate between the ice types (i.e., fast ice has a non-unique signature), and ice motion techniques have various problems, including persistent cloud cover at visible and infrared wavelengths and low spatial resolution for passive microwave sensors. Furthermore, Synthetic Apterture Radar (SAR) imagery is inherently difficult to interpret over the sea-ice zone.

This thesis, presented in a "thesis-by-publication" style, overcomes the problems associated with remotely sensing fast ice at visible and infrared wavelengths to produce cloud-free time-averaged images of the surface from March 2000 to December 2008, enabling discrimination between pack and fast ice. From these, the first East Antarctic (10° W - 172° E) high spatio-temporal resolution (2-km, 20-day) maps of fast-ice extent are created. This allows the first detailed time series analysis of the seasonal to inter-annual variability of East Antarctic fast ice. Fast-ice growth and breakout events are then related to large scale and local atmospheric forcing parameters.

In addition to presenting the first near decade-long, high spatio-temporal resolution time series of fast-ice maps in East Antarctica, the main findings of this thesis are as follows. Using MODerate resolution Imaging Spectroradiometer (MODIS) visible and thermal infrared data, quality cloud-free composite images of the high-latitude surface can generally be constructed using 20 days' raw imagery. The compositing technique developed here involves using a modified MODIS cloud mask to select

cloud-free pixels, which are then composited together over number of days. The MOD35 MODIS cloud mask performs well during daytime, when shortwave tests could be included into the cloud masking algorithm. However, during night-time, cloud mask performance is insufficient to create quality cloud-free composite images. Spatial filtering on the cloud mask is required to produce high-quality composite images. With a sufficiently long compositing interval (i.e., 20 days), pack ice motion acts to "blur" the pack ice zone in the composite imagery, while the fast/pack ice shear zone remains sharply defined. This property of the compositing process is very useful for discriminating between pack and fast ice.

Despite the success of the compositing technique, persistent cloud cover and inaccurate cloud masking are found to lower composite image quality at times. Thus, a technique is developed to augment lower quality composite images with Advanced Microwave Scanning Radiometer - EOS (AMSR-E) and additional MODIS data. Fast-ice maps are generated from the resulting imagery. An error analysis shows that fast-ice extent can be retrieved to within $\sim \pm 3\%$ for over 80% of the 159 consecutive fast-ice maps comprising the 8.8-year time series, with the remainder retrieved to within $\sim \pm 9\%$.

Analysis of the 8.8-year East Antarctic fast-ice time series shows a statistically-significant increase in fast-ice extent ($1.43 \pm 0.30\%$ yr^{-1}), albeit based upon a relatively short period. Regionally, there is a stronger increase observed in the Indian Ocean sector (20 - 90° E) of $4.07 \pm 0.42\%$ yr^{-1}, compared to a slight (non-significant) decrease in the Western Pacific Ocean sector (90 - 160° E) of $-0.40 \pm 0.37\%$ yr^{-1}. In the Indian Ocean sector, a slightly decreasing trend in fast-ice extent changes to a strongly increasing trend from 2004 - 2008. An analysis of the timing of maximum and minimum fast-ice extent shows high variability compared to that of overall sea ice. Analysis of the shape of the mean annual fast-ice extent cycle reveals a limit to maximum fast-ice extent, apparently related to the locations of grounded icebergs. Ten fast-ice regimes were identified across the coast, relating to bathymetry, coastal configuration, and prevailing atmospheric conditions. The percentage of fast ice comprising overall sea-ice extent varies seasonally from $\sim$19% during the summer minimum extent to $\sim$3.8% during the winter maximum extent.

Nine case studies of anomalous fast-ice breakout or growth are conducted in four regions around the East Antarctic coast. These anomalous fast-ice extents are observed in conjunction with locally anomalous wind speeds and directions, surface air temperatures, and pack ice conditions. On a hemisphere-wide scale, a reasonably strong correlation is found between the Southern Oscillation Index (SOI) and fast-ice extent in the Indian Ocean sector (R=+0.45). No strong correlation is observed in the Western Pacific Ocean sector, and, in contrast to previous work, the correlation between SAM and fast-ice extent is weak in both sectors.

This work has greatly improved our knowledge of fast-ice distribution and variability around the East Antarctic coast, and provides benefits for many areas of current research. It has also provided an important new climatic dataset that is directly comparable to, and complements, the widely-used passive microwave-derived time series of overall sea-ice extent.

ACKNOWLEDGEMENTS

This thesis is dedicated to Abby, my lovely wife. Without her smiley face and sense of humour, writing this thesis would have been much harder work.

To all the Frasers and the Badcocks, thanks for the support and encouragement over these 3.75 years.

To Cameron Watchorn and Pete Greenwood, thanks for all the 'gate, for being our groomsmen, and for all the bromance. Chal nak.

To Guy Williams, thanks for the boat times! Like Vince and that polar bear, "we just clicked". To all the SIPEX participants, thanks for providing me with an amazing experience. In particular, I fondly remember conversations about sea ice and music with Takenobu Toyota (University of Hokkaido).

To Andrew Martin, thanks getting beached in Hobart. I hope you can stick around for a while!

To all the staff and students at the Antarctic Climate & Ecosystems Cooperative Research Centre (ACE CRC), the Institute for Antarctic and Southern Ocean Studies (IASOS), the Institute for Marine and Antarctic Studies (IMAS) and the University of Tasmania (UTAS), thanks for providing such a great workplace vibe. In particular, thanks to Ben Galton-Fenzi, Takeshi Tamura, Glenn Hyland, Roland Warner, Des Fitzgerald, Leigh Gordon, Ben Joseph and James Culverhouse, for the many conversations about oceanography, remote sensing, statistics, and technical computing issues. Further afield, but still in Tasmania, I'd like to thank Andrew Klekociuk from the Australian Antarctic Division (AAD), Neil Adams and Phil Reid from the Bureau of Meteorology (BOM) for conversations about the atmosphere. Also, thanks to Phil for all the internal paper reviews - much appreciated! To Kate Maloney and Suzie Gaynor, thanks for your "unrelenting encouragement"! To Denbeigh Armstrong, thanks for your help with the submission process.

Internationally, I'd like to acknowledge Ed Masuoka from the NASA Level 1 and Atmosphere Archive and Distribution System (LAADS), who assisted with the transfer 12 TB of MODIS data over the internet! Thanks also to Richard Frey (Space Science and Engineering Center, University of Wisconsin-Madison) for assistance with technical aspects of the MODIS cloud mask. To Andy Mahoney (University of Alaska, Fairbanks), it was invaluable talking about fast ice with you in Norway.

The following organisations are acknowledged for their financial and in-kind support during candidature:

- The Australian Government and the ACE CRC, for my Ph.D. scholarship;
- The AAD and ACE CRC, for allowing me to partake in the Sea Ice Physics

and Ecosystems eXperiment (SIPEX) in September/October 2007;

- The International Antarctic Institute (IAI) and the University of Hokkaido, for travel support to the sea-ice field course in Hokkaido, Japan, March 2008;
- The IASOS, ACE CRC, the Institute of Electrical and Electronics Engineers (IEEE) and the Australian Research Council Research Network for Earth System Science (ARCNESS), for travel support to the International Geoscience and Remote Sensing Symposium (IGARSS) in Cape Town, South Africa, July 2009; and
- The International Glaciological Society (IGS), UTAS, IMAS, the Tasmanian Partnership for Advanced Computing (TPAC) and ACE CRC, for travel support to the International Glaciological Society Symposium on Sea Ice in the Physical and Biogeochemical System, in Tromsø, Norway, May 2010.

The following organisations are acknowledged for provision of data:

- MODIS data were obtained from the NASA Level 1 Atmosphere Archive and Distribution System (LAADS) (http://ladsweb.nascom.nasa.gov/);
- AMSR-E ASI sea-ice concentration data were obtained from the University of Hamburg (ftp://ftp-projects.zmaw.de/seaice/AMSR-E_ASI_IceConc/hdf/);
- Smith and Sandwell bathymetry data were obtained from the Scripps Institute of Oceanography (http://topex.ucsd.edu/marine_topo/mar_topo.html);
- SSM/I sea-ice concentration data (dataset reference NSIDC-0079) were obtained from the NASA Earth Observing System Distributed Active Archive Center (DAAC) at the US National Snow and Ice Data Center (NSIDC), University of Colorado, Boulder (http://www.nsidc.org); and
- European Centre for Medium-Range Weather Forecasts (ECMWF) Interim Reanalysis data were obtained from the ECMWF Research Data Server (http://data.ecmwf.int/data/).

This work was carried out with the support of the Australian Government's Cooperative Research Centres Program through the Antarctic Climate and Ecosystems Cooperative Research Centre (ACE CRC) and the Australian Antarctic Science Project 3024.

Thanks to my supervisory team of Kelvin Michael, Jan Lieser, Petra Heil and Tony Worby for all the scientific conversations over the years, and your assistance with the thesis perparation.

Last, but by no means least, I'd like to thank my primary supervisor, Rob Massom. Words can't express how much I have appreciated your supervision and guidance, so I will buy you a beer. Maybe two little ones. Without your truly expert advice, sense of humour, and dedication, this thesis would be a much less comprehensive, coherent and gramatically-correct work.

Publications resulting from research completed during candidature

Published/in press

Refereed:

1. **Fraser, A. D.**, R. A. Massom, and K. J. Michael, A method for compositing polar MODIS satellite images to remove cloud cover for landfast sea-ice detection, *IEEE Transactions on Geoscience and Remote Sensing, 47*, 3272-3282, doi:10.1109/TGRS.2009.2019726, 2009.

2. **Fraser, A. D.**, R. A. Massom, and K. J. Michael, Generation of high-resolution East Antarctic landfast sea-ice maps from cloud-free MODIS satellite composite imagery, *Remote Sensing of Environment, 114 (12)*, 2888-2896, doi:10.1016/ j.rse.2010.07.006, 2010.

3. Massom, R. A., A. B. Giles H. A. Fricker, R. Warner, B. Legrésy, G. Hyland, N. Young and **A. D. Fraser**, Examining the interaction between multi-year landfast sea ice and the Mertz Glacier Tongue, East Antarctica: Another factor in ice sheet stability?, *Journal of Geophysical Research (Oceans) 115*, doi:10.1029/2009JC006083, 2010.

4. Toyota, T., R. A. Massom, K. Tateyama, T. Tamura and **A. D. Fraser**, in press. Properties of snow overlying the sea ice off East Antarctica in late winter, 2007, *Deep-Sea Research Part II: Oceanographic Research Papers*, doi:10.1016/j.dsr2.2010.12.002, 2011.

Non-refereed:

5. **Fraser, A. D.**, R. A. Massom, and K. J. Michael, A method for compositing MODIS satellite images to remove cloud cover, *Proceedings of the 2009 IEEE International Geoscience and Remote Sensing Symposium, 3*, 639-641, doi:10.1109/IGARSS.2009.541784/, 2009.

6. Galton-Fenzi, B. K., S. Marsland, A. Meijers and **A. D. Fraser**, The Influence of Coastal Polynyas on the Basal Melting of Ice Shelves, *European Geophysical Union Research Abstracts, 12*, 2010.

7. Legrésy, B., N. Young, L. Lescarmontier, R. Coleman, R. A. Massom, A. B. Giles, **A. D. Fraser**, R. Warner B. K. Galton-Fenzi, L. Testut, M. Houssais and G. Masse, CRAC!!! In the Mertz glacier, Antarctica, *Press release*, 2010.

In preparation/submitted

Refereed

8. **Fraser, A. D.**, R. A. Massom, K. J. Michael, B. K. Galton-Fenzi and J. L.

Lieser, submitted. East Antarctic landfast sea-ice distribution and variability, 2000-2008, *Journal of Climate*.

9. **Fraser, A. D.**, R. A. Massom and N. Adams, in prep. Forcing of East Antarctic landfast sea ice, to be submitted to Journal of Glaciology.

International conferences attended during candidature

1. IEEE International Geoscience and Remote Sensing Symposium (IGARSS), July 2009, Cape Town, South Africa.

2. International Glaciological Society (IGS) Symposium on Sea Ice in the Physical and Biogeochemical System, June 2010, Tromsø, Norway.

Presentations resulting from research completed during candidature

1. Introductory candidature oral presentation, "East Antarctic landfast sea-ice extent and variability from cloud-free MODIS composite images", Institute for Antarctic and Southern Ocean Studies, University of Tasmania, Australia, February 2008;

2. Invited oral presentation, "Looking Through the Polar Clouds with MODIS", Institute of Low Temperature Science, Hokkaido University, Japan, March 2008;

3. Symposium poster presentation, "A method for compositing MODIS satellite images to remove cloud cover", IEEE IGARSS, Cape Town, South Africa, July 2009;

4. Final candidature oral presentation, "East Antarctic landfast sea-ice distribution and variability" Institute for Marine and Antarctic Studies, University of Tasmania, Australia, May 2010;

5. Symposium oral presentation, "High-resolution East Antarctic landfast sea-ice extent and variability from 2000 to 2008", IGS Symposium on Sea Ice in the Physical and Biogeochemical System, Tromsø, Norway, May 2010. Abstract available at *http://www.igs2010.org/Abstracts/57A008.html*;

6. Invited oral presentation, "East Antarctic landfast sea-ice distribution and variability", Australian Antarctic Division, Australia, July 2010; and

7. Invited oral presentation, "East Antarctic landfast sea-ice variability", The Royal Society of Tasmania, Australia, October 2010.

Statement of Co-Authorship

The following people contributed to the publication of the work undertaken as part of this thesis:

Paper 1/Chapter 2 (*A method for compositing polar MODIS satellite images to remove cloud cover for landfast sea-ice detection*):

- **Alexander D. Fraser** (85%)
- Robert A. Massom (10%)
- Kelvin J. Michael (5%)

Paper 2/Chapter 3 (*Generation of high-resolution East Antarctic landfast sea-ice maps from cloud-free MODIS satellite composite imagery*):

- **Alexander D. Fraser** (88%)
- Robert A. Massom (8%)
- Kelvin J. Michael (4%)

Paper 3/Chapter 4, submitted (*East Antarctic landfast sea-ice distribution and variability, 2000-2008*):

- **Alexander D. Fraser** (85%)
- Robert A. Massom (8%)
- Kelvin J. Michael (4%)
- Benjamin K. Galton-Fenzi (2%)
- Jan L. Lieser (1%)

Paper 4/Chapter 5, in preparation (*Atmospheric influences on East Antarctic landfast sea ice formation and breakout*):

- **Alexander D. Fraser** (84%)
- Robert A. Massom (10%)
- Neil Adams (6%)

Details of the authors' roles:

Rob Massom contributed with project development and refinement, technical and conceptual discussion, and document preparation.

Kelvin Michael and Jan Lieser assisted with technical and conceptual aspects of the papers, as well as document preparation.

Neil Adams provided meteorological data and expert meteorological advice.

Benjamin Galton-Fenzi provided assistance with oceanographical aspects and document prepation.

We the undersigned agree with the above stated proportion of work undertaken for each of the above published (or submitted) peer-reviewed manuscripts contributing to this thesis:

Signed: _____

Dr. Robert A. Massom

Supervisor

Australian Antarctic Division, and

Antarctic Climate & Ecosystems Cooperative Research Centre

Date: _____

Signed: _____

Prof. Mike Coffin

Director

Institute for Marine and Antarctic Studies

Date: _____

Table of Contents

List of Tables **v**

List of Figures **vi**

Glossary **ix**

1 Introduction **1**

1.1 An Introduction to Landfast Sea Ice 1

1.2 The Importance of Fast Ice 3

1.3 Gaps in Our Knowledge 5

1.4 Satellite Techniques 10

1.4.1 Microwave Remote Sensing of Fast Ice 10

1.4.2 Visible/Thermal Infrared Remote Sensing of Fast Ice 15

1.5 Aims of the Project 19

1.6 Format of the Thesis 21

2 A Method for Compositing Polar MODIS Satellite Images to Remove Cloud Cover for Landfast Sea-Ice Detection **23**

2.1 Abstract 23

2.2 Introduction 24

2.3 Image Enhancement and Data Preparation 30

2.3.1 Principal Component Analysis 33

2.3.2 Cloud Masking 35

2.3.3 Swath Trimming 44

2.3.4 Image Georegistration and Bowtie Correction 48

2.3.5 Coastline Masking and Solar Zenith Angle Correction 50

2.3.6 Compositing Algorithm 51

2.4 Compositing Results 52
2.5 Summary and Conclusions 54

3 Generation of High-Resolution East Antarctic Landfast Sea-Ice Maps from Cloud-Free MODIS Satellite Composite Imagery 58

3.1 Abstract 58
3.2 Introduction 59
3.3 Methods 60
3.3.1 Study Area and Projection 60
3.3.2 Datasets 60
3.3.3 Generation of Fast-Ice Maps 65
3.3.4 Bias Reduction and Error Analysis 69
3.3.5 Iceberg Masking 72
3.4 Results and Discussion 72
3.5 Conclusions and Future Work 78

4 East Antarctic Landfast Sea-Ice Distribution and Variability, 2000-2008 81

4.1 Abstract 81
4.2 Aims, Datasets and Methods 82
4.3 Results and Discussion 85
4.3.1 Location and Seasonality of Fast-Ice Features 85
4.3.2 Fast-Ice Time Series, Annual Cycle, and Overall Trend Analysis 92
4.3.3 Fast-Ice Extent Climatology and Annual Minimum-to-Minimum Averages 99
4.3.4 Comparison Between Fast-Ice Extent and Overall Regional Sea-Ice Extent and Area 103
4.3.5 Variability in the Timing of Fast-Ice Maxima and Minima . . 107
4.3.6 Percentage of Fast Ice Comprising Overall Sea-Ice Extent/Area 113
4.4 Summary and Further Work 116

5 Atmospheric Influences on East Antarctic Landfast Sea-Ice Formation and Breakout 119

5.1 Abstract 119
5.2 Introduction 120

5.2.1 Fast-Ice Response to Local Atmospheric Forcing: Work to Date 121
5.2.2 Large-Scale Climate Modes and Indices 127
5.2.3 Dominant Modes of Atmospheric Variability at High Southern Latitudes 127
5.2.4 Impacts of Large-Scale Atmospheric Variability on Antarctic Pack Ice 130
5.2.5 Impacts of Large-Scale Atmospheric Variability on Fast Ice . 133
5.3 Datasets and Methods 135
5.4 Correlation with SOI and SAM Indices 141
5.5 The Influence of Atmospheric Conditions 144
5.5.1 Case Study 1: Near-Average Fast-Ice Conditions, Syowa Station Sub-Region, 2000 146
5.5.2 Case Study 2: Low Minimum Fast-Ice Extent, Syowa Station Sub-Region, 2004 149
5.5.3 Case Study 3: High Minimum Fast-Ice Extent, Syowa Station Sub-Region, 2008 150
5.5.4 Case Study 4: Near-Average Fast-Ice Conditions, Mawson/ Cape Darnley Sub-Region, 2000 154
5.5.5 Case Study 5: High Minimum Fast-Ice Extent, Mawson Station/Cape Darnley Sub-Region, 2008 156
5.5.6 Case Study 6: Early and Near-Complete Fast-Ice Breakout, Dumont d'Urville Station Sub-Region, Late 2000 158
5.5.7 Case Study 7: Near-Average Fast-Ice Conditions, Dumont d'Urville Sub-Region, Mid-Late 2004 160
5.5.8 Case Study 8: Low Minimum Fast-Ice Extent, Mertz Glacier/B-9B Sub-Region, 2002 162
5.5.9 Case Study 9: High Wintertime Maximum Fast-Ice Extent, Mertz Glacier/B-9B Sub-Region, 2006 164
5.6 Discussion, Conclusions and Further Work 166
5.6.1 Summary of Regional-Scale Atmospheric Influences on Fast Ice 166
5.6.2 Summary of Large-Scale Atmospheric Influences on Fast-Ice Growth and Breakout 169
5.6.3 Suggested Further Research 171

6 Overall Summary and Conclusions 172

6.1 Response to Atmospheric Change and Variability 177
6.1.1 Rising Temperatures 177

6.1.2 Increasing Wind Speed and Storminess 178
6.1.3 Reduction in Pack-Ice Cover 179
6.1.4 Increase in Precipitation 180
6.2 Suggested Future Work 181

Bibliography **183**

Appendices

Appendix A: Paper 1 - A method for compositing polar MODIS satellite images to remove cloud cover for landfast sea-ice detection

Appendix B: Paper 2 - Generation of high-resolution East Antarctic landfast sea-ice maps from cloud-free MODIS satellite composite imagery

Appendix C: Dataset - Fast-ice extent maps

Chapter 1

Introduction

1.1 An Introduction to Landfast Sea Ice

While overall Antarctic sea ice extent and seasonality, and their global climate and regional ecological ramifications, have been the focal point of significant recent research and concern (e.g., *Comiso*, 2010; *Stammerjohn et al.*, 2008), relatively little is known about Antarctic fast-ice distribution, factors affecting it, its spatio-temporal variability, and the impact of such variability. Landfast sea ice (more commonly known as fast ice) is defined as follows (*World Meteorological Organisation*, 1970):

> **Fast ice:** *sea ice which forms and remains fast along the coast, where it is attached to the shore, to an ice wall, to an ice front, between shoals and grounded icebergs. Vertical fluctuations may be observed during changes of sea-level. Fast ice may be formed in situ from sea water or by freezing of pack ice of any age to the shore, and it may extend a few meters or several hundred kilometres from the coast.*

Though accurate in theory, this definition does not explicitly state the length of time for which ice must remain stationary before it is classed as 'fast' (fast ice in

many regions breaks out and reforms a number of times each season (*Massom et al.*, 2009)). Working in the Arctic, *Mahoney et al.* (2005) define fast ice as sea ice which has remained stationary for at least 20 days. This time period is long enough to preclude transient events such as pack ice being temporarily driven shoreward by oceanic or atmospheric forcing, but short enough to resolve intra-annual events, such as seasonal fast ice growth or breakup.

Fast ice is a pre-eminent feature of the Antarctic coastal zone, and an important interface between the ice sheet and pack ice/ocean. The reliance of fast ice upon coastal features (e.g., promontories, embayments and grounded icebergs) as anchor points means that it tends to form in narrow bands of widely varying widths, but rarely exceeding 150 km around East Antarctica (*Giles et al.*, 2008). There are strong hemispheric contrasts in fast-ice extent and persistence. In the Arctic, a lack of grounded icebergs means fast ice typically grounds itself in shallow waters, with the seaward fast-ice edge often located around the 20-30 m isobath (*Mahoney et al.*, 2007a; *Lieser*, 2004; *Kovacs and Mellor*, 1974; *Wadhams*, 1986). By contrast, Antarctic icebergs ground in water depths of up to ∼400 m (*Massom et al.*, 2001b), and act as fast-ice anchor points, leading to extensive fast-ice formation over deeper water. Shoals also occur some distance offshore along the East Antarctic coast, leading to formation of fast-ice "islands" in some regions.

Fast ice can form either thermodynamically, growing *in situ* (*Kawamura et al.*, 1997; *Tison et al.*, 1998), or dynamically, being advected by winds and ocean currents into and subsequently attaching to existing fast ice and/or stationary coastal features (e.g., grounded icebergs or coastal promontories (*Massom et al.*, 2001b)). One striking feature of fast ice formation is its inter-annual recurrence in certain locations (*Giles et al.*, 2008) such as near the Mertz Glacier Tongue (MGT), East Antarctica (67.5° S, 144.75° E) (*Massom et al.*, 2010a). This phenomenon is

linked to local bathymetry, associated grounded iceberg distribution, and the shape of the coastline and the protective effects of adjacent areas of sea ice and icebergs (*Massom et al.*, 2001a; *Massom*, 2003).

Figure 1.1: Research and Supply Vessel (RSV) *Aurora Australis* parked in fast ice, near the pack ice/fast ice interface, ∼65.5° S, 124.75° E, September, 2007. *Picture credit: Adam Steer.*

1.2 The Importance of Fast Ice

Given the lack of knowledge about Antarctic fast ice, developing an improved understanding of its distribution and variability is of crucial importance for a number of reasons:

- Fast ice forms an important interface between the Antarctic ice sheet and pack ice/ocean, and is a pre-eminent feature of the coastal zone (where it reforms in the same locatation each year, or persists year-round in more sheltered locations, as noted above). As well as prolonging the residence times of ungrounded icebergs (*Massom*, 2003), recent work has shown that fast ice may

act to mechanically stabilise floating glacier tongues and ice shelves, delaying their calving and ultimately affecting ice sheet mass balance (*Massom et al.*, 2010a), with possible implications for sea level rise;

- despite the physical significance of fast ice, it is currently not represented in global climate circulation models or coupled ice-ocean-atmosphere models;

- since fast-ice extent responds rapidly to both atmospheric and oceanic forcing (*Mahoney et al.*, 2007b; *Heil*, 2006; *Massom et al.*, 2009), it is probable that it is a sensitive indicator of climate change (*Murphy et al.*, 1995; *Mahoney et al.*, 2007a; *Divine et al.*, 2003);

- as it can attain considerable thickness of >5 m and possibly up to 50 m for perennial fast ice (*Massom et al.*, 2010a), it forms an important component of the ocean freshwater budget. Indeed, *Giles et al.* (2008) estimated from Radarsat Synthetic Aperture Radar (SAR) snapshots in the Novembers of 1997 and 1999 that while fast ice forms only ∼8% of total sea ice area in the region 75.15 - 170.30° E, it may comprise ∼30-40% of the ice by total volume;

- fast-ice features are often associated and coupled with coastal polynyas (*Massom et al.*, 2001b). These areas of open water, thin ice or lower pack-ice concentration within the interior of the pack ice zone are important sea-ice production factories (*Tamura et al.*, 2008; *Barber and Massom*, 2007; *Martin*, 2001; *Massom et al.*, 1998; *Cavalieri and Martin*, 1985). In a few key locations around the Antarctic coast, these "windows" into the high-latitude Southern Ocean are globally important sites of Antarctic Bottom Water formation (*Rintoul*, 1998), and influence global thermohaline circulation (*Rintoul*, 1998; *Williams et al.*, 2008);

- along with pack ice, fast ice is biologically important at various trophic levels,

providing a habitat for both micro-organisms (*McMinn et al.*, 2000; *Arrigo et al.*, 1993; *Garrison*, 1991; *Swadling et al.*, 2000; *Günther and Dieckmann*, 2001) and large animals such as Weddell seals (*Leptonychotes weddellii*) and Emperor penguins (*Aptenodytes forsteri*) (*Massom et al.*, 2009; *Kooyman and Burns*, 1999; *Lake et al.*, 1997; *Kirkwood and Robertson*, 1997; *Wienecke and Robertson*, 1997; *Reijnders et al.*, 1990). The seaward fast ice edge forms the interface between stationary and moving ice, the location of which is an important factor in determining the breeding success of Emperor penguins (*Massom et al.*, 2009); and

- the distribution and seasonality of fast ice has significant implications for polar marine navigation and logistics, particularly for bases such as the Japanese Syowa Station located in Lützow-Holm Bay (*Uto et al.*, 2006; *Ushio*, 2006).

The work in this thesis has been motivated by the need to provide a much improved understanding of fast-ice extent and variability to contribute to all of these areas. The techniques developed in this thesis are also potentially applicable to the Arctic, where fast ice forms a margin for flaw lead formation. Another factor in the Arctic is the role of fast ice in decelerating coastal erosion (*Mahoney et al.*, 2007a). Fast ice also plays a prominent role in the daily lives of indigenous Arctic cultures (*George et al.*, 2004).

1.3 Gaps in Our Knowledge

The current lack of knowledge of large-scale Antarctic fast-ice distribution and variability largely stems from difficulties associated with discriminating fast ice from pack ice in satellite data, and the narrow though zonally-extensive coverage of fast ice. Section 1.4 presents an overview of the technical difficulties of fast-ice

remote sensing. Here, we focus on current fundamental gaps in our knowledge.

To date, Antarctic sea-ice research has focused almost exclusively (with a few notable exceptions, e.g., *Giles et al.* (2008); *Massom et al.* (2009)) on studies and climatologies of overall sea-ice extent without discriminating between pack and fast ice, e.g., *Comiso* (2010); *Comiso and Nishio* (2008); *Cavalieri and Parkinson* (2008); *Lemke et al.* (2007); *Zwally et al.* (2002). As a result, relatively little is known about larger-scale aspects of Antarctic fast-ice distribution and its spatio-temporal variability. By the same token, little is currently known about the relative role of environmental factors (e.g., meteorological forcing, ocean currents, wave-ice interaction), both individually and as an ensemble, as they affect the growth and breakout of fast ice around the Antarctic coast. It follows that the possible response of fast ice to climate change cannot be accurately predicted (fast ice is also not included in current global climate models).

To date, the majority of Antarctic fast-ice research has largely focused on the localised, *in situ* acquisition and analysis of physical and/or biological measurements close to bases, e.g., *Higashi et al.* (1982), *Kawamura et al.* (1997), *Ohshima et al.* (2000) and *Uto et al.* (2006) in and around Lützow-Holm Bay (∼69° S, 37.5° E); *Heil* (2006), *Lei et al.* (2010) and *Tang et al.* (2007) around Davis Station (∼68.5° E, 78° S); and *Pringle et al.* (2007), *Purdie et al.* (2006) and *Smith et al.* (2001) in the Ross Sea.

Fast ice formation/break-up behaviour have been monitored at a limited number of Antarctic sites using satellite imagery, but only on regional spatial scales (covering <∼300 km of coastline at most). These studies have taken place primarily in and around Lützow-Holm Bay (*Enomoto et al.*, 2002; *Mae et al.*, 1987; *Ushio*, 2006, 2008; *Yamanouchi and Seko*, 1992), the Ross Sea (*Brunt et al.*, 2006; *Lythe et al.*, 1999), the Adélie Land Coast (∼134 to 143° E, *Massom et al.*, 2009), and

the South Orkney Islands (∼45.5° W, 60.5° S, *Murphy et al.*, 1995). The studies based in the vicinity of Lützow-Holm Bay and Dumont d'Urville Station (i.e., the East Antarctic studies) are discussed here in greater detail, to indicate the nature of the work to date.

Massom et al. (2009) used cloud-free National Oceanic and Atmospheric Administration (NOAA) Advanced Very High Resolution Radiometer (AVHRR) data to create a time series of fast ice off the Terra Adélie coast (134 to 143° E) from 1992 to 1999, and highlighted the strong links between fast-ice parameters (overall extent and nearest distance to open water for foraging) and Emperor penguin breeding success at a colony near Dumont d'Urville Station. A case study of anomalously low fast-ice extent during 1998 revealed the strong links between fast-ice breakout and strong offshore wind anomalies (i.e., changes in wind direction and strength). In another study using AVHRR imagery, *Massom et al.* (2003) documented the large-scale breakout of perennial fast ice in the region to the east of the Mertz Glacier Tongue (off the George V Land coast). This occurred in response to an anomalous shift in the pattern of atmospheric circulation in the October-February period of 1999-2000.

Further to the west, *Ushio* (2006) used sequences of AVHRR channel 4 (thermal infrared) images to detect and identify fast ice in Lützow-Holm Bay from 1980 to 2004. Though this work was at a high temporal resolution (i.e., 10 days), fast-ice extent and its variability was not quantified within the bay - rather, the fast-ice morphology was manually classified into broad classes. Snow depth was found to be associated with fast-ice stability (deep snow gives greater stability) at this location, a finding also reported in a later work (*Ushio*, 2008). This enhanced stability was attributed to the formation of superimposed ice from melted snow during summertime, which acts to mechanically strengthen the ice (*Kawamura et al.*,

1997). *Mae et al.* (1987) also used AVHRR observations of the bay to associate fast-ice breakout with an increase in the thermal infrared brightness temperature of the ice. *Enomoto et al.* (2002) used a number of satellite instruments (the Advanced Visible and Near Infrared Radiometer (AVNIR) on the ADvanced Earth Observing Satellite (ADEOS), as well as the Scanning Multichannel Microwave Radiometer (SMMR) and the Special Sensor Microwave/Imager (SSM/I), both of which are passive microwave instruments) to observe the near-complete fast-ice breakout in Lützow-Holm Bay during 1997 and 1998. SMMR and SSM/I observations of snow melt revealed that significant fast-ice breakout events in the bay were associated with long melting periods during the preceding summer.

Two remote-sensing studies of Antarctic fast-ice extent have been conducted on a broader spatial scale: *Kozlovsky et al.* (1977, cited in Fedotov et al. 1998); and *Giles et al.* (2008). *Kozlovsky et al.* (1977, cited in Fedotov et al. 1998) measured fast-ice extent across East Antarctica (0° E to 160° E), but sampling was sparse and sporadic (conducted mainly using aircraft-based observations), and insufficient to study fast-ice formation or breakup. In a more contemporary study, *Giles et al.* (2008) applied image cross-correlation techniques to Radarsat Synthetic Aperture Radar (SAR) image pairs to produce "snapshots" only of fast-ice extent along the East Antarctic coast (75 - 170° E) during the Novembers of 1997 and 1999. Ice volume was then roughly estimated by using ice roughness as a proxy for ice thickness, based upon limited *in situ* observations. "First-year"/low SAR backscatter ("multi-year"/high SAR backscatter) fast ice was prescribed a thickness of 1 m (5 m). East Antarctic fast ice in November was found to comprise an estimated 8% of total sea-ice cover by areal extent, but a much more significant ∼30% of the total sea-ice volume (averaged over the sector 86 - 151° E). To date, no study of Antarctic fast ice has combined large-scale coverage, multi-annual time series and

high spatio-temporal resolution.

Considerable work has been conducted on fast-ice extent and variability in parts of the Arctic. There, it has focused on fast-ice variability and extent within the Kara Sea, north-western Russia (*Divine et al.*, 2005, 2003) and along the north coast of Alaska, i.e., the Beaufort Sea (*Mahoney et al.*, 2007a,b, 2004; *George et al.*, 2004).

Mahoney et al. (2004) developed techniques to determine the location of the Seaward Landfast Ice Edge (SLIE) from sequences of Radarsat SAR imagery. These techniques were used in a later study (*Mahoney et al.*, 2007a) to produce a climatology (1996-2004) of fast ice along the north coast of Alaska, and to assess the variability of fast-ice extent in conjunction with atmospheric parameters. *Mahoney et al.* (2007b) used a land-based marine radar situated at Point Barrow, Alaska, to study fast-ice formation and breakup events in unprecedented spatio-temporal resolution over a more limited area. *George et al.* (2004) detailed observations (including anecdotes, weather station data and satellite images) of two unexpected fast-ice breakouts which threatened indigenous hunters in Arctic Alaska. It is likely that events such as these will become more commonplace under the predicted tropospheric warming scenarios (*IPCC*, 2007; *Flato and Brown*, 1996) and as Arctic pack-ice cover diminishes (*Perovich et al.*, 2008).

As mentioned, fast-ice extent and variability have also been studied in the Kara Sea (*Divine et al.*, 2005, 2003). These studies used 12.5 km resolution Arctic and Antarctic Research Institute (AARI) ice charts (created from Russian aircraft and satellite observations), with a temporal resolution of between 10 and 30 days, to determine fast-ice extent and variability. The studies linked fast-ice extent (from 1953 to 1990) with large-scale atmospheric circulation. The strength of the climatological Arctic High was found to modulate fast-ice extent, by blocking the passage

of destructive cyclonic systems.

While detailed studies of Arctic fast-ice formation, breakup and extent have taken place, (e.g., *Mahoney et al.*, 2007a), there has been no similar Antarctic study to provide "big picture" information on fast-ice distribution and its spatio-temporal variability. Work carried out in this thesis aims to address this deficiency.

1.4 Satellite Techniques for Remote Sensing of Fast Ice

As briefly outlined in the previous section, a number of methods have been used to detect and monitor fast ice from space, in both the Antarctic and Arctic. These can be broadly classed as i) microwave-based (including SAR), and ii) visible/thermal infrared-based. A key difference between these two classes is the effect of cloud, which presents a major problem for visible/infrared wavelengths but has little effect at the frequencies used in microwave techniques aimed at sensing the Earth's surface.

1.4.1 Microwave Remote Sensing of Fast Ice

A number of fast-ice studies have made use of the ability of microwave sensors to penetrate cloud cover and darkness, e.g., *Giles et al.* (2008); *Mahoney et al.* (2004). The tendency of fast ice to form in narrow bands around the coast precludes the use of relatively low-resolution passive microwave remote sensing (the key tool for studying overall sea ice extent and seasonality) for remotely discriminating pack from fast ice. Passive microwave imagery has been used to determine sea-ice velocity (*Maslanik et al.*, 1998), but its low spatial resolution offers little promise for detecting the small-scale ice motion which separates the pack ice from the fast ice. Indeed, the distance from the coast to the seaward fast-ice edge is at times less than the footprint of a passive microwave sensor channel. This is due in large part to the diffraction-

limited angular extent (and subsequent ground footprint size/spatial resolution) of an aperture, which is directly proportional to wavelength and inversely proportional to aperture dimension (*Born and Wolf*, 1975). This results in a relatively low resolution image of the Earth's surface, with footprint sizes on the order of 5 to 50 km (frequency-dependent). Ice concentration products range in resolution from 6.25 to 25 km (*Lubin and Massom*, 2006). Errors are introduced when pixels span areas including both the continental ice sheet and sea ice (mixed pixel effects). This problem is again exacerbated by the relatively large pixel sizes of passive microwave imaging.

SAR techniques, on the other hand, excel at obtaining high resolution images which may be suitable for fast-ice studies, e.g., *Giles et al.* (2008); *Mahoney et al.* (2007a). Using SAR techniques, phase information recovered from the backscattered signal can be processed in order to provide extremely high resolution images of the surface, with pixel sizes down to $\sim$1 m in some current implementations (*Jackson and Apel*, 2004; *Werninghaus*, 2004), but more typically of the order of 100 m. However, fast ice is often indistinguishable from pack ice and wind-roughened open water based upon "snapshot" analysis of normalised backscatter values alone (*Lythe et al.*, 1999). Though SAR imagery is of a much higher spatial resolution (i.e., typically tens of metres) than passive microwave imagery, it is inherently difficult to interpret (*Oliver and Quegan*, 1998), particularly over polar oceans (*Beaven et al.*, 1997).

Gill and Valeur (1999) used single SAR images in an attempt to classify ice types off the coast of Greenland based on first-order texture parameters such as Power-to-Mean Ratio (PMR), skewness (the asymmetry of pixel backscatter distribution) and kurtosis (a measure of the shape of the peak of the pixel backscatter distribution). It was found that fast ice could not be differentiated from open water

using this technique. However, fast ice and open water could be differentiated from thin ice and ice of concentration between 40% and 90%.

Lythe et al. (1999) also used single SAR images for fast-ice classification in the Ross Sea, Antarctica, during late winter/early spring ice, but combined observations with coincident AVHRR cloud-free imagery. It was found that (thermodynamically-formed) fast ice uniquely exhibits a signature of low SAR backscatter and low AVHRR band 4 (thermal infrared) radiance. The low AVHRR radiance was attributed to fast ice being generally thicker than pack ice, thus being better insulated from the warm ocean and having a lower brightness temperature and radiance, though it was expected that thermal emission is also strongly dependent on surface air temperature. The low SAR backscatter was attributed to the relative lack of deformation inherent to fast ice that formed in situ in a sheltered location.

Working along the north coast of Alaska, *Mahoney et al.* (2004) presented an automated technique for determining the SLIE from SAR data (applied to Arctic regions). The SAR data were first smoothed by sub-sampling, then the horizontal and vertical vector gradients of the scalar (smoothed SAR backscatter) field were calculated. Differences between successive processed SAR images were then calculated, clearly showing the SLIE. This technique was used (again in Arctic regions) by *Mahoney et al.* (2005), but with less success due to variable SAR backscatter during times other than mid-winter. Manual classification was required for these times. Ice type discrimination using SAR is typically difficult outside of winter/early spring due to the inclusion of water into the snow volume, thus reducing the backscatter similarities between ice types (see *Lubin and Massom* (2006) and references therein).

SAR interferometry (InSAR) also holds some promise for automated fast-ice detection (*Dammert et al.*, 1997; *Morris et al.*, 1999). To produce a SAR interferogram, two complex SAR images are required (separated by a suitable spatio-

temporal baseline), and phase information is retained for each pixel. One image is conjugated, then the images are multiplied on a per-pixel basis (*Massom et al.*, 2006b). The resulting phase is then extracted, producing the interferogram. The equation for this phase difference is given as follows (after *Dammert et al.*, 1997):

$$\Delta\varphi = \frac{4\pi B_n}{\lambda R sin\theta}\Delta h + \frac{4\pi}{\lambda}\Delta\eta + \Phi_{noise} + n \times 2\pi \tag{1.1}$$

where $\Delta\varphi$ is the phase difference produced by interfering the images, B_n is the baseline between the two positions of the satellite, R is the mean satellite position to a point of interest on the surface, θ is the angle to nadir, h is the height of a feature on the surface, and η is a horizontal displacement (in the look direction). The first term is sensitive only to changes in height, while the second term is sensitive only to changes is displacement (in the look direction). Φ_{noise} is the phase noise due to decorrelation of scatterers. The final term arises due to ambiguity inherent to any phase measurement.

Using InSAR processing of ERS-1 SAR data (3 to 6 day temporal baseline), *Dammert et al.* (1997) found the displacement required to produce a phase difference of 2π in the interferogram to be 65 m in the vertical or 28 mm in horizontal displacement, making this technique incredibly sensitive to horizontal motion but much less sensitive to changes in height. For this reason, this technique can be applied to fast-ice detection where tidal variations produce negligible phase changes - or tidal displacement can be effectively removed - but horizontal movements contribute considerably to the phase difference. Due to the extreme sensitivity of the technique to horizontal motion, the moving pack ice produces random phase difference between successive images (i.e., in the interferogram). The coherent interference fringes produced over fast ice are relatively easy to separate from the random phase difference produced over pack ice in the resulting interferogram.

Morris et al. (1999) produced a series of ERS-1 SAR-derived data products covering a section of fast ice situated in the East Siberian Sea during late 1993 - early 1994. In addition to the phase fringe interferogram used by *Dammert et al.* (1997), a phase correlation image was produced for SAR image pairs, which showed discontinuities of the phase fringes. These phase correlation images were particularly useful in finding small-scale flaw leads in the sea ice which were not detected by single SAR images. Though not designed with interferometry in mind, the ERS-1 instrument with its 3-day repeat orbit is in theory well suited to SAR interferometry, and useful interferograms can be generated from pairs of images separated by 3 days (*Coulson and Guignard*, 1994). In practice, however, relatively few suitable image pairs are available for interferometric analysis, particularly in the Antarctic coastal zone. The ERS Tandem Mission (October 1995 to June 1996), with its repeat orbit of one day achieved using the ERS-1 and ERS-2 platforms, was also well suited to producing useful short temporal baseline interferograms (*Zandbergen et al.*, 1997). It is worth noting that single-pass SAR interferometry will likely be of less use to fast-ice detection since the second term in equation 1.1 will vanish, meaning that the interferogram will no longer be sensitive to horizontal motion.

More recent SAR systems are also suitable for interferometric SAR analysis, but application of these techniques is still limited by fundamental constraints (*Massom and Lubin*, 2006). Historical data are often unavailable due to suitable data being collected only when programmed to do so; and SAR interferometry performs best when viewing geometry is identical between two passes, meaning that the minimum temporal baseline is equal to the repeat orbit interval. This ranges from 35 days with the European Space Agency (ESA) Envisat Advanced SAR (ASAR, 2002 - present) to 11 days with the German Aerospace Center's TerraSAR-X (2007 - present). Furthermore, the cost of acquiring sufficient SAR data for large-scale

fast-ice analysis is often prohibitive for scientific users.

A relatively new SAR capability is the inclusion of polarimetric observation capabilities. SAR systems such as ASAR, launched in 2002, include the ability to acquire SAR data simultaneously at different polarisations (*Zink et al.*, 2001). The Japanese Aerospace eXploration Agency (JAXA) Phased Array L-band SAR (PALSAR), the Canadian Space Agency's Radarsat-2 and the German Aerospace Center's TerraSAR-X instruments also support polarimetric SAR capability (*Lubin and Massom*, 2006). It remains to be seen how the inclusion of polarimetric data into SAR analyses will influence discrimination between pack and fast ice (see references in *Massom and Lubin* (2006)). Techniques for using polarimetric SAR imagery for ice classification are still under development, and coverage of SARs operating in full polarimetric mode is typically limited to swath widths of a few tens of km. This precludes broad-scale coverage and analysis.

1.4.2 Visible/Thermal Infrared Remote Sensing of Fast Ice

Given the constraints and limitations outlined above, wide-swath visible/thermal infrared sensors offer a viable alternative for broad-scale fast-ice detection and monitoring, provided cloud cover can be accurately detected and removed (thermal infrared data can be used during darkness). The Advanced Very High Resolution Radiometer (AVHRR), a visible/thermal infrared imager onboard several NOAA satellites, observes the Earth at a resolution of 1.1 km with a 2,500 km-wide swath. It covers a wide range of wavelengths (0.6 μm to 12 μm), though only in 4 to 6 spectral channels (*Cracknell*, 1997). Although the AVHRR was first launched in 1978, coverage of Antarctic coastal regions tends to be somewhat patchy (particularly prior to the early 1990s). This was due in large part to a lack of sufficient onboard image storage capacity, the need to downlink in real-time to

dedicated receiving stations to gain full-resolution (1 km) coverage, and a lack of digital archiving. In regions with no dedicated receiving stations, e.g., much of the East Antarctic coast prior to the early 1990s (when an AVHRR receiving station was installed at Casey Station), data are only collected at a 4 km spatial resolution. Where available, however, AVHRR data have been used extensively for sea-ice motion detection studies (e.g., *Heacock et al.*, 1993; *Ninnis et al.*, 1986), but with the exception of a few analyses of small regions (see Section 1.3), it has not been used extensively for fast-ice studies in either hemisphere. Geolocation accuracy is also an issue when using AVHRR data in remote polar regions with few ground-control points.

Pixel sizes for passive visible - TIR instruments currently in orbit vary considerably from ∼1 km (AVHRR, MODIS TIR channels) to an impressive submetre resolution with satellites such as WorldView-2 (46 cm resolution, *Glass et al.* (2010)). The Landsat Multi-Spectral Scanner (MSS) and Enhanced Thematic Mapper (ETM+) instruments are other examples of widely-used, high-resolution visible imagers, with horizontal resolution up to 15 m. Despite the obvious advantages of the high resolution Landsat imagery for ice classification applications, one particularly limiting drawback of these imagers is their narrow swath width, which adversely affects the temporal coverage of the instrument for any given point on the surface and means that many images are required to cover extensive coastal regions.

For this study, we use data from a newer and much improved instrument - the MODerate resolution Imaging Spectroradiometer (MODIS) onboard the two NASA Earth Observing System (EOS) satellites Terra and Aqua (launched in December 1999 and May 2002, respectively). An excellent introduction to MODIS (and several other EOS instruments) is provided by *Parkinson* (2003), and data and specifications are available from the MODIS website (http://modis.gsfc.nasa.gov/).

MODIS images are acquired over a wide swath (2,330 km), and cover a wide range of wavelengths (see Table 2.1 in Chapter 2 for a complete list of MODIS channel centroid wavelengths). The 36 MODIS spectral channels cover wavelengths from visible (0.415 μm) to TIR (14.235 μm), offering a higher spectral resolution than AVHRR sensors. The TIR pixel size is an AVHRR-equalling 1 km at nadir, but 500 m for channels 3-6 and 250 m for channels 1 and 2. The polar orbit of the Terra and Aqua satellites produces excellent temporal coverage at high latitudes. The wide range of spectral channels available allows production of an accurate spectral cloud mask (*Ackerman et al.*, 2006). Terra MODIS was commissioned in 2000, with Aqua MODIS following in 2003. Calibrated MODIS imagery is readily and freely available from the Level 1 Atmosphere Archive Distribution System website (http://ladsweb.nascom.nasa.gov/). MODIS holds several advantages over AVHRR for this application. In particular, the wealth of spectral channels enables the production of a more accurate cloud mask product than is possible with AVHRR, a key to the success of the procedures detailed in this thesis. Furthermore, routine coverage of the Earth and full-resolution recording at all times facilitates the regular and frequent temporal coverage for a given point on the surface. More accurate geolocation is also possible with MODIS versus AVHRR images around Antarctica. Despite the technical superiority of MODIS over AVHRR (particularly its higher spectral resolution), it has yet to be extensively used for fast-ice detection. AVHRR is still useful when long time series of data are required (i.e. pre-2000).

It is theoretically possible to identify fast ice from a single satellite image by detecting areas of ice which are consolidated and contiguous with the coast. However, this technique presents difficulties for automation, requires high-quality, cloud-free imagery, and is unable to discriminate between fast ice and pack ice which has been temporarily advected against the coast and/or existing fast ice by

ocean currents and winds. Fast ice is in general spectrally identical to pack ice of a similar thickness and roughness (*Lythe et al.*, 1999), making accurate "snapshot" differentiation difficult in many locations.

An alternative technique for discriminating fast from pack ice is to use time series of satellite imagery to distinguish between moving (pack) and stationary (fast) ice. The detection of ice motion using satellite imagery is generally achieved by performing image cross-correlation techniques on series of temporally closely-spaced satellite image pairs which are accurately geolocated (*Fowler et al.*, 2001; *Giles et al.*, 2008, 2009; *Mahoney et al.*, 2004). Due to the adverse affects of cloud on visible/TIR imagery, this technique is generally applied to radar imagery (either passive or active), e.g., *Giles et al.* (2008).

Figure 1.2: RSV *Aurora Australis* parked in fast ice off the East Antarctic coast, near Davis Station (∼68.5° S, 78° E) in November, 2008. The fast ice is anchored to grounded icebergs in the background. *Picture credit: Adam Steer.*

The MODIS dataset was chosen for this work because it combines excellent polar synoptic coverage (a 2,330 km-wide swath, compared with SAR swath width

of less than 500 km) with sufficient resolution for discriminating pack from fast ice (1 km in thermal infrared (TIR) bands). Moreover, MODIS imagery is routinely acquired, without data complications associated with changing sensor modes as found with SAR instruments (*Lubin and Massom*, 2006). Furthermore, MODIS imagery is readily available and free of cost (as opposed to SAR imagery), and relatively easy to process and interpret (especially compared with SAR over the sea-ice zone). The MODIS dataset has broad and regular coverage of the narrow but zonally-extensive fast-ice zone - an extensive zone that cannot easily be covered and monitored by satellite SAR data and high-resolution (narrow-swath) visible imagery, and remains largely unresolved in coarse resolution (i.e., 6.25 - 25.0 km) passive microwave sea-ice concentration data.

A major challenge using the MODIS visible-TIR time series is to derive reasonable coverage of the fast ice is in the treatment of cloud cover (*Fraser et al.*, 2009). The East Antarctic coast has persistent cloud cover, averaging 93% in October, compared with a global average of 70% (*Spinhirne et al.*, 2005). Large parts of Chapters 2 and 3 are devoted to overcoming the problems associated with cloud-cover detection over sea ice and its removal to produce uncontaminated time series of MODIS-derived fast-ice maps.

1.5 Aims of the Project

The aims of this work were threefold:

1. To use visible-TIR MODIS satellite data, supplemented by Advanced Microwave Scanning Radiometer - Earth Observing System (AMSR-E) data when required (i.e., to fill in gaps in MODIS coverage), to detect Antarctic fast ice and to build up a continuous time series of fast ice extent based

upon cloud-free images over the period March 2000 - December 2008;

2. to use this time series to carry out a detailed analysis of the spatio-temporal characteristics of fast ice in the East Antarctic sector from 10° W to 172° E, a distance of ∼8,600 km; and

3. to investigate the influence of atmospheric parameters (on scales ranging from local to hemispheric) on fast-ice formation and breakout.

An overall motivation is to produce a new time series of fast-ice extent that will form a key climatic baseline against which to gauge future change, and which is equivalent to the widely-used pack-ice products, e.g., *Comiso* (2010); *Cavalieri and Parkinson* (2008). Such data are also required by, for example, the biological community to assist with interpretation of biological datasets, and the ocean modeling community, who will use fast-ice maps as part of their domain definition.

Figure 1.3: Aerial photograph of the RSV *Aurora Australis* at the fast ice/ocean interface off the East Antarctic coast near Davis Station (∼68.5° S, 78° E) in November, 2008. *Picture credit: Australian Antarctic Division.*

1.6 Format of the Thesis

This thesis is formatted in the "thesis by publication" style, with each main chapter presenting and expanding upon the work of each of four refereed publications (two published, one submitted, and one in preparation) in high-profile international scientific journals. The thesis is structured as follows:

- Chapter 2 outlines the methods used to produce the MODIS composite images (based on *Fraser et al.*, 2009);
- Chapter 3 extends this work by combining MODIS composite images with AMSR-E images in order to generate maps of fast-ice extent (based on *Fraser et al.*, 2010a);
- Chapter 4 presents the fast-ice time series, and an in-depth analysis of fast-ice extent/timing trends and their relation to sea-ice extent (based on *Fraser et al.,* subm.);
- Chapter 5 investigates the influence of atmospheric parameters on fast-ice formation and breakout (based on *Fraser et al.,* in prep.); and
- Chapter 6 presents an overall conclusion, and suggests further work.

Three appendices are included at the end of the thesis:

- Appendix A includes a reprint of the paper upon which Chapter 2 is based, published in IEEE Transactions on Geoscience and Remote Sensing and entitled *A method for compositing polar MODIS satellite images to remove cloud cover for landfast sea-ice detection.*
- Appendix B includes a reprint of the paper upon which Chapter 3 is based. This is published in Remote Sensing of Environment, and is entitled *Gener-*

ation of high-resolution East Antarctic landfast sea-ice maps from cloud-free MODIS satellite composite imagery.

- Appendix C, presented on a CD-ROM disc, is the full time series of fast-ice maps (March 2000 - December 2008), including associated information on georeferencing the maps to aid end users in viewing the maps in the context of other spatial data.

Chapter 2

A Method for Compositing Polar MODIS Satellite Images to Remove Cloud Cover for Landfast Sea-Ice Detection

This chapter is an edited version of a paper which has been published as:

Fraser, A. D., R. A. Massom, and K. J. Michael, A method for compositing polar MODIS satellite images to remove cloud cover for landfast sea-ice detection, *IEEE Transactions on Geoscience and Remote Sensing, 47* (9), 3272-3282, doi:10.1109/TGRS.2009.2019726, 2009.

A reprint of this publication is included in Appendix A.

2.1 Abstract

This chapter presents details of techniques for generating thermal infrared and visible composite images from the cloud-free portions of temporally closely-spaced MODIS images, with a focus on deriving consistent time series maps of the extent of landfast sea ice (hereafter referred to as fast ice) along the entire East Antarctic coast (10° W to 172° E). Composite image inclusion criteria are based on

a modified MODIS cloud mask product. The compositing process presented places emphasis on retaining maximum spatial resolution while minimising storage space requirements. Composite images can be produced either as a regular product (e.g., on a 20-day grid), or dynamically (whenever enough information is acquired to produce a new output image). These techniques are applicable at any latitude, are available for all MODIS channels at their native resolution, can combine Aqua and Terra images, and can produce maps in any output projection. However, due to the polar orbit of NASA's Terra and Aqua satellites which host the MODIS instrument, more frequent coverage is produced at higher latitudes. Thus, the techniques presented are particularly applicable to polar research. Examples composite images covering the fast ice around the Mertz Glacier region, East Antarctica (∼67.5° S, 144.75° E), are presented for both winter and summer.

2.2 Introduction

Nadir-imaging radiometers operating at visible to thermal infrared (TIR) wavelengths, such as the 36-channel MODIS (MODerate resolution Imaging Spectroradiometer) instrument (*Parkinson*, 2003) onboard the NASA (National Aeronautics and Space Administration) satellites Aqua and Terra, have significantly contributed to our understanding of many polar geophysical processes and phenomena (*Khalsa et al.*, 2006; *Lubin and Massom*, 2006; *Massom and Lubin*, 2006). However the Antarctic coast and sea-ice zone are notorious for having a persistently high cloud cover fraction, particularly in summer. *Spinhirne et al.* (2005) report the zonally-averaged East Antarctic coastal cloud cover during October 2003 to be 93%, compared to a global average of around 70% (*Spinhirne et al.*, 2004). This limits the applicability of individual MODIS images for observations of the polar surface.

Significant research has been conducted on cloud detection using multi-

spectral imaging instruments, e.g., MODIS or NOAA AVHRR sensors (see *Lubin and Massom* (2006) and the references therein). While cloud detection is relatively simple during daytime and over most surfaces (e.g., *Ackerman et al.* (2006)), difficulties in are encountered over snow-covered surfaces, particularly during hours of darkness (*Liu et al.*, 2004b). This is due to the small contrast in both albedo (during daytime), and brightness temperature of clouds versus snow-/ice-covered surface (*Lubin and Morrow*, 1998; *Welch et al.*, 1992). The incorporation of MODIS channel 26 (1.375 μm) into the MODIS cloud mask product allows improved polar cloud discrimination during daytime (*Gao et al.*, 2003), though significant difficulties remain during hours of darkness, when this channel is unavailable. *Liu et al.* (2004b) have made improvements in night-time polar cloud detection with MODIS, by means of new spectral tests and revised thresholds over polar regions. These have been incorporated into the latest official MODIS MOD35 cloud mask product (*Ackerman et al.*, 2006).

One solution for minimising the effect of cloud cover at visible-TIR wavelengths is to produce a composite image of cloud-free pixels selected from several satellite passes separated by time. For low-Earth orbit satellites such as Terra and Aqua (in contrast to a geosynchronous orbit), accurate geolocation and reprojection from the original swath to a common map is essential for successful generation of the composite image. Selection of "cloud-free" pixels from component images is also critical to the success of a compositing algorithm. Cloud-free pixel selection is typically performed using either Maximum Value Compositing or by using spectral tests to pre-determine the probability of cloud contamination for each pixel before gridding (*Haines et al.*, 2007).

Maximum Value Compositing (MVC) is a class of compositing algorithm where several component images are first mapped to a common grid, then each

gridded pixel's probability of cloud contamination is assessed by comparing its value to the corresponding pixel from the other gridded images (*Comiso*, 1994, 1999; *Chen et al.*, 2003). One frequently-used MVC criterion is the maximum Normalised Difference Vegetation Index (NDVI) test (*Chen et al.*, 2003). This test involves reprojecting a number of different overpass swaths (which are closely spaced in time) onto a common grid to form a "pool" of pixels from which compositing algorithms can choose the most likely to be cloud-free for composition. Then on a per-pixel basis, the pixel with the maximum NDVI is chosen for compositing (*Rouse et al.*, 1974). This test relies on the assumption that for a given pixel over land, a higher NDVI usually indicates a lower cloud fraction. However, this test fails over ocean and snow/ice surfaces, due to their negative NDVI values (*Luo et al.*, 2007). Other simple MVC tests which fail over polar regions include the visible reflectance test (failure due to high reflectance from both surface and cloud) and brightness temperature test (failure due to the similar temperatures of surface and cloud in these regions) (*Ebert*, 1987).

Comiso (1994, 1999) used a two-stage MVC-style compositing algorithm to produce cloud-free Nimbus 7 Temperature Humidity Infrared Radiometer (THIR) polar composite images of surface temperature. The first stage involved choosing a pixel with the highest IR radiance, relying on the fact that tropospheric cloud is usually colder than the underlying surface. Secondarily, for areas of persistent cloud cover (such as the Antarctic sea ice zone), a rudimentary cloud motion detection feature was implemented. This motion detection algorithm excluded adding to the composite image during times when the brightness temperature differed by more than 12 K daily, a figure determined from histograms of daily brightness temperature difference. MVC has also been used with MODIS images to aid high-resolution mid-latitude burned-area mapping (*Dempewolf et al.*, 2007).

MODIS data are negatively affected by detector striping, particularly in some TIR channels (*Yang et al.*, 2003; *Ackerman et al.*, 2002). Striping occurs when, in a multi-detector instrument, there is inconsistent calibration between detectors. The effect is to produce darker or lighter "stripes" within the image, aligned in the cross-track direction. Spatial domain image convolution can be applied to rectify affected MODIS images, but important data can be lost due to image blurring. Users of other data products prone to striping - such as Landsat MSS (Multi-Spectral Scanner) images - have used techniques such as histogram matching, which are broadly applicable to MODIS imagery (*Horn and Woodham*, 1979). Several papers (*Antonelli et al.*, 2004; *di Bisceglie et al.*, 2009) have reported the use of the 'bow-tie effect' inherent to MODIS level 1b data as a form of data redundancy, facilitating the correction of data from the poorly calibrated detectors.

Using MODIS data to detect and monitor surface parameters depends upon the successful implementation of cloud masking to identify cloud-free pixels. The Earth Observing System (EOS) level 2 MOD35 cloud mask product (hereafter referred to as the MOD35 cloud mask) has been developed for this purpose, and is routinely created for each MODIS data granule (*Ackerman et al.*, 1998, 2006). Level 2 products are generally derived fields with quality control, but still at swath level. The MOD35 product gives the results of a series of spectral, per-pixel cloud mask tests generated from MODIS imagery (*Ackerman et al.*, 2006). Information on surface conditions (ocean, land, sea ice, snow) is provided by SSM/I passive microwave data. Table 2.1 gives spectral information on all MODIS channels and indicates which are used in the cloud mask product.

However, despite the MOD35 product's wide-ranging, comprehensive spectral tests and proven accuracy, especially at mid/lower latitudes, few compositing algorithms have made use of it for cloud masking. One exception is the MODIS

Table 2.1: The complete list of MODIS channels, including each channel's use in the MOD35 cloud mask product (reproduced after *Ackerman et al.* (2006))

Band	**Centroid** Wavelength μm	**Used in Cloud Mask**	**Primary Application**
1 (250m)	0.659	Y	(250 m and 1 km) clouds, shadow
2 (250m)	0.865	Y	(250 m and 1 km) low clouds
3 (500m)	0.470	N	
4 (500m)	0.555	Y	snow
5 (500m)	1.240	Y	snow
6 (500m)	1.640	Y	snow, shadow
7 (500m)	2.130	N	
8	0.415	N	
9	0.443	N	
10	0.490	N	
11	0.531	N	
12	0.565	N	
13	0.653	N	
14	0.681	N	
15	0.750	N	
16	0.865	N	
17	0.905	N	
18	0.936	Y	low clouds
19	0.940	Y	shadows
26	1.375	Y	thin cirrus
20	3.750	Y	shadow
21/22	3.959	Y(21)/N(22)	window
23	4.050	N	
24	4.465	N	
25	4.515	N	
27	6.715	Y	high moisture
28	7.325	N	
29	8.550	Y	mid moisture
30	9.730	N	
31	11.030	Y	window
32	12.020	Y	low moisture
33	13.335	N	
34	13.635	N	
35	13.935	Y	high cloud
36	14.235	N	

Sea Surface Temperature (SST) composite produced by *Haines et al.* (2007). Pixel inclusion into the composite image is based upon the MOD35 cloud mask. Day and night images from Terra and Aqua MODIS are respectively composited into four separate images to minimise biases between satellites and to isolate diurnal changes in SST. In this study, we use the MOD35 cloud mask, as well as a modified version of this mask (see Section 2.3.2).

Overly-conservative performance of the MOD35 product was reported by *Riggs and Hall* (2003) over snow-covered surfaces (i.e., clear-sky areas are often reported as cloudy). In response to this, *Riggs and Hall* (2003) developed a new cloud-masking algorithm (dubbed "the liberal cloud mask") for use with the mid-latitude MODIS snow cover product. Utilising a small subset of the MOD35 cloud mask tests plus some additional visible and near-infrared tests, the liberal cloud mask was developed to mask only those clouds obscuring the surface in shortwave channels, i.e., radiation with wavelength less than $\sim 2\mu$m. The heavy reliance on shortwave channels precludes the use of this style of technique for year-round polar work.

When generating composite images, it is important to consider the timescales of events which need to be resolved. While detailed studies of the timescales of fast-ice breakout/formation have not taken place in either hemisphere, 20 days has been suggested as a reasonable minimum time for Arctic ice to remain stationary before being classified as "fast" (*Mahoney et al.*, 2005). The challenge here is to generate composite images with sufficient temporal resolution to resolve fast-ice formation/breakout events, while at the same time producing composite images of a high quality, i.e., keeping the compositing interval as short as possible, while ensuring it is long enough to generate a cloud-free view of the surface in all parts of the map.

A further challenge here is to remove cloud cover contamination as accurately as possible. Due to the lack of sunlight during "winter" in Antarctica (in practice, approximately from mid-April until mid-October), it is necessary to generate TIR composite images for this time period. This poses additional challenges, particularly regarding the MOD35 cloud mask which suffers from reduced accuracy during darkness due to the unavailability of important shortwave cloud tests (*Ackerman et al.*, 2006; *Liu et al.*, 2004b). The solution employed here is to produce a modified version of the MOD35 cloud mask, hereafter referred to as the modified cloud mask. A large part of this chapter (see Section 2.3.2) is devoted to overcoming such problems with the MOD35 cloud mask during wintertime.

The study region in this chapter is centred around the Mertz Glacier Tongue (MGT) (see Figure 2.1). This region was chosen because it includes a diverse range of surface conditions such as continental (glacial) ice, fast ice, pack ice and open ocean (including polynyas). See *Massom et al.* (2001b) and *Barber and Massom* (2007) for a detailed description of the "ice-scape" of this region. It is also the site of recent work investigating the mechanical coupling between fast ice and the floating glacier tongue (*Massom et al.*, 2010a), and is a focus area for biological research (e.g., *Massom et al.* (2009)). Though the examples presented in this chapter are tailored for fast-ice detection applications, the techniques are generally suitable for other applications at any latitude.

2.3 Image Enhancement and Data Preparation

The concept behind the composite image generation process is to use cloud-free portions of temporally closely-spaced images to build one composite cloud-free image. Figure 2.2 schematically depicts the process of producing a composite MODIS image from individual MODIS granules. This involves accurate cloud mask-

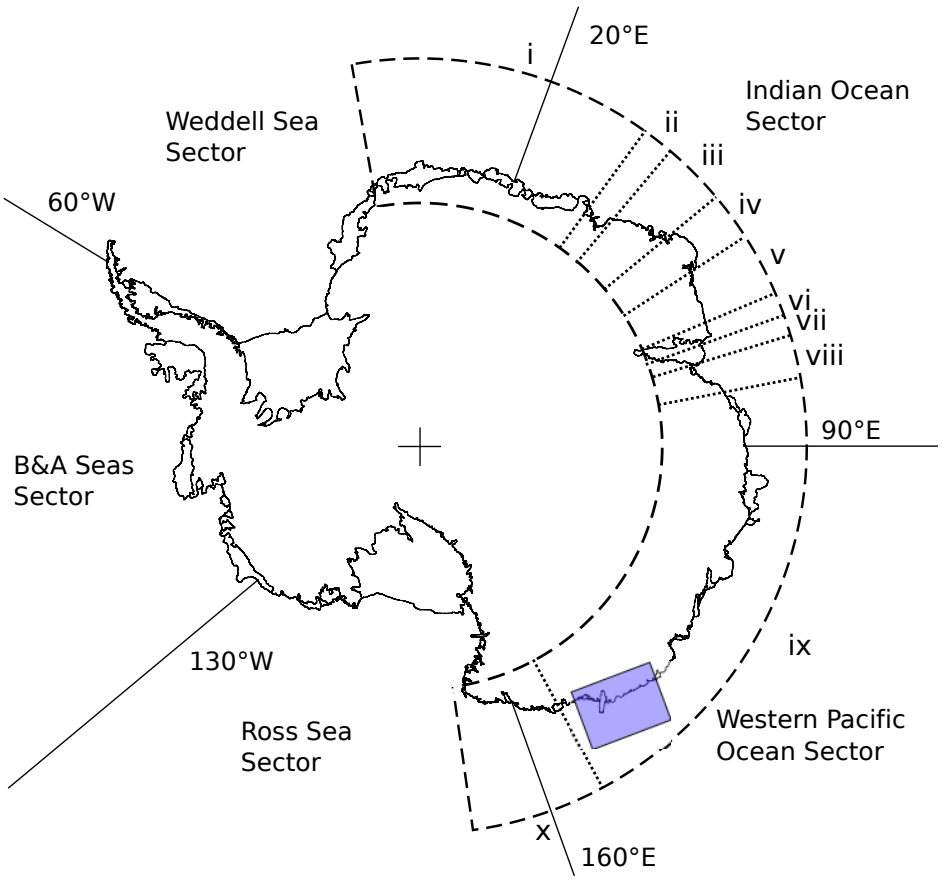

Figure 2.1: The study regions used in Chapters 2, 3 and 4. Chapter 2: the blue box shows the extents of the MODIS composite images created, in a region including the Mertz Glacier Tongue and surrounding fast ice, pack ice, continental (glacier) ice and open ocean. Chapter 3: the dashed line shows the extents of the fast-ice maps generated from MODIS composite images, covering the East Antarctic coast (from 10° W to 172° E). Chapter 4: the dotted lines (labelled i - x) delineate the boundaries of different fast-ice regimes examined in this thesis.

ing, gridding, coast masking, and finally, composite image generation.

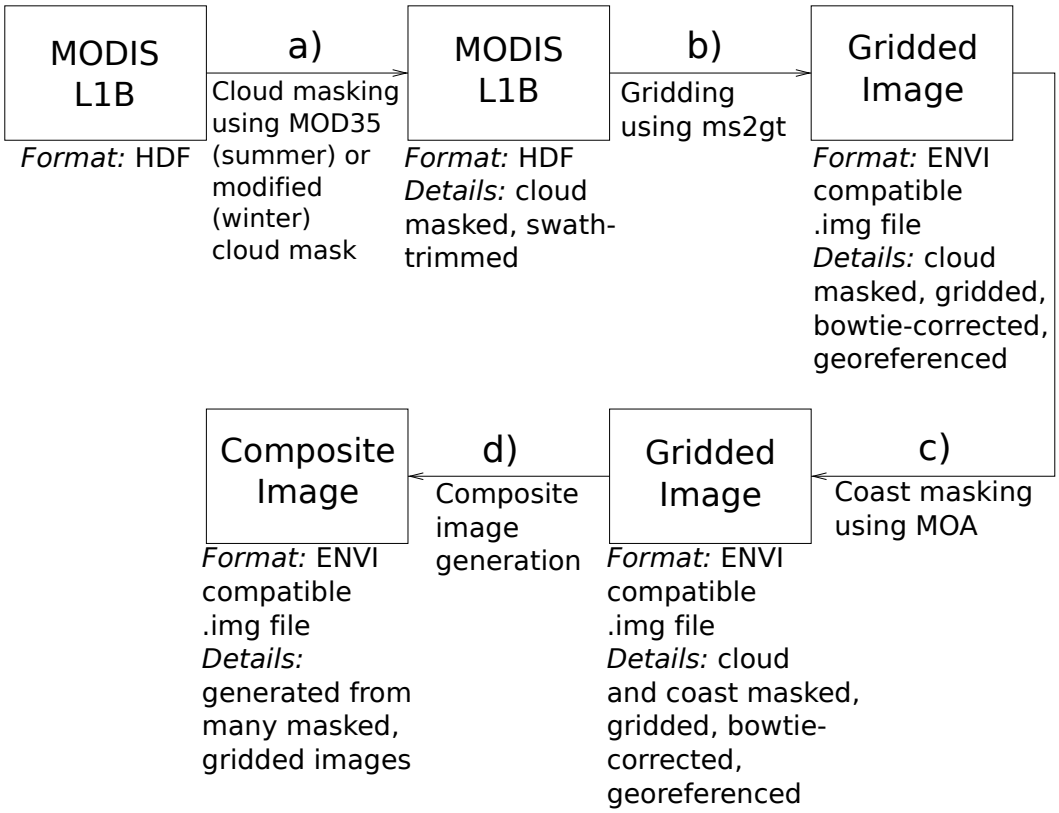

Figure 2.2: Schematic of the composite image generation process starting from MODIS Hierarchical Data Format (HDF) files. a) The MOD35 (modified) MODIS cloud mask product is used to mask the original HDF files during "summer" ("winter"). Swath trimming also occurs at this point (see section 2.3.3). b) The MODIS Swath-To-Grid Toolbox (ms2gt) suite of programs (*Haran et al.*, 2002) is used to grid, geolocate and remove bowtie artefacts (discontinuities between adjacent detector array scans) from MODIS images. c) The Mosaic Of Antarctica (MOA) coastline product (*Scambos et al.*, 2007) is used to mask the continent. At this stage, Solar Zenith Angle (SZA) normalisations were performed where applicable (shortwave bands only). d) Composite images are generated from cloud-free portions of many subsequent MODIS images covering the same area.

MODIS level 1B (reprocessed version 5) data, covering the periods from Day Of Year (DOY) 161 to 170 and from DOY 341 to 350, in 2005, were obtained from the MODIS Level 1 and Atmosphere Archive and Distribution System (LAADS) archives at the NASA Goddard Space Flight Center (currently accessible at http://ladsweb.nascom.nasa.gov/data/search.html). Level 1B fields are cali-

brated, low level data (in this case, radiances and reflectances).

Manual examination of a number of test scenes revealed that the 1 km-aggregated visible channel 1 (λ = 0.659 μm) and native 1 km TIR channel 31 (λ = 11.030 μm) were largely free from detector striping issues on both Terra and Aqua platforms. Image destriping issues (*Haran et al.*, 2002) were thus avoided by choosing only MODIS channels 1 and 31 for analysis. Throughout this thesis, infrared images are presented in a non-inverted colour scale, i.e., cold objects (such as high clouds) are darker than warm objects. It is worth noting that any temporal averaging process such as the techniques used when generating composite images as described in this chapter may also reduce the negative effects of striping, due to the different viewing geometry from each MODIS granule. Note that the techniques presented in this chapter are equally applicable to any channels. Analogues to MODIS channels 1 and 31 exist in the National Oceanographic and Atmospheric Administration (NOAA) Advanced Very High Resolution Radiometer (AVHRR) instrument, raising the possibility of temporally extending the composite cloud-free MODIS data set back in time (prior to 2000). However, due to AVHRR's relatively limited spectral observations and this compositing technique requiring an accurate cloud mask, AVHRR composites would likely be of a lower quality than MODIS composites - particularly during the polar night time when shortwave channel observations are unavailable. Full resolution (i.e., 1 km) AVHRR image availability is also an issue in polar regions with no receiving station (*Massom et al.*, 2009).

2.3.1 Principal Component Analysis

Principal Component Analysis (PCA) is a statistical technique that is frequently applied to multispectral remote sensing imagery to examine or reduce the

dimensionality obtained in non-independent spectral channels (*Eklundh and Singh*, 1993). Often, the transformation to orthogonal axes inherent to PCA generates "enhanced" images (either lower in noise than the component channels' images, or excluding certain features while enhancing others, or both). *Hillger and Clark* (2002), for example, used PCA to enhance MODIS imagery for volcanic cloud detection. Shortwave and longwave bands were analysed separately. The shortwave PCA was found to produce no Principal Component (PC) images which enhanced the volcanic ash clouds being studied. However, many IR PC images successfully displayed the location of the volcanic ash cloud, allowing discrimination between these regions and the cloud-free regions and water/ice clouds in the image.

In the current work, the use of PCA was investigated for the purpose of enhancing the information content of both MODIS TIR and visible wavelength images. It was initially hoped that the use of PCA might produce PC images which "penetrate" thin cloud, enabling an unobscured view of the surface.

In order to test this, sixteen PC images (PC1 through PC16, with PC1 representing the greatest variance) were generated from the sixteen MODIS IR channels. Flaw lead discrimination or cloud penetration was not noticeably improved on any of the PC images (see Figure 2.3). It was concluded that, for this application, PCA holds no advantage for thin cloud penetration compared to other methods. Furthermore, detector striping was enhanced in all output PC images (not shown). Similar artefacts were observed when excluding the obviously noisy channels from the PCA, i.e., performing a PCA using only channels 20, 22, 23, 25, 29, 31 and 32.

In the analysis of all 20 shortwave channels, PCA images were heavily influenced by detector saturation in channels 8-16, producing low-quality output (see Figure 2.4). When these saturated channels, plus channel 6 which exhibited detector striping, were excluded from the PCA, output images closely resembled either the

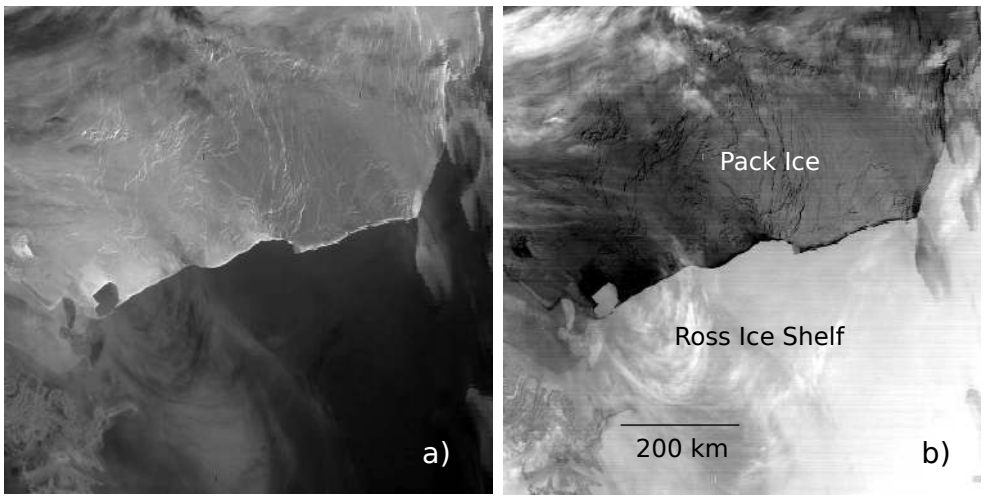

Figure 2.3: Results of the IR PC analysis. a) A typical Antarctic original MODIS channel 31 (IR) scene, showing the Ross Ice Shelf and pack ice in the Ross Sea, acquired on June 2, 2005 at 2040 UT. b) PC1 (of 6) generated from the six low noise IR channels (20, 22, 23, 25, 31 and 32). PC1 (and lower-order PC images - not shown) shows no advantage for cloud penetration. The image is ∼800 km across.

original shortwave channels or the near-IR channel 26 (see Figure 2.5). In summary, none of the PC images generated here showed clear advantages over the raw MODIS imagery for the purposes of cloud penetration or fast-ice discrimination. Because the computationally-expensive PCA provided little advantage over the raw MODIS imagery, it was not used to preprocess images used for fast ice detection.

With reference to Figure 2.2, the following processing steps were used to produce composite images. These steps are necessary in order to produce cloud-free composite imagery, and to combine MODIS images from different orbits/viewing geometries.

2.3.2 Cloud Masking

The MOD35 cloud mask can erroneously mask out regions of fast ice and consolidated pack ice, as shown in the example in Figure 2.6b. This problem arises

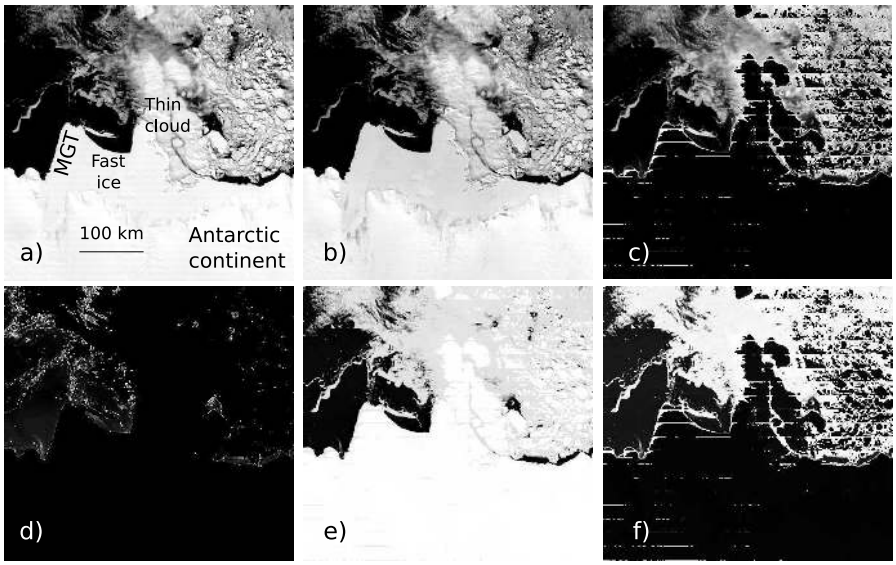

Figure 2.4: Visible PCA images of the Mertz Glacier region, generated from all shortwave MODIS channels. a) A typical Antarctic original MODIS channel 1 scene, acquired at 2320 UT on DOY 335 (December 1), 2005. b) MODIS channel 2 image of the same scene. c) MODIS channel 7 image of the same scene. Note the saturation over continental and consolidated sea ice, producing a "striped" effect (a separate issue to the MODIS detector striping). d) MODIS channel 16 image of the same scene. Saturation is occurring even over unconsolidated pack ice. e) PC1. Note the effects of the saturated channels on the image. f) PC2. Saturation effects are even more obvious, and detrimental to the image.

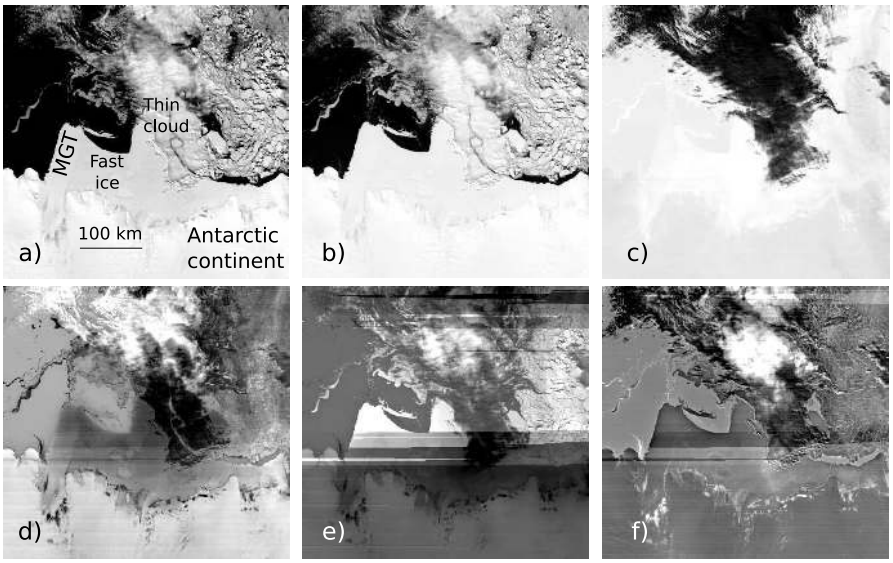

Figure 2.5: Visible PCA images of the Mertz Glacier region, generated from all shortwave channels (channels 1 to 19, plus 26) which exhibited no detector striping or saturation. a) A MODIS channel 2 scene, acquired on 2320 UT on DOY 335 (December 1), 2005. b) The first PC image generated from the visible channels which were free from detector striping and detector saturation. Note the similarity to channel 2. c) The second PC image, effectively showing the location of the thin cloud in the image. d) PC3. e) PC4. f) PC5. Note that no PC images were superior to the original MODIS image in terms of penetrating cloud cover.

during daylight hours over snow- or ice-covered surfaces when the atmosphere is particularly dry (R. Frey, personal communication, 2007). A strong water vapour absorption feature at around 1.38 μm (*Gao et al.*, 1993) means that the drier-than-normal atmosphere brings the band 26 radiance above the predefined cloud threshold (bit 16 in the MOD35 cloud mask), leading to false cloud detection (*Ackerman et al.*, 2006). It can be seen that the overall MOD35 cloud mask result closely matches the contribution from this test, particularly over the sea ice zone. Fortunately, this problem was encountered infrequently, and did not require corrective measures for fast-ice detection analysis to take place. For daytime scenes, the MOD35 cloud mask was found to be consistently accurate enough to use without spatial filtering of any kind.

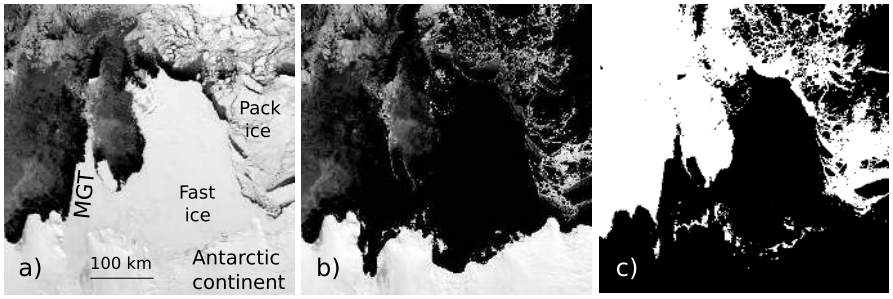

Figure 2.6: Example of erroneous masking of consolidated sea ice. a) The original MODIS channel 1 scene (acquired on DOY 296 (October 23) in 2001, at 23:00 UT). b) The result of MOD35 cloud masking. Pixels not classed as "confident clear" or "probably clear" were masked. c) The 1.38 μm cloud mask test contribution to the overall MOD35 cloud mask. White indicates cloud-free pixels, and black indicates cloudy pixels.

Manual examination of the MOD35 cloud mask revealed some unexpected behaviour over the sea ice zone during night-time/wintertime (see Figure 2.7, panels b and c): a large proportion of the areas covered by flaw leads and polynyas (i.e., areas of thin ice and open water) were erroneously classified as cloudy. Upon manual examination of individual cloud mask tests, it became apparent that the MOD35

high cloud test (3.7 - 12 μm) was the main contributor to the false cloud detection over flaw leads and polynyas.

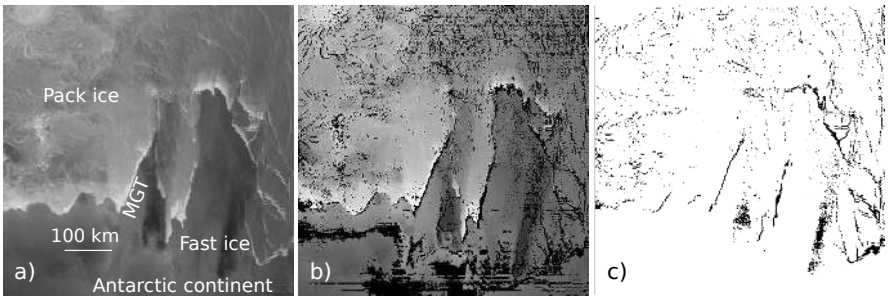

Figure 2.7: Erroneous masking of flaw leads and polynyas. a) The original MODIS channel 31 scene (acquired on DOY 161 (June 10) in 2005, at 00:00 UT). b) The result of MOD35 cloud masking. Pixels not classed as "confident clear" or "probably clear" were masked. c) Cloud masking results from the high cloud test (3.7 - 12 μm). White indicates cloud-free pixels, black indicates cloudy pixels. It can clearly be seen that this channel is a major contributor to the false cloud detection in flaw leads.

Detailed investigation of the processing path for the particular MODIS granule shown in Figure 2.7 showed that the surface conditions were derived from the relatively low-resolution ($\sim$25 km) SSM/I passive microwave data. Knowledge of the surface conditions (i.e., sea-ice concentration) is a key factor for producing an accurate cloud mask (*Ackerman et al.*, 2006). The spatial resolution of the SSM/I ice concentration product is insufficiently fine to resolve the flaw leads and polynyas in the scene. As a result, the high cloud test was applied by the MOD35 cloud mask processing algorithm over the flaw leads and polynyas, despite not being designed for regions of open water/thin ice. The high cloud test involves calculation of the brightness temperature from the infrared radiance in the 3.7 and 12 μm channels (MODIS channels 20 and 32). The Brightness Temperature Difference (BTD) is then calculated, to generate an image clearly showing cloud. A threshold is then applied, to produce the high cloud mask. In these regions, the BTD was well over the threshold of 4.5 K used to define cloud-free regions (*Ackerman et al.*, 2006) (see

Figure 2.8). This problem is essentially unavoidable, and is a consequence of the spatial resolution of passive microwave sea-ice products always being lower than the MODIS data. The problem was only observed with night-time MODIS scenes (including winter scenes). It is also worth noting that accurate cloud detection and ice surface temperature retrieval over polynyas and flaw leads is difficult due to the frost smoke/fog often associated with these regions (*Qu et al.*, 2006). This is an additional source of uncertainty which is difficult to quantify. Negative effects of this test were not observed during "summertime", i.e., daylight MODIS granules.

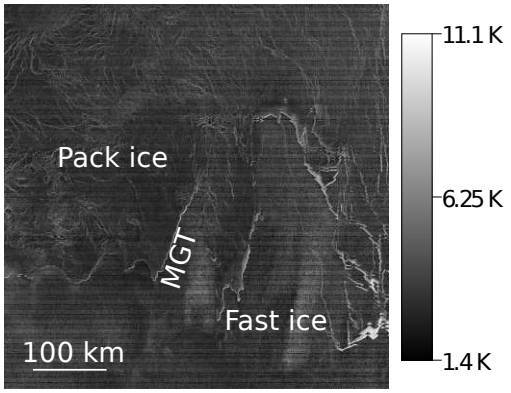

Figure 2.8: A BTD image of the channel 20 - 32 difference (3.7 - 12 μm), acquired on June 10, 2005, at 0000 UT. A small amount of detector striping is visible. Note that the difference over flaw leads and polynyas is much greater than the 4.5 K cloud threshold in this example, resulting in a false positive cloud detection.

In order to overcome the wintertime problem of erroneous flaw lead masking in the MOD35 cloud mask, a modified cloud mask was developed. Due to the narrow width of flaw leads (typically narrower than 5 km), spatial smoothing with a convolution kernel followed by thresholding of the cloud mask was found to be effective at correctly reclassifying these pixels as cloud-free in most cases. This technique forms the basis of the modified cloud mask. Figure 2.9 demonstrates the problem, and shows the results after spatial filtering. A constant-weight convolution kernel was used to perform the spatial filtering. Effective results (see Figure 2.9d, e

and f) were achieved using a 3×3 convolution kernel with a constant weight of 1/9, and a 5×5 convolution kernel with a constant weight of 1/25, thus transforming the cloud mask from a binary map (containing only values of 1, corresponding to clear, and 0, corresponding to cloudy) into a greyscale image (containing values between 0 and 1 inclusive). Following convolution, the mask was thresholded to produce a new cloud mask, with a lower threshold producing a new cloud mask with fewer cloudy pixels. After experimentation, a threshold value of 0.25 was found to work well, and is used here.

A spatial averaging process such as this has the potential to inadvertently reclassify "confident clear" or "probably clear" pixels as "cloudy" once thresholding has been performed. For this reason, all pixels originally classified as "confident clear" or "probably clear" were restored to their original value after smoothing and thresholding.

This inaccurate masking of flaw leads was notably absent during daytime, where visible and near-infrared channel tests can be added to the MOD35 cloud mask algorithm to increase its accuracy (*Ackerman et al.*, 2006). Thus, the modified cloud mask was only used for night-time granules. This spatial filtering had little detrimental effect on real cloud edges (see Figure 2.10), i.e., little or no previously masked cloud was unmasked by this process.

MODIS granules were cloud-masked using the modified cloud mask product during the "winter" (DOY 100 - 280), and the MOD35 cloud mask (*Ackerman et al.*, 2006) during the "summer" (DOY 280 - 100). For each pixel in the level 1B granule, a mask value of "0" was assigned if the cloud mask had been calculated for that pixel and that pixel had not been classified as "confident clear" (confidence greater than 0.99) or "probably clear" (confidence greater than 0.95). "Clear" pixels were assigned a value of "1".

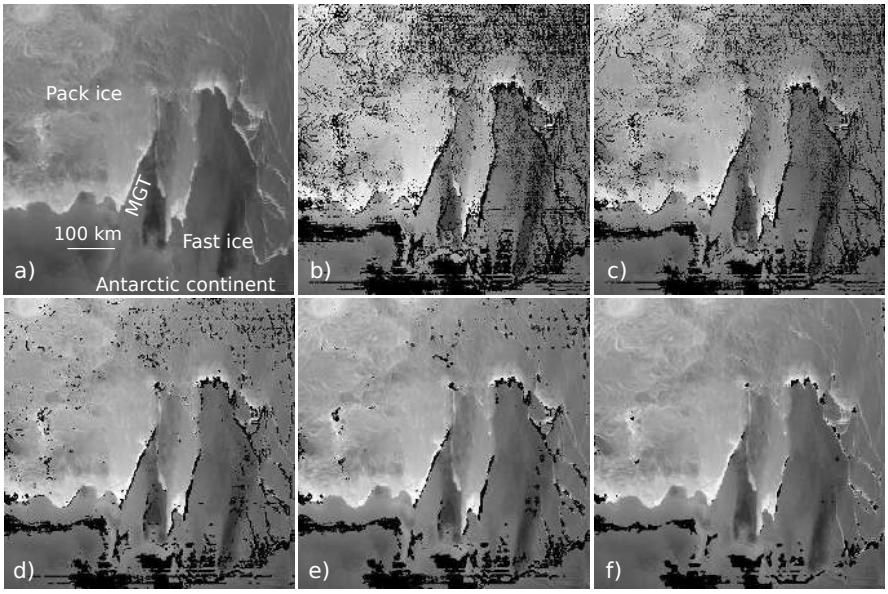

Figure 2.9: A demonstration of the procedure used to solve the flaw lead masking problem using spatial filtering of the cloud mask. a) The original MODIS channel 31 scene of the Mertz Glacier region (acquired on DOY 161 (June 10) in 2005, at 0000 UT). b) MODIS image after MOD35 cloud masking: only pixels classified as "confident clear" are unmasked. A small amount of striping is visible in the cloud mask. c) MODIS image after MOD35 cloud masking: only pixels classified as "confident clear" or "probably clear" are unmasked. d) Same cloud mask as image c, but the mask was convolved by a 3×3 smoothing filter. Following convolution, the smoothed cloud mask was thresholded at the midway point between a masked and an unmasked pixel (a threshold of 0.5). e) Same as image d, but using a 5×5 smoothing filter instead. f) Same as image e, but with a more relaxed threshold of 0.25. This convolution forms the modified cloud mask.

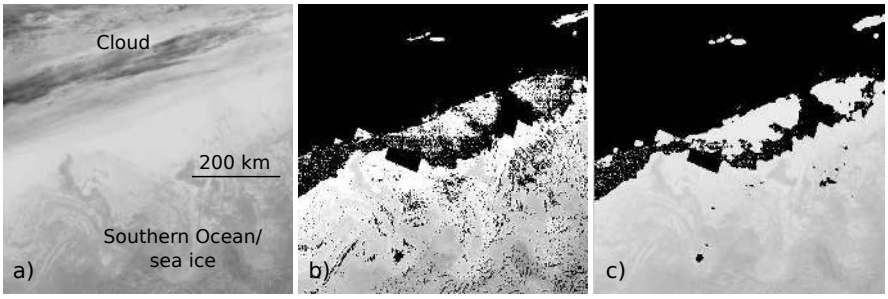

Figure 2.10: A demonstration of the effects of the modified cloud mask on a genuine cloud. a) The original MODIS channel 31 scene (acquired on DOY 161 (June 10) in 2005, at 0000 UT, centred at ∼60° S, 140° E). b) The result of cloud masking, using the MOD35 mask. Pixels not classed as "confident clear" or "probably clear" were masked. c) The result of masking using the modified cloud mask. A 5×5 convolution kernel was used (with all weights set to 1/25), thresholded at 0.25. Note the general lack of cloud at the edge of the filtered mask.

Despite the presence of a spectral cloud shadow contamination test in the MOD35 cloud mask product for identifying pixels affected by cloud shadow, the test is only applied over non-snow/ice covered land, due to the variable reflectance and high Solar Zenith Angles (SZAs) at the poles (*Ackerman et al.*, 2006). Geometric calculation of cloud shadows is possible, but computationally expensive. Avoiding the problem of being unable to accurately retrieve cloud top and base heights from MODIS data alone, *Luo et al.* (2007) assumed a vertical cloud extent of 0.5 - 10 km for cloudy pixels - almost always an overestimation. Cloud shadows were then geometrically calculated using satellite and solar ephemeris data. Pixels now classified as "shadow-contaminated" were then spectrally compared in order to restore obviously shadow-free pixels to their correct, shadow-free status.

While removing cloud shadow effects is important when radiometrically-accurate data are required, e.g., for a time series of albedo distribution (*Stroeve and Nolin*, 2002), the negative effects are less important for determining fast-ice extent. Thus, cloud shadows remain unmasked in this project (and remain a minor source of error in subsequent calculations of fast-ice area). Shadow effects are obvious in

component images (see Figure 2.11b), but are unlikely to significantly affect the generation of composite images due to the dynamic nature of cloud. At lower latitudes, the inclusion of the spectral cloud shadow test within the MOD35 cloud mask test suite should only serve to enhance the accuracy of the resulting cloud-free image, and shadow-contaminated pixels should be masked if possible.

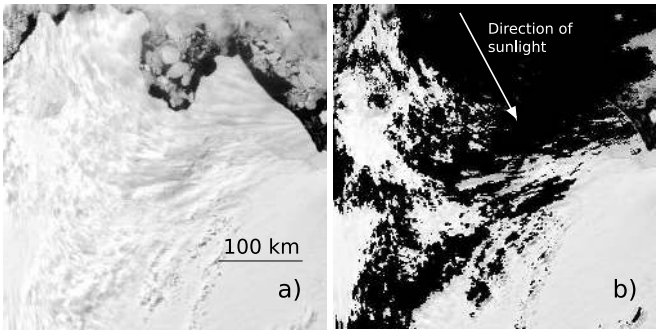

Figure 2.11: The effect of cloud shadow on a shortwave MODIS image, centred near 67° S, 127° E. a) An original MODIS channel 1 scene (acquired on DOY 340 (December 6) in 2005, at 0605 UT). b) The result of MOD35 cloud masking. Pixels not classed as "confident clear" or "probably clear" were masked. Note the cloud shadow remains unmasked.

2.3.3 Swath Trimming

One consequence of MODIS having a constant-rotation scan mirror with constant focal length optics is a deterioration of pixel resolution toward the edge of the swath. That is to say, the ground area covered by one pixel's Field Of View (FOV) becomes larger toward the edge of the swath. The pixel size factor is derived below (with reference to Figure 2.12).

Using the law of sines,

$$\frac{Sin\theta_l}{R} = \frac{Sin(\theta_g + 90)}{R + h} \tag{2.1}$$

where θ_l is the look angle in the cross-track direction, θ_g is the angle between the tangent to the Earth and the satellite, R is the polar radius of the Earth (here set to 6,357 km, after *NIMA* (2000)), and h is the height of the satellite above the Earth (here set to 705 km, after *Parkinson* (2003)). All angles are in degrees. It follows that:

$$Sin(\theta_g + 90) = \frac{R+h}{R} Sin\theta_l \tag{2.2}$$

$$\theta_g = 180 - Arcsin\left(\frac{R+h}{R} Sin\theta_l\right) - 90 \tag{2.3}$$

By virtue of the fact that the interior angles of a triangle add up to 180 degrees,

$$\theta_e = 180 - \theta_l - (\theta_g + 90) = 90 - \theta_l - \theta_g \tag{2.4}$$

Again, using the law of sines, and for a given MODIS pixel,

$$\frac{Sin\theta_e}{d} = \frac{Sin\theta_l}{R} \tag{2.5}$$

where d is the distance between the satellite and the observation point on the ground. It follows that:

$$d = R\frac{Sin\theta_e}{Sin\theta_l} \tag{2.6}$$

Now, consider the angle subtended by one pixel at nadir. Let this angle be θ_p. The size of the pixel projected onto the ground scales linearly with the distance from the sensor to the ground. Thus, the along-track resolution scaling factor (f_a) as a function of cross-track look angle, θ_l, is:

$$f_a = \frac{d}{h} \tag{2.7}$$

$$= \frac{R}{h}\frac{Sin\theta_e}{Sin\theta_l} \tag{2.8}$$

$$= \frac{R}{h}\frac{Sin(90 - \theta_l - \theta_g)}{Sin\theta_l} \tag{2.9}$$

where θ_g is given in equation 2.3.

Let $x = 180 - Arcsin(\frac{R+h}{R} Sin\theta_l)$, then

$$f_a = \frac{R}{h} \frac{Sin(180 - \theta_l - x)}{Sin\theta_l} \tag{2.10}$$

Similarly, the cross-track resolution scaling factor (f_c) as a function of cross-track look angle, θ_l, is:

$$f_c = \frac{d}{h} \frac{1}{Sin\theta_g} \tag{2.11}$$

$$= \frac{R}{h} \frac{Sin\theta_e}{Sin\theta_l} \frac{1}{Sin(x - 90)} \tag{2.12}$$

$$= \frac{R}{h} \frac{Sin(90 - \theta_l - \theta_g)}{Sin\theta_l} \frac{1}{Sin(x - 90)} \tag{2.13}$$

$$= \frac{R}{h} \frac{Sin(90 - \theta_l - (x - 90))}{Sin\theta_l \times Sin(x - 90)} \tag{2.14}$$

$$= \frac{R}{h} \frac{Sin(180 - \theta_l - x)}{Sin\theta_l \times Sin(x - 90)} \tag{2.15}$$

Using equation 2.10, this reduces to:

$$f_c = \frac{f_a}{Sin(x - 90)} \tag{2.16}$$

To determine the dimensions of a pixel at the swath edge, we substitute $\theta_l = 55$ degrees, the maximum MODIS cross-track look angle, into Equation 2.10, and then substitute the resulting value into Equation 2.16, to obtain $f_a = 2.01$ and $f_c = 4.83$. Thus, for a pixel of dimensions 250 m $\times$ 250 m at nadir, the dimensions increase to 503 m $\times$ 1208 m at the swath edge, an increase in area by a factor of 9.72. The same factors apply to the 1 km nadir resolution images. The resolution decrease factors f_a and f_c, and their product, are plotted in Figure 2.13. It can be seen from the solid line in Figure 2.13 that the effective MODIS pixel resolution decreases by a factor of $\sim$2 at a cross-track look angle of $\pm 35^\circ$. In the interest of retaining only high resolution data for image analysis, this angle of $\pm 35^\circ$ was chosen as the cutoff angle for swath trimming, resulting in a resolution range of 1-2 km for

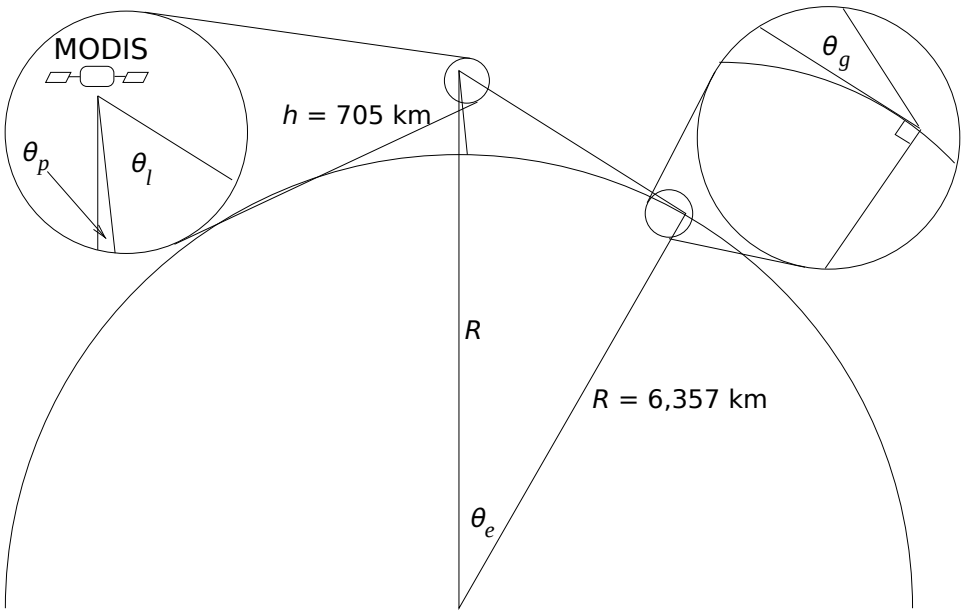

Figure 2.12: Diagram of angles used to calculate MODIS pixel size given the cross track look angle, θ_l (see Section 2.3.3 for full derivation). Other important angles are θ_g, the acute angle between the tangent to the Earth and the satellite; θ_e, the angle subtended by the MODIS satellite and the pixel of interest on the ground, from the centre of the Earth; and θ_p, the angle subtended by one pixel at nadir from the satellite.

1 km granules, and 250-500 m for 250 m granules. As a consequence, swath width was reduced from the normal value of 2,330 km to 1,017 km.

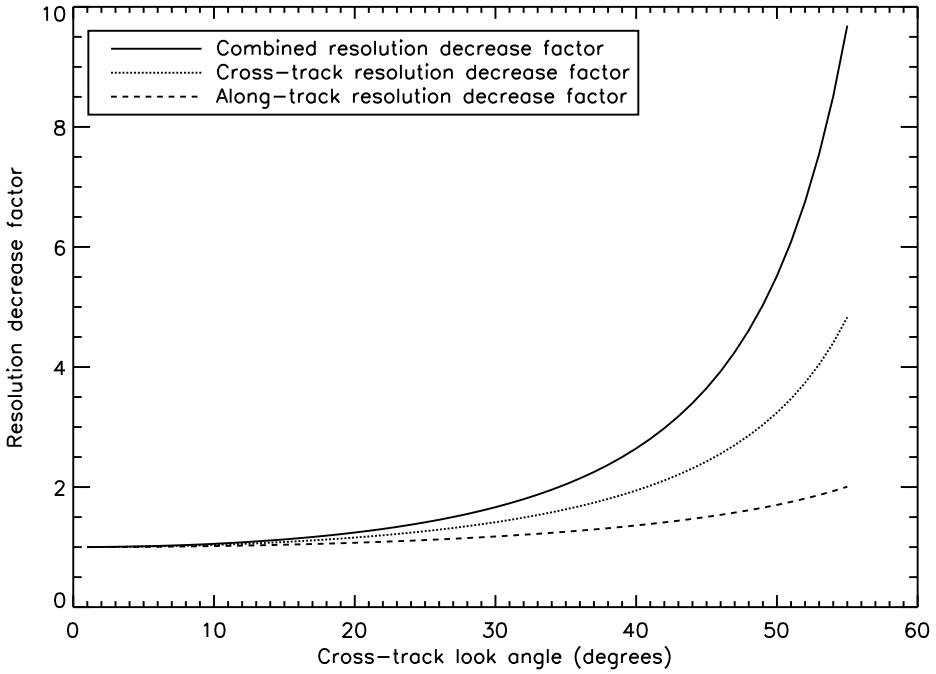

Figure 2.13: A plot of the MODIS cross-track and along-track resolution decrease factors, and their product, as a function of cross-track look angle. A similar plot is shown in the MODIS Level 1A Earth Location Algorithm Theoretical Basis Document (*Nishihama et al.*, 1997).

2.3.4 Image Georegistration and Bowtie Correction

Following cloud masking and swath trimming, the MODIS images were reprojected to a common grid using the ms2gt (MODIS Swath-To-Grid Toolbox) software (*Haran et al.*, 2002). All cloud masking and swath trimming was performed by editing the original HDF-EOS pixel values, thus outputting a fully compatible HDF-EOS file which could be gridded by ms2gt. Images of Solar Zenith Angle (SZA) were also generated for visible images, which were later used for SZA correction (see Section 2.3.5). A cylindrical, equal-area grid was chosen as the output projection, due to the ease of calculating fast-ice areal extents over an extensive band of the

Antarctic coastal region. In the interest of minimising file size, conversion to 8-bit greyscale PNG (Portable Network Graphics) files was investigated, but the relative lack of dynamic range was found to be detrimental to image quality. The output file format was thus chosen to be unformatted 32-bit floating point, representing reflectance for the visible images and brightness temperature for the TIR images.

Optional high resolution geolocation data from the MOD03 files were not used to georegister component images - the sub-sampled geolocation data in the MOD/MYD02 data set were deemed sufficient to produce accurate maps at a 1-km output composite resolution. However, use of the higher resolution (1 km at nadir) geolocation data may be advisable for composites made from higher resolution MODIS imagery (250 or 500 m nadir pixel resolution).

As part of the gridding process, "bowtie" corrections were also computed. The bowtie problem is a manifestation of the increase in pixel size at the swath edges in a whiskbroom imager (*Lubin and Massom*, 2006). The ms2gt software was found to produce accurate (i.e., artefact-free) output from the centre to the extreme edge of the swath - particularly compared to ITT's ENvironment for Visualising Images (ENVI) software suite, which often included seaming artefacts at the edges of overlapping scan segments. The bowtie correction and geolocation algorithm employed by ms2gt also performed much faster than ENVI's implementation. The agreement between the location of the MOA coastline product (see Section 2.3.5) and the coastline observed in MODIS imagery indicates that images gridded using ms2gt were extremely accurately geolocated - an indicator of the high level of accuracy of both ms2gt's bowtie-correction, as well as the EOS platforms' ephemeris data.

Following image preprocessing, all images were at this initial stage manually examined, and unsuitable images were rejected. Most of the rejected images were unsuitable for composite image generation due to the swath-trimming process - the

resulting reduction in swath width produced many blank gridded images. This process was subsequently automated, given the large volume of images processed for this study (∼125,000 individual MODIS granules).

2.3.5 Coastline Masking and Solar Zenith Angle Correction

To aid fast-ice detection, the Antarctic continent was masked using the MOA coastline product (*Scambos et al.*, 2007) after image georegistration. This is a high-resolution Antarctic coastline dataset produced from MODIS imagery mosaics, and was found to be consistently accurate around the coast of East Antarctica (excepting dynamic areas such as glacier tongues and ice shelves).

Simple SZA corrections (normalisations) were computed at this point for shortwave images, by dividing the original reflectance by the cosine of the SZA, following *Lindsay and Rothrock* (1994). The decision was made to perform the SZA corrections at this point due to the relative efficiency of array operations in the chosen development language (ITT's Interactive Data Language (IDL), in this case). Additionally, very high SZAs (greater than 89°) were found to produce unrealistic corrected reflectances in visible images, and performing SZA calculations at this stage allowed these regions to be excluded. The simple assumption of snow as a Lambertian reflector - and hence the implementation of only a simple inverse-cosine SZA correction - proved sufficient to produce quality composites from many different component images including a wide range of SZA illuminations. For radiometrically accurate work, a more sophisticated bidirectional reflectance distribution function can be implemented (e.g., *Li et al.*, 2007).

In this way, all component images are cloud-masked, swath-trimmed, gridded, georeferenced, bowtie-corrected, coast-masked and SZA-corrected, with an output file format of 32-bit unformatted floating point. Each component image typi-

cally contains many "useful" pixels (unmasked, cloud-free pixels falling within the new swath edge) and "holes" (pixels which have been masked due to cloud contamination, falling over the masked Antarctic continent, or falling outside the new swath edge). The compositing process, described in the next section, generates near-complete composite images from these component images.

2.3.6 Compositing Algorithm

After all image pre-processing (described above), composite images of the Adélie Land coast (∼130 to 151° E) were generated. The compositing algorithm was developed to average "useful" pixels from several component images on a per-pixel basis until a full composite was generated (i.e., there were no more "holes" in the image), or no component images remained to be assimilated into the composite. For the purposes of this chapter, composite images were generated from component images acquired over 10 consecutive days. However, the composite image generation program was written to also generate composite images over dynamic (adjustable) time periods, starting a new composite image whenever the previous composite is full. A compositing interval of 20 days was adopted for the remainder of this thesis, in order to reduce the negative effects of inaccurate cloud masking, and ensure composite images were of the highest possible quality. Cloud mask shortcomings (such as the erroneous masking of flaw leads and polynyas not correctly reclassified using the techniques described in Section 2.3.2) can lead to persistent "holes" located over the same area, meaning a composite image might never become complete. It is possible to either begin a new composite either when the current composite becomes nearly "full" (when the percentage of "holes" in the composite image falls below a preset value, say 95%), or after a predefined time period has passed. Examples of the composite images generated over a fixed time period are presented in this

chapter.

Images from both the Terra and Aqua MODIS sensors can be composited together to increase the temporal coverage for a given point on the surface, and thus reduce the time span required to generate a full composite image. Both composite images presented in Section 2.4 contain component images from both platforms. The performance of channels 1 and 31 in both Aqua and Terra MODIS is excellent (*Barnes et al.*, 2003).

2.4 Compositing Results

Two composite images are presented here, produced from MODIS channels 1 (0.659 μm) and 31 (11.030 μm). Both are of the same region near the Mertz Glacier Tongue, East Antarctica. The TIR image (Figure 2.14) was generated from 17 wintertime MODIS images acquired between 1 June, 2005 and 10 June, 2005. The visible image (Figure 2.15) was generated from 27 summertime MODIS images acquired between 1 December, 2005 and 10 December, 2005. Electronic copies of these composite images are available from http://seaice.acecrc.org.au/modis/pubimages/.

Both nearest-neighbour and bilinear interpolation techniques were examined during gridding resampling, to determine which produced higher quality composite imagery. For visible composites, bilinear interpolation produced dark bands in the composite image at the edges of component images (not shown). This was a consequence of choosing zero reflectance/brightness temperature to represent masked cloud: bilinear resampling produces intermediate values along the edge of the boundary. Nearest-neighbour resampling was found to correct this problem. No dark bands were visible using either resampling method for TIR composites.

Close manual examination reveals that no cloud is visible in either image

(although sub-pixel scale cloud may be present, this will not affect the fast-ice extent retrieval). Due to its relatively static nature, the fast ice edge is well defined over these 10 day periods, whereas the moving pack ice becomes blurred, as expected (labelled e on Figures 2.14 and 2.15). The sharply-defined nature of the fast-ice edge is an indication of the accuracy of both the MODIS satellites' ephemeris data and ms2gt's geolocation and bowtie-correction algorithms. No bowtie-correction edge artefacts are present. Additionally, the resolution of the composite image is maintained to a satisfactory level, i.e., 2 km/pixel, with the aid of swath trimming at $\pm 35°$.

Other notable features in the example images (determined by manual examination) include:

- an "island" of fast ice, labelled f on Figure 2.14. This island appears to be held fast by grounded icebergs (which are still visible in the visible composite image during the summertime) (see also *Massom et al.* (2001b, 2009));
- a vast tabular iceberg, rotating over the 10-day summer period (labelled f on Figure 2.15);
- a seasonally-recurring fast-ice "buttress "(labelled c in Figure 2.14) (see *Massom et al.* (2009)); and
- thick fast ice to the immediate east of the Mertz Glacier Tongue. This is the focus of a study on the possible role of thick fast ice in stabilising the glacier tongue, by *Massom et al.* (2010a).

The compositing technique holds great promise for discriminating between pack and fast ice throughout the year, and is the basis of this study. However, some difficulties are encountered during winter periods in places where the boundary

between fast ice and pack ice is not clear cut. An example of this occurs to the west of the Mertz Glacier Polynya (*Massom et al.*, 2001b), where newly-formed sea ice is advected westward in the Antarctic Coastal Current towards a pre-existing fast-ice feature (between c and f in Figure 2.14). This advection of pack ice leaves no open water interface between the pack and the fast ice, making it difficult to unambiguously delineate the fast-ice edge. A suggested solution is to use passive microwave data to determine where the sea-ice concentration reaches 100% as a proxy for fast ice extent, albeit at a lower spatial resolution. The best available imagery for this purpose is the 6.25 km resolution Advanced Microwave Scanning Radiometer - EOS (AMSR-E) sea-ice concentration product, which is available as a daily composite image. This technique is developed in Chapter 3.

2.5 Summary and Conclusions

This chapter describes an algorithm and techniques that have been developed for compositing MODIS satellite imagery, in order to remove cloud cover over polar regions. The algorithm makes use of the MOD/MYD35 cloud presence flags to mask cloudy pixels before images are composited. Ten-day compositing periods were found to be sufficient to produce almost-complete composites during both the winter (using TIR wavelength data) and summer (using visible wavelength data), though longer compositing periods may be required during particularly cloudy intervals (20-day intervals are used for the remainder of this thesis). Composite images created during autumn and spring (not shown) were also of sufficient quality to discriminate between pack and fast ice. The techniques described here can produce composite images of any MODIS channel, can combine component images from both MODIS platforms (Aqua and Terra), can be used at any latitude, and can produce output maps in many projections whilst maintaining the highest possible resolution.

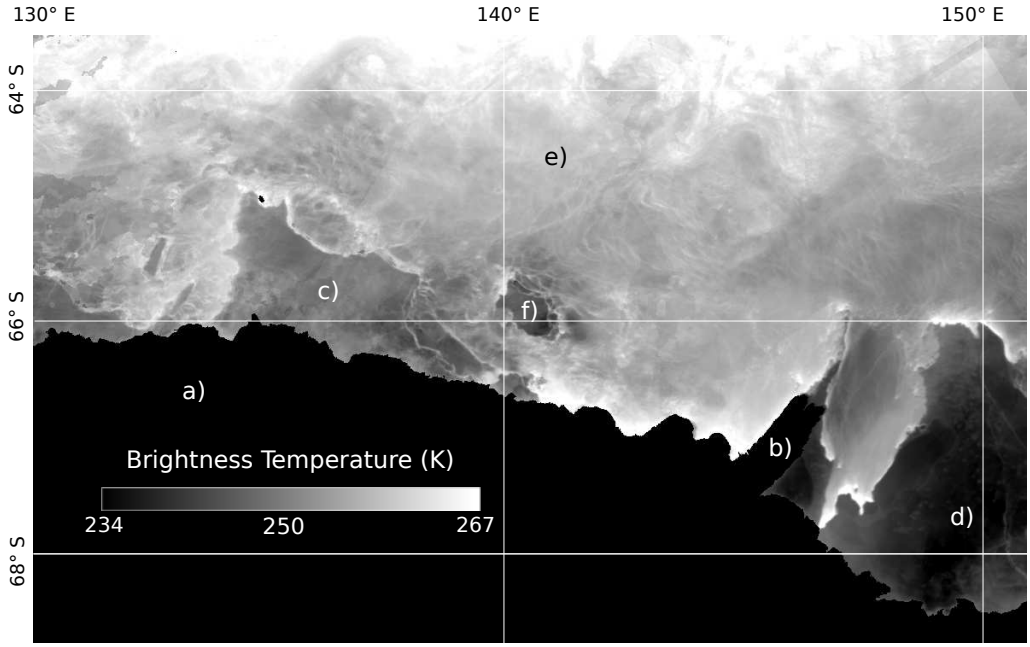

Figure 2.14: 1 km resolution TIR (channel 31) composite of the Mertz Glacier region, generated from 17 wintertime MODIS images. a) The Antarctic continent (masked to aid fast ice detection). b) The Mertz Glacier Tongue (also masked). Note the thick (dark in this TIR image) fast ice immediately to the east of the Tongue. c) Seasonally recurring fast ice buttress. Note the small "hole" in the composite image at the north-western point of the buttress. This "hole" exists due to the erroneous masking of the persistent flaw lead to the north. d) Extensive fast ice held in place by grounded icebergs. e) Pack ice extends to the northern border of this wintertime image. f) "Island" of fast ice, held in place by grounded bergs.

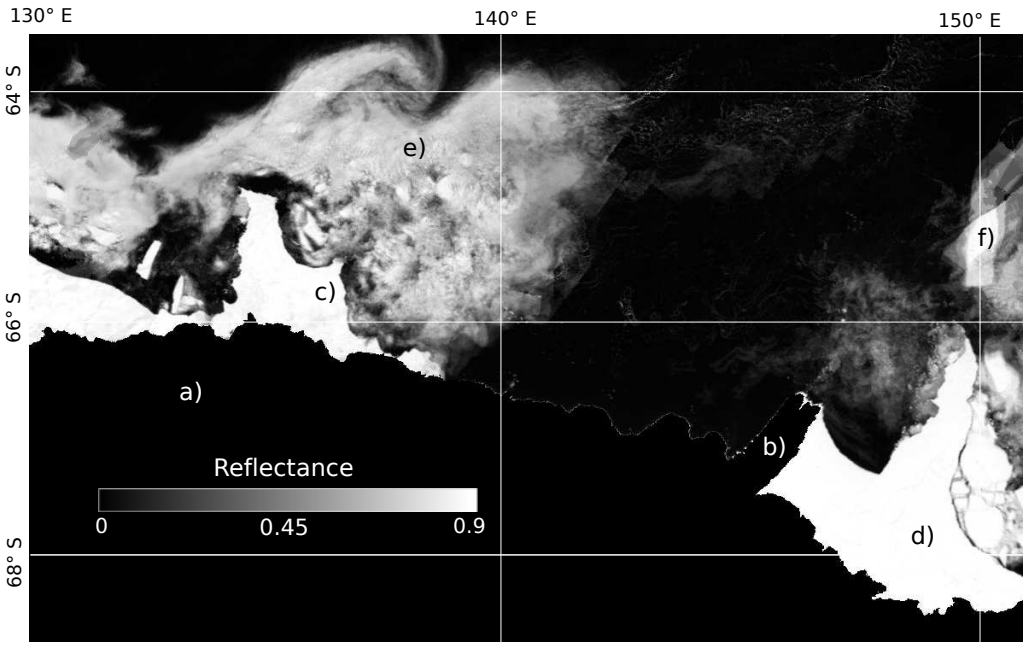

Figure 2.15: 1 km resolution visible (channel 1) composite of the Mertz Glacier region, generated from 27 summertime MODIS images. a) The Antarctic continent (masked to aid fast ice detection). b) The Mertz Glacier Tongue (also masked). c) Seasonally recurring fast ice buttress. d) Extensive summertime fast ice to the east of the Tongue. e) Summertime pack ice (much less extensive than the wintertime pack). f) A massive tabular iceberg which has rotated during the 10-day period covered by the 27 MODIS images comprising the composite.

The techniques presented here were developed to aid fast-ice detection using visible/TIR satellite imagery. Importantly, this technique works equally well at all times of the year. Thus, visible (TIR) composites can be generated during the summer (winter) months and parts of spring and autumn, i.e., DOY 280 to 100 (DOY 100 to 280). This avoids the problem of having a low temperature contrast between ocean and sea ice during summer, and hence low contrast in a TIR image. Conversely, TIR composite images can be successfully used in the wintertime where few visible images are captured, but the larger temperature difference between sea ice and ocean gives sufficiently high contrast in the TIR images to discriminate between open ocean and sea ice.

Due to the relatively static nature of fast ice compared to pack ice, and the accurate geolocation of MODIS data, the compositing process preserves sharp edges at the shear zone between pack and fast ice over a multi-day period, enabling fast-ice classification. This technique forms the basis of a time series of maps of East Antarctic fast-ice extent derived from composite MODIS imagery, detailed in Chapter 3 of this thesis.

Although these techniques were developed to aid in fast ice detection, alternative potential applications exist, such as cloud-free NDVI, SST and land/ice surface temperature composites, as well as cloud-free spectral land usage retrieval.

Chapter 3

Generation of High-Resolution East Antarctic Landfast Sea-Ice Maps from Cloud-Free MODIS Satellite Composite Imagery

This chapter is an edited version of a paper which has been published as:

Fraser, A. D., R. A. Massom, and K. J. Michael, Generation of high-resolution East Antarctic landfast sea-ice maps from cloud-free MODIS satellite composite imagery, *Remote Sensing of Environment, 114* (12), 2888-2896, doi:10.1016/j.rse.2010.07.006, 2010.

A reprint of this publication is included in Appendix B.

3.1 Abstract

A method to generate high spatio-temporal resolution maps of landfast sea ice from cloud-free MODIS composite imagery is presented. Visible (from Day Of Year (DOY) 280 to DOY 100 in the following year) and thermal infrared (DOY 100 to 280) cloud-free 20-day MODIS composite images are used as the basis for these maps, augmented by AMSR-E sea-ice concentration composite images (when

MODIS composite image quality is poor). The success of this technique is dependent upon effective cloud removal during the compositing process (see Chapter 2). Example wintertime maximum (∼374,000 km^2) and summertime minimum (∼112,000 km^2) fast-ice maps for the entire East Antarctic coast are presented. The summertime minimum map provides an indication of multi-year fast-ice extent, which may be used to help assess changes in Antarctic sea-ice volume. Errors in fast-ice extent to 2σ level are estimated to be $\pm 3\%$ when $\geq 90\%$ of the fast-ice pixels in a 20-day period are classified using the MODIS composite, or $\pm 8.8\%$ otherwise (when augmenting AMSR-E or the previous/next MODIS composite image is used to classify $>10\%$ of the fast ice). Imperfect composite image quality, caused by persistent cloud, inaccurate cloud masking or a highly dynamic or unclear fast-ice edge, was the biggest impediment to automating the fast-ice detection procedure.

3.2 Introduction

Much of the original introductory material and literature review from this chapter (paper) has been moved to the introductory Chapter 1 to avoid repetition.

The aim of this chapter is to develop a method for retrieving maps of fast-ice areal extent from 20-day cloud-free MODIS (MODerate resolution Imaging Spectroradiometer) composite images, augmented with AMSR-E 20-day composite imagery when required. The fast-ice maps generated using these techniques form the basis of an 8.8-year time series of East Antarctic fast-ice extent. An analysis of the variability of fast-ice extent is presented in Chapter 4, and Chapter 5 investigates the links between fast-ice extent and atmospheric forcing on both local and hemispheric scales.

3.3 Methods

3.3.1 Study Area and Projection

Figure 2.1 in Chapter 2 shows the study region used in this chapter. The longitudinal extents of the composite images were chosen to cover the entire East Antarctic coast - from 10° W (near Neumayer station) to 172° E (Cape Adare). Latitudinal extents are from 63.5° to 72° S, to sufficiently cover the maximum extent of wintertime fast ice.

A cylindrical, equal-area projection was used to produce the composite images in this chapter. The latitudinal range of fast ice along the East Antarctic coast meant that such a projection minimised pixel "wastage". A polar stereographic projection covering the same area would include a lot of lower-latitude Southern Ocean and higher latitude Antarctic continent, i.e., regions without fast-ice coverage.

3.3.2 Datasets

MODIS Composite Images

The main dataset used in this chapter, hereafter referred to as "the MODIS composites" or simply "composites", was a series of 159 contiguous cloud-free MODIS composite images, generated from cloud-free portions of ∼125,000 individual MODIS granules, covering the time interval 2000,061 to 2008,365 (in "year,day of year" format). Each MODIS composite represents a 20-day cloud-free mean image of the surface (infrared during winter, visible during summer), rather than a daily snapshot. This length interval was chosen for several reasons. Firstly, 20 days has been used as a fast-ice criterion in the Arctic (*Mahoney et al.*, 2005), being long enough to exclude transient fast-ice growth events associated with the passage of synoptic scale weather systems and short enough to resolve genuine fast-ice growth and

breakout events. Additionally, MODIS composite images generated from 20 days' imagery are generally of a high quality, with few gaps due to persistent cloud. To facilitate interannual comparisons, the compositing period was set at exactly 20 days for the first 17 composites in each year, with the final composite image covering the remaining days in the year (25 for non-leap years, 26 for leap years).

The techniques presented have been developed in order to classify fast ice by identifying ice which is contiguous with the coast, rather than ice which is not moving. The use of mean-value compositing was preferable to maximum/minimum value compositing in this case due to the difficulties of the latter in polar regions, arising from the similarities in brightness temperature and albedo between snow and polar cloud. Mean-value compositing is tolerant, to some degree, of imperfect cloud masking. Furthermore, due to the motion of the pack ice over the 20 day compositing period, the pack ice becomes blurred with mean value compositing, while fast-ice features typically remain more clearly defined (unless growth or breakout occurs), whereas this would not be the case for minimum/maximum value compositing. This enhances the utility of this technique for fast-ice detection. The details of the compositing procedure are given in Chapter 2, Section 2.3 (and also presented in *Fraser et al.* (2009)).

Only 1 km resolution MODIS images were used in this chapter, despite the availability of higher-resolution 250 m imagery in some visible channels. The reason for this was twofold: i) in winter, few visible images are acquired at high latitudes, and no 250 m resolution infrared channels exist on MODIS; and ii) the CPU time required to produce these composite images at 250 m resolution is prohibitive (a factor of 16 higher in both CPU time and disk space requirements). Because the MODIS 1 km channel resolution is only 1 km at nadir (with pixels at the edges of the swath growing to $\simeq$10 km^2 due to the combined effects of a curved Earth and

a longer path to the swath edges, see Section 2.3.3), the output resolution of the composite images was set at 2 km.

Both the Terra and Aqua satellites provide one MODIS granule every 5 minutes (288 per day). This equates to ∼16,000 granules per platform per year over the region of interest i.e., over 32,000/year from both platforms, or a total of ∼250,000 granules for the entire time series (2000-2008). The average file size for a MODIS L1B 1 km-resolution granule is ≃100 MB (higher in summer when visible images are captured, and less during winter). Thus, the total size of the MODIS archive required to produce the 159 composites is on the order of 25 TB. This presents a challenge for both storage and processing of the data. One practical solution (adopted here) is to pre-select only the least cloudy MODIS granules for inclusion into the composites. This solution is possible because the MOD35 cloud mask product is a much smaller download than the equivalent L1B granule - averaging about 3MB. Thus, for this project, all ∼250,000 MOD35 granules were downloaded, and the cloud-content of each granule evaluated. These data were acquired from the Level 1 and Atmosphere Archive and Distribution Center (LAADS), available at http://ladsweb.nascom.nasa.gov.

To illustrate the cloud content of MODIS scenes along the East Antarctic coast, Figure 3.1 shows a histogram of cloud-free percentage, including all MODIS swaths covering the study region for the year 2007. The strong peak at a modal value of ≃7% cloud-free pixels confirms this region as one of the cloudiest on Earth (*Spinhirne et al.*, 2004, 2005). A cutoff at 30% cloud-free pixels roughly bisects the histogram. After some experimentation, it was determined that using only those granules with 30% or more pixels classified as cloud-free produced composite images similar in quality to composite images produced using all granules, but requiring half the storage space and CPU processing time.

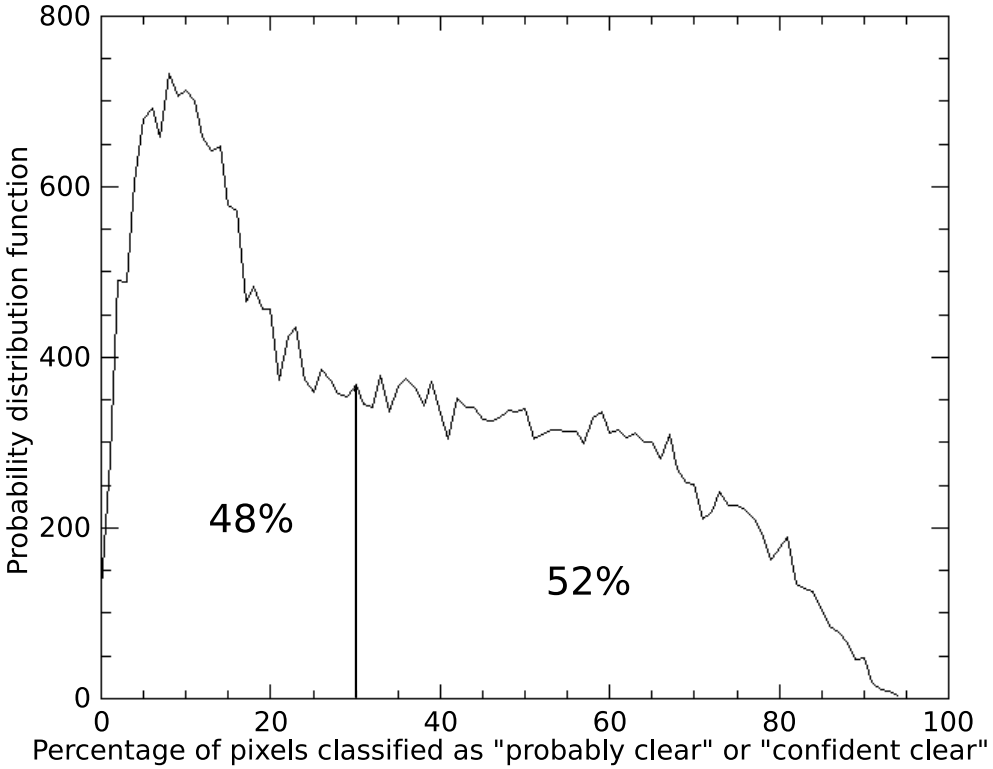

Figure 3.1: A histogram of "cloud-free percentage" (the percentage of pixels within a granule classified by the MOD35 product as "confident clear" or "probably clear") for 2007. This histogram is representative of other years within the study period. In order to reduce storage and CPU requirements, only granules with $\geq$30% cloud-free pixels were used in the compositing process. Resulting composites were similar in quality to those which used all available granules.

AMSR-E Sea-Ice Concentration Composite Images

Coincident sea-ice concentration data from the AMSR-E (Advanced Microwave Scanning Radiometer - EOS) instrument onboard the NASA Aqua platform were occasionally used to supplement the MODIS composites during times when the MODIS composite image (and the previous/next MODIS composite images) were of poor quality. In fact, 30 out of 159 fast-ice maps (or ∼19%) required augmentation using AMSR-E imagery in this way. Daily AMSR-E ARTIST Sea Ice (ASI) 6.25 km resolution daily sea-ice concentration data were obtained from http://www.iup.uni-bremen.de:8084/amsr/ for this purpose (*Spreen et al.*, 2008). AMSR-E composite images were then generated for the same time intervals as the MODIS composite images, and using the same projection.

Intercomparisons between MODIS and AMSR-E composite images show generally good agreement in the location of the fast-ice edge (see Figure 3.2), although the use of the lower resolution AMSR-E data leads to ambiguities in fast-ice detection at times. Additionally, the AMSR-E composite images erroneously show lower sea-ice concentration at the locations of large tabular icebergs and ice tongues (a phenomenon which arises due to the intrinsically different radiometric properties of sea ice and icebergs, noted by *Kern et al.* (2007)). This proved useful in the exclusion of large icebergs from the fast-ice maps in highly dynamic locations (e.g., east of the Mertz Glacier Tongue), though identification of the location of sub-pixel scale icebergs remains a problem.

Fusion of AMSR-E and MODIS data has been reported several times in the literature, e.g., using AMSR-E data to reduce the effects of cloud obscuration in the MODIS snow cover product at mid-latitudes (*Gao et al.*, 2010), and using a combination of MODIS and AMSR-E products to retrieve Ice Water Path in clouds

over ocean (*Huang et al.*, 2006). This is, however, the first effort to combine the two different satellite sensor datasets for fast-ice detection.

Despite the reasonable agreement between AMSR-E and MODIS composites on the location of the fast-ice edge noted above, the ASI algorithm appears to sometimes underestimate the concentration of fast ice. Examples of this "behaviour" are shown in Figure 3.2 - particularly the area surrounding the large grounded iceberg D15. In this region, the ASI-reported fast-ice concentration is as low as ∼55%. The 89-GHz channel used by the ASI algorithm to obtain high-resolution sea-ice concentration also has the potential to be adversely affected by cloud and water vapour (*Ulaby et al.*, 1981). The ASI algorithm (*Spreen et al.*, 2008) uses lower-frequency AMSR-E channels as weather filters to remove spurious sea-ice concentration in open water areas, where the contaminating effect of weather systems is largest. The algorithm is expected to be at its most accurate for retrieving high sea-ice concentrations, e.g., in the fast-ice zone (*Spreen et al.*, 2008).

3.3.3 Generation of Fast-Ice Maps

Automation of a fast-ice detection and classification algorithm is technically difficult, particularly when using only visible/infrared imagery where image quality is sensitive to cloud masking accuracy. Automated fast-ice classification from a nadir-viewing orbital imaging instrument has been achieved in the past, e.g., *Mahoney et al.* (2004); *Lythe et al.* (1999), but only when using microwave imagery (high-resolution SAR imagery, in particular), to essentially see through the cloud to the surface. Even so, these automated techniques have only worked during certain times of the year (*Mahoney et al.*, 2004) or in combination with imagery at other wavelengths (*Lythe et al.*, 1999).

Initially in this study, it was thought that the MODIS composite images

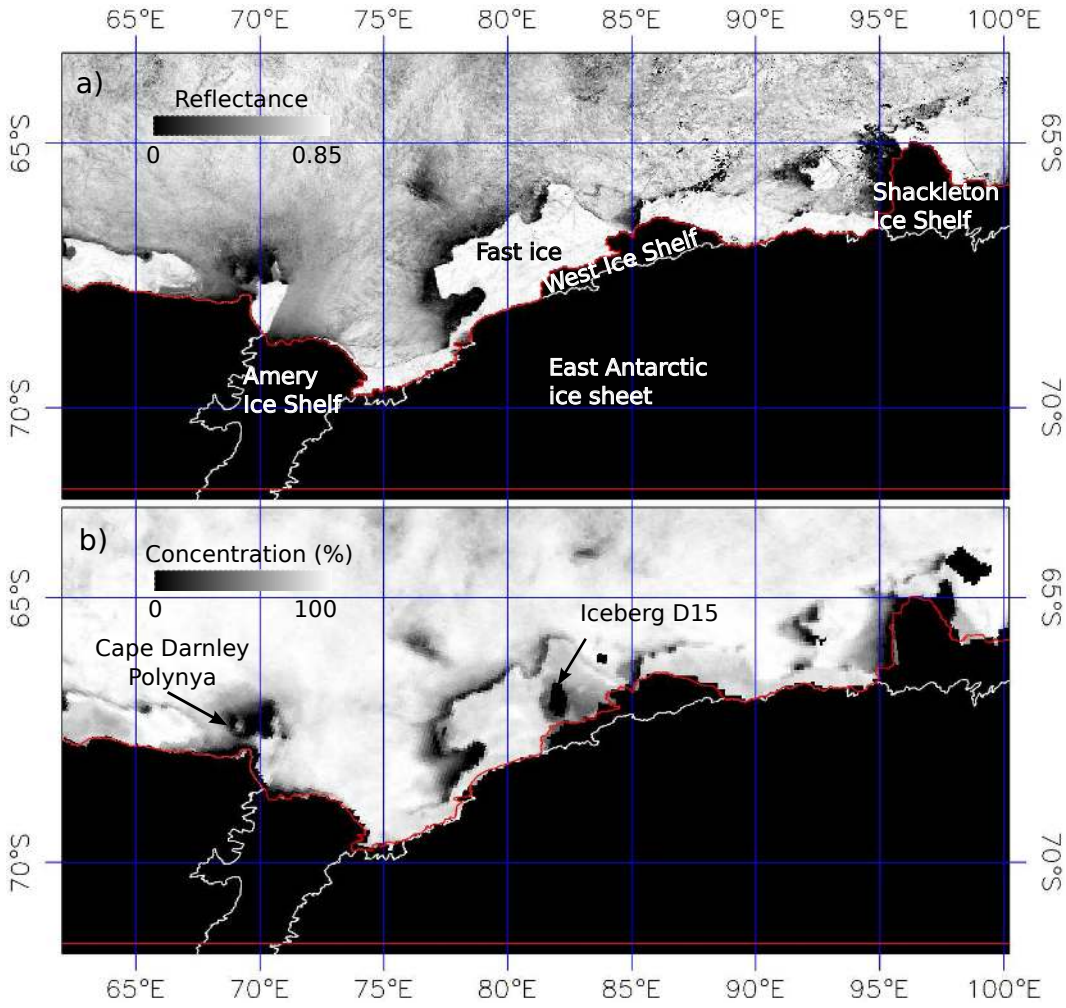

Figure 3.2: a) Spatial subset of a MODIS 20-day composite image covering the time period from DOY 281 to 300, 2008 (7 to 26 October), from ∼65 to 100° E. b) AMSR-E ASI sea-ice concentration composite image covering the same time period. Note the agreement between both composite images on the location of the fast-ice edge. The AMSR-E composite image also gives some indication of the location of icebergs and ice tongues, e.g., iceberg D15 at 82° E.

could be analysed using an automated edge-detection algorithm in order to find the fast-ice edge. Consecutive MODIS composites would be analysed together in order to see which edges persisted between composites, forming a likely candidate for the fast-ice edge (maximum areal extent). Though this hypothetical "persistence of edges" style approach had the inherent disadvantage of extending the temporal scale (two or more consecutive composites would be needed to determine the location of the fast-ice edge), the advantages of automating such a process would mean that compositing periods could be kept shorter (e.g., ∼10 days), thus maintaining a temporal resolution of ∼20 days.

In practice, the MODIS composite image quality was at times found to be imperfect, even when using a compositing period as long as 20 days (see Figure 3.3b for an example). These lower-quality regions were encountered under one or more of the following conditions:

- The cloud mask performed poorly and allowed cloudy pixels into the composite image, thus partly obscuring the surface (this problem was most frequently encountered for the wintertime (TIR) composites, when shortwave tests could not be used by the cloud masking algorithm);

- Cloud was persistent in a certain region over the 20-day period, giving few/no images of the surface (this was particularly the case off the coast of Enderby Land around 40° - 50° E, where a persistent high pressure ridge often prevents cyclonic systems from passing to the east (*Carleton*, 1979; *Kuga*, 1962)); and/or

- The region is highly dynamic, with fast-ice growth/breakout "blurring" the fast-ice edge (a problem frequently encountered during the late spring/early summer fast-ice minimum, when rates of change of the fast-ice edge are high-

est).

Because of these imperfections in the MODIS composites, each image was classified manually. A discussion of the biases and errors introduced by this process is presented in Section 3.3.4. The majority of pixels in each fast-ice map were classified from a single MODIS composite image corresponding to the time interval of interest. These pixels are henceforth referred to as "confident fast ice", or simply "confident" pixels. For regions/time intervals of lower image quality, two auxiliary datasets were used to augment the "confident" composite:

- AMSR-E ASI sea-ice composite images covering the same 20-day period as the "confident" composite (hereafter referred to as "AMSR-E"); and
- The previous and/or next MODIS 20-day composite was used (hereafter referred to as "prev/next" - note that previous/next AMSR-E composite images were never used in the analysis).

Each of these auxiliary datasets has associated strengths and weaknesses. Importantly, the AMSR-E dataset is available at a highest resolution of 6.25 km/pixel, significantly lower than the 1 km (nadir) MODIS resolution. Additionally, the lower resolution of the AMSR-E imagery exacerbates the problem encountered when pack ice is advected against a fast-ice feature, leaving no flaw lead or shear zone between the pack and fast ice and making it difficult to discriminate fast ice from pack (*Fraser et al.*, 2009). Prev/next imagery is at the native projection resolution, but its use degrades the temporal scale of the fast-ice classification by 20 or 40 days. Often, when a low-quality section was encountered in a particular MODIS composite, both the previous and next composites showed the fast-ice edge in the same location, thereby providing a good indication of the likely position of the fast-ice edge during the intervening time. At other times of poor composite image quality,

fast-ice growth or breakout was identified from analysis of the prev/next composites, and the AMSR-E composite could give more information about the location of the fast-ice edge at the time of interest.

Figure 3.3 shows a portion of a fast-ice map (from DOY 121 to 140, 2006 (May 1 to 20)) which required the current MODIS composite, the associated AMSR-E ASI sea-ice concentration composite, and the next MODIS composite to classify the image. Much of the fast-ice classification in scene a) came from the associated MODIS composite image b), but the fast-ice edge is not well defined in this composite image at ∼111° and ∼116° E, either due to persistent cloud, inaccurate cloud masking, or a highly dynamic fast-ice edge. For this reason, c), which is the associated AMSR-E composite image, was used to classify the fast-ice feature at ∼111° E. The "next" MODIS composite, d), was used for fast-ice classification at ∼116° E, because both the MODIS and AMSR-E composites for DOY 121-140 showed that no flaw lead was present between the pack ice and fast ice.

3.3.4 Bias Reduction and Error Analysis

The next step involved identification and reduction of any biases introduced by manual processing of the composites into fast-ice maps. Primarily, systematic biases were removed by processing composites in a randomised order. A second pass of each image (also randomised) was conducted to verify (and, if required, adjust) the fast-ice map. Additionally, 14 randomly-selected composites were completely and independently re-processed, and the differences in area compared (see Figure 3.4).

Two error regimes were identified from Figure 3.4: regime 1 (to the right of the dashed line) - composites in which ≥90% of the pixels classified as "fast ice" were classified from a single MODIS composite (i.e., pixels which were "confidently"

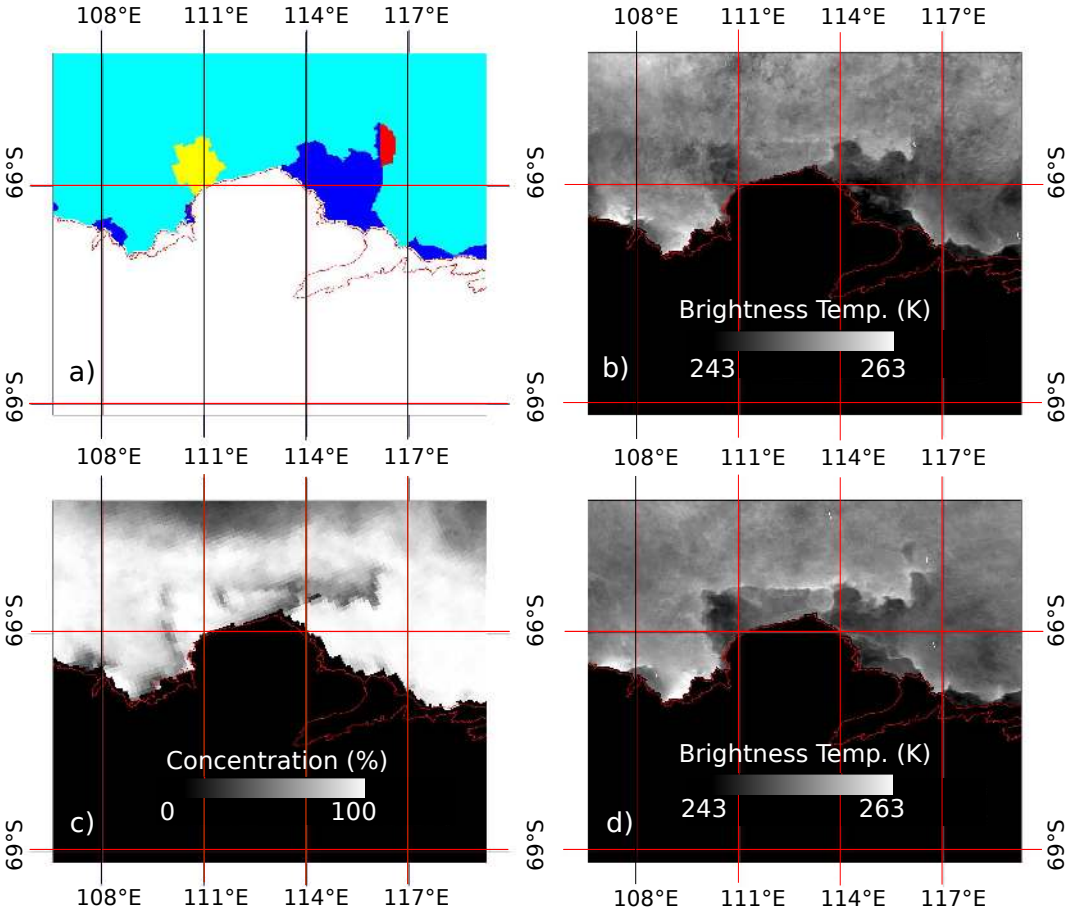

Figure 3.3: An example illustration of the process of converting a MODIS composite into a fast-ice map. a) The fast-ice map for the time interval DOY 2006,121-140, as generated from images b), c) and d). The continent is shown in white, and the Southern Ocean/pack ice/large tabular icebergs are shown in light blue. Fast ice is shown in dark blue (classified from a single MODIS composite), yellow (classified from a single AMSR-E composite image, and red (classified from the next MODIS 20-day composite image). b) The MODIS brightness temperature composite covering the time interval 2006,121-140. c) An AMSR-E ASI sea-ice concentration image of the same region over the same time interval. d) The "next" MODIS image (covering the time interval 2006,141-160).

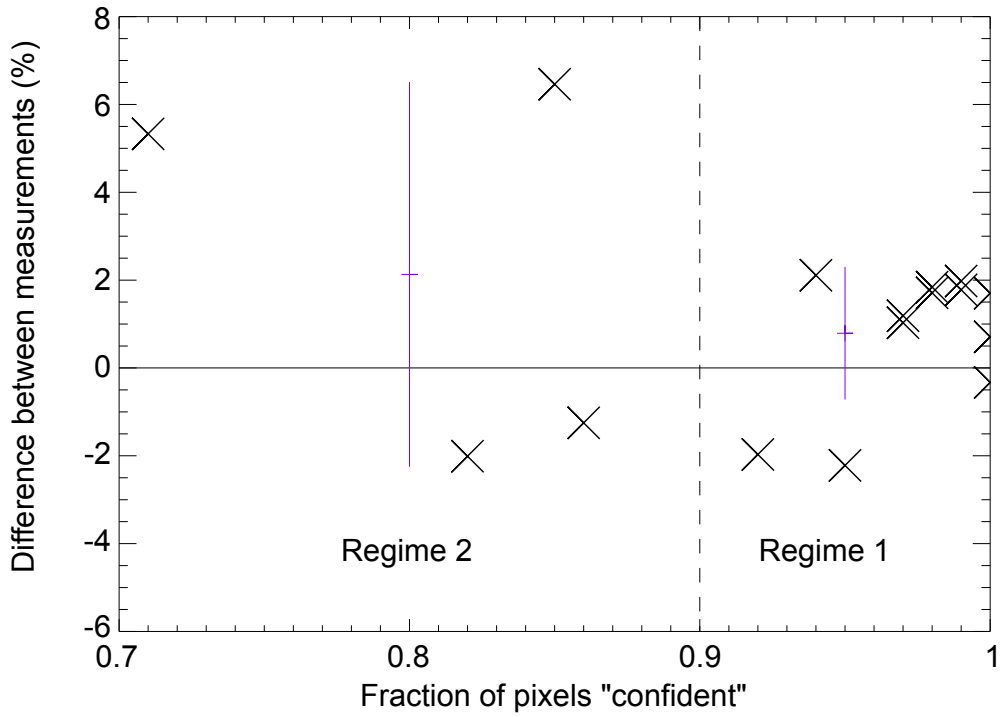

Figure 3.4: A graph showing the percentage difference between independent estimates of area of 16 randomly-chosen composites. The abscissa represents the fraction of each composite image's fast-ice map which was determined from a single MODIS composite image ("confident"). For those points in regime 1 (regime 2), the mean difference between fast-ice area measurements was found to be 0.79% (2.13%), and one standard deviation was 1.51% (4.38%). These values are represented here as error bars in their respective regimes.

classified); and regime 2 (to the left of the dashed line) - in which <90% of pixels were classified from a single MODIS composite. Regime 1 has a much lower sample estimation of the population standard deviation (1.49%) compared with regime 2 (4.38%). This finding was expected, considering that "fraction of pixels classified as confident" is essentially a proxy for "composite image quality", and higher quality composite images are expected to produce more consistent fast-ice maps. Two standard deviations are used as the error bars for the fast-ice time series (i.e., $\pm \simeq 3\%$ for regime 1 or $\pm \simeq 9\%$ for regime 2) in Chapter 4 (*Fraser et al.*, 2010b).

3.3.5 Iceberg Masking

Icebergs much larger in area than the MODIS composite pixel size (4 km^2) were manually detected in each composite image, and removed from fast-ice classification. Identification and tracking/removal of these icebergs in fast-ice zones was aided by the representation of icebergs as lower concentration (i.e., <25%) sea ice in the AMSR-E ASI sea-ice concentration algorithm (*Kern et al.* (2007); see also Figure 3.2 in this chapter).

Some areas of fast ice around the East Antarctic coast contain sub-pixel scale (i.e., less than 4 km^2) icebergs. Thus, for these regions (often adjacent to calving glaciers), the actual area of fast ice will be less than the reported area, by up to an estimated factor of $\simeq$15% in some regions. For example, Figure 3.5 shows a SAR enlargement of the recurring region of fast ice located at $\sim$121°30' E (*Jezek*, 2002). Accurate removal, by masking, of icebergs is not possible in such cases. Large icebergs have, however, been masked manually.

3.4 Results and Discussion

Figure 3.6 shows, for the first time, examples of fast-ice maximum (2005,241-260) and minimum (2006,061-080) extent maps along the entire East Antarctic coast. These maps confirm that fast-ice typically forms narrow bands (up to $\sim$200 km wide) along the coast. They also show that much of the coast becomes fast-ice free during the summertime minimum, particularly to the west of 80° E where the only significant fast-ice feature is found in Lützow-Holm Bay, and to the east of 155° E. Between 80° and 155° E, several coastal promontories, iceberg tongues, glacier tongues and fields of grounded icebergs act to couple with and stabilise fast-ice features on their eastern sides. This allows these fast-ice features to remain

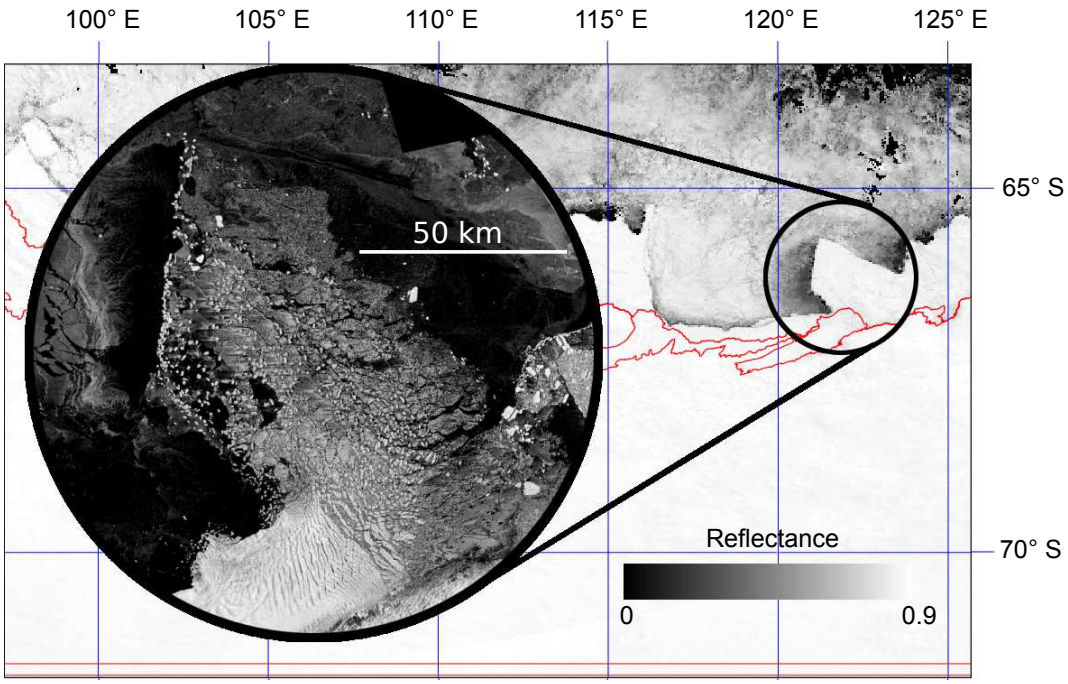

Figure 3.5: A Radarsat-1 C-band SAR image (inset) acquired in 1997, enlarging part of a MODIS composite image (covering the dates 2001,301-320) of the East Antarctic coast (*Jezek*, 2002). The Radarsat image was acquired from http://nsidc.org/data/docs/daac/nsidc0103_ramp_mosaic.gd.html. The SAR enlargement shows that this particular fast-ice feature is interspersed with hundreds of sub-pixel-scale icebergs (forming the Dalton Iceberg Tongue), likely calved from the nearby Moscow University Ice Shelf. Radarsat image © Radarsat International, 1997.

throughout the summertime minimum and become multi-year fast ice (see also *Giles et al.* (2008)).

The fast-ice minimum map likely provides an accurate indication of the distribution of multi-year fast ice (MYFI). When combined with *in situ* or remotely-sensed measurements of freeboard and snow depth, these MYFI maps could contribute to estimates of sea-ice volume, an important yet largely unknown quantity in Antarctica. This work is beyond the scope of this thesis.

Statistics for these two fast-ice maps are shown in Table 3.1. The ratio of overall maximum to minimum area shown in these maps is ∼3.3 to 1 - much lower than the ratio in this region of ∼10 to 1 for overall sea ice extent (including pack ice and fast ice) (*Comiso*, 2010) and the overall seasonal sea-ice ratio of ∼6 to 1 for the entire Antarctic region (*Gloersen et al.*, 1992).

We propose that some form of physical limit exists on the maximum fast-ice extent in this region: large-scale fast-ice distribution is inextricably linked with grounded iceberg (both large- and small-scale) distribution, and thus the bathymetry of the region (*Massom et al.*, 2001b, 2009; *Giles et al.*, 2008). Icebergs ground at depths of up to ∼400 to 500 m in this region (*Beaman and Harris*, 2005; *Massom et al.*, 2001b). Grounded icebergs (including both large tabular grounded icebergs and fields of smaller grounded icebergs) are thought to affect fast-ice distribution in this region in two significant ways (*Massom et al.*, 2001b). They intercept and trap encroaching pack ice drifting westwards in the Antarctic Coastal Current, thus dynamically forming fast ice. They also act as anchor points for fast-ice formation. Evidence of these fast ice-iceberg interactions can be seen in Figures 3.5 (showing fast-ice formation within a field of small grounded icebergs) and 3.6 (displaying the occurrence of fast-ice features to the east of coastal promontories, iceberg tongues and large tabular icebergs). Both interactions rely on similar, relatively shallow

bathymetric conditions, and thus fast-ice features generally tend not to exist outside of these regions (though exceptions exist, and are covered in Chapter 4, Section 4.3). This forms an upper limit to fast-ice areal extent. This limit may vary seasonally due to large tabular iceberg grounding location/distribution, and prevailing ocean current/wind direction.

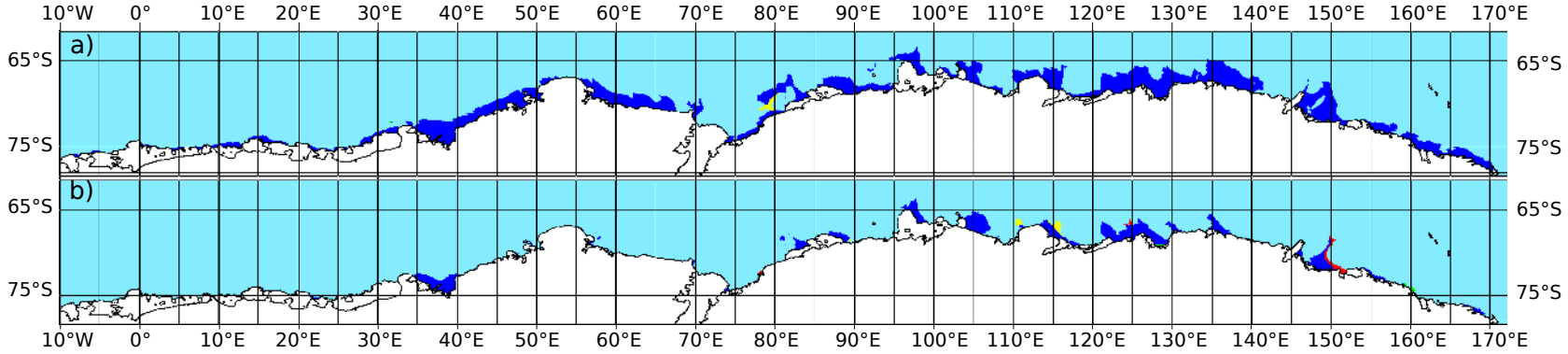

Figure 3.6: Typical fast-ice a) maximum (2005, DOY 241-260) and b) minimum (2006, DOY 061-080) extent maps. The Antarctic continent, ice shelves and floating glacier tongues are shown in white, and the southern ocean/pack ice/large tabular icebergs in light blue. Dark blue represents fast ice determined from a single MODIS composite ("confident"), yellow represents fast ice determined from a AMSR-E ASI composite ("AMSR-E"), and red represents fast ice determined from the previous/next MODIS composite ("prev/next"). Areas of fast ice in the lower panel (fast-ice minimum) essentially show multi-year fast ice.

Table 3.1: Statistics relating to Figures 3.4 and 3.6.

	Date	**Area (km^2)**	**2σ Error (km^2)**	**Fraction pixels "confident"**	**Error regime**
Maximum	2005,241-260	374,108	11,148	0.99	1 (±3%)
Minimum	2006,061-080	111,952	3,336	0.91	1 (±3%)

Caveats for this method of fast-ice detection can be summarised as follows:

- Using only the 20-day composite imagery, no statements can be made about the specific date of fast-ice growth/breakout events - only that the event happened within the 20-day interval. To achieve higher temporal resolution, the component images comprising the composite must be analysed separately.

- Regarding the treatment of pixel edge effects, if a pixel had any fast-ice content, then it was classed as fast ice. As a corollary of this, leads within the fast ice with widths on the order of $\simeq$1 pixel ($\simeq$2 km) were classified as fast ice. This may have implications for end-users who are advised to consider the MODIS composite image product as well as the fast-ice map. Also, leads narrower than 2 km are likely not resolved by maps of this resolution.

- Due to the resolution limitations associated with passive microwave remote sensing, the highest resolution AMSR-E ASI sea-ice concentration data are available at 6.25 km (compared with the map projection's resolution of 2 km). Thus, when AMSR-E composites are used to detect fast ice, smaller flaw leads ($<\sim$2 km width) will not be resolved, the seaward fast-ice edge will be of a lower resolution, and fast-ice edge effects will be more pronounced.

- Although every effort has been made to remove icebergs larger than one pixel (4 km^2) from the fast-ice maps, some may remain.

- Sub-pixel scale icebergs remain unmasked and unaccounted for in the fast-ice area calculations. These icebergs can occupy as much as 15% of the area in some regions, as shown in Figure 3.5.

- The MODIS Mosaic Of Antarctica product (*Scambos et al.*, 2007) was used to mask the Antarctic continent throughout the study period, and no adjust-

ments were made to account for subsequent change in coastal configuration. This will result in small errors in the location of the southern fast-ice edge, and hence small errors in fast-ice area retrieval. Generally, the effect of a changing coastline should have minimal influence on the location of fast-ice features over the 8.8 year study period. However, abrupt change may be regionally significant, e.g., the calving of the Mertz Glacier Tongue in early 2010 (*Young et al.*, 2010).

- The problem of discriminating pack ice from fast ice during times when the pack ice is consistently advected against a fast-ice feature remains. However, using the previous/next MODIS composite to aid in fast-ice classification goes a long way toward fixing this problem. It is estimated that this problem is the cause of a large proportion of the uncertainty associated with estimating fast-ice extent from satellite imagery. Other techniques which detect fast ice by observing ice motion (e.g., *Mahoney et al.*, 2005, 2007a; *Dammert et al.*, 1997; *Morris et al.*, 1999) are not susceptible to this problem, but such techniques are not well suited to visible to TIR imagery due to cloud obscuration. Despite this advantage of SAR over visible/TIR imagery in terms of cloud penetration, it is not well suited to large-scale studies such as this, due to its typically narrow swath width.

3.5 Conclusions and Future Work

This work presents a method for retrieving the first high spatio-temporal resolution time series of fast-ice extent along the entire East Antarctic coast, as well as some examples of fast-ice maps created using these techniques. The technique uses 20-day MODIS composite images (visible in the summertime, thermal infrared in the wintertime) to discriminate pack ice from fast ice. Rather than detecting

sea-ice motion to differentiate between pack and fast ice, the technique aims to enhance the difference between moving ice and stationary ice contiguous with the coast (i.e., fast ice). The motion of the pack ice during the 20-day period "blurs" the pack-ice zone, whereas fast-ice features are clearly defined in the composite imagery. The production of these maps represents a significant improvement in our ability to map and monitor Antarctic fast ice. Despite the technique relying on manual classification, the 2σ error is $\pm 3\%$ for the majority of images, and $\pm 9\%$ otherwise. It is likely that maps of the fast-ice minima show multi-year fast ice extent.

For the first time, measurements of a typical maximum ($\sim$374,000 km^2) and minimum ($\sim$112,000 km^2) fast-ice extent for the entire East Antarctic coast have been presented. This gives a seasonal maximum to minimum ratio of $\sim$3.3 to 1, a much lower ratio than that of overall sea-ice extent in this region ($\sim$10 to 1, *Comiso* (2010)) or around Antarctica ($\sim$6 to 1, *Gloersen et al.* (1992)). This lower ratio reflects the upper limit imposed on fast-ice extent by the locations of grounded icebergs.

A more accurate cloud mask would lead to higher-quality MODIS composite images, particularly during wintertime when accurate cloud masking is most difficult. At the expense of creation of a regular (e.g., 20-day) product, a running mean may also provide higher quality MODIS composite images, and potentially a higher temporal resolution (during prolonged cloud-free periods). Gridding and subsequent re-assessment of the cloud mask product over the East Antarctic coast (rather than evaluating the cloud content of a MODIS granule on a granule-wide basis) would also lead to higher quality composite images, and potentially reduce the data volume required even further. These improvements may be introduced into a future version of the composite image creation software.

The techniques presented here are used to map the fast-ice extent along the

entire East Antarctic coast from March 2000 - December 2008. This work, along with an analysis of the variability of the time series, is presented in Chapter 4.

Chapter 4

East Antarctic Landfast Sea-Ice Distribution and Variability, 2000-2008

An abridged version of this chapter has been submitted for publication to *Journal of Climate*. As with Chapter 3, much of the original introductory material from this chapter has been moved to Chapter 1, to avoid repetition and duplication.

4.1 Abstract

This chapter presents the first continuous high spatio-temporal resolution (2 km, 20 day) time series of landfast sea-ice extent along the East Antarctic coast (10° W to 172° E), in this case for the period March 2000 to December 2008. The time series was derived from consecutive 20-day cloud-free MODIS composite images. Fast-ice extent across the East Antarctic coast shows a statistically-significant ($1.43 \pm 0.30\%$ yr^{-1}) increase (albeit based on this short time series). Regionally, there is a strong increase in the Indian Ocean sector (20° E to 90° E, $4.07 \pm 0.42\%$ yr^{-1}), and a slight (but not significant) decrease in the Western Pacific Ocean sector (90° E to 160° E, -0.40 $\pm$0.37% yr^{-1}). An apparent shift from a negative to a positive fast-ice extent trend is observed in the Indian Ocean sector from 2004. This shift also coincides with a greater amount of interannual variability. No such

shift in apparent trend is observed in the Western Pacific Ocean sector, where fast-ice extents are typically higher and variability lower than the Indian Ocean sector. Fast-ice distribution along the East Antarctic coast is closely related to bathymetry as it affects the positions of grounded icebergs, which act to anchor the fast ice. The limit to the maximum fast-ice areal extent imposed by the location of icebergs modulates the shape of the mean annual fast-ice extent cycle, to give a broad maximum and an abrupt, relatively transient minimum. Ten distinct fast-ice regimes were identified, related to regional variations in bathymetry and coastal configuration. Fast ice is observed to form in sheltered bays, adjacent to large grounded icebergs (particularly on the windward side), between groups of smaller grounded icebergs, between promontories, and upwind of coastal features (e.g., glacier tongues). Fast-ice extent was compared to passive microwave-derived time series of sea-ice extent in the Western Pacific Ocean and Indian Ocean sectors. While sea-ice minimum area/extent is strongly correlated with fast-ice minimum extent (R^2=0.86 across entire East Antarctic coast), maxima appear to be uncorrelated. Analysis of the timing of fast-ice maxima and minima is also presented and compared with overall sea-ice maxima/minima timing.

4.2 Aims, Datasets and Methods

Much of the original introductory material from this chapter has been moved to Chapter 1. The aims of the work in this chapter are: a) to produce a continuous 8.8-year time series of fast-ice extent across the entire East Antarctic coast, and to analyse its spatio-temporal variability in the Indian Ocean and Western Pacific Ocean sectors; b) to detect and quantify trends in fast-ice extent in these three regions; c) to identify possible fast-ice formation regimes across the study region, and relate these regimes to regional variations in coastal configuration and bathymetry;

and d) to compare the regional fast-ice time series to the overall regional pack ice time series over the 8.8-year study period.

A series of 159 consecutive 2-km, 20-day resolution cloud-free MODIS composite images, from March 2000 to December 2008, of the East Antarctic fast-ice zone (63.5° to 72° S, 10° W to 172° E, see dashed box of Figure 2.1 in Chapter 2) were created, using the methods outlined in Chapters 2 and 3 (*Fraser et al.*, 2009, 2010a).

European Centre for Medium-Range Weather Forecasts (ECMWF) Interim Reanalysis data (*Berrisford et al.*, 2009) from 1989-2008 (Mean Sea Level Pressure (MSLP), 10 m wind vectors and 2 m surface temperatures on a 1.5° grid) were formed into 20-day and annual climatologies to assist in interpretation of fast-ice variability. Moreover, 20-day sea-ice concentration composite images were also created from the NSIDC (National Snow and Ice Data Center) combined SMMR (Scanning Multichannel Microwave Radiometer) and SSM/I (Special Sensor Microwave/Imager) dataset (*Comiso*, 1999), in order to compare overall sea-ice extent/area with fast-ice extent. Note that only SSM/I data are used after 1987. This product, known as NSIDC-0079, uses the Bootstrap algorithm, and a threshold of 15% was used to compute sea-ice area. These data are available from http://nsidc.org/data/nsidc-0079.html. Bathymetric information was obtained from the *Smith and Sandwell* (1997) dataset (version 11.1, updated in 2008; available at http://topex.ucsd.edu/WWW_html/mar_topo.html).

The evaluation of trend significance for the fast-ice extent time series closely follows the methodology used by *Cavalieri and Parkinson* (2008), with the metric of a continuous "R-value" (the ratio of the linear trend to the standard deviation) used to indicate the significance of a particular trend. This R-value was converted to a confidence interval by assuming a two-tailed Student's t-distribution and using

a lookup table with the appropriate number of Degrees Of Freedom (DOFs). More details about this analysis are available in many introductory statistical texts (e.g., *Anderson et al.*, 1981). It is important to note that the use of Null Hypothesis Significance Testing (NHST) has been criticised because of the arbitrary nature of significance levels, the effect of sample size on significance levels, and the difficulty of correctly interpreting the result when rejecting or accepting the null hypothesis (e.g., *Nicholls*, 2001). These criticisms are overcome to some extent here by using and reporting the R-value (thus providing a continuum of significance), and reiterating that care must be taken when interpreting the results of the NHST.

Care must also be taken when considering the number of DOFs in the statistical analysis. For truly independent, repeated measurements of a value, the number of DOFs is equal to the number of observations minus two (when fitting a linear model). For example, this fast-ice time series consists of 159 measurements of fast-ice extent. If these measurements were truly independent, then DOFs = 157. However, these measurements are far from independent (for example, it is unphysical for fast-ice extent to jump from a typical maximum value to a typical minimum value in the space of one 20-day window). Thus, the number of DOFs must be reduced to represent this. One typical approach (e.g., used by *Cavalieri and Parkinson*, 2008) is to set DOFs = (number of years in time series) - 2, regardless of how many observations were conducted per year. This approach is equivalent to assigning each year a single value based upon the average ice conditions over that year. Perhaps a more realistic approach may be to assign at least two DOFs per year, allowing for a limited amount of variability within the year, but not to the extent of letting all observations be statistically independent. Nevertheless, in the interest of comparability with other papers in the field, our statistical analyses will be conducted assuming 7 DOFs (i.e., 9 years' data - 2).

4.3 Results and Discussion

This section first presents a discussion of regional differences in fast-ice distribution and morphology around the East Antarctic coast, and then presents the 8.8-year time series of fast-ice extent. This includes a regional analysis, and comparison with pack-ice area/extent within those regions.

4.3.1 Location and Seasonality of Fast-Ice Features

Figures 4.1 and 4.2 show maps of the average percentage of time with fast-ice cover throughout the 8.8-year study period (e.g., a value of 50% likely indicates that fast ice is present for half of each year on average), and the bathymetry for the study region (*Smith and Sandwell*, 1997). Ten distinct regimes of fast-ice cover can be identified from Figures 4.1 and 4.2. These regimes were identified with the assistance of a SAR image mosaic of Antarctica, the RADARSAT-1 Antarctic Mapping Project (RAMP) (*Jezek*, 2002). The SAR mosaic was compared with the bathymetric map to determine the approximate location of zones of grounded icebergs, i.e., in waters shallower that 400 to 500 m. In SAR imagery, icebergs are shown as consistently bright (i.e., high backscatter) targets under freezing conditions, compared with the typically lower backscatter values from sea ice (*Williams et al.*, 1999; *Gladstone and Bigg*, 2002). From west to east, these regimes are classified as follows:

i. *10° W to 35° E (Haakon VII Sea Coast)* - This region is characterised by low fast-ice extents, with little to no multi-year fast ice. This is a possible consequence of the continental shelf break being close (∼20 km) to the coast, leading to few grounded icebergs to act as anchor points for fast ice. Localised exceptions are at 11° E and 15° E where the shallow continental shelf region is wider (i.e., ∼50 km), allowing a number of small icebergs to ground and provide

anchors for fast ice. A thin (up to 30 km) strip of seasonally-recurring fast ice is also found at 27° to 35° E, again where icebergs ground in shallow regions.

ii. *35° to 40° E (Lützow-Holm Bay)* - A region of extensive multi-year fast ice surrounds Syowa base. Despite relatively deep bathymetry in the centre of the bay (up to ∼900 m), groups of icebergs grounded to the west of Riiser-Larsenhalvøya (∼69° S, 34° E) and to the north of Syowa Station (at ∼69° S, 39.5° E) anchor fast-ice formations. These icebergs naturally reinforce the sheltering effect of Lützow-Holm Bay, maintaining the frequently extensive fast ice. Additionally, relatively calm atmospheric conditions are often encountered in the bay (according to ECMWF Interim Reanalysis data, not shown), likely reducing the occurrence of wind-driven fast-ice breakout. Fast ice formed under such quiescent conditions is mainly thermodynaically-formed, and can attain considerable thickness (*Ushio*, 2006).

iii. *40° to 50° E (Enderby Land Coast)* - A seasonally-recurring, approximately 50 km wide strip of fast ice is found along this coastline, of which little is multi-year fast ice. Several thousand small grounded icebergs, clustered along several NW-SE-aligned bathymetric ridges, act to anchor the fast ice between the coast and the 400-500 m isobath.

iv. *50° to 57° E (Amundsen Bay to Cape Boothby)* - Fast-ice rarely forms extensively in this region, despite the fact that the shallow bathymetry permits a line of grounded icebergs about 40 km from the coast. Few grounded icebergs exist between this line and the coast. It is possible that this distance is too wide for fast ice to span in the absence of suitable onshore atmospheric/oceanic forcing, though verification of this assertion would require a detailed analysis of fast-ice extent in coastal embayments and/or between the coast and known grounded

icebergs. Furthermore, the continental shelf is narrow here, possibly allowing warmer waters from the divergence of the Weddell Gyre and the Antarctic Circumpolar Current to penetrate more easily onto the continental shelf (*Meijers et al.*, 2010), which could explain the reduced fast-ice extent here.

v. *57° to 68° E (Mawson Coast)* - Small grounded icebergs closely follow the contour of undersea ridges, leading to recurring and distinctively-shaped fast-ice features extending ∼50 km from the coast in this area. Fast ice is present for much of the year, particularly in the 57° - 62° E section. Multi-year fast ice is found only in the most sheltered bays (e.g., Edward VIII Gulf, ∼57° E).

vi. *68° to 71° E (Cape Darnley)* - A line of small grounded icebergs extends north-east from Cape Darnley, leading to extensive and frequent (though not typically multi-year) fast-ice coverage. This fast-ice feature frequently extends to the western edge of the Amery Ice Shelf.

vii. *71° to 74° E (north face of Amery Ice Shelf terminus)* - No significant fast ice forms in this dynamic polynya region, likely due to the deep bathymetry (600-700 m) in Prydz Bay. The depth here precludes iceberg grounding, leading to a lack of fast-ice anchor points.

viii. *74° to 81° E (Ingrid Christensen Coast)* - A narrow strip of fast ice often covers this coast, forming along the eastern margin of the Amery Ice Shelf, the Polar Record Glacier, and hundreds of small grounded icebergs. Multi-year fast ice is found at the eastern edge of the Amery Ice Shelf. Further offshore (∼100 km), a large, seasonally-recurring "island" of fast ice exists, of which the main body is present for around half of each season. This is anchored around a group of small grounded icebergs (centred on approximately 78.5° E, 67° S).

ix. *81° to 152° E (West Ice Shelf to Cook Ice Shelf)* - This zonally-extensive region is characterised by several coastal features that are north-south aligned, e.g., iceberg tongues, glacier tongues, ice shelves, coastal promontories, and groups of smaller grounded icebergs. Irregular-shaped fast-ice regions are located on the eastern (windward) side of these coastal features (as opposed to the majority of fast-ice features found from 10° W to 81° E, which typically run parallel to the coast). Latent heat polynyas (driven by katabatic winds) are typically found on the western (lee) side of the features (*Barber and Massom*, 2007). Several extensive (a few 1,000 km^2 in area) regions of multi-year fast ice are encountered in this region. In fact, every major north-south protrusion (i.e., the West Ice Shelf, Shackleton Ice Shelf, line of grounded icebergs north of Vincennes Bay, Dalton Iceberg Tongue, Dibble Iceberg Tongue and Mertz Glacier Tongue) has a latent heat polynya on its western side (*Massom et al.*, 1998; *Tamura et al.*, 2008), and a fast-ice feature on its eastern side.

x. *152° to 172° E (Cook Ice Shelf to Cape Adare)* - This final region is characterised by a relatively narrow ($\sim$ 50 km) strip of fast ice which is oriented parallel to the coast, similar to the fast-ice morphology found in the aforementioned Enderby Land Coast and Mawson Coast regions (regions iii and v). The strip of fast ice is more extensive in the western half of this region. Multi-year fast ice is found between Lauritzen and Slava Bays (154° E -156° E), and also off the coast of the closed Russian Leningradskaya Station ($\sim$159.5° E). Few grounded icebergs are present in this region. The recurring fast-ice feature to the east of this region likely forms in the oceanic lee of Cape Adare. Wind speeds in the region, as shown in ECMWF Interim Reanalyses (*Berrisford et al.*, 2009), are typically relatively low, which precludes the formation of a significant latent heat polynya from the Cape. The presence of the ocean ridge, reportedly centred

at 157°, 68.5° S (*Smith and Sandwell*, 1997), is unlikely as there appear to be no grounded icebergs at this location. The ridge is also not present in other more recent bathymetry products, e.g., *Timmermann et al.* (2010).

We suggest that these regimes can be broadly combined into two larger regions with broadly different fast-ice characteristics: a) west of 81° E, where relatively few coastal protrusions exist; and b) east of 81° E, a region characterised by a large number of coastal protrusions. In the former region, it is expected that the northern margin on these elongated fast-ice zones (i.e., regions iii and v) form boundaries with extensive flaw lead systems, suggesting strong flow in the Antarctic Coastal Current (*Barber and Massom*, 2007).

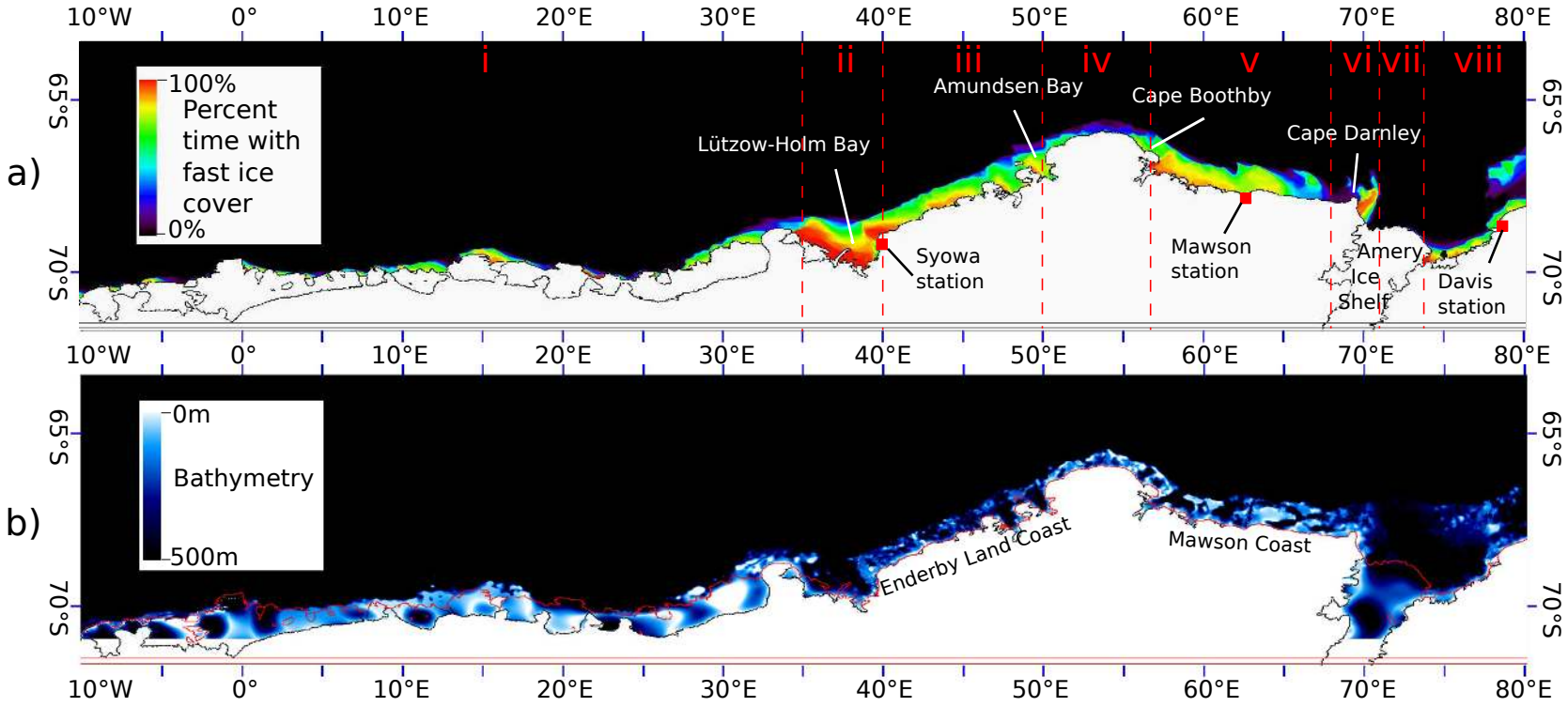

Figure 4.1: a) Fast-ice coverage map (10° W - 80° E) averaged over the 8.8-year study period (from March 2000 - December 2008). A value of 100% is given to fast ice that covers the pixel for the entire time series of 159 images spanning the 8.8 year study period. b) Corresponding bathymetry map for a). Bathymetry from *Smith and Sandwell* (1997). Coastline from *Scambos et al.* (2007). See the text for a full discussion of fast-ice formation regimes. The maximum width of the fast-ice zone varies widely across the East Antarctic coast, reaching a maximum width of ∼225 km at around 150° E (immediately east of the iceberg B-9B).

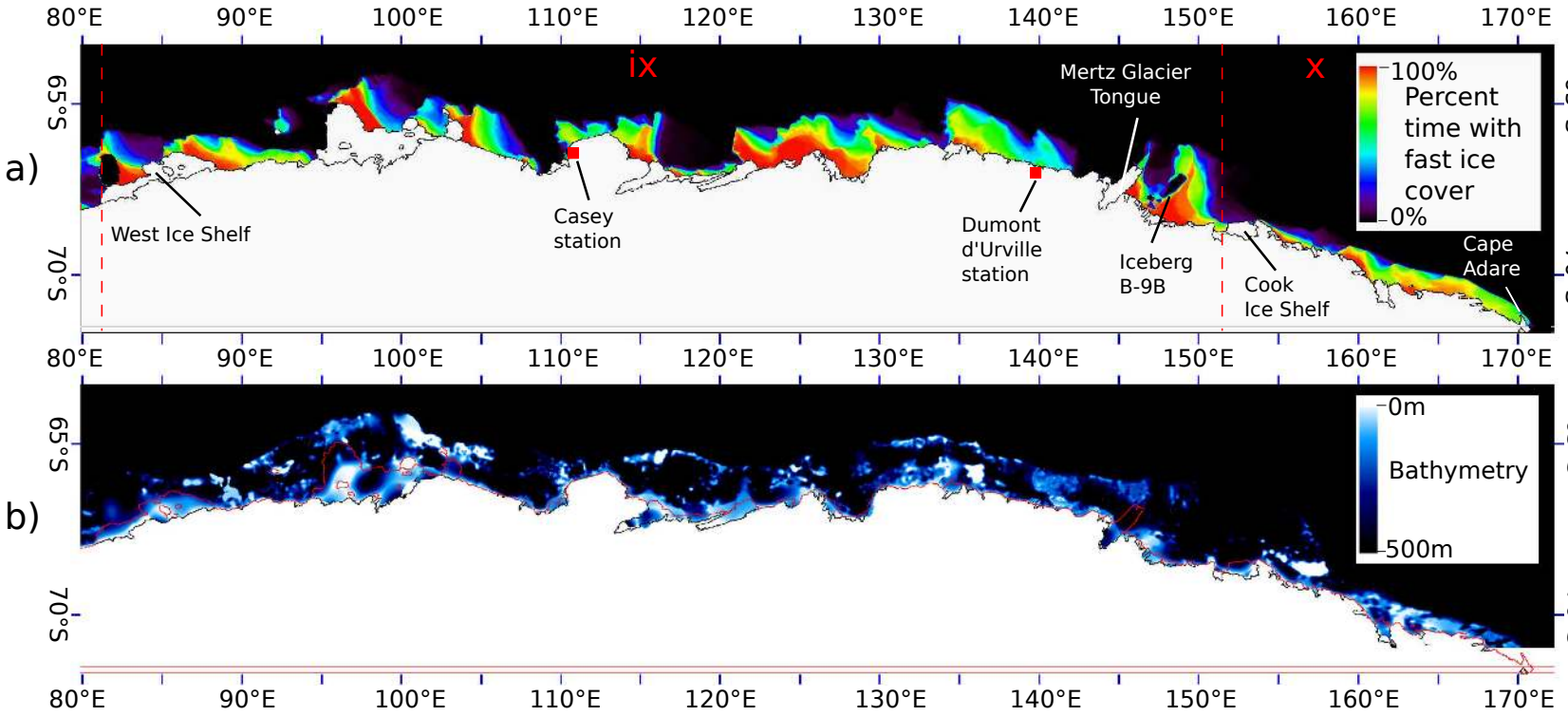

Figure 4.2: a) Fast-ice coverage map (80° E - 172° E) averaged over the 8.8-year study period (from March 2000 - December 2008). A value of 100% is given to fast ice that covers the pixel for the entire time series of 159 images spanning the 8.8 year study period. b) Corresponding bathymetry map for a). Bathymetry from *Smith and Sandwell* (1997). Coastline from *Scambos et al.* (2007). See the text for a full discussion of fast-ice formation regimes.

4.3.2 Fast-Ice Time Series, Annual Cycle, and Overall Trend Analysis

The time series of fast-ice extent for the entire region (10° W - 172° E) is shown in Figure 4.3, with the mean annual cycle given in panel b. The 8.8-year mean annual cycle begins by steadily declining to the fast-ice minimum of ∼120,000 km^2 at around Day Of Year (DOY) 61-80 (early mid-March). This is followed by a period of rapid fast-ice growth to a relatively broad maximum of ∼388,000 km^2 (persisting from ∼DOY 141 to 300, or mid May to late October). Following DOY 300, the fast-ice extent declines until the end of the year. In contrast, the shape of the overall sea-ice extent and area cycles is more sinusoidal, with fairly slow seasonal formation (from mid march to late September) being followed by relatively rapid retreat, typically from mid-October to early February (*Gloersen et al.*, 1992).

The annual cycle is smoother in the Indian Ocean sector (Figure 4.4) than the Western Pacific Ocean sector (Figure 4.5), though it is still substantially broader around the maximum than the minimum. This may be a consequence of relative spatial scales of averaging and fast-ice variability. A smooth time series may result if the averaging scale is significantly larger than the scale at which fast ice varies. Alternatively, this possibly reflects the different formation regimes in each region. The proportion of thermodynamically- rather than dynamically-formed fast ice in the Indian Ocean sector is likely higher than that in the Western Pacific Ocean sector, due to the greater number of north-south coastal promontories in the latter sector. These features act to intercept pack ice that is drifting westwards around the coast within the Antarctic Coastal Current, leading to more dynamically-formed fast ice (*Giles et al.*, 2008; *Jezek*, 2002). This pattern is also shown in the maps of *Giles et al.* (2008), which indicate higher radar backscatter (indicating rougher ice) for fast-ice on the "upstream" side of these coastal promontories. It is hypothesised here

that the dynamic formation leads to the "jagged" shape of the mean annual cycle in regions containing a high proportion of dynamically-formed fast ice. Significant fast-ice breakout also typically begins to occur earlier in the Western Pacific Ocean sector than the Indian Ocean sector (see Figures 4.4b and 4.5b), and continues at a steady rate throughout the summer breakout season. This suggests that dynamically-formed fast ice may be mechanically weaker, leading to episodic breakout which may occur at the interfaces between existing fast ice and newer dynamically-formed fast ice. This result showing the more transient nature of dynamically-formed fast ice in Antarctica, characterised by series of breakouts and reformations, has also been observed in the Arctic by *Mahoney et al.* (2007b).

There is a pronounced peak in the mean annual fast-ice extent cycle in the Western Pacific Ocean sector at DOY 261-280. Initially, it was suspected that an anomalously high maximum in 2006 (discussed in detail later in Chapter 5) was solely contributing to this peak. The contribution of these data to the annual cycle was tested by calculating a truncated mean (whereby the maximum and minimum values are removed from the mean calculation). The truncated mean annual cycle also exhibited a peak at DOY 261-280, however, so the timing of the fast-ice maximum extent is genuinely believed to occur within this period.

We also performed a regional analysis on the fast-ice time series, comparing the Indian Ocean and Western Pacific Ocean sectors. One caveat of this approach is that it involves spatial averaging on large spatial scales (several thousand km), possibly masking regional variability of fast ice. This decision was made in order to allow intercomparisons between this fast-ice time series, and the overall sea-ice time series from passive microwave data analysis (e.g., *Cavalieri and Parkinson* (2008)). Table 4.1 summarises the results of the trend analyses, and Table 4.2 shows the value of the fast-ice minimum/maximum areal extent in each year.

Table 4.1: Table of fast-ice extent trend results by region. The R-value represents the ratio of trend slope to its standard deviation. An R-value greater than 3.5 indicates a statistically-significant trend with greater than 99% confidence, and is shown here in a bold and italic font.

Sector	$km^2\ yr^{-1}$	$\%\ yr^{-1}$	R-value
East Antarctica (10° W - 172° E)	4012 ± 830	1.43 ± 0.30	***4.84***
Indian Ocean (20° - 90° E)	4444 ± 457	4.07 ± 0.42	***9.73***
Western Pacific Ocean (90° - 160° E)	-579 ± 525	-0.40 ± 0.37	-1.10

Table 4.2: Table of fast-ice maximum and minimum extents (km^2) for East Antarctic coast, Indian Ocean and Western Pacific Ocean sectors.

	East Antarctica (10° W - 172° E)		Indian Ocean sector (20° - 90° E)		Western Pacific Ocean (90° - 160° E)	
	Minimum FI extent $\times 10^3$	Maximum FI extent $\times 10^3$	Minimum FI extent $\times 10^3$	Maximum FI extent $\times 10^3$	Minimum FI extent $\times 10^3$	Maximum FI extent $\times 10^3$
2000		392		144		206
2001	133	375	34	140	87	199
2002	96	400	41	148	51	226
2003	110	362	24	146	79	211
2004	83	341	8.9	137	69	184
2005	115	374	46	150	68	192
2006	104	447	26	179	72	238
2007	127	395	66	162	54	195
2008	191	407	92	173	76	199
Mean	120	388	42	153	69	205

For the entire East Antarctic coast and from 2000 to 2008, a positive trend (increase) in fast-ice extent of 4012 ± 830 km^2 yr^{-1} is observed. Though this trend is statistically significant (at the 99% confidence level), the time series is too short to determine whether or not it is part of a longer-term positive trend. The observed increase is concentrated mainly in the Indian Ocean sector (see Figure 4.4), with a trend of 4444 ± 457 km^2 yr^{-1}. Interannual variability in areal extent in this region is relatively large, especially in fast-ice minima. As with the entire East Antarctic coast, annual minima in the Indian Ocean sector seem to have little relation to previous or subsequent maxima. Fast-ice maxima in this region appear to follow a bi-modal distribution, with the 2000-2005 maxima falling near the 8.8-year mean cycle value, while the 2006-2008 maxima are considerably higher. In contrast, there is no significant trend in fast-ice extent for the Western Pacific Ocean sector (-579 ± 525 km^2 yr^{-1}).

An apparent change in fast-ice extent trend is observed in the Indian Ocean sector from ∼2004 onwards (Figure 4.4). Prior to 2004, a slightly negative trend is observed, and interannual variability is relatively small. From 2004 onwards, the trend becomes strongly positive and variability increases. This change in trend in the Indian Ocean sector contributes strongly to the trend observed for the entire East Antarctic coast. In the Indian Ocean sector, minima range from ∼9,000 km^2 (in 2004) to ∼92,000 km^2 (2008), while maxima range from ∼137,000 km^2 (2004) to ∼179,000 km^2 (2006). No such change is observed in the Western Pacific Ocean sector (Figure 4.5), where variability is uniformly relatively small (but values still span a large range), and the negative trend continues throughout the 8.8-year record. In this sector, minima range from ∼51,000 km^2 (in 2002) to ∼87,000 km^2 (2001), while maxima range from ∼184,000 km^2 (2004) to ∼238,000 km^2 (2006).

The relationship between each year's fast-ice maximum and the subsequent

minimum was also analysed. Below-average minima are observed in 2002 (∼96,000 km^2), 2004 (∼83,000 km^2) and 2006 (∼104,000 km^2, compared with the mean of ∼120,000 km^2). Of these years, only the 2004 maximum was more than 40,000 km^2 below average (∼341,000 km^2 compared with the mean maximum extent of ∼388,000 km^2). In fact, the 2006 maximum was 70,000 km^2 above average (∼447,000 km^2), despite the preceding below-average minimum. The only strongly above-average (∼191,000 km^2) was encountered in 2008, which was followed by an above-average maximum (∼407,000 km^2). It appears that there is little correlation between maxima and subsequent minima, except from 2006 to 2008 in the Indian Ocean sector, which recorded strongly positive extent anomalies for almost the entire 3-year period.

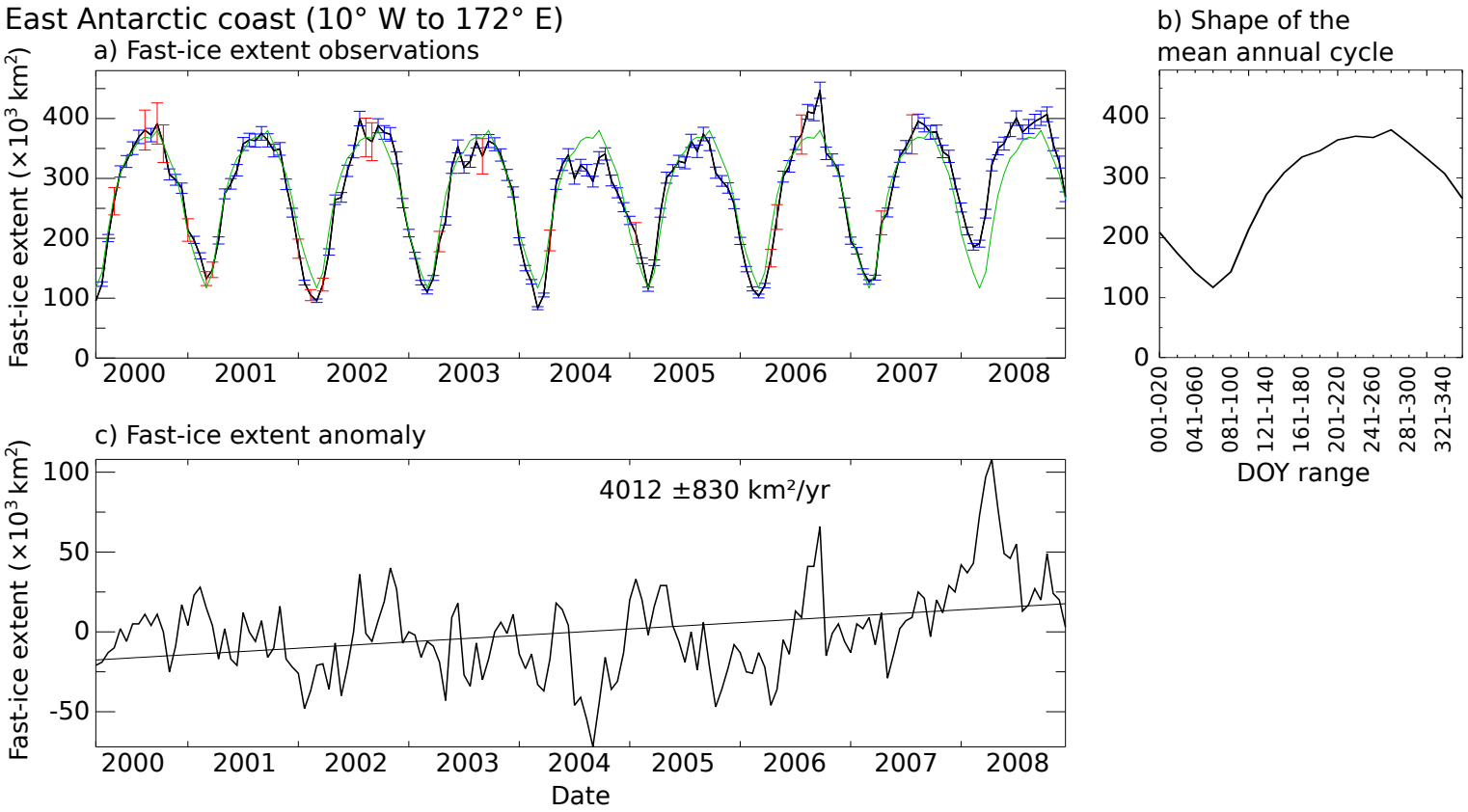

Figure 4.3: a) Fast-ice time series for the East Antarctic coast (10° W to 172° E), showing a statistically significant (at the 99% confidence level) increase of 4012 ± 830 km^2 yr^{-1}. Errors bars ($\pm 2\sigma$) are shown in blue (corresponding to error regime 1) and red (error regime 2, see text). Note the major impact of extraordinarily extensive fast ice along the Enderby Land and Mawson coasts from 2006 to 2008. b) The shape of the annual fast-ice cycle, produced from the 8.8 year dataset. The repetition of this cycle is also shown as a thin green line in a). c) Fast-ice extent anomaly (differences between the observed fast-ice extent and the 8.8-year mean for that time period).

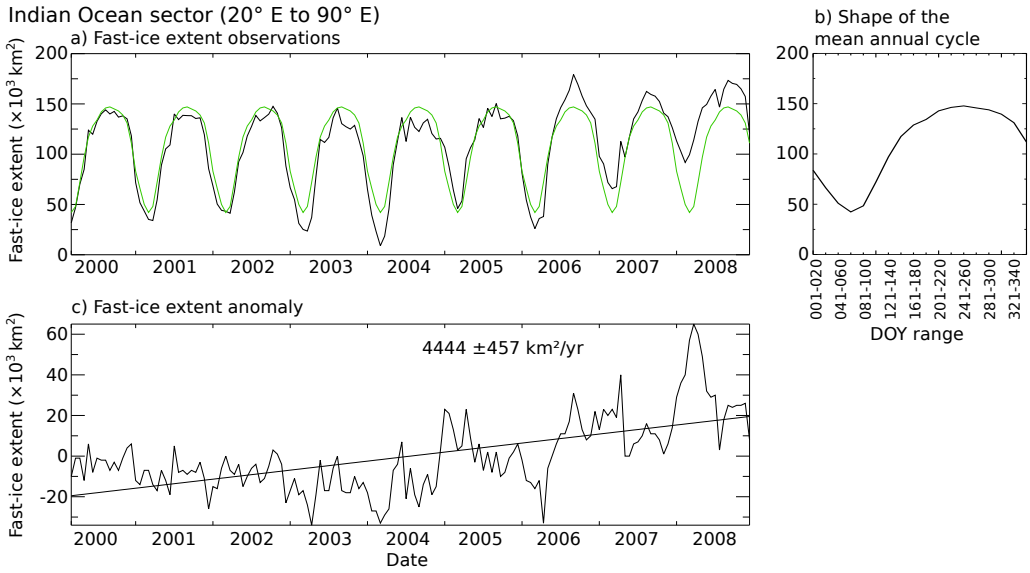

Figure 4.4: a) Fast-ice time series for the Indian Ocean sector (black line), showing a statistically significant increase (at the 99% confidence level) of 4444 ± 457 km^2 yr^{-1}. Error bars are as shown in Figure 4.3. b) The shape of the annual fast-ice cycle, produced from the 8.8 year dataset. The repetition of this cycle is also shown as a thin green line in a). Note the smooth annual cycle, possibly reflecting the relatively high portion of thermodynamically-formed fast ice in this region. c) Fast-ice extent anomaly (differences between the observed fast-ice extent and the 8.8-year mean for that time period).

Comparing fast-ice extent by sector (see Figure 4.6), it can be seen that while minima of the Indian Ocean and Western Pacific Ocean sectors are uncorrelated (R^2=0.03), maxima have a slightly higher correlation coefficient (R^2=0.21). The Indian Ocean sector includes generally less fast ice than the Western Pacific Ocean sector until late 2006, when their fast-ice extents become comparable (see Figure 4.6).

4.3.3 Fast-Ice Extent Climatology and Annual Minimum-to-Minimum Averages

The fast-ice extent by time of year, averaged over the 8.8-year time series, is shown in Figures 4.7 and 4.8. These figures represent a fast-ice climatology. Com-

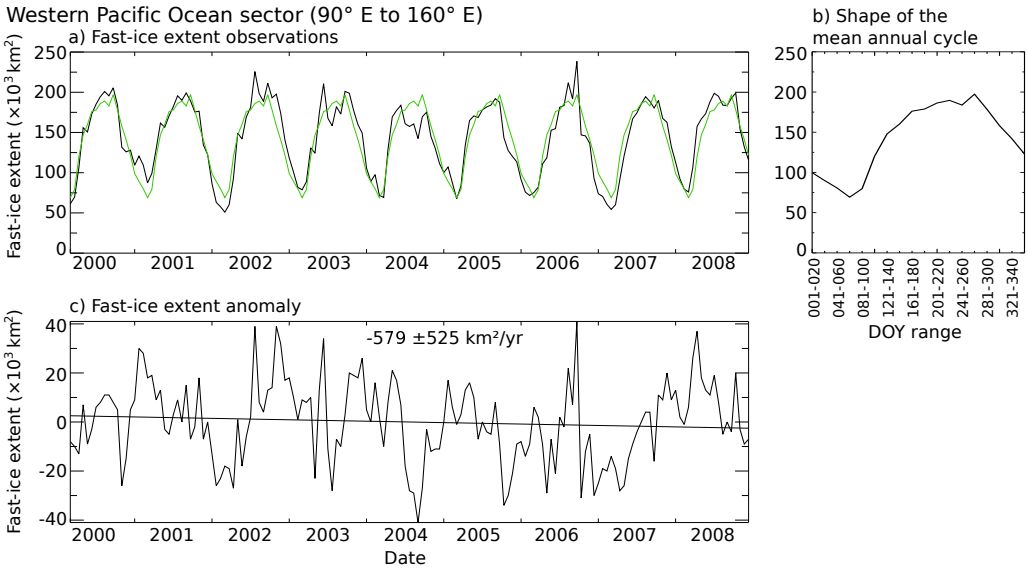

Figure 4.5: a) As in 4.4 but for the Western Pacific Ocean sector, showing a slight but non-significant decrease (579 ± 525 km^2 yr^{-1}). b) The shape of the annual fast-ice cycle, produced from the 8.8 year dataset. The repetition of this cycle is also shown as a thin green line in a). c) Fast-ice extent anomaly (differences between the observed fast-ice extent and the 8.8-year mean for that time period).

parison between these figures and Figures 4.1a and 4.2a reaffirms the close links between bathymetry, iceberg grounding and fast-ice extent discussed in previous sections. In many regions, and particularly where minimal coastal protrusions are present, fast ice reaches its maximum extent early in the season, and is unable to "grow" past this due to a lack of grounded icebergs in waters deeper than approximately 400 to 500 m. We suggest that these regions (e.g., the Mawson and Enderby Land coasts) may have a higher fraction of thermodynamically-formed fast ice.

Annually-averaged (annual minimum to subsequent annual minimum) fast-ice conditions are shown in Figure 4.9 (except for the image labelled "2008", where no data from 2009 were analysed and hence the 2009 minimum was unavailable, making this image more biased toward greater fast-ice coverage). This figure clearly shows the origin of the positive trend in the Indian Ocean sector (Figure 4.4),

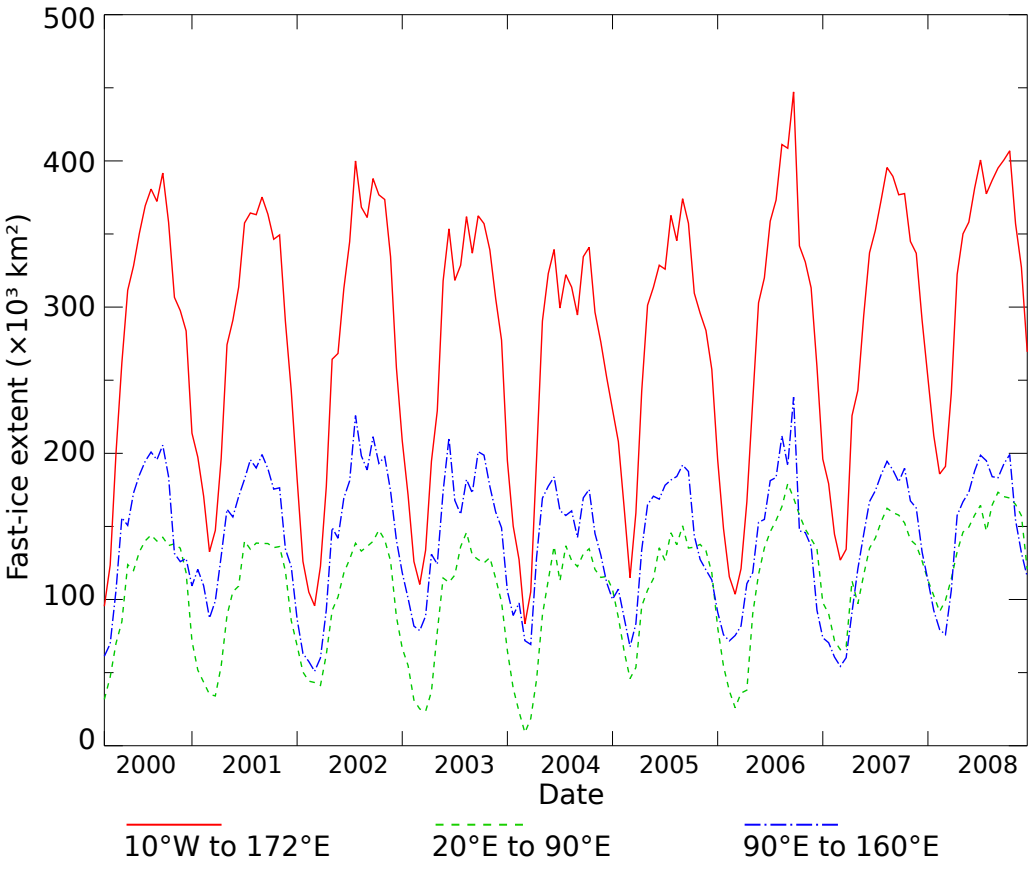

Figure 4.6: Fast-ice extent time series by region. The 90 - 160° E (Western Pacific Ocean) sector generally has more extensive fast-ice cover than the 20 - 90° E (Indian Ocean) sector due to the presence of substantially more north-south aligned coastal features, and a higher proportion of perennial fast ice.

especially over the period 2006-2008. In particular, much more of the fast ice along the Mawson and Enderby Land coasts survives the summertime melt during 2007 and 2008, contributing to the progressively higher minimum fast-ice extents during these years. Additionally, more fast ice forms north of the region from Amundsen Bay to Cape Boothby (50 - 57° E) during the maxima of 2006, 2007 and 2008, contributing to the higher maximum extent observed in the Indian Ocean sector during these years.

In the Western Pacific Ocean sector, the main contribution to the origin of the anomalously high maximum extent in 2006 (DOY 261-280) can be traced to an extensive fast-ice feature to the east of iceberg B-9B (until recently (*Young et al.*, 2010), centred at approximately 67°20' S, 148°23' E). Here, the westward-flowing Antarctic Coastal Current advects pack ice into the region between B-9B and the coast, often forming heavily consolidated pack ice which can temporarily form fast ice (*Massom et al.*, 2001b; *Barber and Massom*, 2007). Dense clusters of small grounded icebergs, i.e., those to the north of B-9B, act in a similar fashion to individual large grounded icebergs (*Massom et al.*, 2001b; *Barber and Massom*, 2007). In this way, fast ice can extend across waters deeper than the maximum depth of iceberg grounding (∼450 m), and be present more than 200 km offshore. The 2006 maximum is likely an extreme manifestation of this phenomenon. Examination of ECMWF Interim Reanalysis data for this period shows anomalously strong easterly winds. This provides evidence for pack-ice advection being an important contributor to fast-ice growth in this region. Ocean currents are also likely to be an important factor in this region, but data are lacking. This event is studied in detail, in Chapter 5, Section 5.5.9.

Analysis of the fast-ice climatology (Figures 4.7 and 4.8) reveals important differences in the nature of fast-ice formation and breakout in each sector. Fast-ice

growth and breakout along the Enderby Land and Mawson coasts, and also the region to the east of the Cook Ice Shelf (∼152° E) both occur largely in a north-south direction, i.e., the strip of fast ice along the coast becomes wider as the season progresses, before gradually retreating back towards the coast in summer. This is in contrast to much of the fast ice in the Western Pacific Ocean sector. As previously mentioned, in this region, several coastal protrusions allow fast-ice to form windward of these features. As the season progresses, the fast ice grows more in an eastward direction as more pack ice is intercepted by the pre-existing fast ice. Fast-ice retreat in this sector then occurs by recession of the fast ice largely from east to west in spring/summer.

The length of the fast-ice coverage per year at a given location, i.e., the seasonality or fast-ice "season" duration, is an important parameter, responding to both oceanic and atmospheric forcing (*Heil*, 2006; *Heil et al.*, 2006; *Mahoney et al.*, 2005). Due to the large spatial scale of this dataset, detailed analysis of fast-ice seasonality is outside of the scope of this work.

4.3.4 Comparison Between Fast-Ice Extent and Overall Regional Sea-Ice Extent and Area

The relationship between fast-ice extent and overall sea-ice extent was examined using SSM/I passive microwave sea-ice concentration 20-day composite images generated over the same time period. Sea-ice area is defined as the area of ocean which is covered by sea-ice of concentration >15%. Sea-ice extent is defined as the area of ocean covered by sea ice, weighted by the concentration. Comparisons for the whole coast, the Indian Ocean sector, and the Western Pacific Ocean sector are shown in Figures 4.10, 4.11 and 4.12 respectively. Note the difference in overall sea-ice extent and area between the Indian Ocean and Western Pacific Ocean

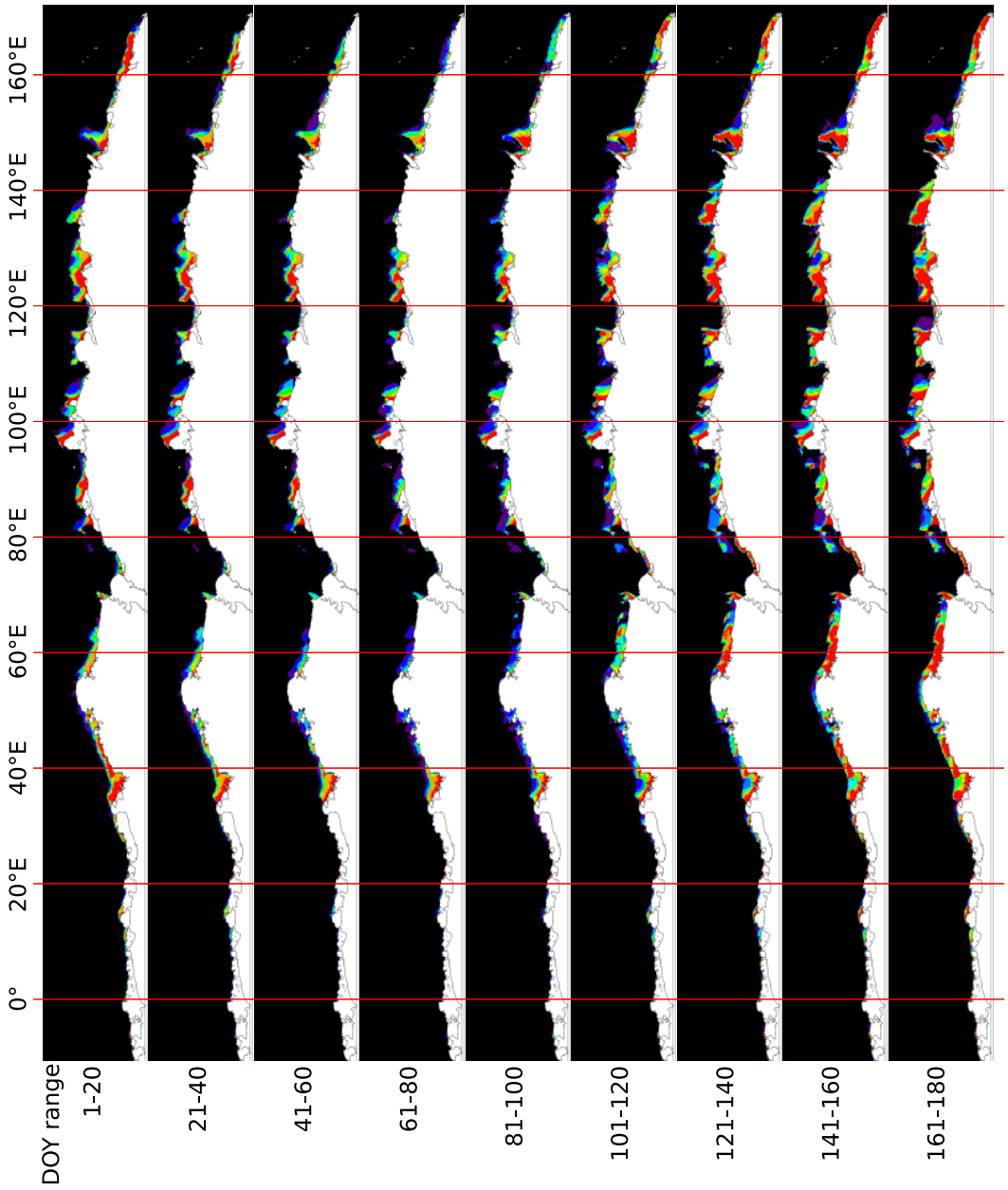

Figure 4.7: Fast-ice climatology for the 8.8-year period, in 20-day increments, from DOY 1 - 180 (see Figure 4.8 for DOY 181 - 365). Each panel shows the fraction of observations during that DOY interval with fast-ice cover. The colour scale is the same as that used in Figures 4.1 and 4.2, i.e., it represents the proportion of time over which fast ice coverage occurs.

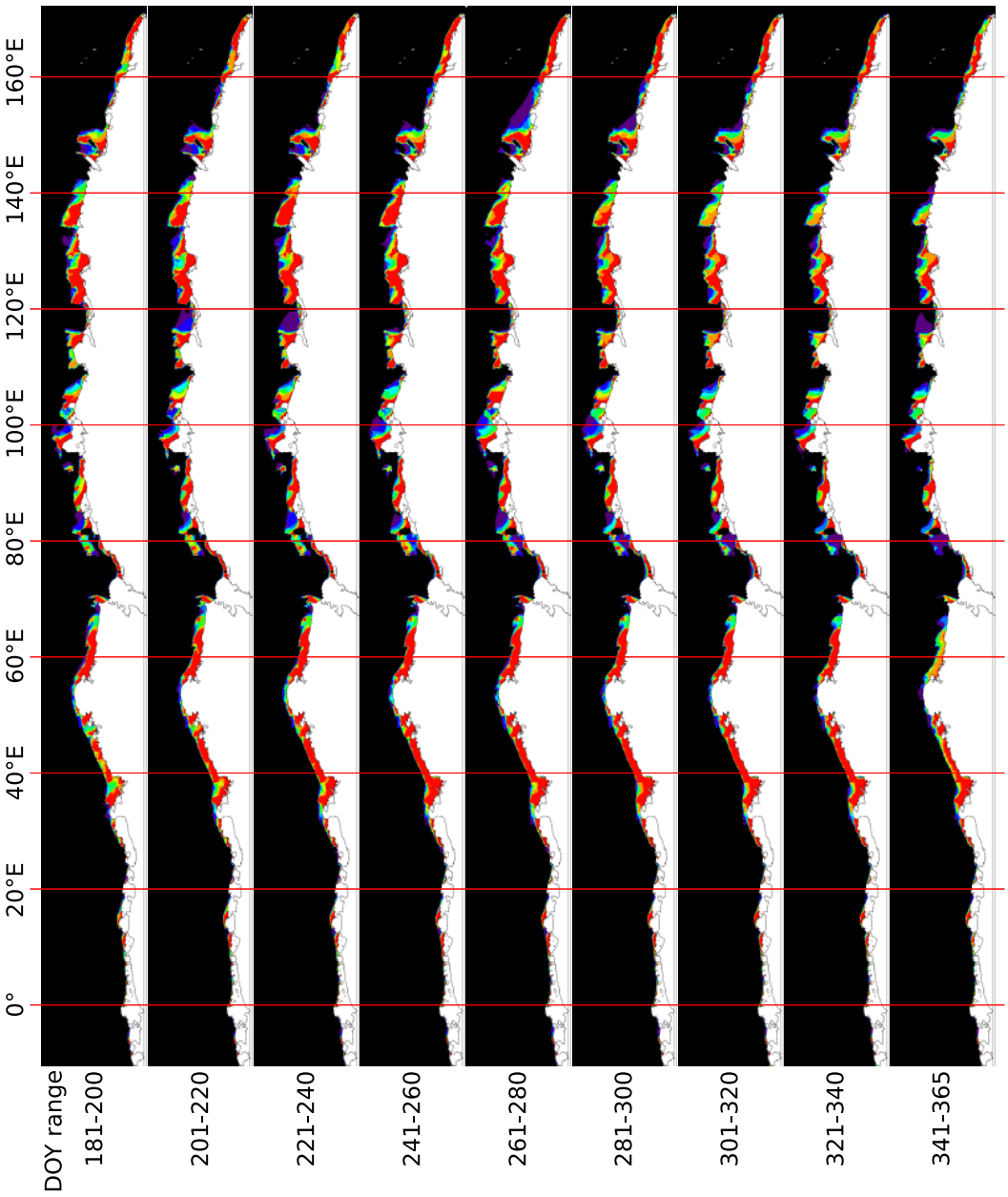

Figure 4.8: Fast-ice climatology for the 8.8-year period, in 20-day increments, from DOY 181 - 365 (see Figure 4.7 for DOY 1 - 180). Each panel shows the fraction of observations during that DOY interval with fast-ice cover. The colour scale is the same as that used in Figures 4.1 and 4.2, i.e., it represents the proportion of time over which fast ice coverage occurs.

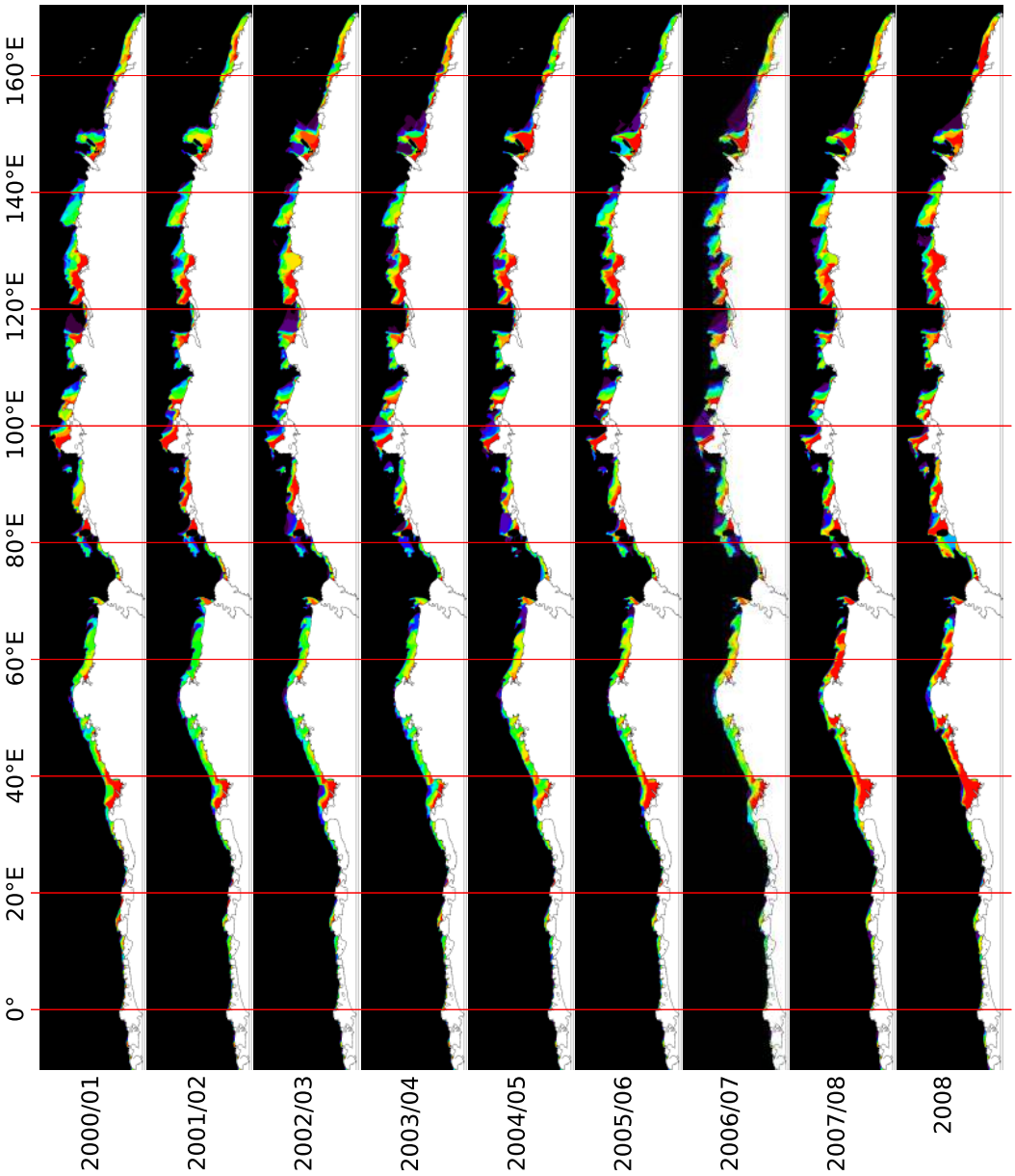

Figure 4.9: Fast-ice conditions by season (from one minimum to the subsequent minimum), using the same colour scale as Figures 4.1 and 4.2, i.e., it represents the proportion of time over which fast ice coverage occurs.. Since no 2009 data were analysed, the 2008 "season" is incomplete, and biased toward higher fast-ice coverage.

sectors, a consequence of the greater pack-ice extent in the Indian Ocean sector, relating to the location of the eastern part of the Weddell Gyre and the southern boundary of the Antarctic Circumpolar Current (*Gloersen et al.*, 1992). Across the East Antarctic coast and both sub-regions, pack ice area/extent maxima are uncorrelated with fast-ice maxima, with R^2 values of 0.05, 0.02 and 0.04 for the entire coast, Indian Ocean and Western Pacific ocean sectors respectively. However, the minima are strongly correlated (R^2 values of 0.86, 0.89 and 0.65 respectively). This is not necessarily an indication that fast-ice extent and overall sea-ice extent share a common forcing; rather the relative fraction of fast ice comprising overall sea ice increases (i.e., the ratio of sea ice to fast ice decreases to a minimum) during the summertime sea-ice minimum (see Figure 4.2). Additionally, fast ice is highly vulnerable to ocean waves (*Crocker and Wadhams*, 1988, 1989; *Langhorne et al.*, 2001), and it may be that pack ice acts as a protective buffer to their destructive effect, leading to larger fast-ice minimum extents during years when more extensive pack ice is present.

This fast-ice time series mirrors the longer-term trends in overall sea-ice extent/area in the region (dating back to 1978). For example, both *Comiso* (2010) and *Cavalieri and Parkinson* (2008) show a larger increase in sea-ice extent in the Indian Ocean sector ($\sim$1.9 $\pm$1.4% decade^{-1}) than the Western Pacific Ocean sector ($\sim$1.4 $\pm$1.9% decade^{-1}), though neither trend is significant at the 95% confidence level (*Cavalieri and Parkinson*, 2008).

4.3.5 Variability in the Timing of Fast-Ice Maxima and Minima

Timing of maximum and minimum fast-ice extent are important fast-ice parameters, and are sensitive to changes in climate (*Heil et al.*, 2006; *Mahoney et al.*,

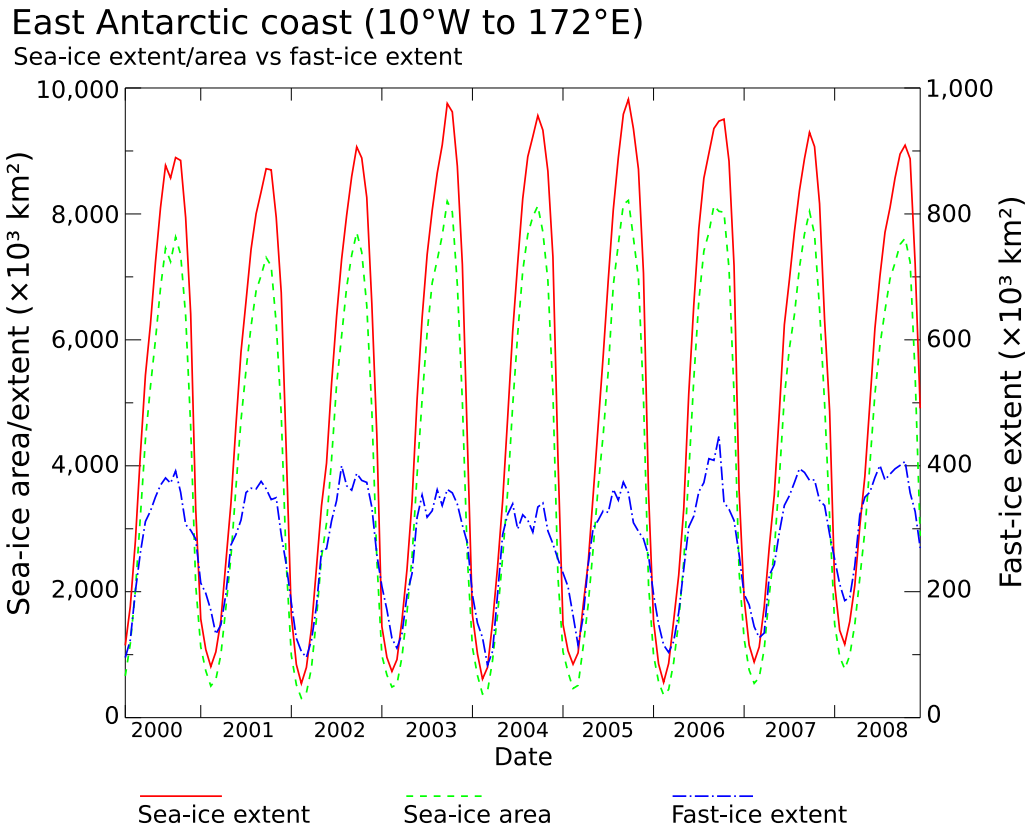

Figure 4.10: Time series comparison between overall sea-ice extent/area and fast-ice extent along the entire East Antarctic coast (10° W to 172° E). The scale for overall sea-ice extent and area is on the left. Fast-ice extent has been scaled by a factor of 10 for intercomparison purposes, and uses the scale on the right.

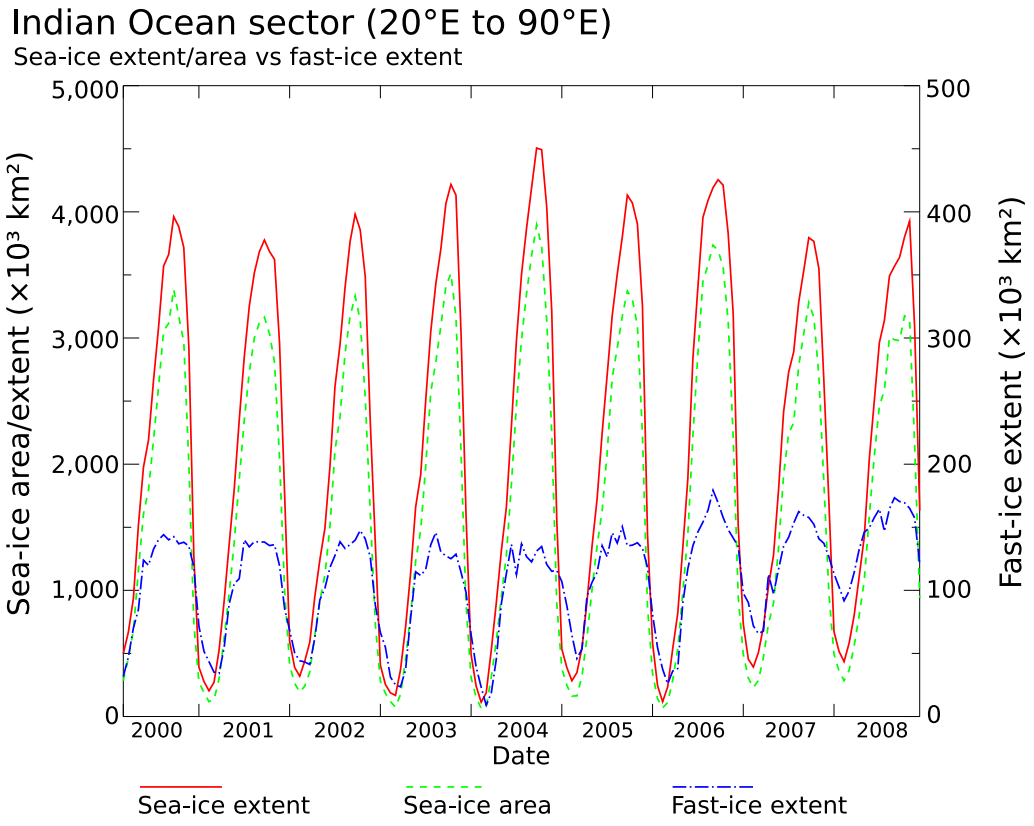

Figure 4.11: Time series comparison between overall sea-ice extent/area and fast-ice extent in the Indian Ocean sector (20° E to 90° E). The scale for overall sea-ice extent and area is on the left. Fast-ice extent has been scaled by a factor of 10 for intercomparison purposes, and uses the scale on the right.

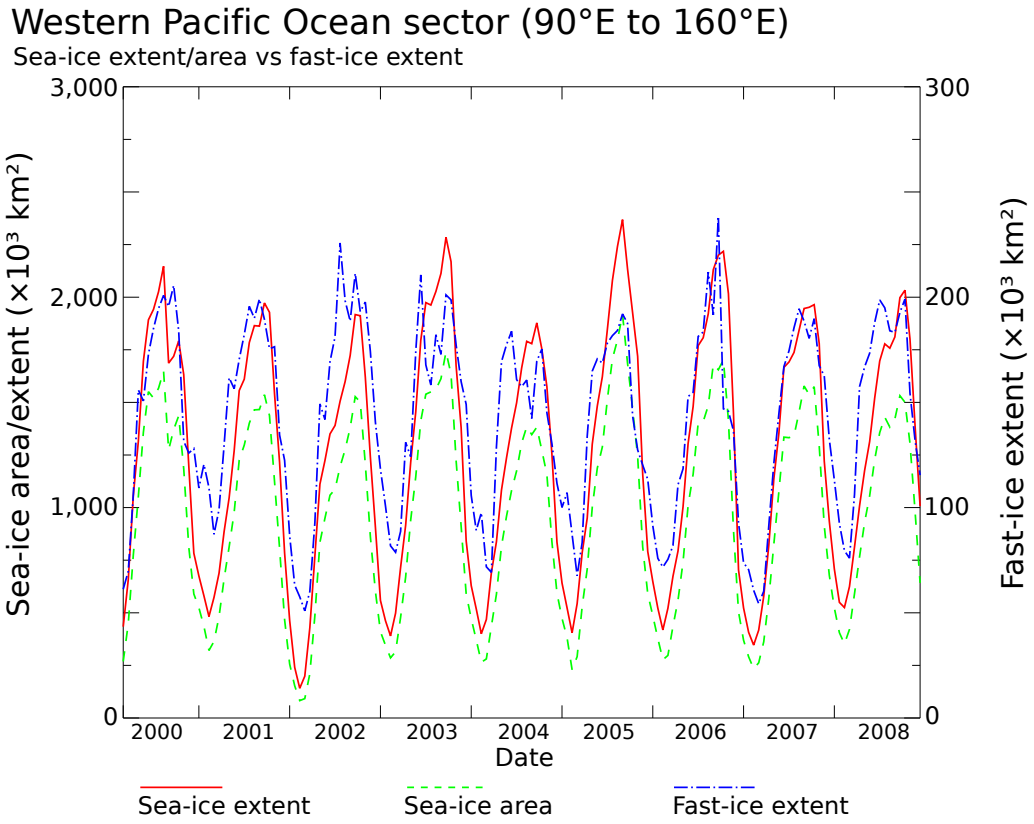

Figure 4.12: Time series comparison between overall sea-ice extent/area and fast-ice extent in the Western Pacific Ocean sector (90° E to 160° E). The scale for overall sea-ice extent and area is on the left. Fast-ice extent has been scaled by a factor of 10 for intercomparison purposes, and uses the scale on the right. Note that fast-ice extent in this sector comprises a much greater portion of overall sea-ice extent compared to the Indian Ocean sector (Figure 4.11).

2005). The minimum fast-ice extent, averaged across the entire region, typically occurs during DOY 61-80 (early/mid March), with a mean value of ∼120,000 km^2. Maximum typically occurs during DOY 261-280 (mid/late September), with a mean value of ∼388,000 km^2 (see Figure 4.13) - i.e., the ratio of maximum to minimum fast-ice extent is typically ∼3.2 to 1. In comparison, the mean regional minimum and maximum overall sea-ice extent over the same time period (2000-2008) is ∼770,000 and ∼9,300,000 km^2 respectively (*Comiso*, 1999), i.e., a ratio of ∼12 to 1 for overall sea ice to fast ice. The fast-ice minimum almost always occurs later than the overall sea-ice minimum, a likely consequence of the pack ice protecting the fast ice from swell-induced breakout.

The timing of fast-ice minimum extent is observed to occur progressively earlier in the Indian Ocean sector (on the order of 5 days/year) throughout the 8.8-year time series (see Figure 4.13). No obvious trend is observed in the timing of the overall sea-ice extent in the Indian Ocean sector. In general, the timing of maximum/minimum fast-ice extent displays higher variability than the corresponding timing of overall sea-ice maximum/minimum extent, reflecting both the lower fast-ice extent compared to overall sea ice, and the complex controls which limit fast-ice extent (e.g., grounded icebergs acting as anchor points).

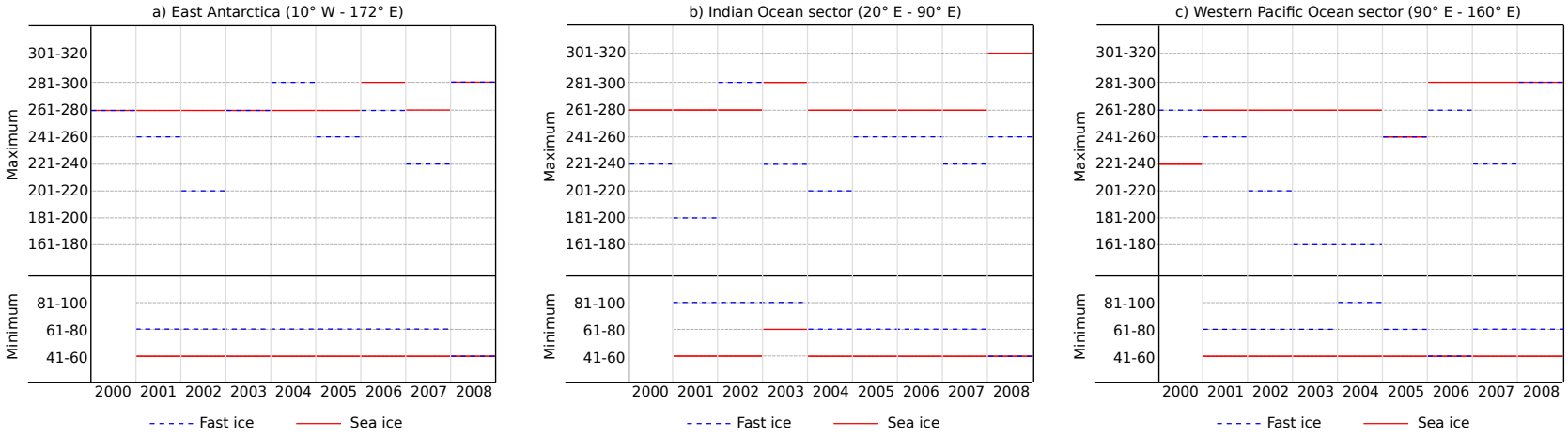

Figure 4.13: Diagram of the timing of fast-ice and overall sea-ice minimum and maximum extent, shown in DOY range format for the period March 2000 - December 2008.

4.3.6 Percentage of Fast Ice Comprising Overall Sea-Ice Extent/Area

The percentage of fast-ice area comprising overall sea-ice area throughout the 8.8-year time series for the East Antarctic coast is shown in Figure 4.14. The percentage of fast-ice extent comprising overall sea-ice extent is also shown in this figure. Minimum, maximum and mean values for each year are shown in Table 4.3. We assume here that fast-ice concentration is 100%; hence fast-ice extent is equivalent to fast-ice area. This is a reasonable assumption based on field observations.

A strong seasonal cycle is observed in the fraction of overall sea-ice area/extent which is fast ice. Following the maximum fast-ice percentage early in the season, i.e., around DOY 41-60, or late February, the fast-ice extent (area) percentage slowly decreases to a broad minimum, with a mean value of 3.77% (4.51%). A rapid increase in the fast-ice percentage is observed from around DOY 341-365 (mid-December), with maximum percentage occurring during DOY 41-60 in most years, excepting 2003 and 2005, when the maximum fast-ice extent percentage occurred during DOY 21-40. The value of the maximum (minimum) extent percentage varies between 16.0% and 21.0% (3.2% to 4.2%), with the maximum (minimum) area percentage showing similar variability.

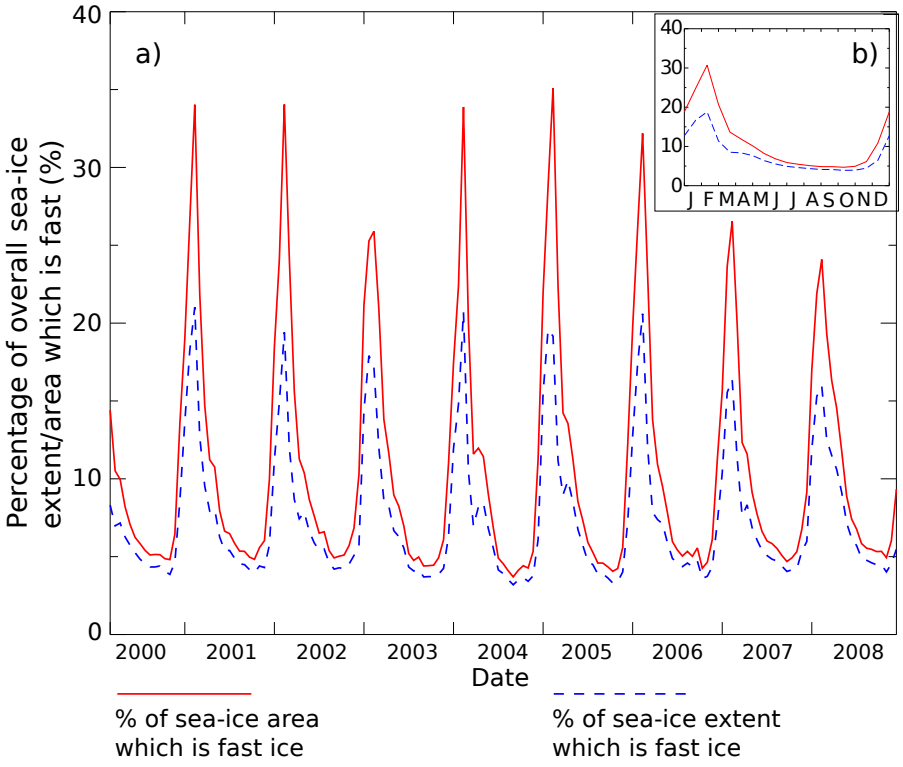

Figure 4.14: a) Percentage of overall sea ice which is fast ice, throughout the 8.8-year time series. b) Monthly climatology of a), generated from the 8.8-year time series. Minimum maximum and mean values for each year are given in Table 4.2. Maximum fast-ice percentage typically occurs at approximately the same time as the sea-ice minimum. Timing of minimum fast-ice percentage has larger variability, reflecting the large variability in timing of the fast-ice maximum.

Table 4.3: Table of maximum and minimum percentage of overall sea-ice extent/area which is fast ice (see Figure 4.14).

	East Antarctica (10° W - 172° E)			
	Maximum fast-ice percentage compared to:		**Minimum** fast-ice percentage compared to:	
	Overall sea-ice extent (%)	Overall sea-ice area (%)	Overall sea-ice extent (%)	Overall sea-ice area (%)
2000			3.9	4.8
2001	21.0	34.0	4.0	4.8
2002	19.4	34.1	4.2	4.9
2003	17.9	25.9	3.7	4.4
2004	20.7	33.9	3.2	3.7
2005	19.6	35.1	3.3	4.1
2006	20.6	32.2	3.6	4.3
2007	16.4	26.6	4.1	4.7
2008	16.0	24.1	4.0	4.9
Mean	19.0	30.7	3.8	4.5

4.4 Summary and Further Work

This work presents the first multi-year, high spatio-temporal resolution maps and time series of fast-ice extent along the entire East Antarctic coast (and indeed any large section of the Antarctic coast). For the first time, a gap-free multi-year climatology of Antarctic fast ice is presented. This product is directly comparable to the widely-used overall sea-ice extent products derived from passive microwave imagery (e.g., *Comiso*, 2010).

The major findings of this study can be summarized as follows:

1. A statistically-significant (at the 99% confidence level) increase in fast-ice extent occurred across the entire study region, from 2000 to 2008, of 4,012 ±830 km^2 yr^{-1}, equivalent to 1.43 ±0.3% yr^{-1} (albeit over a short time series);

2. Regionally and over the entire 8.8-year time series, a strong (and also significant) increase in fast-ice extent in the Indian Ocean sector of 4,444 ±457 km^2 yr^{-1} (4.07 ±0.42% yr^{-1}). At the same time, a (non-significant) decrease occurred in the Western Pacific Ocean sector of 579 ±525 km^2 yr^{-1} (0.40 ±0.37% yr^{-1}). In other words, the statistically-significant increase in overall fast-ice extent is due mainly to the contribution of the Indian Ocean sector;

3. In the Indian Ocean sector, a weak decrease in fast-ice extent with low variability is observed for the first four years (2000-2003), followed by a strong increase (with higher variability) for the remainder of the time series (2004-2008);

4. The observed relatively abrupt change in fast-ice extent trend in the Indian Ocean sector is due mainly to the presence of extraordinarily extensive fast-ice conditions along the Mawson and Enderby Land coasts, particularly from 2006 to 2008, both in summer and winter (and to a lesser extent during the

"shoulder" seasons of spring and autumn);

5. Generally, greater fast-ice extents and lower variability were observed in the Western Pacific Ocean sector, likely due to the different fast-ice formation regimes and existence of several north-south oriented coastal features here; and

6. A physical limit is effectively imposed on fast-ice growth (in most regions) by a lack of anchor points in the form of grounded icebergs in deeper water ($\geq$500 m depth). This results in an annual cycle which is characterised by a temporally-broad fast-ice maximum, and an abrupt, relatively short minimum.

Although significant trends were detected in the (relatively short) 8.8-year time series, these trends are not necessarily indicative of longer-term variability. The fast-ice trends broadly agree, however, with longer-term (1979 - 2008) overall sea-ice (including both pack ice and fast ice) observations (e.g., *Cavalieri and Parkinson*, 2008; *Comiso*, 2010). Fast-ice extent displays more variability than overall sea-ice extent/area on both medium (i.e., monthly) and long (seasonal to inter-annual) timescales, which is likely due to the often abrupt transitions between fast-ice breakout and growth. Fast-ice maxima are uncorrelated with sea-ice area and extent maxima, while fast-ice minima are correlated with overall sea-ice minima. This relationship is indicative of the protective effects of consolidated pack ice against ocean swell/wave-induced fast-ice breakout. The fast-ice minimum almost always occurs after the overall sea-ice minimum, which further suggests that the presence of pack ice protects the fast ice from swell-induced breakout (*Langhorne et al.*, 2001). Fast-ice minima (maxima) are found to be generally uncorrelated with subsequent maxima (minima).

Significant inter-annual variability is also observed in the timing of fast-ice

minima and maxima. The fast-ice timing analysis performed is likely of limited value (particularly the analysis of fast-ice maximum timing) due to the shape of the annual cycle: the broad peak in the maximum confounds the precise dating of maximum extent. The minimum extent of fast-ice is observed to occur progressively earlier in the Indian Ocean sector, despite there being no corresponding trend observed in the timing of the minimum in overall sea-ice extent. The shape of the annual cycle itself (in particular the broad maximum) reinforces the link between fast-ice presence and shallow bathymetry: 400-500 m is the maximum depth at which icebergs ground (*Massom et al.*, 2001b), and as such forms an upper limit to the fast-ice extent, which is attained relatively early in the winter. Further fast-ice growth past this natural barrier is achieved only in the most sheltered regions (e.g., Lützow-Holm Bay) or regions where pack ice is continually advected into other protruding coastal features.

Work is currently underway to relate fast-ice variability to atmospheric forcing parameters. Further work is planned to automate the production of, and extend this fast-ice time series further back in time, using AVHRR data where available, and around the entire Antarctic coast. We also plan to extend this dataset forward in time, using both MODIS and successive instruments such as the Ocean Land Colour Instrument (OLCI) on the European Space Agency's Sentinel-3 satellite. Sentinel-3 is due for launch in 2013, and further information can be obtained from http://www.eoportal.org/directory/pres_GMESSentinel3Mission.html. This work can also be extended to both polar regions.

Chapter 5

Atmospheric Influences on East Antarctic Landfast Sea-Ice Formation and Breakout

This chapter is being prepared for publication.

5.1 Abstract

This chapter presents a preliminary investigation into the links between patterns of East Antarctic fast-ice formation/breakout and atmospheric forcing on both local and hemisphere-wide scales. To investigate local-scale forcing, several case studies of anomalous fast-ice formation/breakup events are identified from regional ($\sim$10° of longitude wide) time series of fast-ice extent located near Syowa Station (34 - 42° E), Mawson Station/Cape Darnley (60 - 71° E), Dumont d'Urville Station (134 - 145° E) and the Mertz Glacier region (145 - 154° E). These anomalous cases are investigated by relating fast-ice extent to atmospheric parameters including surface air temperature and wind velocity, as well as regional pack-ice distribution and concentration. Anomalously strong winds, particularly from anomalous directions, are found to play an important role in both fast-ice formation and breakout. The relationship between wind direction and local coastal configuration is found to

be a particularly important factor. Strong surface air temperature anomalies are observed in conjunction with anomalous fast-ice growth/breakout events in some regions, with high (low) temperatures observed during times of anomalous fast-ice breakout (growth). The influence of the Southern Annular Mode (SAM) and El Niño-Southern Oscillation (ENSO) on East Antarctic fast-ice extent is assessed. A strong correlation ($R \simeq 0.45$) is found between the Southern Oscillation Index (SOI) and fast-ice extent in the Indian Ocean sector (20 - 90° E), with a time lag of 6 months (SOI leading fast-ice extent). This correlation in the Indian Ocean sector contributes strongly to a high correlation ($R = \simeq 0.4$) between SOI and fast-ice extent across the entire East Antarctic coast (10° W - 172° E). The mechanism of teleconnection is unclear, but similar correlations between SOI and overall sea-ice extent have been previously reported. No significant correlation is found between SAM index and fast-ice extent ($R < 0.2$ in all regions).

5.2 Introduction

Chapter 4 presented the first gap-free time series of fast-ice extent around the entire East Antarctic coast. This work provided, for the first time, a detailed, large-scale picture of fast-ice extent and variability with sufficient temporal resolution to resolve variability in East Antarctic fast ice over a range of spatial scales. The aims of this chapter are to analyse this new time series in conjunction with meteorological reanalysis data to investigate the response of fast-ice extent to large-scale modes of atmospheric variability, and to determine which regional-scale atmospheric parameters contribute to episodes of anomalous fast-ice extent. This work builds upon recent work by *Heil* (2006) and *Massom et al.* (2009), which have investigated the role of synoptic weather patterns in fast-ice formation and breakup near Davis Station and off the Adélie Land coast respectively.

5.2.1 Fast-Ice Response to Local Atmospheric Forcing: Work to Date

The formation and breakup of Antarctic fast ice is complex and poorly understood. It is driven by the interaction of a number of atmospheric and oceanic processes (including ocean waves), in addition to interactions with the ice sheet, icebergs, and the surrounding pack-ice cover (e.g., *Massom et al.*, 2009, 2010a; *Crocker and Wadhams*, 1988). Here, we initially examine factors which have been reported from both the Arctic and Antarctic (noting that fast-ice conditions are significantly different in the Arctic - see Chapter 1). Although ocean currents, temperature (*Heil et al.*, 1996) and waves (*Crocker and Wadhams*, 1988) play key roles in fast-ice formation and breakup, analysis of these parameters is beyond the scope of this thesis. Here, we focus on atmospheric parameters.

Working near Davis Station, East Antarctica, *Heil* (2006) found that several fast-ice parameters appear to be modulated by atmospheric temperature, including maximum annual ice thickness (anti-correlated with temperature), and timing of maximum ice thickness (higher air temperature leads to later maximum thickness). Temperature was also found to be closely associated with fast-ice formation and breakout in studies of fast ice formation modes in the Kara Sea, in the Arctic Ocean (*Divine et al.*, 2003, 2005). Here, a bimodality was observed in fast-ice maximum extent relating to the locations of different islands within the Kara Sea. Anomalously cold air temperatures (on the order of 6 °C below the monthly mean) led to an expansion of the fast-ice edge. Fast-ice area was significantly correlated (R $\simeq$0.55) with mean winter temperature (*Divine et al.*, 2003). *Mahoney et al.* (2007a) found that the breakup of fast ice off the coast of northern Alaska was correlated with the onset of thawing air temperatures. With the exception of a few notable studies (e.g., *Heil et al.* (1996); *Heil* (2006)), the role of sea/ocean temperature in

fast-ice formation and decay has not been widely studied in either polar region, but in addition to lateral and basal melt, warm sea temperatures are likely to contribute to grounded keel erosion in the Arctic, leading to fast-ice breakout (*Mahoney et al.*, 2007b). Ice keels play a key role in anchoring fast ice to the seabed in shallow Arctic coastal areas such as the north Alaskan coast.

Snow cover thickness has also been suggested as a factor controlling the stability and thus duration of fast ice. Working in Lützow-Holm Bay, East Antarctica, *Ushio* (2008) determined that a thin snow cover led to significant fast-ice melt, precluding formation of superimposed ice during the summertime melt season. Superimposed ice forms from snow meltwater that percolates down through the snow column and freezes on the sea-ice surface (*Haas et al.*, 2001). Superimposed ice acts to strengthen fast ice by both "hardening" its surface and increasing its thickness (*Ushio*, 2006). Fast-ice breakout events were frequently observed at this location when snow cover was relatively thin.

Using a 1-dimensional modeling study set in the Arctic, *Flato and Brown* (1996) investigated the role of snow cover and air temperature on fast ice. While increasing the air temperature led to lower maximum fast-ice thickness and longer open water duration, the effect of a changing snowfall rate was more complex: from 0 to $\sim$3 mm/day, an increasing snowfall rate led to a lower maximum ice thickness and longer open water duration. However, for snowfall rates greater than $\sim$3 mm/day, an increasing snowfall rate led to a higher fast-ice thickness, primarily by production of snow ice (ice which forms when the snow loading is heavy enough to flood the snow/ice interface, resulting in a frozen mixture of snow and sea water (*Haas et al.*, 2001)). While this model study included no dynamic component, it serves to illustrate the complex effects of snow cover on fast-ice growth and decay, and the probable importance of a projected increase in high-latitude snowfall under

a climate warming scenario (*Bracegirdle et al.*, 2008).

Using passive microwave satellite data, fast-ice melt was also investigated as a factor contributing to breakout by *Enomoto et al.* (2002). This study found that warmer than average air temperatures led to extensive fast-ice melt, often followed by large-scale fast-ice breakout within Lützow-Holm Bay.

The influence of waves and swell on fast ice has been studied both theoretically, e.g., *Langhorne et al.* (2001); *Chung and Fox* (2001) and experimentally in situ vis a vis observed fast-ice breakout events, e.g., *Higashi et al.* (1982). From the *Higashi et al.* (1982) study, it was concluded that an extreme fast-ice breakout event observed in Lützow-Holm Bay in 1980 was caused by ocean swell, probably generated by a nearby low pressure system. Waves with a long period may be responsible for fast-ice breakout in the Arctic via ungrounding of fast-ice keels (*Mahoney et al.*, 2007b). The possible impact of long-period swell on Antarctic fast-ice breakup is complicated by the presence of numerous icebergs acting as "anchors".

Most of the observational work on wave-induced fast-ice breakout has been conducted in McMurdo Sound, in the Ross Sea (*Crocker and Wadhams*, 1988, 1989; *Langhorne et al.*, 2001). *Langhorne et al.* (2001) used a theoretical fast ice model to determine the number of flexural cycles a fast-ice sheet can sustain before fracturing. *Crocker and Wadhams* (1988) related regional wind speed to waves detected within the fast ice using strain gauges. There appeared to be a critical wind speed of 10 m/s, below which waves are undetectable in the ice, and above which wave energy increases significantly. However, the maximum strain induced by such waves was still one order of magnitude below the theoretical fracture strain for the relatively thick fast ice in the study region (>1 m thick). *Crocker and Wadhams* (1989), also working in McMurdo Sound extended this work to attribute fast-ice breakout to wind-induced tensile failure throughout most of the year. For a short period during

summertime, the influence of ocean swell becomes more important than than wind-induced tensile failure. The authors also commented on the protective effects of a high concentration regional ice pack against wave-induced breakout.

In general, changes in spatio-temporal characteristics and distribution of fast ice are determined by the complex interaction of atmospheric and oceanic parameters, with some studies reporting a stronger role played by ocean current velocity (e.g., *Mahoney et al.*, 2007b), while others report a more important role played by winds, e.g., *Heil* (2006). *Heil et al.* (1996) attribute strong interannual variability in oceanic heat flux under fast ice off the Mawson coast to seasonal variations in both polynya activity, and ocean currents within the nearby Prydz Bay. *Nunes Vaz and Lennon* (1996) and *Heil* (2006) note that shallow sites of fast-ice formation are effectively decoupled from horizontal advection of water masses and the influence of warmer water past the continental shelf break and onto the shelf itself. However, Arctic fast ice typically forms in much shallower regions than Antarctic fast ice. Thus, the differences between the *Heil* (2006) and *Mahoney et al.* (2007b) studies may reflect the local study region, with the former located in the sheltered Davis Harbour, East Antarctica, and the latter along the more exposed Barrow coast, northern Alaska. Surrounding pack-ice distributions and conditions are also likely to be different, and hence their potential buffering effects will differ.

As noted in Chapter 1, the bathymetry of the continental shelf plays an important role in determining the spatial distribution of Antarctic fast-ice features by means of determining the location of grounded icebergs (*Massom et al.*, 2001b). Though it has not been extensively covered in the literature, the spatial scale of coastal features (promontories) is also expected to be an important parameter in determining the location of fast-ice features (R. Smith, personal communication, July 2010, *Mahoney et al.*, 2007a). This is beyond the scope of this thesis, but

investigation of this factor is planned.

Ocean current and wind velocities can have complex and directionally- dependent effects on fast ice. Offshore winds are known to be a major factor affecting fast-ice breakup (*Heil*, 2006; *Massom et al.*, 2009), by potentially producing a drag force on pressure ridges and causing fast ice to fracture. Ephemeral fast-ice breakout and re-formation events can occur throughout the fast-ice season in certain regions, e.g., north of Dumont d'Urville. In this location, this phenomenon occurs where there are gaps in the distribution of grounded icebergs over ocean troughs, and is related to changes in wind direction and strength (*Massom et al.*, 2009). The synoptic-scale passage of storm systems has also been associated with fast-ice breakout in several studies, e.g., *Heil et al.* (2006); *Divine et al.* (2005); *Higashi et al.* (1982). Model studies (*König Beatty and Holland*, 2010) have associated offshore winds with fast-ice breakout due to mechanical creep (i.e., thinning and stretching) induced within the fast ice, though these model studies largely neglected other factors potentially more likely to contribute to breakout (wind gusts, waves, etc.). Though no study has explicitly investigated the effects of katabatic wind on Antarctic fast-ice formation/breakout, it is likely that such winds have a similar effect to offshore winds associated with synoptic-scale systems.

In a detailed case study, *Massom et al.* (2009) examined the extreme breakout of fast ice north-west of Dumont d'Urville in 1998 using AVHRR satellite imagery. This breakout event was explained by unusually strong and persistent winds from the south-west, i.e., at an angle of almost 45° to the coastline, but in line with a bathymetric trough free from grounded icebergs. Similar wind anomalies with an even stronger southerly (i.e., offshore) wind component were observed during the winter and spring of 1963, when a "snapshot" of conditions shown in recently declassified spy satellite images revealed near-zero fast-ice extents along the Adélie

Land coast in August and October of that year. Further to the east, *Massom et al.* (2003) observed a major breakout of the multi-year fast-ice zone adjacent to iceberg B-9B in the spring-early summer of 1999-2000, due to an anomalous and sustained reversal of the large-scale wind field.

As noted earlier, onshore winds and currents generally contribute to fast-ice growth by advecting pack ice toward the coast or pre-existing fast ice (*Massom et al.*, 2001b, 2009). Moderate winds and currents parallel to the coast can advect pack ice onto pre-existing fast-ice features or coastal protrusions into the ocean, to dynamically form new fast ice (*Fraser et al.*, 2010b; *Massom et al.*, 2001b, 2009). Conversely, observations in the Alaskan Arctic show that strong currents or winds parallel to the coast advect large pack-ice floes or ungrounded icebergs at such high speed that a collision with fast ice may shear off pre-existing fast ice (e.g., the "freight train" event observed off northern Alaska using coastal radar by *Mahoney et al.*, 2007b). In fact, persistent but weaker offshore winds and currents in the Arctic appear to actually stabilise fast-ice features by precluding this shearing flow (A. Mahoney, personal communication, July 2010). Offshore airflow was correlated with larger fast-ice extents in the Kara Sea, off the northern coast of Russia (*Divine et al.*, 2005, 2003). Here, offshore airflow was associated with the control of synoptic-scale weather systems by the climatological Arctic High, blocking the passage of destructive cyclonic systems and the milder air temperatures associated with these systems.

This chapter presents an initial investigation into the effects of wind speed, direction and air temperature on fast-ice formation and breakout on a local scale. The results shown are preliminary only, at this stage. The following section presents a review of large-scale modes of atmospheric circulation in the Southern Hemisphere, with particular emphasis on effects on sea ice.

5.2.2 Large-Scale Climate Modes and Indices

Several large-scale modes of atmospheric variability have been identified at mid to high southern latitudes (see *Simmonds and King* (2004) and *Simmonds* (2003), and the references therein, for reviews). These modes control the spatial and temporal distribution of several climate parameters. Surface manifestations of these modes of variability, e.g., wind speed and direction, surface air temperature, are key drivers of sea-ice variability (*Massom et al.*, 2009; *Lefebvre and Goosse*, 2008; *Stammerjohn et al.*, 2008; *Yuan and Li*, 2008; *Raphael*, 2007; *Fogt and Bromwich*, 2006; *Yuan*, 2004; *Kwok and Comiso*, 2002). In this section, we carry out a preliminary assessment of the possible impacts of phases of these large-scale atmospheric modes on fast-ice distribution and its variability.

5.2.3 Dominant Modes of Atmospheric Variability at High Southern Latitudes

It is possible to identify large-scale modes of climate variability by conducting an Empirical Orthogonal Function (EOF) analysis on time series of geopotential height or Mean Sea Level Pressure (MSLP) (*Peixóto and Oort*, 1992). When performing such an analysis over the the mid- to high-latitude Southern Hemisphere, the first EOF shows a near zonally-symmetric pattern, with a broad pressure feature centred over the Antarctic continent, and pressures of opposite sign at mid latitudes (e.g., *Simmonds and King*, 2004). This EOF is known as the Southern Annular Mode (SAM), and is the dominant large-scale mode of variability in MSLP/geopotential height at southern polar latitudes (*Mo and Ghil*, 1987). SAM (also known as the Antarctic Oscillation or Southern Hemisphere Annular Mode) varies from weekly (*Baldwin*, 2001) to intra-decadal (*Kidson*, 1999) timescales. A positive index indicates lower pressures over the continent, resulting in a stronger

Polar Vortex, and stronger westerly winds around the coast of East Antarctica (*Stammerjohn et al.*, 2008). SAM has become increasingly positive in recent decades (*Marshall*, 2003), and a corresponding increase in westerly wind strength has been observed around the East Antarctic coast (*Turner et al.*, 2005).

The second EOF is known as the Pacific-South American (PSA) pattern, showing a "dipole"-like pattern between the Amundsen and Weddell seas. This is characterised by a pressure centre located near Drake Passage, bordered to the east and west by pressure centres of the opposite sign (*Mo and Ghil*, 1987). This region is known as the Antarctic Dipole (ADP). The variability of the PSA pattern is thought to be driven by the El Niño-Southern Oscillation (ENSO) via a teleconnection from the source of the Southern Oscillation, the tropical Pacific Ocean (*Mo and White*, 1985; *Karoly*, 1989; *Harangozo*, 2000; *Turner*, 2004). Its signal is transmitted poleward by both oceanic currents and atmospheric Rossby waves (*Platzman*, 1968; *Turner*, 2004). The propagation of Rossby waves to high southern latitudes can affect the trajectories of storm systems, thereby influencing the sea level pressure (*Hoskins and Karoly*, 1981). ENSO, and thus the PSA pattern, varies on timescales from 2 to 6 years (*Diaz and Pulwarty*, 1994). Because the pressure centres of the PSA pattern are concentrated over the ADP region, this pattern is thought to have little influence along the East Antarctic coast (*Simmonds and King*, 2004). Oceanic propagation of ENSO signals around Antarctica has been linked to the Antarctic Circumpolar Wave (ACW), a wave 2 pattern with a period of ~ 8 years, propagating eastward with the Antarctic Circumpolar Current (*White and Peterson*, 1996; *Jacobs and Mitchell*, 1996; *White et al.*, 1998). Signals of ENSO are detected in Antarctic meteorological, ice core and sea-ice records (*Turner*, 2004).

The third EOF of high-latitude Southern Hemisphere MSLP shows three quasi-stationary pressure centres located near the three major mid-latitude land

masses of Australia, South America and Africa (*Raphael*, 2004, 2007). This is known as the Zonal Wave 3 (ZW3) pattern. A ZW3 index was developed by *Raphael* (2004), and used to investigate the influence of the ZW3 pattern on sea-ice variability (*Raphael*, 2007). A strong positive correlation was observed between the ZW3 index and sea-ice concentration anomaly between 60 and 90° E (*Raphael*, 2007).

In addition, there are several modes of large-scale climate variability which vary both spatially and temporally and cannot be captured by EOF analyses. As such, Extended Empirical Orthogonal Function (EEOF) analysis is required for detection (*Peixóto and Oort*, 1992). These modes include:

- The Semi-Annual Oscillation (SAO), a twice-annual cycle in SLP and air temperature which is a consequence of complex interactions between ocean, atmosphere and incoming shortwave radiation (*van Loon*, 1967; *Simmonds and Jones*, 1998); and
- the Antarctic Circumpolar Wave (*White and Peterson*, 1996; *White et al.*, 1998; *Haarsma et al.*, 2000).

The SAO, ACW and ZW3 indices are not considered in this work for the following reasons. The variability in the SAO is largely represented in the ERA Interim climatology used here (as detailed in Section 5.3). In addition, the ZW3 index is currently only available up to 2005 (M. Raphael, personal communication, June 2010). Moreover, the magnitude of the ACW becomes greatly attenuated in the Indian Ocean and Western Pacific Ocean sectors (*Yuan and Li*, 2008), and its existence and persistence, and mechanism of generation, have been the subject of recent debate in the literature (*Aiken et al.*, 2006; *Mélice et al.*, 2005; *Venegas*, 2003; *Haarsma et al.*, 2000; *White et al.*, 1998).

5.2.4 Impacts of Large-Scale Atmospheric Variability on Antarctic Pack Ice

Large-scale modes of atmospheric variability affect sea-ice extent, concentration and seasonality indirectly via changes in surface climate parameters, e.g., surface air and sea surface temperature, and wind fields influenced by changes in the spatial distribution of MSLP. Some of the more recent publications investigating the effects of these modes of variability on sea ice include *Stammerjohn et al.* (2008); *Yuan and Li* (2008); *Raphael* (2007); *Fogt and Bromwich* (2006); *Turner* (2004); *Lefebvre and Goosse* (2008); *Liu et al.* (2004a); *Yuan* (2004); *Kwok and Comiso* (2002). The findings of these publications will be briefly summarised below, with particular emphasis on links in East Antarctica where possible.

Stammerjohn et al. (2008) and *Fogt and Bromwich* (2006) noted a shift in the interactions between ENSO and SAM in the ADP region between the 1980s and 1990s. Destructive interference between the patterns (i.e., opposite effects of SAM and ENSO on MSLP) in the ADP region, leading to a weaker ENSO teleconnection during the 1980s, changed to constructive interference and a strong teleconnection during the 1990s. The strongest teleconnections were observed in the ADP region when negative SAM indices were coincident with negative SOI (El Niño) conditions, or positive SAM with positive SOI (La Niña). This is in contrast to earlier work, which suggested that SAM and SOI indices of the same sign produced qualitatively opposite effects on sea-ice concentration (*Liu et al.*, 2004a). Interactions between the SAM and PSA patterns are thus particularly strong in the ADP region (*Kwok and Comiso*, 2002; *Liu et al.*, 2004a; *Yuan*, 2004; *Yuan and Li*, 2008; *Stammerjohn et al.*, 2008; *Fogt and Bromwich*, 2006), and correspondingly weaker/more variable along the East Antarctic coast (*Stammerjohn et al.*, 2008).

Liu et al. (2004a) analysed recent sea-ice variability in West Antarctica in the context of SAM and SOI indices. It was concluded that although SAM and ENSO influence the changes in sea-ice concentration observed in the Ross, Bellingshausen and Amundsen seas, the SOI and SAM indices alone could not explain the regional sea-ice trends observed. The authors recommend further work examining the influence of other high-latitude atmospheric modes on sea ice (i.e., SAO and PSA).

Despite the complex teleconnections between the tropical Pacific Ocean and the ADP region (*van Loon and Jenne*, 1972), and significant attenuation of the ENSO by the time it propagates to the East Antarctic coast (*Turner*, 2004), correlations have been found between overall sea-ice edge location and SOI (*Simmonds and Jacka*, 1995), particularly in the Indian Ocean sector (35 - 65° E). *Simmonds and Jacka* (1995) observed a positive correlation between SOI and fast-ice edge location, with a maximum correlation at ∼6 to 10 months (SOI leading sea ice). *Simmonds and Jacka* (1995) observed other, weaker correlations in different sectors around the Antarctic coast, but SOI was generally observed to lead anomalies in the sea-ice edge location (except for "Australian longitudes", i.e., the Western Pacific Ocean sector). Correlations were strongest during April - October, which the authors attributed to a seasonally-variable teleconnection strength, though this may also be a reflection of the lower relative variability of the overall pack-ice edge location during the wintertime maximum. *Hall and Visbeck* (2002) conducted an investigation into the influence of SAM on June-to-November modeled Antarctic sea-ice thickness distribution. The highest correlations were found in the Indian Ocean sector, but in the marginal ice zone (MIZ). Correlations between SAM index and sea-ice thickness near the coast were close to zero. *Hall and Visbeck* (2002) concluded that sea-ice thickness is more strongly controlled by thermodynamic pro-

cesses than wind velocity anomalies associated with SAM. On the other hand, sea-ice extent and the location of the ice edge appears to be modulated by the SAM index, with a positive SAM leading to divergent sea-ice conditions, and a northward expansion of the ice edge (*Hall and Visbeck*, 2002). In contrast, *Massom et al.* (2006a) observed extreme dynamic thickening of pack ice in the West Antarctic Peninsula region due to wind-driven ice convergence against the Peninsula in the spring of 2001. This was related to a positive SAM index, and a strong ZW3 pattern.

Kwok and Comiso (2002) also found that the links between ENSO and coastal parameters were stronger in the Indian Ocean sector than the Western Pacific Ocean sector. In particular, a negative correlation between Sea Surface Temperature (SST) anomaly and SOI was observed in the Indian Ocean sector, significant at the 95% confidence level, giving a difference of $\sim$1.0 °C between a strong La Niña (SOI $>$ 0) and a strong El Niño (SOI $<$ -1). Correlations between SOI and surface air temperature, and SOI and sea level pressure, were close to zero across the East Antarctic coast.

Raphael (2007) investigated the effects of the ZW3 pattern on sea-ice variability. During times of a positive ZW3 index, three positive geopotential height (GPH) anomalies are found at approximately 70° W, 50° E and 160° E, with three GPH minima between. These GPH anomalies lead to anomalous northward airflow at approximately 170° W, 40° W and 80° E, and southward airflow at approximately 100° W, 20° E and 130° E. Regions of anomalous northward (southward) airflow had higher (lower) sea-ice concentrations during time of positive ZW3 index, which was attributed to modified temperature differences between the ocean and atmosphere rather than a response to modified surface winds.

Yuan and Li (2008) investigated the links between several climate modes (PSA, ZW3, SAM and SAO) and sea-ice concentration, from 1978 - 2002. The

ENSO signal itself was not one of the four indices correlated with sea-ice extent. Instead, the PSA pattern, a manifestation of the ENSO signal as SLP anomalies, was used. All four large-scale climate modes were found to be correlated with sea-ice concentration anomalies, particularly along the West Antarctic Peninsula and in the Weddell Sea, using a lag of two months (with sea-ice concentration anomalies lagging each climate index). However, correlations along the East Antarctic coast were close to zero for all four modes, especially adjacent to the coast where fast ice forms. The effect of these four modes on sea-ice extent was also examined by *Lefebvre and Goosse* (2008). In the *Lefebvre and Goosse* (2008) study, only the summertime SAO index was significantly correlated with hemisphically-integrated sea-ice extent, despite being poorly correlated regionally. The authors concluded that the pattern of atmospheric variability which best described sea-ice extent in the Southern Ocean was a combination of uncorrelated regional patterns (i.e., none of the continent-wide, large-scale modes), and that the response of sea-ice extent to large-scale atmospheric forcing should be studied regionally.

5.2.5 Impacts of Large-Scale Atmospheric Variability on Fast Ice

Despite the recent work on the complex response of the overall Antarctic sea-ice cover to change and variability in large-scale atmospheric forcing, relatively little is known about the response of fast ice to such forcing. This has in large part been due to the lack of a suitable large-scale time series of fast-ice extent for the purpose (this is also the case for the Arctic). The generation of the new MODIS-derived fast-ice time series gives the opportunity to carry out an analysis of the large-scale response of East Antarctic fast ice to atmospheric variability (and change) for the first time.

As well as covering the fast-ice response to local atmospheric forcing, *Heil*

(2006) described the localised multi-decadal response of fast-ice thickness and seasonality near Davis Station, East Antarctica, under what appeared to be a climate modulated by an increasing SAM index (negative MSLP trend, positive wind speed trend, winter/springtime warming, summer/autumn cooling). Positive trends in precipitation were also observed (except during summer), along with an increase in storm activity (over the period 1969-2003). Significant (at the 90% confidence level or higher) negative correlations were found between fast-ice thickness and air temperature, snowfall, cyclonicity (using a storm index related to the power spectrum of MSLP variability), and wind speed. Air temperature was also correlated with date of maximum fast-ice thickness, and cyclonicity with breakout date.

Working in Arctic Alaska, *Mahoney et al.* (2007a), analysed Radarsat SAR-derived fast-ice extent from 1996 to 2004 in conjunction with Characteristic Patterns (CPs) of Sea Level Pressure (SLP) in the region. Though different in concept to an EOF on time series of SLP, the CPs represent broad-scale synoptic features from which wind vectors can be inferred. No correlation was found between CP occurrence and fast-ice events (date of first ice, stable ice, break-up, ice-free). Similar work has been done in the Kara Sea in the Russian Arctic (*Divine et al.*, 2003, 2005), where an observed bimodality in fast-ice distribution was related to monthly MSLP. MSLP anomalies were also analysed during times of breakout and formation. Fast-ice expansion phases were associated with the presence of the climatological Arctic High to the north, producing a strong meridional pressure gradient and blocking the passage of storm systems. Conversely, the presence of a trough was associated with fast-ice breakout events. It was concluded that storminess plays a role in fast-ice breakup in this region (*Divine et al.*, 2003, 2005).

Massom et al. (2009) conducted the most comprehensive study to date on the influence of SAM and SOI on Antarctic fast-ice extent, albeit confined to a

sector of the Adélie Land coast. Working on a region of largely annual fast ice to the north/northwest of Dumont d'Urville Station, they related Emperor penguin (*Aptenodytes forsteri*) breeding success to AVHRR-derived fast-ice extent and nearest distance from the colony to open water. In this region and for the limited period from 1992 to 1999, SAM index was strongly correlated with nearest distance to open water (R^2=0.75), and fast-ice areal extent (R^2=0.58). Corresponding correlations with SOI instead of SAM yielded values of 0.31 and 0.17 respectively. These results indicate that wind anomalies associated with SAM play a key role in modulating fast-ice variability on a regional scale.

Section 5.3 will next outline the datasets and methods used in this chapter to investigate links between fast ice and atmospheric parameters. Section 5.4 follows with several correlation analyses to investigate the response of fast-ice extent to SOI and SAM indices. Section 5.5 then presents several case studies in sub-regions around the East Antarctic coast, to investigate which local-scale atmospheric parameters are important influences on fast-ice extent.

5.3 Datasets and Methods

The fast-ice extent time series was generated from cloud-free composite MODIS imagery (*Fraser et al.*, 2009, Chapter 2 of this thesis), augmented with AMSR-E data when required (*Fraser et al.*, 2010a, Chapter 3). The 8.8-year time series is presented in Chapter 4 (*Fraser et al.,* subm.), and is comprised of 159 consecutive 20-day resolution fast-ice maps.

For the purposes of this chapter, the East Antarctica-wide dataset was spatially subsetted into four sub-regions, each around 10° of longitude wide, as shown in Figure 5.1. Two are from the Indian Ocean sector, while the other two are from the

Western Pacific Ocean sector. These sub-regions, and the justification for choosing each sub-region, are as follows:

- a) The Syowa Station region, including extensive annual and multi-year fast ice in and around Lützow-Holm Bay (34 - 42° E). This is a site of intensive satellite- and surface-based observational work on fast-ice extent and characteristics by Japanese researchers, e.g., *Ushio* (2006, 2008); *Uto et al.* (2006); *Enomoto et al.* (2002);

- b) The Mawson Station/Cape Darnley region, covering the largely annual fast-ice feature off the Mawson coast (60 - 71° E). This sub-region includes several Emperor penguin rookeries (*Fretwell and Trathan*, 2009), e.g., the Taylor rookery, ∼61° E, and the Auster rookery, ∼64° E. The breeding success of Emperor penguins is closely linked with fast-ice extent and seasonality (*Massom et al.*, 2009). This is also the site of an important new Japanese-led field programme which aims to investigate and quantify the formation of Antarctic Bottom Water (AABW) from the Cape Darnley Polynya (*Ohshima et al.*, 2009; *Fukamachi et al.*, 2010; *Tamura et al.*, 2008). Fast ice plays a key role in polynya dynamics here. Due to the lack of north-south aligned in coastal protrusions, this region can be considered representative of fast-ice sub-regions *i, iii, v* and *x* (see Section 4.3.1);

- c) The Dumont d'Urville Station region, covering the largely annual fast-ice feature extending from the Dibble Iceberg Tongue to Commonwealth Bay (134 - 145° E). This work will build upon similar work in the region by *Massom et al.* (2009), which related atmospheric parameters to fast-ice extent (and Emperor penguin breeding success). The fast ice in this region is also inhabited by Weddell seals (*Andrews-Goff et al.*, 2010). Due to the line of grounded

icebergs to the west of this region, it can be considered representative of much of fast-ice sub-section *ix* (see Section 4.3.1); and

- d) The Mertz Glacier/B-9B region (145 - 154° E), including the annual and multi year fast-ice features to the east of the Mertz Glacier Tongue. This region is the focus of a new study analysing the possible role of fast ice in stabilising floating ice tongues (*Massom et al.*, 2010a). Fast ice also plays a crucial role in, and interplays with, the globally-important Mertz Glacier Polynya (*Barber and Massom*, 2007; *Massom et al.*, 2001b). It has also changed dramatically with the recent calving (in February 2010) of the glacier tongue (*Young et al.*, 2010).

Additionally, the correlation between SAM/SOI and fast-ice extent in the Indian Ocean (20 - 90° E) and Western Pacific Ocean sectors (90 - 160° E) is investigated. These regions are shown in Figure 5.1.

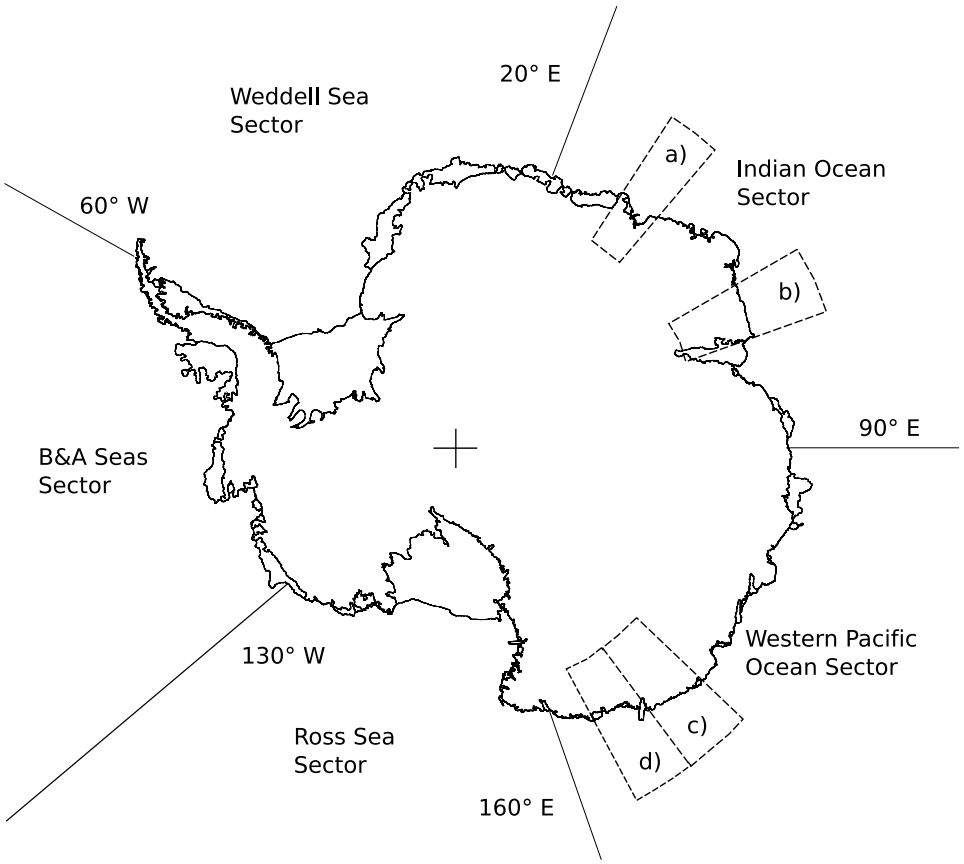

Figure 5.1: Map showing the sub-regions used in this chapter (a to d). a): The Syowa sub-region (34 - 42° E). b): The Mawson/Cape Darnley sub-region (60 - 71° E). c): The Dumont d'Urville sub-region (134 - 145° E). d): The Mertz/B-9B sub-region (145 - 154° E).

European Centre for Medium-range Weather Forecasts (ECMWF) ERA Interim Reanalysis data (*Berrisford et al.*, 2009) are used to provide surface-level meteorological data on local scales. The ERA data, obtained from http://data-portal.ecmwf.int/data/d/interim_daily/, are provided at a 1.5° × 1.5° resolution, and apparently provide more realistic data than the equivalent NCEP/NCAR (Na-

tional Centers for Environmental Prediction/National Center for Atmospheric Research) reanalysis data around the East Antarctic coast (*Bromwich et al.*, 2007; *Fogt and Bromwich*, 2006). The following ERA fields are used in the analysis:

- Temperature at 2 m (T2M);
- 10 m zonal and meridional winds (U10M and V10M); and
- Mean Sea Level Pressure (MSLP).

These reanalysis fields (T2M, U10M, V10M and MSLP) were formed into 20-day means, to enable direct comparison (analysis) with the MODIS fast-ice maps. Longer-term (1989-2008) climatology fields (means) for T2M, MSLP, U10M and V10M were also produced from the ERA data, in order to study anomalies in these fields.

Specifically, investigation of the response of fast-ice extent to wind conditions was conducted using detailed times series of wind difference plots (20-day wind conditions minus 1989-2008 climatology). These plots were created for each 20-day interval in each case study (see Section 5.5). The wind difference plots are essentially an alternative way of displaying a wind rose (a graphical representation of wind strength and direction over a period of time), with the advantage of being able to subtract the climatology to assess anomalies in strength, frequency and direction together. Such a subtraction is difficult to present/interpret using wind rose plots alone.

These plots are constructed by binning 20 days' wind reanalyses (20 days $\times$ 4 observations per day = 80 wind observations per wind difference plot) into 8 direction bins (cardinal plus ordinal points of the compass) along the x-axis and seven strength bins along the y-axis. Wind strength bins were chosen to be 0-2, 2-5, 5-10, 10-15, 15-20, 20-25, and >25 (all in units of m/s), to sufficiently resolve the ex-

pected range in 6-hourly mean wind strength around the East Antarctic coast. The same process was conducted using long-term mean climatology data, and a subtraction (observed minus climatology) was performed to generate the wind difference, essentially a plot of the wind anomaly in each direction/strength bin. Frequency of wind anomaly from each direction at each strength bin is represented by contours, with blue (red) contours showing winds stronger (weaker) than the climatology. In addition to detailed wind difference plots, a time series of T2M was created for each case study. To assess possible relationships between regional pack-ice distribution and fast-ice extent, 20 day AMSR-E passive microwave sea-ice concentration and MODIS visible/thermal infrared composite images were created, and will be presented where applicable.

A long-term wind plot representing the prevailing wind conditions is created for each case study by combining all wind observations from 1989 - 2008 into a single wind plot. This was found to be useful in assisting interpretation of the wind difference plots.

For computational simplicity, contemporary SAM index values are typically generated using a simple difference formula, rather than performing an EOF analysis. Such a formula usually takes the form

$$SAM = P_{40^\circ S} - P_{65^\circ S} \tag{5.1}$$

where SAM is the SAM index, and $P_{40^\circ S}$ ($P_{65^\circ S}$) is the zonal MSLP at 40° S (65° S). This chapter uses this differential form of SAM index, which was obtained from the British Antarctic Survey (*Marshall*, 2003). Values for the SOI were obtained from the Australian Bureau of Meteorology, which uses the Troup SOI (*Troup*, 1965). The formula for the monthly Troup SOI is as follows:

$$SOI = 10\frac{\Delta P - \Delta P_{av}}{\sigma_{av}} \tag{5.2}$$

where SOI is the SOI, ΔP is the Tahiti MSLP minus the Darwin MSLP for the month in question, ΔP_{av} is the long-term mean pressure difference between Tahiti and Darwin for the month in question, and σ_{av} is the long-term mean standard deviation of ΔP for the month in question. With the conventional multiplication by a factor of 10, Troup SOI values typically range from -35 to +35. SAM and SOI indices for March 2000 - December 2008 are shown in Figure 5.2.

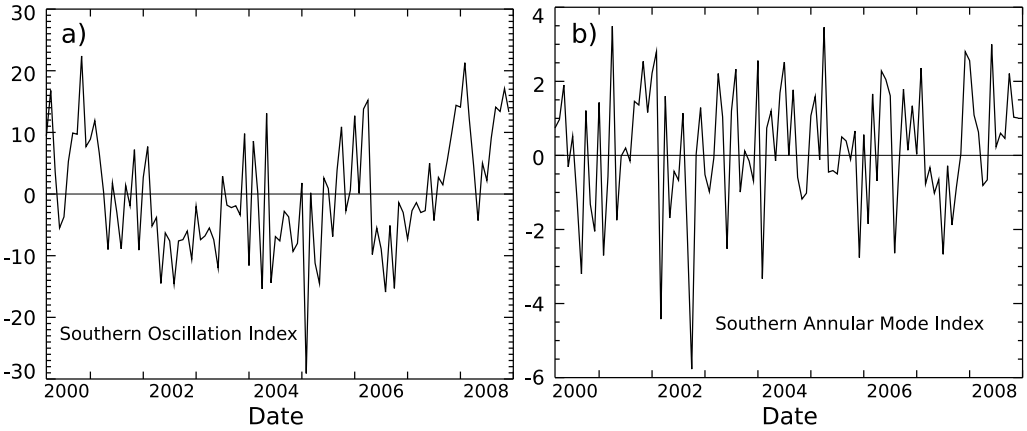

Figure 5.2: a) Time series of monthly mean SOI and b) SAM index values from March 2000 to December 2008.

5.4 Correlation of Fast-Ice Extent by Sector with SOI and SAM Indices

A correlation analysis was carried out to investigate possible links between fast-ice extent (across the entire East Antarctic coast and the Indian Ocean and Western Pacific Ocean sectors) and the SOI and SAM indices (see Figure 5.3). Correlations with SAM index values (Figure 5.3, panels b, d and f) generally displayed low correlation coefficients ($R < \pm 0.2$), and high variability as a function of lag. In this preliminary correlation analysis, it appears that the SAM index is uncorrelated with regional fast-ice extent. However, a more in-depth analysis including separate correlation analyses by season or month, may yield higher correlation coefficients.

This is beyond the scope of this thesis, but is planned. The low observed correlation is surprising given the high correlation between SAM and fast-ice extent observed by *Massom et al.* (2009), albeit over a much smaller region.

Again in contrast to *Massom et al.* (2009), there appears to be a high correlation between the SOI and fast-ice extent (see Figure 5.3, panels a, c and e), both in the Indian Ocean sector (maximum R$\simeq$0.45 at a lag of 6 months, SOI leading fast-ice extent) and the East Antarctic coast (maximum R$\simeq$0.4 also at a lag of 6 months, SOI leading fast-ice extent). The mechanism of teleconnection is unknown, but high correlation at a lag of 6 months implies an atmospheric, rather than oceanic, propagation. This is because propagation eastward from the ADP region to the Indian Ocean sector, at the speed of the ACW (*White and Peterson*, 1996), would take approximately 3 years. Compared to correlations against SAM, SOI correlations display much lower variability as a function of lag.

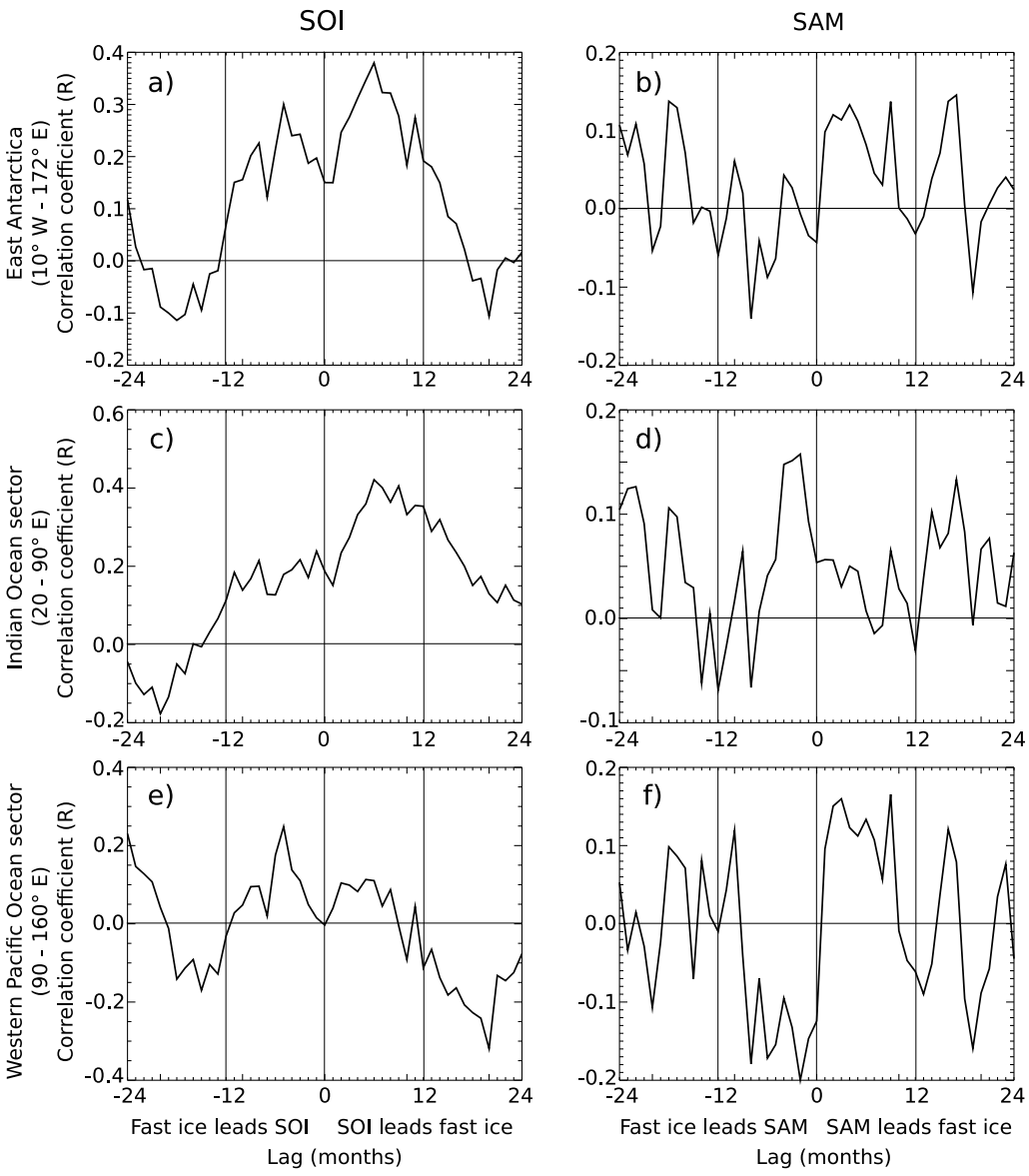

Figure 5.3: Correlation of SOI and SAM indices with fast-ice extent as a function of lag. a) and b): Correlation of SOI and SAM, respectively, with fast-ice extent across East Antarctic coast (10° W - 172° E). c) and d): Correlation of SOI and SAM, respectively, with fast-ice extent across in Indian Ocean sector (20 - 90° E). e) and f): Correlation of SOI and SAM, respectively, with fast-ice extent across the Western Pacific Ocean sector (90 - 160° E).

5.5 The Influence of Atmospheric Conditions on Regional Fast-Ice Variability

The aim of this section is to examine possible relationships between fast-ice changes/ anomalies and regional-scale change/variability in key environmental parameters, e.g., wind direction and strength, surface air temperature, and nearby pack-ice conditions. This is done by carrying out nine case studies which focus on four sub-regions (each $\sim 10^{\circ}$ of longitude wide) around the East Antarctic coast. These are shown in Figure 5.1.

In this preliminary analysis, maps of MSLP were not considered because of the loss of information associated with averaging MSLP over several 20-day intervals. Future extensions of this work will use a "storm index", similar to that used by *Heil* (2006), to provide information on storminess. Oceanographic data, e.g., ocean currents and wave parameters are also not included at this stage.

The fast-ice extent time series, spatially subsetted to these four sub-regions, is shown in Figure 5.4. From these time series, nine temporal case studies were chosen. Three were chosen as "control" case studies (Case Studies 1, 4 and 7), i.e., where the fast-ice extent is similar to the 8.8-year mean annual cycle. The remaining six case studies were chosen by finding large departures from the mean annual cycle in each sub-region, with the aim of determining the cause of such fast-ice extent anomalies. These case studies are marked on Figure 5.4, while table 5.1 details the location, time interval, and the rationale for these case studies. In general, inter-annual variability in each sub-region is much larger than that for the East Antarctic coast as a whole (see Chapter 4). This is a consequence of averaging over a much smaller area.

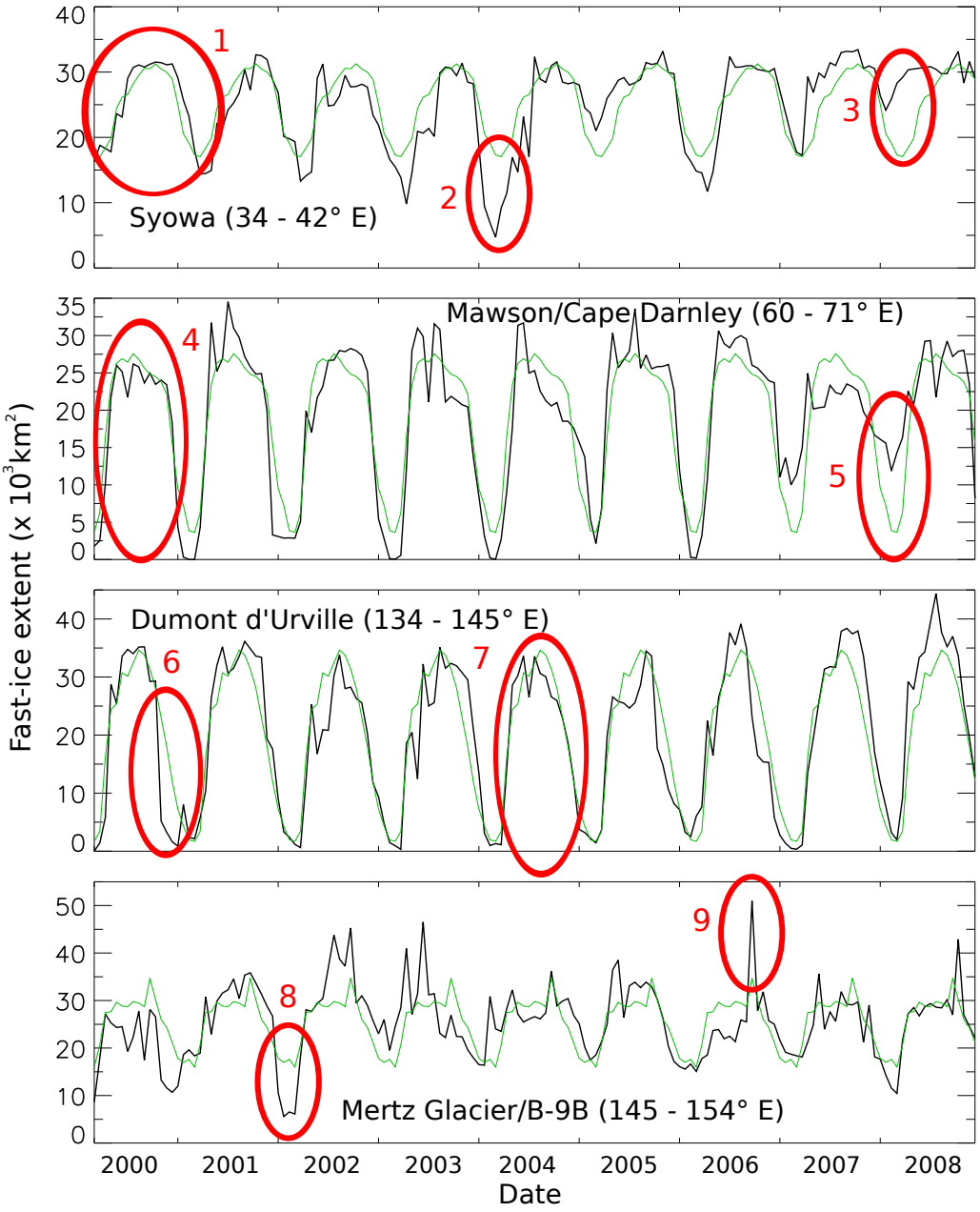

Figure 5.4: Time series of fast-ice extent in each sub-region (see Figure 5.1). The nine case study periods analysed are shown using red circles.

Table 5.1: Details of the nine case studies used to investigate atmospheric influences on fast-ice growth/breakout events (see Figure 5.4). To enable inter-comparisons between years, the final data point in each year spans 25 days (26 in a leap-year).

Case	**Sub-region**	**Date range**	**Rationale**
1	Syowa	2000, 61-80 to 341-366	A "control" case study, where fast-ice extents are similar to the 8.8 year climatology
2	Syowa	2003, 341-365 to 2004, 141-160	Anomalously low summertime extent in Lützow-Holm Bay
3	Syowa	2007, 341-365 to 2008, 141-160	Anomalously extensive summertime fast-ice conditions in Lützow-Holm Bay
4	Mawson/ Cape Darnley	2000, 121-140 to 341-366	A "control" case study, where fast-ice extents are similar to the 8.8 year climatology
5	Mawson/ Cape Darnley	2007, 341-365 to 2008, 101-120	Anomalously extensive summertime fast-ice conditions along Mawson Coast
6	Dumont d'Urville	2000, 261-280 to 2001, 41-60	Early and near-complete fast-ice breakout
7	Dumont d'Urville	2004, 101-120 to 341-366	A "control" case study, where fast-ice extents are similar to the 8.8 year climatology
8	Mertz Glacier/ B-9B	2001, 321-340 to 2002, 121-140	Anomalously low summertime fast-ice extent
9	Mertz Glacier/ B-9B	2006, 221-240 to 301-320	Anomalously high wintertime fast-ice extent

5.5.1 Case Study 1: Near-Average Fast-Ice Conditions, Syowa Station Sub-Region, 2000

Case Study 1 is a "control" case, chosen to investigate atmospheric conditions during a period when fast-ice extent is similar to the 8.8 year climatology (see Figure 5.5a). Aside from a strong negative temperature anomaly in the first two 20-day intervals (of ∼-4 °C), temperature anomalies were within ∼2 °C of the climatology (Figure 5.5b). Figure 5.5c shows a plot of the prevailing wind conditions. Analysis of wind difference plots reveals that wind anomalies were generally small (Figure 5.5d-r). In these wind difference plots, blue (red) contours indicate that the

observed wind over that 20-day interval was stronger (weaker) than the climatology in that direction/strength bin. In contrast to the other case studies, there were no strong positive (i.e., blue contour) wind anomalies greater than 10 m/s throughout the entire case study. Differences between observed wind strength/direction and the climatology are either small in magnitude (e.g., Figure 5.5f and p), from the same direction but differing slightly in strength (e.g., Figure 5.5l), or from a different direction (not greater than 90°) but at a similar strength (e.g., Figure 5.5d and e). Overall sea-ice concentration conditions in the Indian Ocean sector (20-90° E) during 2000 were close to average (see Figure 4.11 in Chapter 4 of this thesis, *Comiso* (2010), and *Cavalieri and Parkinson* (2008)).

Despite the relatively quiescent conditions (calm winds) and cold temperatures in the first two 20-day intervals, no significant fast-ice growth was observed. This may be related to the geometry of Lützow-Holm Bay. Once maximum extent is attained, i.e., the bay is filled with fast ice, no further growth can occur without strong wind from the north, advecting pack ice against the fast ice to lead to the growth of dynamically-formed fast ice.

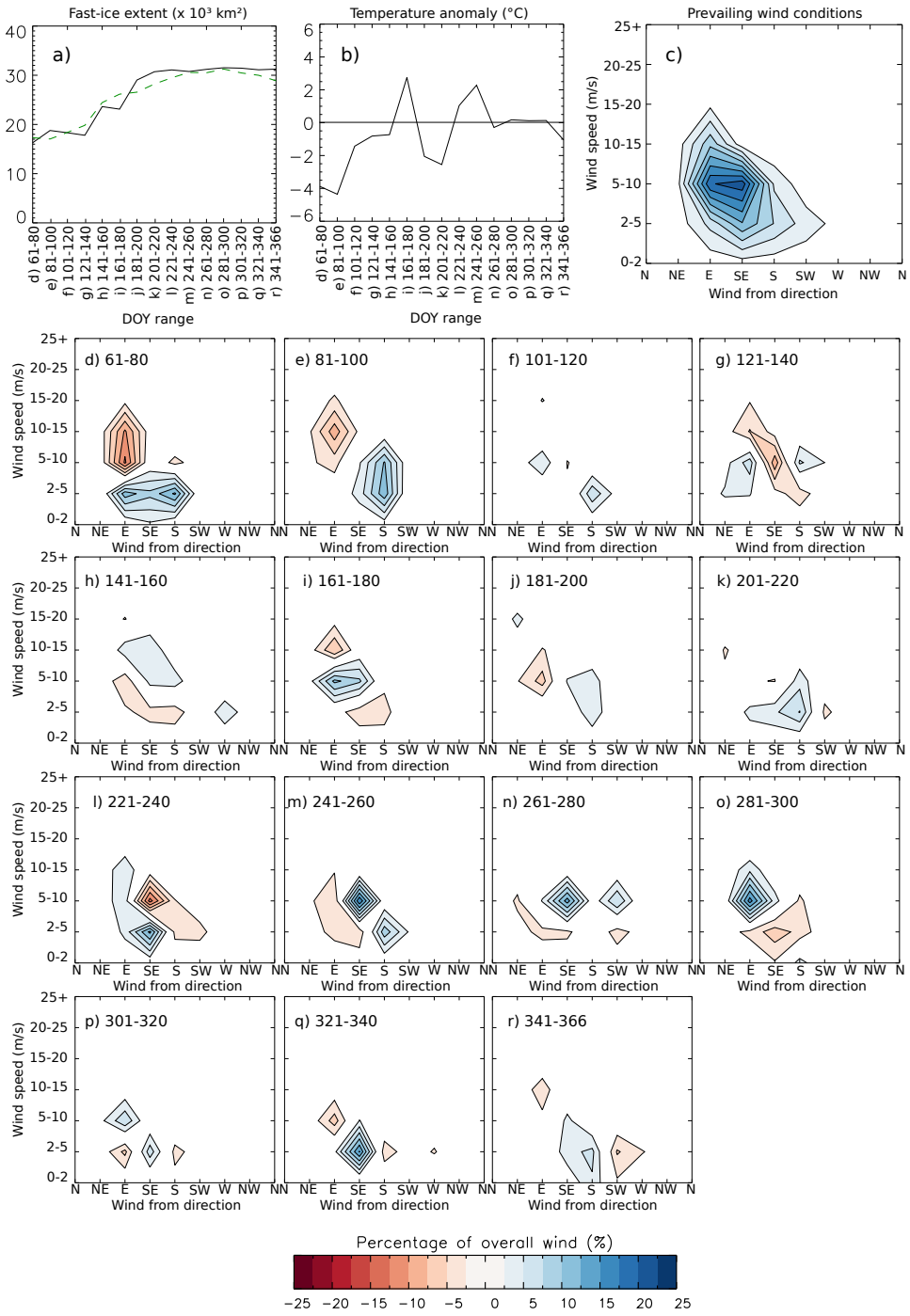

Figure 5.5: Case Study 1, illustrating near-average fast-ice conditions, Syowa Station sub-region, 2000. a): Fast-ice extent (black line) for the Case Study, and the associated 8.8-year climatological fast-ice extent (green line). b): Temperature anomaly time series. c): Wind plot of the prevailing wind conditions, averaged over all seasons, from 1989 to 2008. The x-axis on panels a) to c) is labelled d) to r) for cross-referencing with the wind difference plots (panels d to r). d) to r): Sequential 20-day wind difference plots for DOY intervals 2000, 61-80 to 2000, 341-366 respectively.

5.5.2 Case Study 2: Low Minimum Fast-Ice Extent, Syowa Station Sub-Region, 2004

Case Study 2, also in the Syowa sub-region, investigates a particularly low summertime fast-ice extent in late 2003/early 2004 (minimum of ∼4,500 km^2 at DOY 61-80, compared with the 8.8 year mean extent of ∼17,500 km^2 for that DOY interval, see Figure 5.6a). Temperature anomalies were in general consistently positive throughout the case study period (Figure 5.6b). Analysis of the wind difference plots (Figure 5.6d-l) reveals some more significant anomalies than the control case. In particular, anomalously strong easterly winds changed to anomalous westerlies from DOY 1-20 to 21-40. This is observed in conjunction with the MSLP anomaly time series changing sign (not shown), possibly indicating the passing of a synoptic-scale (storm) system. This hypothesis is strengthed by observations of alternating wind anomalies throughout the early part of the case study. Wind strengths were similar to the climatology throughout the case study interval, with the exception of DOY 341-365 in 2003 (Figure 5.6d) and DOY 101-120 in 2004 (Figure 5.6j) where winds were calmer than the climatology, and DOY 1-20 (Figure 5.6e) where strong easterlies were more frequent.

Of possibly greater importance is the relative lack of a protective pack ice cover north of Lützow-Holm Bay during the 2004 minimum (overall sea-ice extent of ∼31,400 km^2 between 34 and 42° E) (see Figure 5.7), especially compared with the 2008 minimum (overall sea-ice extent of ∼44,000 km^2 in the same longitude range), which is the subject of Case Study 3. The anomalously strong and frequent easterly wind anomaly at DOY 1-20, 2004 may have advected any remaining pack ice away from Lützow-Holm Bay, thus rendering the latter more exposed to wave-induced breakout. The relative lack of a protective pack ice cover (see Figure 5.7) may have left the Lützow-Holm Bay fast ice vulnerable to wave-induced breakout (*Langhorne*

et al., 2001).

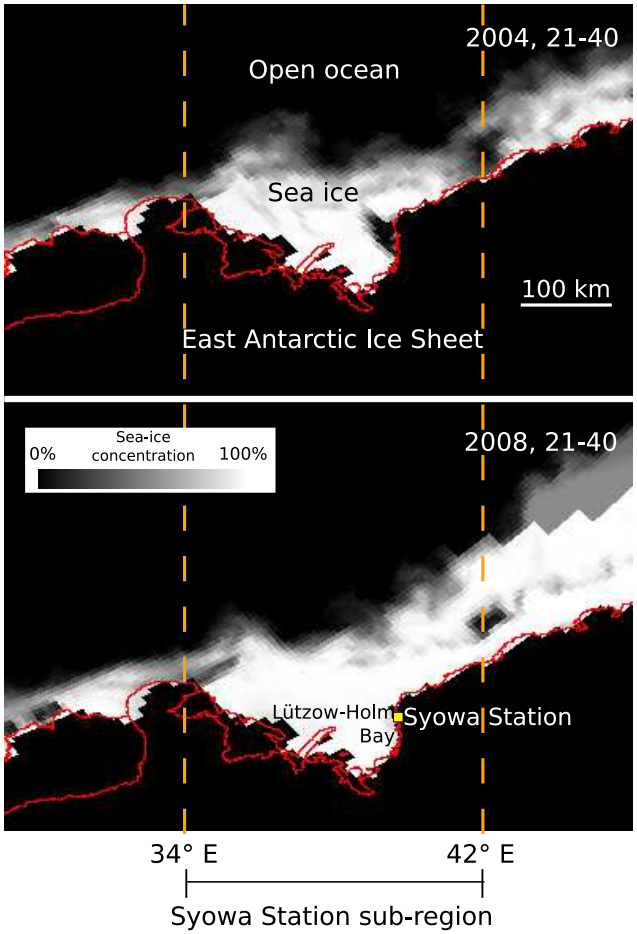

Figure 5.7: AMSR-E sea-ice concentration maps during 2004, 21-40 (top) and 2008, 21-40 (bottom). The Mosaic Of Antarctica (MOA) coastline and grounding line (*Scambos et al.*, 2007) are shown in red. There is much less protective pack ice north of Lützow-Holm Bay during the 2004 summer minimum compared to 2008. Artefacts of the ASI concentration retrieval algorithm can be seen in the eastern part of the lower panel (*Spreen et al.*, 2008).

5.5.3 Case Study 3: High Minimum Fast-Ice Extent, Syowa Station Sub-Region, 2008

Case Study 3, again situated in the Syowa sub-region, examines the summertime fast-ice extent in 2008 (covering the same time of year as Case Study 2). During this summer, fast-ice extent was anomalously high in and around Lützow-

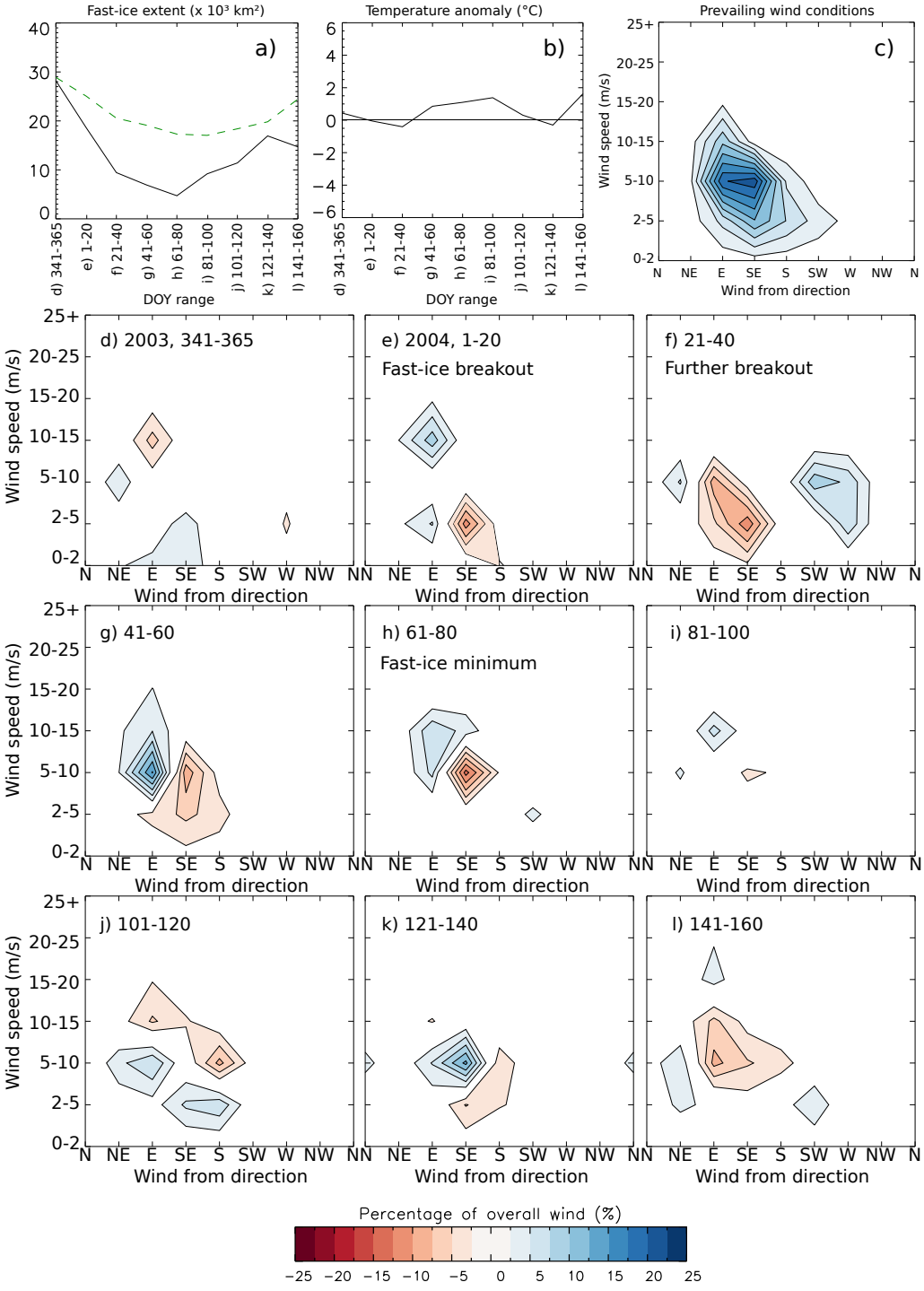

Figure 5.6: Case Study 2, illustrating low minimum fast-ice extent, Syowa Station sub-region, 2004. a) to c): As in Figure 5.5, but for Case Study 2. d) to l): Sequential 20-day wind difference plots for DOY intervals 2003, 341-365 to 2004, 141-160 respectively.

Holm Bay (see Figure 5.8a). In contrast to Case Study 2, temperature anomalies (Figure 5.8b) were consistently negative, ranging from 0 to -2.5 °C. Additionally, pack ice around Lützow-Holm Bay and along the Enderby Land coast (40 - 50° E) was much more extensive than normal (*Massom et al.* (2010b), also see Figure 5.7), to again possibly protect the fast ice from wave-induced breakout. Furthermore, Sea Surface Temperatures (SSTs) north of Lützow-Holm Bay were 0.3 to 0.6 °C below climatological values (*Xue and Reynolds*, 2010), with surface temperatures around Lützow-Holm Bay being 1 to 2 standard deviations below the mean at this time (*Fogt and Barreira*, 2010). This is likely related to the positive SAM index at this time, leading to a stronger polar vortex, and more effective isolation from warmer mid-latitude winds (*Xue and Reynolds*, 2010). However, effects of a stronger polar vortex, e.g., stronger westerly winds, are not shown in the localised wind anomaly plots for this case study (Figure 5.8d-l). As with Case Study 2, the increased fast-ice extent does not appear to be directly related to observed wind conditions (see Figure 5.8). No wind anomalies with a strong northerly component, which may have led to dynamically-formed fast-ice growth via advection of pack ice into pre-existing fast ice, were observed at this time. Thus, favourable pack-ice conditions combined with colder than average temperatures may explain this positive fast-ice extent anomaly.

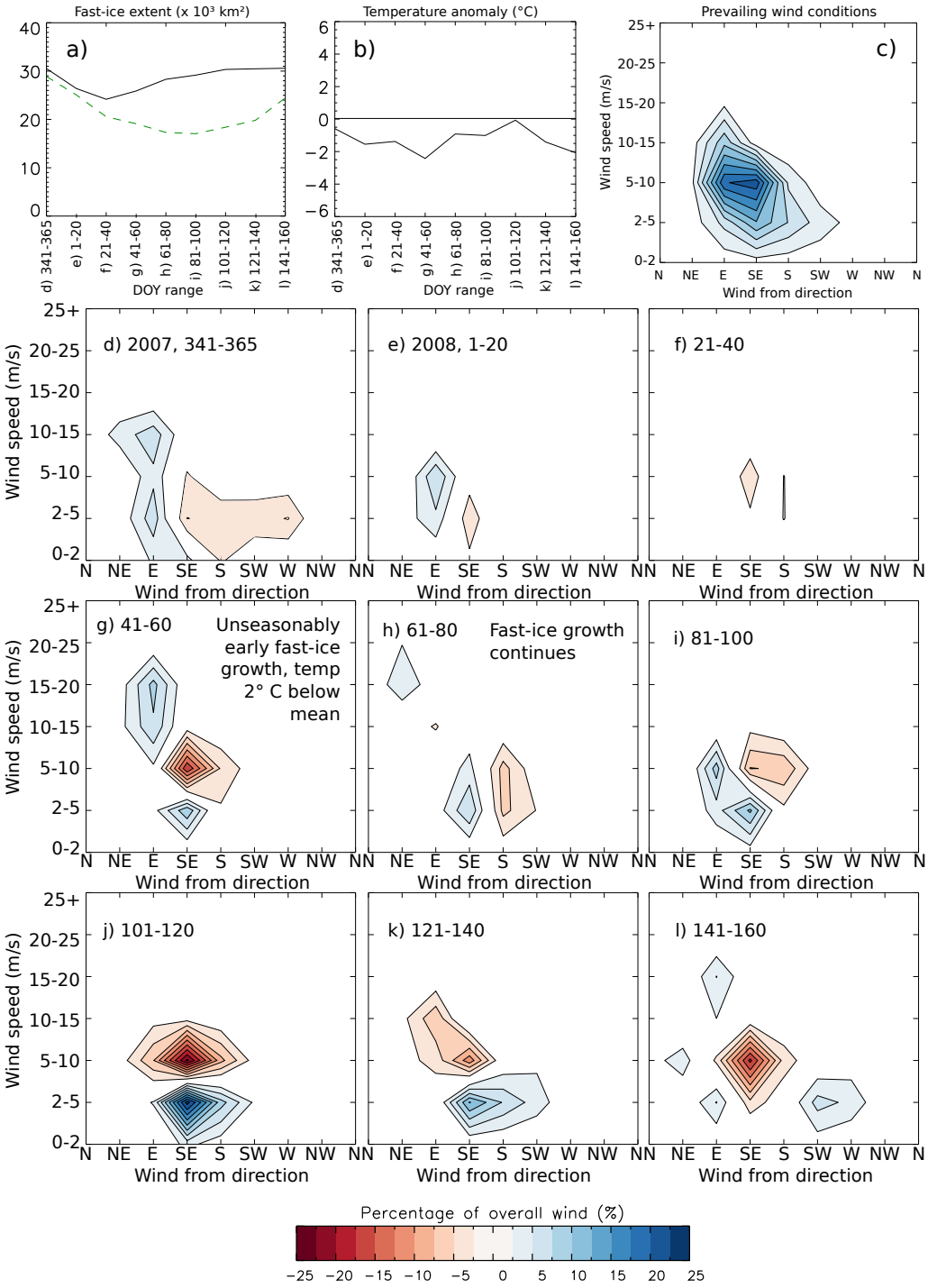

Figure 5.8: Case Study 3, illustrating high minimum fast-ice extent, Syowa Station sub-region, 2008. a) to c): As in Figure 5.5, but for Case Study 3. d) to l): Sequential 20-day wind difference plots for DOY intervals 2007, 341-365 to 2008, 141-160 respectively.

5.5.4 Case Study 4: Near-Average Fast-Ice Conditions, Mawson/ Cape Darnley Sub-Region, 2000

Case Study 4 is another "control" case, chosen to investigate the near-average fast-ice extent in the Mawson/Cape Darnley Sub-Region in 2000, from DOY 121-140 to 341-365 (see Figure 5.9). The fast-ice extent is within 5,000 km^3 of the 8.8-year mean extent for all 20-day time periods within this interval, except for DOY 181-200 when the fast-ice extent is $\sim$10,000 km^3 below the 8.8-year mean, despite strong wind anomalies during several of the 20-day windows within the time interval, e.g., Figure 5.9d, h, j, k and n. Strong temperature anomalies are also observed throughout the case study period (Figure 5.9b), although there appears to be no strong relationship between temperature anomaly and fast-ice extent at this time. During this period, pack-ice area/extent in the Indian Ocean sector was close to average (see Figure 4.11 in Chapter 4 of this thesis, *Comiso* (2010), *Cavalieri and Parkinson* (2008)). This suggests that the extent of adjacent pack ice may influence fast-ice extent in this location.

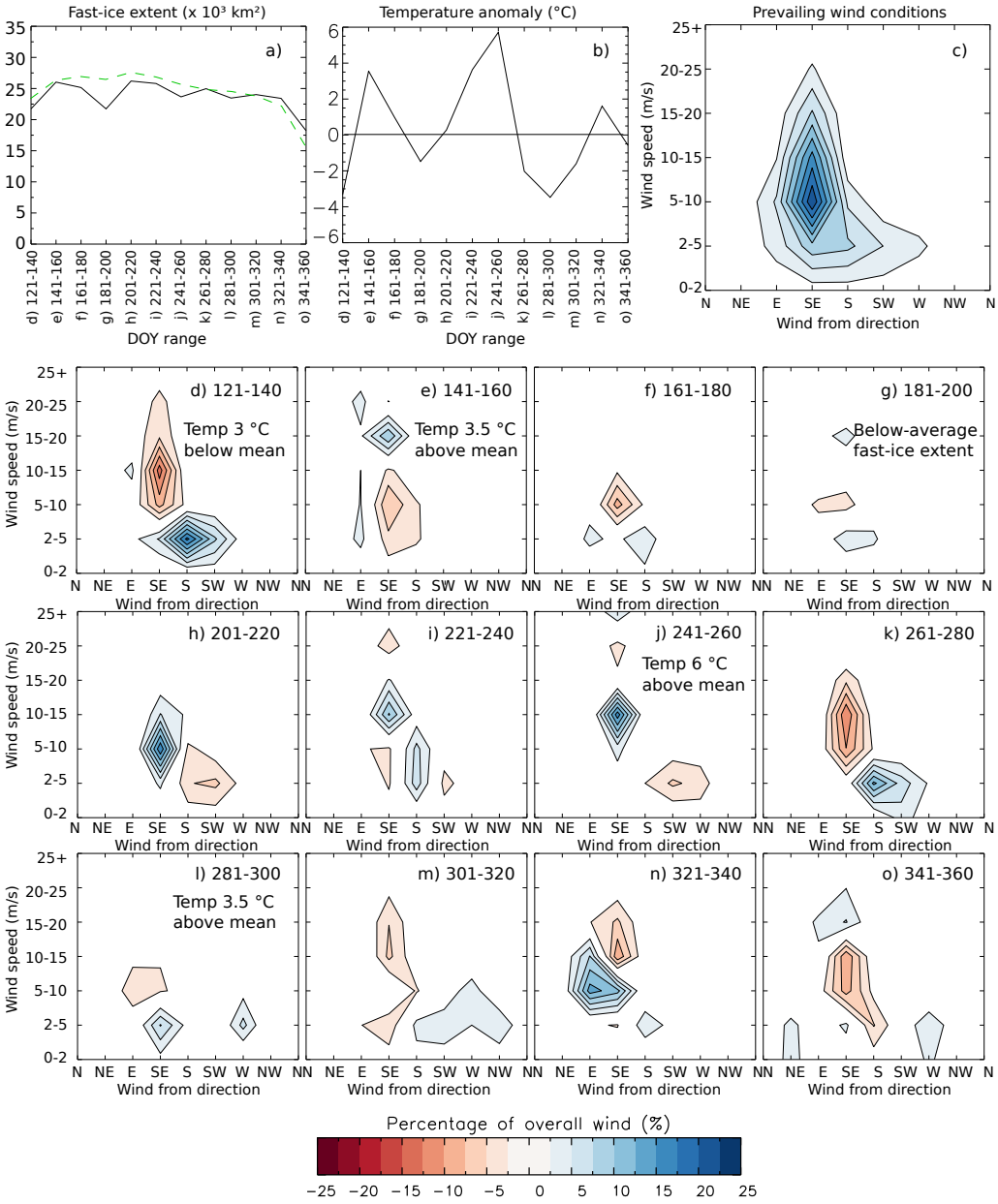

Figure 5.9: Case Study 4, illustrating near-average fast-ice conditions, Mawson/Cape Darnley sub-region, 2000. a) to c): As in Figure 5.5, but for Case Study 4. d) to o): Sequential 20-day wind difference plots for DOY intervals 2000, 121-140 to 341-365 respectively.

5.5.5 Case Study 5: High Minimum Fast-Ice Extent, Mawson Station/Cape Darnley Sub-Region, 2008

Case Study 5, again in late 2007/early 2008 but this time located in the Mawson Station/Cape Darnley sub-region, investigates a positive fast-ice extent anomaly along the Mawson coast (Figure 5.10a). Pack-ice concentration and extent in early 2008 in this region were well above average (*Massom et al.*, 2010b). Temperature anomalies (Figure 5.10b) increased from ∼-2 to +3.5 °C over the case study period. Wind difference plots (Figure 5.10d to j) showed repeating, strong anomalies from the east and south-east (Figure 5.10d, g and j). The lack of observed wind anomalies from the north/north west, which would advect pack ice into the pre-existing fast-ice features, leads to the conclusion that wind strength and direction did not, in this case, play a large part in this anomalously large fast-ice minimum extent. Again, the persistently extensive surrounding pack ice may have provided significant protection from wave-induced breakout, to combine with the negative temperature anomalies early in the case study. Similarly to Case Study 3, a strongly positive SAM index at this time led to a stronger polar vortex and effective isolation of the region from warmer, lower latitude air. This possibly contributed to negative (i.e., 0.3 to 0.6 °C below the mean) SST anomalies observed in the region (*Xue and Reynolds*, 2010; *Fogt and Barreira*, 2010). Though no study has examined the effect of regional SST on Antarctic fast-ice extent, it follows that less sea-ice melt would occur during years of colder SSTs, possibly leading to less summertime fast-ice melt/breakout.

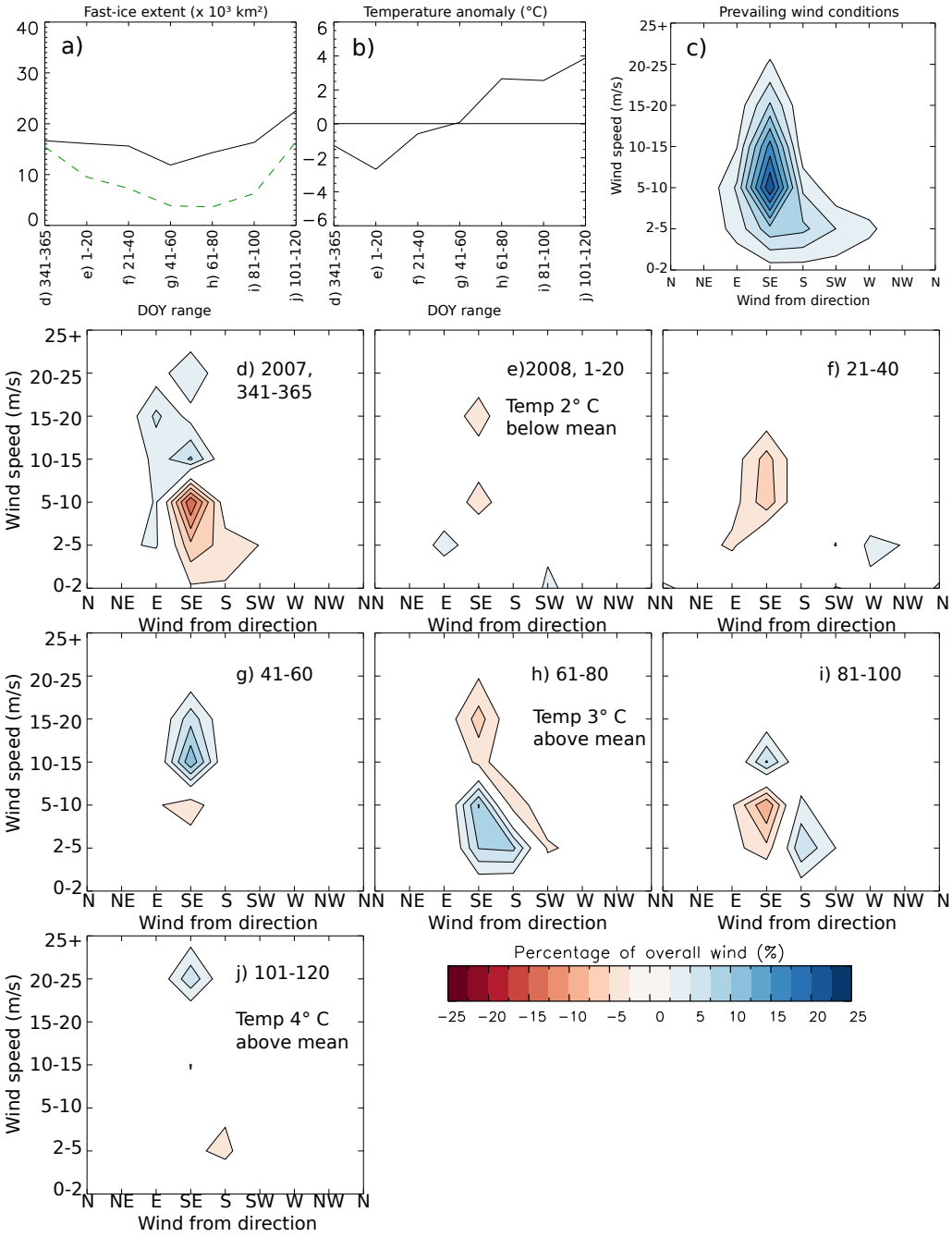

Figure 5.10: Case Study 5, illustrating high minimum fast-ice extent, Mawson Station/Cape Darnley sub-region, 2008. a) to c): As in Figure 5.5, but for Case Study 5. d) to j): Sequential 20-day wind difference plots for DOY intervals 2007, 341-365 to 2008, 101-120 respectively.

5.5.6 Case Study 6: Early and Near-Complete Fast-Ice Breakout, Dumont d'Urville Station Sub-Region, Late 2000

Case Study 6 examines the unseasonably early (compared to the 8.8-year mean), abrupt (occurring largely within a single 20-day time interval) and almost complete fast-ice breakout in the Dumont d'Urville Station sub-region in late 2000 (Figure 5.11a). This extensive breakout occurred in spite of the protective effects of extensive pack ice surrounding the fast-ice feature (not shown). In fact, the observed breakout coincided with several consecutive positive temperature anomalies (up to +1.5 °C, Figure 5.11b). As with the *Massom et al.* (2009) study, a strong positive south-easterly anomaly was observed during DOY 280-301, although this occurred before the observed breakout. The wind anomaly regime switched to a persistent, moderately strong (5-10 m/s) westerly wind anomaly in the subsequent 20-day period, before again switching to strong easterlies. This pattern may be indicative of the passage of one or more storm systems. Wind anomalies (Figure 5.11d-k) were generally small before a persistent westerly anomaly during the time of fast-ice breakout (DOY 2000, 301-320), followed by a strong easterly anomaly during DOY 321-340 then a persistent easterly/south easterly anomaly (DOY 341-366). It is likely that these strong wind anomalies, as well as the positive temperature anomaly, contributed to the abrupt fast-ice breakout.

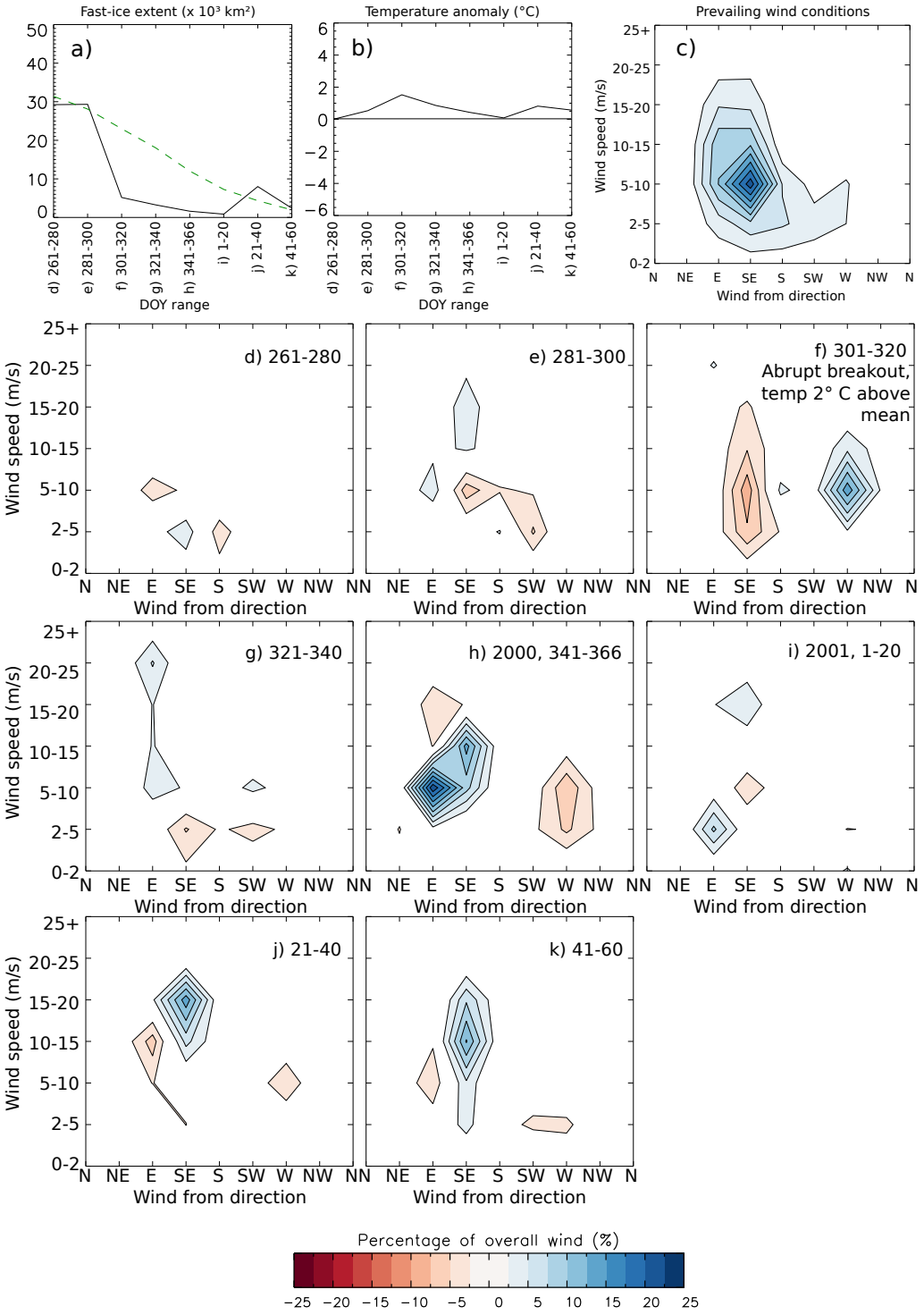

Figure 5.11: Case Study 6, illustrating early and near-complete fast-ice breakout, Dumont d'Urville Station sub-region, late 2000. a) to c): As in Figure 5.5, but for Case Study 6. d) to k): Sequential 20-day wind difference plots for DOY intervals 2000, 261-280 to 2001, 41-60 respectively.

5.5.7 Case Study 7: Near-Average Fast-Ice Conditions, Dumont d'Urville Sub-Region, Mid-Late 2004

Case Study 7, is another "control" case, chosen to investigate the near-average fast-ice conditions in the Dumont d'Urville sub-region in mid-late 2004 (see Figure 5.12). The fast-ice extent within the sub-region was within ∼5,000 km^2 of the 8.8-year mean cycle throughout the study period. As with Case Study 4, another "control" case (see Figure 5.9), strong temperature anomalies (both positive and negative) were observed (see Figure 5.12b), although the magnitude of wind anomalies was smaller here than in Case Study 4 (see Fig 5.12d-p). Pack-ice extent was below the climatological mean for the latter part of 2004 in the Western Pacific Ocean sector (*Comiso*, 2010; *Cavalieri and Parkinson*, 2008).

A transient fast-ice breakout occurred at DOY 181-200, which was followed by reformation in DOY 201-220. This ephemeral breakout was preceded by a strong (+5.5 °C) positive temperature anomaly in the previous 20-day window (DOY 161-180). The subsequent fast-ice re-formation occurred during a 20-day window where temperatures were ∼3.5 °C below the climatological mean, supporting the conclusion that temperature may play a predominant role in modulating fast-ice extent during this case study.

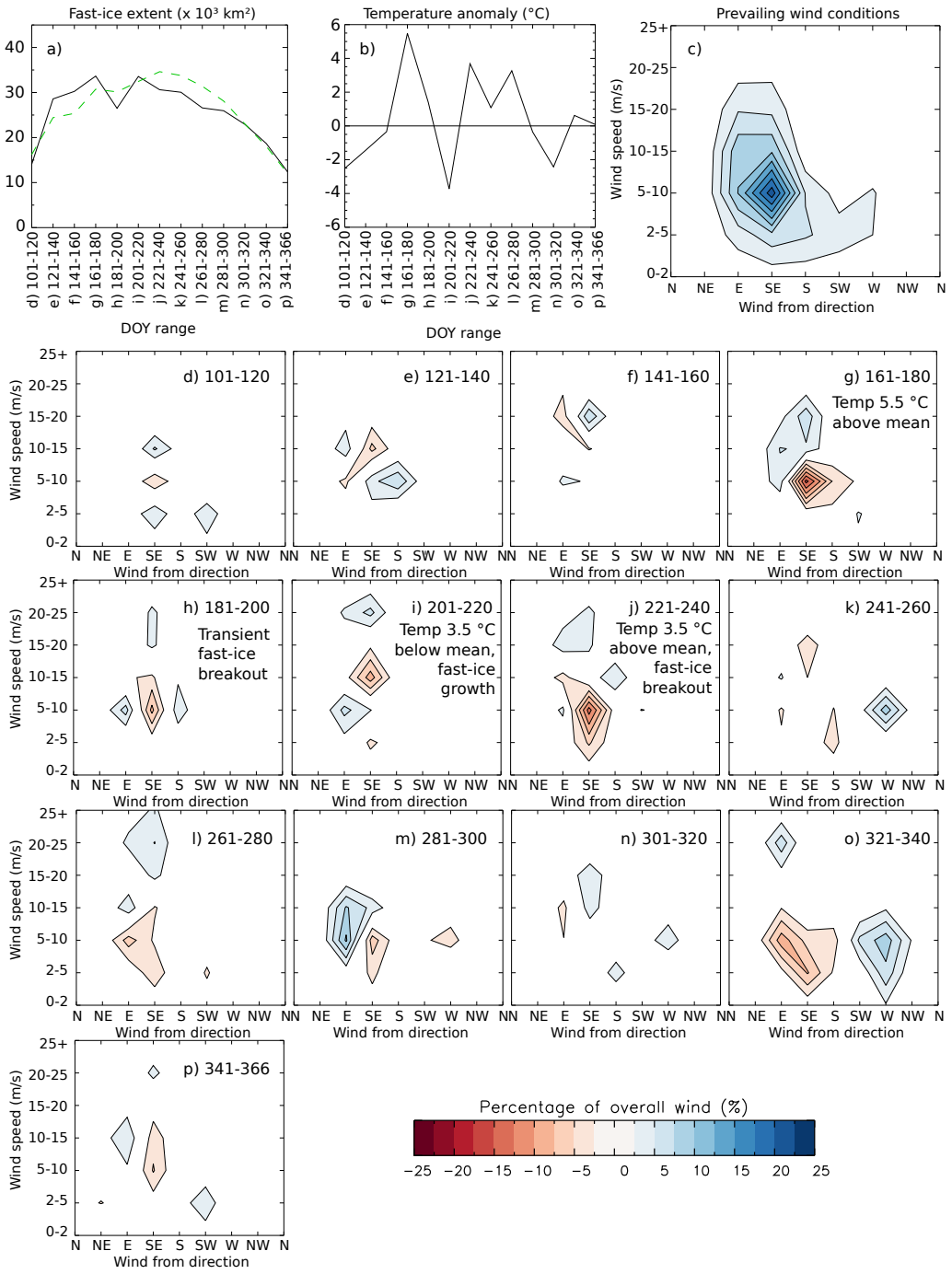

Figure 5.12: Case Study 7, illustrating near-average fast-ice conditions, Dumont d'Urville sub-region, mid-late 2004. a) to c): As in Figure 5.5, but for Case Study 7. d) to p): Sequential 20-day wind difference plots for DOY intervals 2004, 101-120 to 341-365 respectively.

5.5.8 Case Study 8: Low Minimum Fast-Ice Extent, Mertz Glacier/B-9B Sub-Region, 2002

Case Study 8 investigates an extensive breakout in the fast-ice feature to the east of the Mertz Glacier Tongue in early 2002. *Barber and Massom* (2007) give an in-depth description of the "ice-scape" of this region. A similarly abrupt (though less complete) breakout in this region in late October 1999 was discussed by *Massom et al.* (2003). Pack ice concentration in the region was well below average in 2002 (*Waple and Schnell*, 2003). This may have led to wave-induced fast-ice breakout. Surface air temperature was generally above average (Figure 5.13b). Persistent wind anomalies from the west/north west were observed for the first 80 days of the Case Study (Figure 5.13d-g), close to 180° from the climatological mean. The combination of these three factors likely led to the observed breakout, which resulted in the lowest fast-ice extent in the region over the entire 8.8-year time series, i.e., ∼5,500 km^2. The lack of fast ice surrounding the large tabular iceberg B-9B at this time allowed it to rotate clockwise (as seen from above), the most significant movement of the iceberg observed throughout the 8.8-year time series (*Massom*, 2003). Similar fast-ice conditions during early 2010 may have precipitated the major rotation of B-9B that led to its collision with the Mertz Glacier Tongue (MGT), resulting in calving of the MGT (*Young et al.*, 2010).

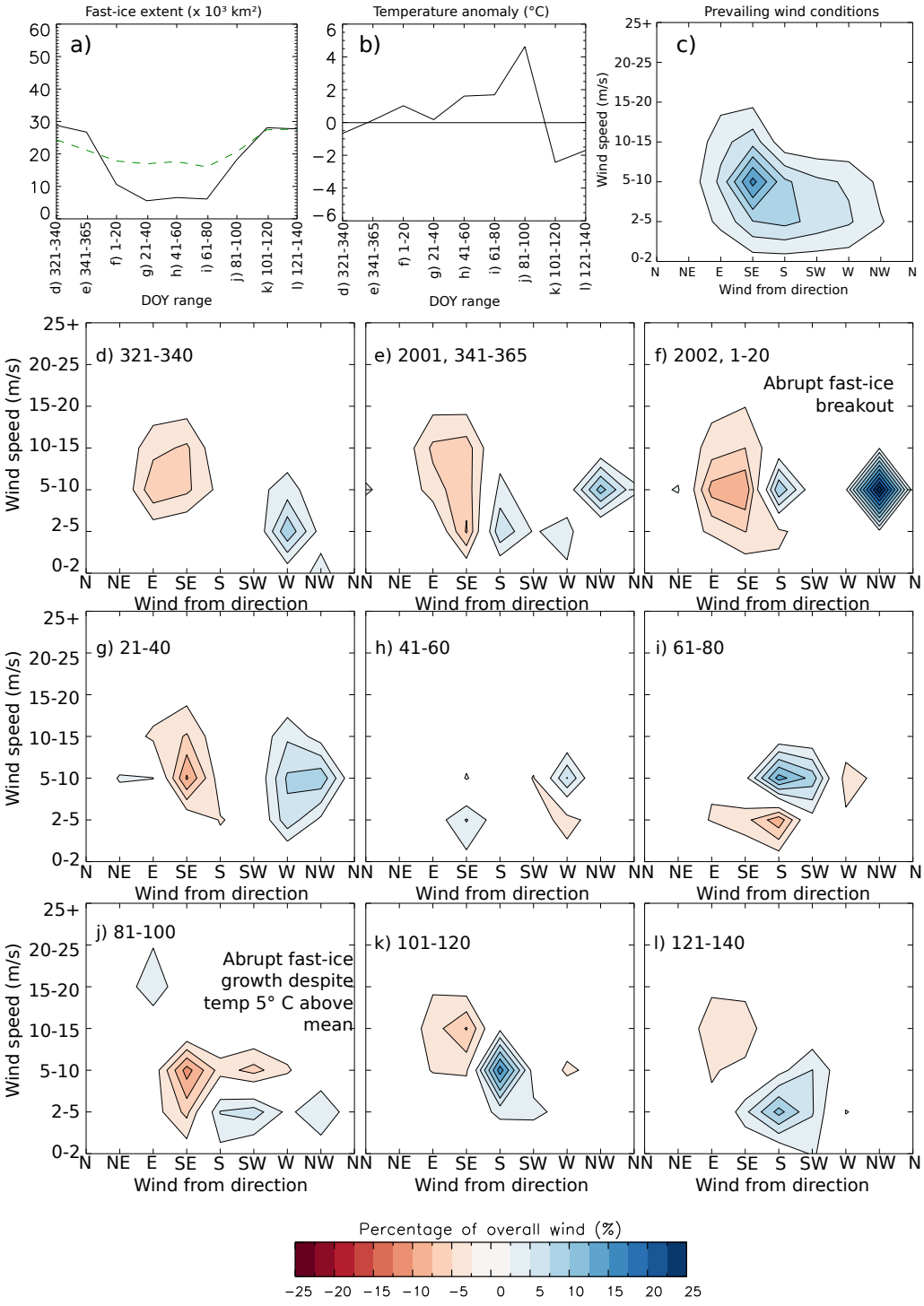

Figure 5.13: Case Study 8, illustrating low minimum fast-ice extent, Mertz Glacier/B-9B sub-region, 2002. a) to c): As in Figure 5.5, but for Case Study 8. d) to l): Sequential 20-day wind difference plots for DOY intervals 2001, 321-340 to 2002, 121-140 respectively.

5.5.9 Case Study 9: High Wintertime Maximum Fast-Ice Extent, Mertz Glacier/B-9B Sub-Region, 2006

Case Study 9 details the anomalously high, transient (persisting for only one 20-day time interval) maximum fast-ice extent in 2006. This event may be akin to the "stable extension" events observed in the Alaskan Arctic (*Mahoney et al.*, 2007a; *Stringer et al.*, 1980), where fast ice ephemerally extends well beyond the climatological maximum in a certain region. The most significant wind anomaly (see Figure 5.14f) occurred during the timing of the anomalous maximum, when strong wind anomalies were observed from the east and south-east. At this time of year (DOY 261-280), which is near the annual sea-ice maximum extent (*Gloersen et al.*, 1992), strong easterly winds such as this would advect pack ice against the pre-existing fast-ice feature east of B-9B. In this case, it appears that much of this pack ice became temporarily consolidated and formed fast ice. This conversion of pack ice to fast ice may have been aided by anomalously cold temperatures in the preceding 20-day interval (nearly 6 °C colder than average, Figure 5.14b), although the temperature anomaly became positive ($\sim$+2 °C) during the fast-ice maximum.

This case study raises the issue of what is fast ice, and more specifically, how long sea ice must remain stationary before it is considered fast ice. This issue was discussed to some extent by *Mahoney et al.* (2005), who also used a 20-day motion threshold to define fast ice.

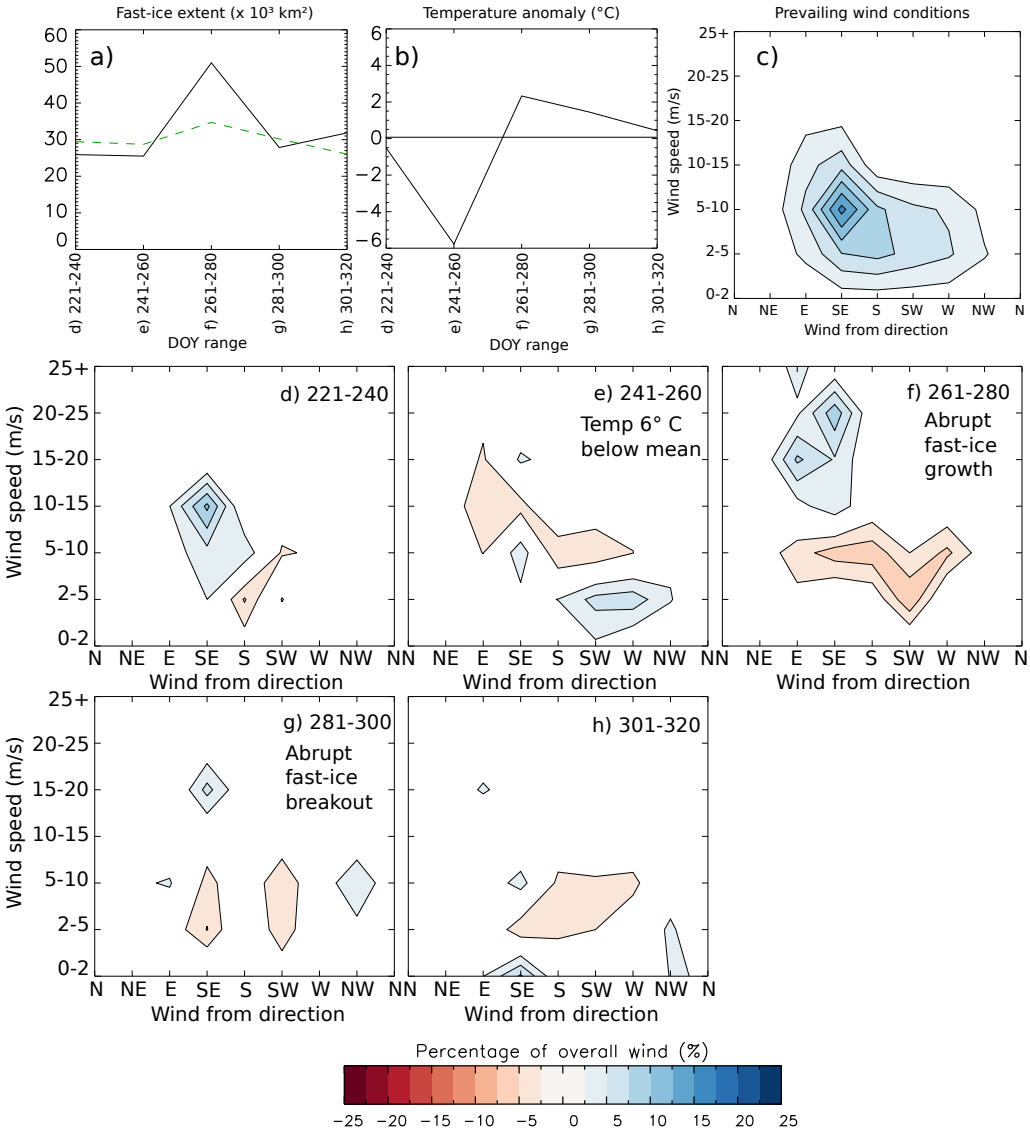

Figure 5.14: Case Study 9, illustrating high wintertime maximum fast-ice extent, Mertz Glacier/B-9B sub-region, 2006. a) to c): As in Figure 5.5, but for Case Study 9. d) to h): Sequential 20-day wind difference plots for DOY intervals 2006, 221-240 to 2006, 301-320 respectively.

5.6 Discussion, Conclusions and Further Work

5.6.1 Summary of Regional-Scale Atmospheric Influences on Fast Ice

Analysis of these nine case studies reveals that the response of fast-ice extent to changes in atmospheric parameters varies by region. Table 5.2 summarises which factors are important in each sub-region.

Table 5.2: Summary table of factors influencing fast-ice growth/breakout in each sub-region. An "x" indicates the factor that was identified as a strong influence on fast-ice extent, while a "∼" indicates the factor that may influence fast-ice formation/breakout to a lesser extent.

Study sub-region	**Wind**	**Temperature**	**Pack-ice**
Syowa		x	x
Mawson/Cape Darnley			x
Dumont d'Urville	x	∼	
Mertz Glacier/B-9B	x		x

In the Syowa Station sub-region (Case Studies 1-3), surface air temperature and pack-ice extent anomalies were found to control fast-ice extent. No strong relationship between wind and fast-ice extent was observed. This is likely due to the sheltering effect of Lützow-Holm Bay, which surrounds much of the fast ice in this sub-region. Wind-driven fast-ice breakout in such a bay would require a strong southerly wind, whereas prevailing wind conditions are primarily from the east and south east.

Below-average adjacent pack-ice concentration/extent was also found to be a major factor contributing to fast-ice breakup in this region by *Higashi et al.* (1982) and *Ushio* (2006). In the *Ushio* (2006) study, a southerly wind anomaly was directly implicated in a fast-ice breakout event in 2007, but more generally, the largest effect of wind is to control the distribution of pack ice. *Ushio* (2006) also comment on

the effect of surface air temperature on fast-ice stability in this region, stating that warmer temperatures lead to mechanically weaker fast ice within the bay.

In the Mawson Station/Cape Darnley sub-region (Case Studies 4 and 5), pack-ice extent anomalies were found be most closely linked to fast-ice extent. This is likely a consequence of the coastal configuration here. The relative lack of north-south protrusions into the Antarctic Coastal Current (ACC) leads to a narrow fast-ice zone forming parallel to the coast, which is exposed along its northern edge to wave-induced breakout (see previous chapter). The relative lack of influence of wind anomalies on fast-ice extent here, as also observed in the Syowa Station sub-region, is somewhat surprising given the differences in coastal configuration between the two sub-regions.

In the Dumont d'Urville sub-region (Case Studies 6 and 7), anomalous wind events were found to be an important influence on fast-ice extent, a finding also reported by *Massom et al.* (2009) in the same location. Fast ice above the bathymetric trough located to the north-west of Dumont d'Urville Station is particularly susceptible to ephemeral fast-ice breakout (*Massom et al.*, 2009), though the near-complete and abrupt fast-ice breakout in Case Study 6 suggests that much of the fast ice in this sub-region is also relatively prone to such breakouts. As in the other sub-regions, wave-ice interaction may also be a key factor, but this requires further investigation.

Pack ice and wind conditions were both found to play important roles in influencing fast-ice extent in the Mertz Glacier/B-9B sub-region (Case Studies 8 and 9). This may be because the fast ice here is likely largely dynamically-formed *Barber and Massom* (2007), and thus favourable wind strength/direction (i.e., onshore, or against B-9B/the Mertz Glacier Tongue) and pack-ice conditions are required for fast-ice formation under such a regime.

In the light of these nine case studies, we suggest that coastal configuration is the single largest determinant of which atmospheric/oceanic conditions control or influence fast-ice extent. Where dynamic fast-ice formation predominates (i.e., regions on the eastern "upstream" side of north-south protrusions into the ACC), wind direction and pack-ice concentration/extent/presence may be the primary factors controlling fast-ice growth, while the presence or absence of adjacent pack ice also likely influences breakout events by acting as a protective buffer against wave-induced breakout. In regions containing a larger percentage of thermodynamically-formed fast ice, temperature anomalies become a relatively important factor.

As mentioned, the effect of wind anomalies on fast-ice extent is complex. It may be the case that wind-driven fast-ice variability is more of an indirect process, with wind directly affecting pack-ice concentration via advection (as shown in *Massom et al.* (2009)). Though it is outside the scope of this work, analysis of storm conditions throughout each case study would be valuable, given that storminess has been identified as a contributor to fast-ice breakout in both hemispheres (e.g., *Heil*, 2006; *Divine et al.*, 2003, 2005). Such work is planned for the future.

Perhaps the main difficulty associated with attributing fast-ice formation and breakout events to changes in atmospheric parameters is the mismatch in time-scales. Fast-ice extent can respond quickly to synoptic-scale atmospheric changes (*Heil*, 2006; *Mahoney et al.*, 2007a; *Massom et al.*, 2009), on a timescale which is poorly resolved in the 20-day resolution product detailed in this thesis. Thus, confident attribution of fast-ice breakout/formation events to particular atmospheric/pack ice parameters requires a higher temporal resolution fast-ice extent time series. Nevertheless, the results of this chapter suggest that the response of fast-ice to atmospheric and pack ice conditions differs regionally, possibly reflecting the differences in coastal configuration between the sub-regions studied here.

5.6.2 Summary of Large-Scale Atmospheric Influences on Fast-Ice Growth and Breakout

Fast-ice extent across the East Antarctic coast and in both the Indian Ocean and Western Pacific Ocean sectors was found to be uncorrelated with SAM index ($R<0.2$). However, correlations with SOI index were substantially higher, particularly in the Indian Ocean sector ($R\simeq+0.45$) and the East Antarctic coast ($R\simeq+0.4$). In these SOI correlation analyses, the maximum correlation coefficient was obtained with a lag of 6 months (SOI leading fast-ice extent), implying an atmospheric ENSO teleconnection.

These results stand in contrast to those of *Massom et al.* (2009), who found a much stronger fast-ice response to SAM than SOI (in a regional study along the Adélie Land coast). However, this correlation study involved only eight data points for eight years, with fast-ice extent, distance to open water, SAM and SOI values all averaged over the June - December period. The smaller-scale spatial averaging used by *Massom et al.* (2009) may also be responsible for the differences in observed correlations. It is also possible that the stability of the annual "buttress" of annual fast ice to the north-west of Dumont d'Urville Station is particularly susceptible to anomalies in wind speed and direction, given the strong response to wind anomalies observed both in the *Massom et al.* (2009) paper and Case Study 6 presented here. A significant factor here is the presence of a bathymetric trough (and an associated lack of grounded icebergs) extending north to northwestwards from the coast near Dumont d'Urville. The ephemeral breakouts and re-formations largely occur in this area. Similar sensitivity to wind anomalies is also observed in the Mertz Glacier/B-9B sub-region, with wind identified as a possible influence on fast-ice anomalies on both Case Studies 8 and 9. Much of this persistent fast-ice feature - particularly that to the south and south-east of B-9B - is exposed by means of a lack of grounded

icebergs, this time to the east instead of the north. In contrast, the fast ice in the Syowa sub-region is much more sheltered due to the presence of Lützow-Holm Bay, and the fast-ice feature along the Mawson Coast is bounded by grounded icebergs to the north, east and west.

The stronger correlations observed by *Massom et al.* (2009) may be related to the temporal averaging, which would reduce the effects of noise on the data. However, using this style of correlation analysis makes it impossible to compute the lag between SAM index and fast-ice response. It is reasonable to expect that SAM may influence fast-ice extent more strongly than SOI, given that it is the first EOF of MSLP, and thus represents a higher fraction of the MSLP variance than manifestations of SOI.

It is perhaps more difficult to view the relationships between large-scale atmospheric modes of variability and fast-ice extent in the context of works which relate these modes to overall sea-ice (i.e., predominantly pack-ice) parameters such as concentration or length of the annual sea-ice season (e.g., *Stammerjohn et al.*, 2008; *Yuan and Li*, 2008; *Lefebvre and Goosse*, 2008; *Turner*, 2004; *Liu et al.*, 2004a; *Yuan*, 2004; *Kwok and Comiso*, 2002). These works conclude either explicitly or implicitly that the effects of SAM and SOI are much larger in West Antarctica than East Antarctica. Despite this, moderately strong correlations have been found between sea-ice edge location and SOI. The *Simmonds and Jacka* (1995) study, for example, found a positive correlation between SOI and sea-ice edge location in the 35 to 65° E sector, with the strongest correlation observed during the winter months. It is possible that a monthly-resolved SOI/fast-ice extent correlation analysis would yield similar correlation values and variability. It is encouraging that the sign and magnitude of the correlation, as well as the lag of maximum correlation are the same as that reported in the *Simmonds and Jacka* (1995) study of overall sea ice.

The *Simmonds and Jacka* (1995) and *Kwok and Comiso* (2002) studies suggest that the response to SOI is larger in the Indian Ocean sector than the Western Pacific Ocean sector, which is also found in this work. This supports the concept of ENSO signals propagating eastward around the Southern Hemisphere, and becoming more attenuated as the signals travel farther (i.e., into the Western Pacific Ocean sector). *Kwok and Comiso* (2002) found a negative correlation between SST and SOI in the Indian Ocean sector (i.e., colder SSTs during positive SOI). Though the links between large-scale Antarctic fast-ice variability and SST have yet to be studied, *Kwok and Comiso* (2002) qualitatively suggest that colder SSTs occur during times of positive SOI. This broadly agrees with the findings presented here.

5.6.3 Suggested Further Research

As mentioned at the beginning of this chapter, the results presented here from an investigation of atmospheric influences on fast-ice variability are preliminary only. An aim is to subsequently extend this work by performing more in-depth (i.e., seasonally-resolved) correlation analyses between fast-ice extent and SOI, SAM, and when they become available, ZW3 index data (see *Raphael* (2004, 2007)). This research will also benefit greatly from a longer time series of fast-ice extent, so extending the fast-ice series both back and forward in time is a high priority, and is planned. We also plan to incorporate storm/cyclone and wave model data into the fast-ice variability analysis.

Chapter 6

Overall Summary and Conclusions

The main outcomes of the work presented in this thesis are:

- the development of techniques to generate cloud-free composite images of the surface of the Earth in visible/thermal infrared wavelengths from MODIS imagery (Chapter 2);
- the development of techniques for interpretation of this composite imagery in order to consistently and accurately determine fast-ice extent on a large scale (Chapter 3);
- production of the first (near decade-long) time series of fast-ice extent at a 2 km, 20-day spatio-temporal resolution across the entire East Antarctic coast, generated from ∼125,000 individual MODIS images (Chapter 4);
- the identification of ten fast-ice regimes around the coast, which are related to bathymetry (i.e., grounded iceberg distribution) and coastal configuration (Chapter 4);
- the first baseline measurements of East Antarctic fast-ice areal extent, as well as quantification of trends (albeit over a climatologically short, 8.8-year time series) in extent across the East Antarctic coast ($+1.43 \pm 0.30\%$ yr^{-1}) and

its component parts: the Indian Ocean sector (+4.07 ±0.42% yr^{-1}) and the Western Pacific Ocean sector (-0.40 ±0.37% yr^{-1}) (Chapter 4); and

- a preliminary investigation into the influences of local- to large-scale atmospheric variability on anomalous fast-ice growth and breakout events (Chapter 5).

In addition to the scientific outcomes noted above, the work in this thesis will result in four peer-review publications in highly-ranked international journals (currently two are published, one has been submitted, and one is in preparation, and is close to completion), as well as several non-referreed publications and oral and poster presentations (see page viii in the introductory material of this thesis for a complete list with details).

This work has significantly expanded our knowledge of fast-ice extent and variability across the entire East Antarctic coastline. It has not only gone some way toward filling a large gap in our knowledge of this integral part of the climate and physical/biological systems, but has also provided a new baseline for future climate change/variability comparisons and assessments. This is particularly important, given the sensitivity of fast ice to changing oceanic and atmospheric conditions and its potentially important role in stabilising dynamic ice-sheet margins.

Chapter 2 presented details of a procedure for compositing visible and thermal infrared MODIS images to effectively remove cloud cover, and provide an unobscured view of the surface. The success of this technique is highly dependent on the efficacy of the cloud mask used. During times when the Sun is above the horizon and shortwave tests can be incorporated into the suite of tests comprising the cloud mask, no modifications are necessary to produce generally high-quality composite images. However, during times when the Sun is below the horizon (i.e., much of the

polar winter), the lower cloud-mask accuracy necessitate modifications to the cloud mask in order to produce quality output. These modifications are in the form of a spatial smoothing kernel, tuned to enhance the cloud mask efficacy over polynyas and flaw leads. Sample visible and infrared composite images of the Mertz Glacier regions were presented as a proof-of-concept for the techniques.

Following on from this work, Chapter 3 used these techniques to produce a time series of 159 consecutive fast-ice maps spanning the time interval from March 2000 until December 2008. A compositing period of 20 days was found to produce good quality composite images in the majority of cases. This time interval also coincides with the suggested minimum time for ice to remain stationary before it is considered "fast" (based on the Arctic work of *Mahoney et al.*, 2005). However, persistent cloud and inaccurate cloud masking lead to lower quality regions in some composite images. In these cases, AMSR-E data are used to assist in image classification at the expense of spatial resolution. Additionally, the previous and subsequent fast-ice maps are used to help classify lower quality composite images, at the expense of temporal resolution. A study of errors determined that the fast-ice extent in the majority ($\sim$81%) of images, fast-ice extent can be retrieved to within $\sim \pm 3\%$, with the remainder of images within $\sim \pm 9\%$. This chapter also presents the first maximum and minimum fast-ice extent maps for the entire East Antarctic coast, showing fast-ice extents of $\sim$374,000 and $\sim$112,000 km^2 respectively.

Chapter 4 presented the 8.8-year time series of fast-ice extent, including analysis of inter-annual variability, at temporal and spatial resolutions of 20 days and 2 km respectively. This time series and the associated fast-ice maps are comparable to the widely-used passive microwave-derived time series of overall sea-ice extent and area, extending back to 1979 (e.g., *Comiso*, 2010; *Cavalieri and Parkinson*, 2008). As noted above, a statistically-significant increase in fast-ice extent is

observed across the East Antarctic coast (1.43±0.30% yr^{-1}), albeit over the short time series (2000 to 2008). Regionally, a stronger increase is observed in the Indian Ocean sector (20 - 90° E, 4.07±0.42% yr^{-1}) over the 8.8-year time series. The trend in the Indian Ocean sector is slightly negative prior to 2004, but strongly positive thereafter, and this apparent shift in trend coincided with an increase in variability. A slight (non-significant) decrease is observed in the Western Pacific Ocean sector (90 - 160° E, -0.40±0.37% yr^{-1}), with an unchanged level of variability observed through the time series. Interannual variability in fast-ice extent is generally high over the entire East Antarctic coast, but particularly high in the Indian Ocean sector (and particularly from 2004 to 2008). Overall, fast-ice extent in the Western Pacific Ocean sector is lower than that in the Indian Ocean sector, possibly reflecting the different coastal and bathymetric configurations in each sector.

This chapter also presents a 20-day resolution climatology of East Antarctic fast-ice extent for the first time, in addition to maps of fast ice by year (from fast-ice minimum to subsequent fast-ice minimum). Ten regimes of fast-ice formation are identified around the East Antarctic coast, within which regional differences are related to the bathymetry (and associated distribution of grounded icebergs which act as anchor points for fast-ice formation) and the shape of the coastline, e.g., the presence of bays/promontories. Correlations between fast ice and overall sea-ice extent and area are investigated, and are only found to be high during the summer-time sea-ice minimum. This possibly reflects the higher relative fraction of fast ice during the summertime, and/or the protective effect of extensive summertime pack ice. Analysis of the shape of the mean annual fast-ice cycle reveals an upper limit on fast-ice extent: formation in water deeper than 400 to 500 m is rarely observed due to the lack of grounded icebergs acting as anchors there. East Antarctic fast ice is found to comprise between ∼5% (during winter and spring) and 45% (during

summer) of overall sea-ice area in the region (these percentages change to ∼4% and ∼20% when considering overall sea-ice extent rather than area). This agrees well with the Synthetic Aperture Radar-based study by *Giles et al.* (2008), which finds that East Antarctic fast-ice extent (between 75 and 170° E) comprises between 2 and 16 % of overall November sea-ice area, depending on the sub-region (8.3% when averaged over the whole study region).

Chapter 5 presented a preliminary investigation of the role of local to hemispheric atmospheric patterns on influencing fast-ice extent. On local scales, the relative importance of various oceanic/atmospheric parameters on controlling fast-ice extent was found to depend on the fast-ice formation regime. Growth/breakout of dynamically-formed fast ice was found to depend strongly on wind strength/direction and nearby pack-ice concentration. By contrast, temperature was observed to be an important factor in the growth/breakout of thermodynamically-formed fast ice. These results agree broadly with previous studies both in the Arctic and Antarctica, which find that wind strength/direction and air temperature anomalies can influence fast-ice growth and breakout events (*Heil et al.*, 2006; *Massom et al.*, 2009; *Divine et al.*, 2003, 2005). Anomalous fast-ice breakout (formation) is associated with anomalously low (high) local pack-ice concentration, possibly reflecting the buffering effect of a compact pack-ice cover against wave-induced fast-ice breakout. On a hemisphere-wide scale, the correlation between fast-ice extent and the Southern Oscillation Index (SOI)/Southern Annular Mode (SAM) is analysed. Significant correlations ($R \simeq 0.4$ and $R \simeq 0.45$) are found between SOI and fast-ice extent along the East Antarctic coast/Indian Ocean sector respectively. No notable correlations are observed between fast-ice extent and the SAM index. This is in contrast to a study by *Massom et al.* (2009), which found much stronger correlations between SAM and fast-ice extent to the north-west of Dumont d'Urville.

6.1 Potential Response of East Antarctic Fast-Ice to Atmospheric Change and Variability

Model projections of the state of the climate around the Antarctic coast by the end of the 21st century include increases in surface air temperature, snowfall, storminess, waviness and the numbers of icebergs, as well as a general decrease in pack-ice extent (*Turner et al.*, 2009; *Bracegirdle et al.*, 2008; *Bentley et al.*, 2007). The potential impacts of these changes on fast-ice extent are discussed in the following sub-sections. Although this assessment is largely speculative, it is based upon knowledge of current conditions.

6.1.1 Rising Temperatures

Recent decadal-scale temperature changes across coastal Antarctica (e.g., 1950 to present) have so far been mixed, depending on the sector (*Turner et al.*, 2005, 2009; *Steig et al.*, 2009). To date, stations along East Antarctica have generally reported no significant trend or even slight decreases in air temperature. Conversely, stations along the West Antarctic Peninsula (WAP) have reported some of the strongest positive global temperature trends (*Vaughan et al.*, 2003). For example, Faraday (now named Vernadsky) station on the WAP is reporting an increase in mean winter-time air temperature of 0.56 $\pm$0.43 °C/decade for the last 5 decades (*Turner et al.*, 2005).

With East Antarctic coastal temperatures projected to rise between 1.5 and 5 degrees by the year 2100 (*IPCC*, 2007; *Bracegirdle et al.*, 2008; *Convey et al.*, 2009; *Turner et al.*, 2009), more frequent glacier calving is likely (*Scambos et al.*, 2003; *Cook et al.*, 2005; *Bentley et al.*, 2007). *Massom and Stammerjohn* (2010) suggest that this may in fact contribute to larger fast-ice extents by means of more grounded icebergs providing more anchor points for fast-ice formation, or may act to

stabilise the coverage. Alternatively, higher air and sea temperatures may result in a shorter fast-ice growth season (*Heil et al.*, 2006), leading to less extensive/thinner fast ice.

6.1.2 Increasing Wind Speed and Storminess

Trends toward stronger westerly winds and higher SAM index values have also been noted over the last 50 years across the East Antarctic coast (*Turner et al.*, 2009). Winds with a stronger westerly component may counteract westward pack ice advection by the Antarctic Coastal Current, to potentially reduce the amount of fast ice formed dynamically, particularly in the Western Pacific Ocean sector. Additionally, anomalously strong westerly winds were implicated in fast-ice breakout in the Dumont d'Urville case study presented in Chapter 5. A trend toward lower atmospheric pressures over the last 50 years is also noted at Antarctic stations (*Turner et al.*, 2009, 2005), leading to fewer but more intense low pressure systems around the coast of Antarctica (*Turner et al.*, 2009; *Simmonds and Keay*, 2000).

Several models predict an increase in wind, wave and storm occurrence at high southern latitudes throughout the 21st century (*Fyfe and Saenko*, 2006), particularly during winter (*Convey et al.*, 2009). This is a manifestation of the southward shift of storm tracks under the influence of a positive SAM index (*Miller et al.*, 2006). The projected increase in SAM index is itself a consequence of increased greenhouse gas concentrations and a reduction in stratospheric ozone (*Bracegirdle et al.*, 2008; *Massom and Stammerjohn*, 2010). The projected recovery of the ozone hole to 1980 levels by the year 2068 is expected to reduce this windiness to some extent (*Perlwitz et al.*, 2008).

6.1.3 Reduction in Pack-Ice Cover

Several case studies in Chapter 5 have shown the importance of summertime pack-ice coverage for maintaining average summertime fast-ice extents. Pack ice acts as a physical shield to buffer the vulnerable fast ice from wave-induced breakout (*Crocker and Wadhams*, 1988, 1989; *Langhorne et al.*, 1998, 2001). Case studies of anomalously low and high fast-ice extent in Lützow-Holm Bay, presented in Chapter 5 of this thesis, highlight this dependence particularly strongly. Several recent studies (e.g., *Comiso*, 2010; *Cavalieri and Parkinson*, 2008) have shown that overall Antarctic sea-ice extent is slightly increasing ($1\pm0.4\%$ decade^{-1}), despite differing regional trends. Overall sea ice area and extent is generally observed to be increasing in the Indian Ocean ($1.9\pm1.4\%$ decade^{-1}) and Western Pacific Ocean ($1.4\pm1.9\%$ decade^{-1}) sectors (*Cavalieri and Parkinson*, 2008). These trends are valid for the satellite era. Different (decreasing) trends are apparent if the record is extended back in time, however, using proxy estimates derived from whaling records (*de La Mare*, 1997) and ice core data (*Curran et al.*, 2003).

Using a weighted ensemble average of output from 24 climate models, *Bracegirdle et al.* (2008) forecast Antarctic sea-ice concentration to decrease by 33% overall by the end of the 21st century. Regionally, greater decreases in sea-ice concentration are forecast in the Indian Ocean sector than the Western Pacific Ocean sector. The largest fractional decreases are forecast in the winter (June-August) and spring (September-November) seasons, however decreases in sea-ice concentration are forecast throughout the year in both sectors. Despite a large spread in model projections (*Turner et al.*, 2009; *Massom and Stammerjohn*, 2010), other modeling studies have forecast similar decreases in overall sea-ice extent by the end of the century, e.g., (*Arzel et al.*, 2006) predict a reduction in the annual mean sea-ice

extent of 24% by the year 2100 using an ensemble of 15 models.

In the light of these projections of reduced pack-ice concentration and extent, a future reduction in fast-ice extent may occur (all else being equal). Wave-induced fast-ice breakout is likely to increase as a consequence of this projected decrease in pack-ice extent, especially when also taking into account the increase in occurrence of destructive waves associated with increased wind strength and storm occurrence (*Massom and Stammerjohn*, 2010; *Bracegirdle et al.*, 2008). Another anticipated consequence of reduced pack-ice coverage is an enhanced ice-albedo positive feedback effect (*Perovich*, 2009), leading to warmer SSTs and possibly associated fast-ice breakout events.

6.1.4 Increase in Precipitation

One consequence of a warmer atmosphere is its higher atmospheric moisture capacity. When combined with a southward shift in the storm track (*Turner et al.*, 2005), this leads to increases in projected snowfall (*Bracegirdle et al.*, 2008; *Massom and Stammerjohn*, 2010; *Convey et al.*, 2009) over the East Antarctic coast. The net increase in precipitation along the East Antarctic coast has been estimated at 10-20% (*Bracegirdle et al.*, 2008). Snow on fast ice affects heat transfer and ice formation rates in non-linear ways (e.g., *Flato and Brown*, 1996; *Massom and Stammerjohn*, 2010). It can lead to a significant growth in fast-ice thickness by means of snow ice formation if flooding occurs (*Maksym and Jeffries*, 2000). Furthermore, heavy snow cover has been shown to reduce the occurrence of fast-ice breakout (i.e., perpetuate the duration) in Lützow-Holm Bay (*Ushio*, 2006, 2008).

6.2 Suggested Future Work

There are many possible directions for future work building on the outcomes of this project. In particular, the following are suggested:

- Development of a fully-automated fast-ice detection algorithm, to enable automated extension of the MODIS time series forward in time;
- Spatially extending the coverage to provide the first fast ice time series of the entire Antarctic coastline;
- Production of the first detailed maps of the extent and variability of circumpolar Arctic fast ice, enabling a unique bi-polar comparison;
- Providing wider spatio-temporal fast ice information in support of detailed localised measurements made within the Antarctic Fast Ice Network (AFIN) project (*Heil et al.*, 2010);
- Extension of the time series back in time (pre-2000) via implementation of algorithms using NOAA Advanced Very High Resolution Radiometer (AVHRR) satellite data, in order to produce both the first long-term assessment of the effects of climate change on fast ice, and a longer dataset for use by the biological community (although data availability is poorer back in time);
- Modifying the compositing procedure to process high-resolution (300 m visible and thermal infrared) Ocean Land Colour Instrument (OLCI) imagery from the upcoming European Space Agency (ESA) Sentinel-3 platform;
- Detailed case studies investigating links between fast ice and demographic parameters of various biological species (including breeding success, foraging behaviour, and other factors);

- Studies on the role of fast ice in polynya dynamics (in particular, combining these data with passive microwave measurements to more accurately retrieve ice formation rates, and salt water, heat and moisture fluxes); and

- Investigation of possible links between fast ice and the stability of glacier tongues and ice shelves, building upon the work of *Massom et al.* (2010a).

- Regional studies aimed at identifying key scales of spatial variability, and comparisons between regions with similar bathymetry/coastal configurations.

Bibliography

Ackerman, S. A., K. I. Strabala, W. P. Menzel, R. A. Frey, C. C. Moeller, and L. E. Gumley, Discriminating clear sky from clouds with MODIS, *Journal of Geophysical Research*, *103*, 32,141–32,158, 1998.

Ackerman, S. A., C. C. Moeller, R. A. Frey, L. E. Gumley, and W. P. Menzel, Reducing striping and near field response influence in the MODIS 1.38μm cirrus detection band, *AGU Spring Meeting Abstracts*, 2002.

Ackerman, S. A., K. I. Strabala, W. P. Menzel, R. A. Frey, C. C. Moeller, L. E. Gumley, B. Baum, S. W. Seemann, and H. Zhang, Discriminating clear-sky from cloud with MODIS, *Algorithm Theoretical Basis Document ATBD-MOD-06*, NASA Goddard Space Flight Center, Greenbelt, Maryland, 2006.

Aiken, C. M., M. H. England, and C. J. C. Reason, Optimal Growth of Antarctic Circumpolar Waves, *Journal of Physical Oceanography*, *36*, 255–269, doi: 10.1175/JPO2856.1, 2006.

Anderson, D. R., D. J. Sweeney, and T. A. Williams, *Introduction to Statistics - An Applications Approach*, West Publishing Company, Eagan, Minnesota, 1981.

Andrews-Goff, V., M. A. Hindell, I. C. Field, K. E. Wheatley, and J. B. Charrassin, Factors influencing the winter haulout behaviour of Weddell seals: consequences for satellite telemetry, *Endangered Species Research*, *10*, 83–92, 2010.

Antonelli, P., M. di Bisceglie, R. Episcopo, and C. Galdi, Destriping MODIS data using IFOV overlapping, *Proceedings of the IEEE International Geoscience and Remote Sensing Symposium (IGARSS) 2004*, *7*, 4568–4571, 2004.

Arrigo, K. R., J. N. Kremer, and C. W. Sullivan, A simulated Antarctic fast ice ecosystem, *Journal of Geophysical Research*, *98*, 6929–6946, doi: 10.1029/93JC00141, 1993.

Arzel, O., T. Fichefet, and H. Goosse, Sea ice evolution over the 20th and 21st centuries as simulated by current AOGCMs, *Ocean Modelling*, *12*, 401–415, doi: 10.1016/j.ocemod.2005.08.002, 2006.

Baldwin, M. P., Annular modes in global daily surface pressure, *Geophysical Research Letters*, *28*, 4115–4118, doi:10.1029/2001GL013564, 2001.

Barber, D. G., and R. A. Massom, The Role of Sea Ice in Arctic and Antarctic Polynyas, in *Polynyas: Windows to the World*, vol. 74, edited by W. Smith and D. G. Barber, pp. 1–43, Elsevier, Amsterdam, 2007.

Barnes, W. L., X. Xiong, and V. V. Salomonson, Status of terra modis and aqua modis, *Advances in Space Research*, *32*(11), 2099–2106, doi:DOI: 10.1016/S0273-1177(03)90529-1, 2003.

Beaman, R. J., and P. T. Harris, Bioregionalisation of the George V Shelf, East Antarctica, *Continental Shelf Research*, *25*(14), 1657–1691, 2005.

Beaven, S. G., S. G. Gogineni, S. Tjuatja, and A. K. Fung, Model-based interpretation of ERS-1 SAR images of Arctic sea ice, *International Journal of Remote Sensing*, *18 (12)*, 2483–2503, 1997.

Bentley, C. R., R. H. Thomas, and I. Velicogna, Ice Sheets, in *Global Outlook for*

Ice and Snow, edited by P. Prestrud, pp. 99–113, United Nations Environment Programme, Nairobi, 2007.

Berrisford, P., D. Dee, K. Fielding, M. Fuentes, P. Kallberg, S. Kobayashi, and S. Uppala, The ERA-Interim archive, *Tech. Rep. ECMWF ERA Report Series No. 1*, European Centre for Medium-Range Weather Forecasts, Shinfield Park, Reading, 2009.

Born, M., and E. Wolf, *Principles of Optics; Electromagnetic Theory of Propagation, Interference, and Diffraction of Light*, 808 pp., Pergamon Press, Oxford, New York, USA, 1975.

Bracegirdle, T. J., W. M. Connolley, and J. Turner, Antarctic climate change over the twenty first century, *Journal of Geophysical Research (Atmospheres)*, *113*, 3103–3115, doi:10.1029/2007JD008933, 2008.

Bromwich, D. H., R. L. Fogt, K. I. Hodges, and J. E. Walsh, A tropospheric assessment of the ERA-40, NCEP, and JRA-25 global reanalyses in the polar regions, *Journal of Geophysical Research (Atmospheres)*, *112*, 10,111, doi: 10.1029/2006JD007859, 2007.

Brunt, K. M., O. Sergienko, and D. R. MacAyeal, Observations of unusual fast-ice conditions in the southwest Ross Sea, Antarctica: Preliminary analysis of iceberg and storminess effects, *Annals of Glaciology*, *44*, 183–187, 2006.

Carleton, A. M., A synoptic climatology of satellite-observed extratropical cyclone activity for the Southern Hemisphere winter, *Theoretical and Applied Climatology*, *27*(4), 265–279, 1979.

Cavalieri, D. J., and S. Martin, A Passive Microwave Study of Polynyas Along the Antarctic Wilkes Land Coast, in *Oceanology of the Antarctic Continental Shelf*,

edited by S. Jacobs, Antarctic Research Series, volume 43, pp. 227–252, AGU, Washington, D.C., 1985.

Cavalieri, D. J., and C. L. Parkinson, Antarctic sea ice variability and trends, 1979-2006, *Journal of Geophysical Research (Oceans)*, *113*, 7004, doi: 10.1029/2007JC004564, 2008.

Chen, P. Y., R. Srinivasan, G. Fedosejevs, and J. R. Kiniry, Evaluating different NDVI composite techniques using NOAA-14 AVHRR data, *International Journal of Remote Sensing*, *24*(17), 3403–3412, 2003.

Chung, H., and C. Fox, Calculation of wave propagation into land-fast ice, *Annals of Glaciology*, *33*, 322–326, 2001.

Comiso, J., Bootstrap Sea Ice Concentrations from Nimbus-7 SMMR and DMSP SSM/I, 2000-2008, Boulder, Colorado USA: National Snow and Ice Data Center. Digital media., 1999.

Comiso, J., Variability and trends of the global sea ice cover, in *Sea Ice*, edited by D. Thomas and G. Dieckmann, 2nd Edition ed., pp. 205–246, Oxford, UK, 2010.

Comiso, J. C., Surface temperatures in the polar regions from Nimbus 7 Temperature Humidity Infrared Radiometer, *Journal of Geophysical Research*, *99*, 5181–5200, doi:10.1029/93JC03450, 1994.

Comiso, J. C., Variability and trends in Antarctic surface temperatures from in situ and satellite infrared measurements, *Journal of Climate*, *13*, 1674–1696, 1999.

Comiso, J. C., and F. Nishio, Trends in the sea ice cover using enhanced and compatible AMSR-E, SSM/I, and SMMR data, *Journal of Geophysical Research (Oceans)*, *113*, 2, doi:10.1029/2007JC004257, 2008.

Convey, P., R. A. Bindschadler, R. G. Di Prisco, E. Fahrbach, J. Gutt, D. A. Hodgson, P. A. Mayewski, C. P. Summerhayes, J. Turner, and the ACCE Consortium, Antarctic climate change and the environment, *Antarctic Science*, *21*, 541–563, doi:doi:10.1017/S0954102009990642, 2009.

Cook, A. J., A. J. Fox, D. G. Vaughan, and J. G. Ferrigno, Retreating glacier fronts on the Antarctic Peninsula over the past half-century, *Science*, *308*, 541–544, doi:10.1126/science.1104235, 2005.

Coulson, S. N., and J. P. Guignard, SAR interferometry with ERS-1, in *Euro-Latin American Space Days*, *ESA Special Publication*, vol. 363, edited by N. Longdon, 1994.

Cracknell, A. P., *The Advanced Very High Resolution Radiometer*, CRC Press, Florida, 1997.

Crocker, G. B., and P. Wadhams, Observations of Wind-Generated Waves in Antarctic Fast Ice, *Journal of Physical Oceanography*, *18*, 1292–1299, 1988.

Crocker, G. B., and P. Wadhams, Breakup of Antarctic fast ice, *Cold Regions Science and Technology*, *17(1)*, 61–76, 1989.

Curran, M. A. J., T. D. van Ommen, V. I. Morgan, K. L. Phillips, and A. S. Palmer, Ice core evidence for Antarctic sea ice decline since the 1950s, *Science*, *302*(5648), 1203–1206, doi:10.1126/science.1087888, 2003.

Dammert, P. B. G., M. Leppäranta, and J. Askne, Sea-ice displacement measured by ERS-1 SAR interferometry, in *ESA SP-414: Third ERS Symposium on Space at the Service of Our Environment*, edited by T.-D. Guyenne and D. Danesy, 1997.

de La Mare, W. K., Abrupt mid-twentieth-century decline in Antarctic sea-ice extent from whaling records, *Nature*, *389*, doi:10.1038/37956, 1997.

Dempewolf, J., S. Trigg, R. S. Defries, and S. Eby, Burned-area mapping of the Serengeti Mara region using MODIS reflectance data, *IEEE Geoscience and Remote Sensing Letters*, *4*(2), 312–316, doi:10.1109/LGRS.2007.894140, 2007.

di Bisceglie, M., R. Episcopo, C. Galdi, and S. L. Ullo, Destriping MODIS data using overlapping field-of-view method, *IEEE Transactions on Geoscience and Remote Sensing*, *47*, 637–651, doi:10.1109/TGRS.2008.2004034, 2009.

Diaz, H. F., and R. S. Pulwarty, An analysis of the time scales of variability in centuries-long ENSO-sensitive records in the last 1000 years, *Climatic Change*, *26*, 317–342, 1994.

Divine, D. V., R. Korsnes, and A. P. Makshtas, Variability and climate sensitivity of fast ice extent in the north-eastern Kara Sea, *Polar Research*, *22*, 27–34, 2003.

Divine, D. V., R. Korsnes, A. P. Makshtas, F. Godtliebsen, and H. Svendsen, Atmospheric-driven state transfer of shore-fast ice in the northeastern Kara Sea, *Journal of Geophysical Research (Oceans)*, *110*, 9013–9025, 2005.

Ebert, E. E., *Classification and Analysis of Surface and Clouds at High Latitudes from AVHRR Multispectral Satellite Data.*, Ph.D. thesis, The University of Wisconsin, Madison, 1987.

Eklundh, L., and A. Singh, A comparative analysis of standardised and unstandardised principal component analysis in remote sensing, *International Journal of Remote Sensing*, *14*(7), 1359–1370, 1993.

Enomoto, H., F. Nishio, H. Warashina, and S. Ushio, Satellite observation of melting

and break-up of fast ice in Lützow-Holm Bay, East Antarctica, *Polar Meteorology and Glaciology*, *16*, 1–14, 2002.

Flato, G. M., and R. D. Brown, Variability and climate sensitivity of landfast Arctic sea ice, *Journal of Geophysical Research*, *101*, 25,767–25,778, 1996.

Fogt, R. L., and S. Barreira, Antarctica: Atmospheric circulation, in *State of The Climate in 2008*, vol. 91, edited by D. S. Arndt, M. O. Baringer, and M. R. Johnson, pp. S114–S115, Bulletin of the American Meteorological Society, 2010.

Fogt, R. L., and D. H. Bromwich, Decadal variability of the ENSO teleconnection to the high-latitude South Pacific governed by coupling with the Southern Annular Mode, *Journal of Climate*, *19*, 979–997, doi:10.1175/JCLI3671.1, 2006.

Fowler, C. W., W. J. Emery, and J. A. Maslanik, Twenty three years of Antarctic sea ice motion from microwave satellite imagery, in *Proceedings of the IEEE International Geoscience and Remote Sensing Symposium*, pp. 157–159, 2001.

Fraser, A. D., R. A. Massom, and K. J. Michael, A method for compositing polar MODIS satellite images to remove cloud cover for landfast sea-ice detection, *IEEE Transactions on Geoscience and Remote Sensing*, *47*(9), 3272–3282, doi: 10.1109/TGRS.2009.2019726, 2009.

Fraser, A. D., R. A. Massom, and K. J. Michael, Generation of high-resolution East Antarctic landfast sea-ice maps from cloud-free MODIS satellite composite imagery, *Remote Sensing of Environment*, *114*(12), 2888–2896, doi: 10.1016/j.rse.2010.07.006, 2010a.

Fraser, A. D., R. A. Massom, K. J. Michael, P. Heil, and J. L. Lieser, East Antarctic landfast sea-ice distribution and variability, 2000-2008, *Journal of Climate*, *subm.*, 2010b.

Fretwell, P. T., and P. N. Trathan, Penguins from space: Faecal stains reveal the location of emperor penguin colonies, *Global Ecology and Bioecology*, *18*(5), 543–552, Abstract number EA9.1-1.6, 2009.

Fukamachi, Y., K. I. Ohshima, Y. Kitade, T. Tamura, and M. Wakatsuchi, Antarctic Bottom Water revealed by mooring measurement off Cape Darnley, Antarctica, in *International Polar Year Oslo Science Conference*, 2010.

Fyfe, J. C., and O. A. Saenko, Simulated changes in the extra-tropical Southern Hemisphere winds and currents, *Geophysical Research Letters*, *33*, doi: 10.1029/2005GL025332, 2006.

Gao, B., P. Yang, and R. Li, Detection of high clouds in polar regions during the daytime using the MODIS 1.375-μm channel, *IEEE Transactions on Geoscience and Remote Sensing*, *41*, 474–481, doi:10.1109/TGRS.2002.808290, 2003.

Gao, B.-C., A. F. H. Goetz, and W. J. Wiscombe, Cirrus cloud detection from airborne imaging spectrometer data using the 1.38 μm water vapor band, *Geophysical Research Letters*, *20*, 301–304, 1993.

Gao, Y., H. Xie, T. Yao, and C. Xue, Integrated assessment on multi-temporal and multi-sensor combinations for reducing cloud obscuration of MODIS snow cover products of the Pacific Northwest USA, *Remote Sensing of Environment*, *114*, 1662–1675, 2010.

Garrison, D. L., Antarctic sea ice biota, *American Zoologist*, *31*, 17–33, 1991.

George, J. C., H. P. Huntington, K. Brewster, H. Eicken, D. W. Norton, and R. Glenn, Observations on shorefastice dynamics in Arctic Alaska and the responses of the Iñupiat hunting community, *Arctic*, *57*(4), 363–374, 2004.

Giles, A. B., R. A. Massom, and V. I. Lytle, Fast-ice distribution in East Antarctica during 1997 and 1999 determined using RADARSAT data, *Journal of Geophysical Research (Oceans)*, *113*, doi:10.1029/2007JC004139, 2008.

Giles, A. B., R. A. Massom, and R. C. Warner, A method for sub-pixel scale feature-tracking using Radarsat images applied to the Mertz Glacier Tongue, East Antarctica, *Remote Sensing of Environment*, *113*, 1691–1699, 2009.

Gill, R. S., and H. H. Valeur, Ice cover discrimination in the Greenland waters using first-order texture parameters of ERS SAR images, *International Journal of Remote Sensing*, *20*(2), 373–385, 1999.

Gladstone, R., and G. R. Bigg, Satellite tracking of icebergs in the Weddell Sea, *Antarctic Science*, *14*(3), 278–287, 2002.

Glass, L., B. Walker, M. Peters, and L. Dykes, Improving the useability of high resolution satellite imagery for tropical areas: De-glinting, de-hazing and calibration of very high resolution satellite imagery, in *Proceedings of the International Symposium & Exhibition on Geoinformation*, 2010.

Gloersen, P., W. J. Campbell, D. J. Cavalieri, J. C. Comiso, C. L. Parkinson, and H. J. Zwally, Arctic and Antarctic Sea Ice, 1978 - 1987: Satellite Passive Microwave Observations and Analysis, *Special Publication SP-511*, NASA Goddard Space Flight Center, Greenbelt, Maryland, 290 pp., 1992.

Günther, S., and G. S. Dieckmann, Vertical zonation and community transition of sea-ice diatoms in fast ice and platelet layer, Weddell Sea, Antarctica, *Annals of Glaciology*, *33*, 287–296, 2001.

Haarsma, R. J., F. M. Selten, and J. D. Opsteegh, On the mechanism of the Antarctic Circumpolar Wave., *Journal of Climate*, *13*, 1461–1480, 2000.

Haas, C., D. N. Thomas, and J. Bareiss, Surface properties and processes of perennial Antarctic sea ice in summer, *Journal of Glaciology*, *47*, 613–625, doi: 10.3189/172756501781831864, 2001.

Haines, S. L., G. J. Jedlovec, and S. M. Lazarus, A MODIS sea surface temperature composite for regional applications, *IEEE Transactions on Geoscience and Remote Sensing*, *45*, 2919–2927, doi:10.1109/TGRS.2007.898274, 2007.

Hall, A., and M. Visbeck, Synchronous variability in the Southern Hemisphere atmosphere, sea ice, and ocean resulting from the Annular Mode, *Journal of Climate*, *15*, 3043–3057, 2002.

Haran, T. M., M. A. Fahnestock, and T. A. Scambos, De-striping of MODIS optical bands for ice sheet mapping and topography, *EOS Transactions of the American Geophysical Union*, *88*(47), f317, 2002.

Harangozo, S. A., A search for ENSO teleconnections in the west Antarctic Peninsula climate in austral winter, *International Journal of Climatology*, *20*, 663–679, 2000.

Heacock, T., T. Hirose, F. Lee, M. Manore, and B. Ramsay, Sea-ice tracking on the east coast of Canada using NOAA AVHRR imagery, *Annals of Glaciology*, *17*, 405–413, 1993.

Heil, P., Atmospheric conditions and fast ice at Davis, East Antarctica: A case study, *Journal of Geophysical Research (Oceans)*, *111*, 5009–5023, 2006.

Heil, P., I. Allison, and V. I. Lytle, Seasonal and interannual variations of the oceanic heat flux under a landfast Antarctic sea ice cover, *Journal of Geophysical Research*, *101*, 25,741–25,752, doi:10.1029/96JC01921, 1996.

Heil, P., C. W. Fowler, and S. Lake, Antarctic sea-ice velocity as derived from SSM/I imagery, *Annals of Glaciology*, *44*, 361–366, 2006.

Heil, P., S. Gerland, and M. Granskog, Antarctic fast ice thickness from AFIN sites and intercomparison with Arctic fast ice thickness monitoring, *The Cryosphere*, *in prep*, 2010.

Higashi, A., D. J. Goodman, S. Kawaguchi, and S. Mae, The cause of the breakup of fast ice on March 18, 1980 near Syowa station, East Antarctica, *Memoirs of National Institute of Polar Research*, *24*, 222–231, 1982.

Hillger, D. W., and J. D. Clark, Principal component image analysis of MODIS for volcanic ash. Part I: most important bands and implications for future GOES imagers, *Journal of Applied Meteorology*, *41*, 985–1001, 2002.

Horn, B. K. P., and R. J. Woodham, Destriping Landsat MSS images by histogram modification, *Computer Graphics and Images Processing*, *10*, 69–83, 1979.

Hoskins, B. J., and D. J. Karoly, The steady linear response of a spherical atmosphere to thermal and orographic forcing, *Journal of Atmospheric Sciences*, *38*, 1179–1196, 1981.

Huang, J., P. Minnis, B. Lin, Y. Yi, T. Fan, S. Sun-Mack, and J. K. Ayers, Determination of ice water path in ice-over-water cloud systems using combined MODIS and AMSR-E measurements, *Geophysical Research Letters*, *33*, doi:10.1029/2006GL027038, 2006.

IPCC, Summary for Policymakers, in *Climate Change 2007: The Physical Science Basis. Contribution of Working Group I to the Fourth Assessment Report of the Intergovernmental Panel on Climate Change*, edited by S. Solomon, D. Qin, M. Manning, Z. Chen, M. Marquis, K. B. Averyt, M. Tignor, and H. L. Miller, Cambridge University Press, Cambridge, United Kingdom and New York, USA, 2007.

Jackson, C. R., and J. R. Apel (Eds.), *Synthetic Aperture Radar Marine User's Manual*, U.S. Department of Commerce, Washington, DC, 2004.

Jacobs, G. A., and J. L. Mitchell, Ocean circulation variations associated with the Antarctic Circumpolar Wave, *Geophysical Research Letters*, *23*, 2947–2950, doi: 10.1029/96GL02492, 1996.

Jezek, K., RAMP AMM-1 SAR Image Mosaic of Antarctica, Digital media. Available at http://nsidc.org/data/nsidc-0103.html, 2002.

Karoly, D. J., Southern Hemisphere Circulation Features Associated with El Niño-Southern Oscillation Events, *Journal of Climate*, *2*, 1239–1252, 1989.

Kawamura, T., K. I. Ohshima, T. Takizawa, and S. Ushio, Physical, structural, and isotopic characteristics and growth processes of fast sea ice in Lützow-Holm Bay, Antarctica, *Journal of Geophysical Research (Oceans)*, *102(C2)*, 3345–3355, 1997.

Kern, S., G. Spreen, L. Kaleschke, S. de La Rosa, and G. Heygster, Polynya Signature Simulation Method polynya area in comparison to AMSR-E 89 GHz sea-ice concentrations in the Ross Sea and off the Adélie Coast, Antarctica, for 2002-05: First results, *Annals of Glaciology*, *46*, 409–418, 2007.

Khalsa, S. S., T. H. Painter, M. McAllister, and R. Duerr, Applications of MODIS Snow and Ice Products, *AGU Fall Meeting Abstracts*, (C21A-1123), 2006.

Kidson, J. W., Principal modes of southern hemisphere low-frequency variability obtained from NCEP-NCAR reanalyses, *Journal of Climate*, *12*, 2808–2830, 1999.

Kirkwood, R., and G. Robertson, Seasonal change in the foraging ecology of Emperor penguins on the Mawson Coast, Antarctica, *Marine Ecology Progress Series*, *156*, 205–223, 1997.

König Beatty, C., and D. M. Holland, Modeling landfast sea ice by adding tensile strength, *Journal of Physical Oceanography*, *40*, doi:10.1175/2009JPO4105.1, 2010.

Kooyman, G. L., and J. Burns, Weddell seal versus Emperor penguin: Boss of the Ross Sea, *American Zoology*, *39*, 9–19, 1999.

Kovacs, A., and M. Mellor, Sea ice morphology and ice as a geological agent in the southern Beaufort Sea, in *The Coast and Shelf of the Beaufort Sea*, edited by J. C. Reed and J. F. Sater, pp. 113–161, Arctic Institute of North America, Calgary, Canada, 1974.

Kozlovsky, A. M., Y. L. Nazintsev, V. I. Fedotov, and N. V. Cherepanov, Fast ice of the Eastern Antarctic (in Russian), *Proceedings of the Soviet Antarctic Expedition*, *63*, 1–129, 1977, cited in Fedotov et al. 1998.

Kuga, Y., Brief results of the weather analysis during the operations of J.A.R.E. III, 1958-59, *Antarctic Record*, *14*, 1171–1175, 1962.

Kwok, R., and J. C. Comiso, Southern Ocean climate and sea ice anomalies associated with the Southern Oscillation, *Journal of Climate*, *15*, 487–501, 2002.

Lake, S. E., H. R. Burton, and M. A. Hindell, Influence of time of day and month on Weddell seal haul-out patterns at the Vestfold Hills, Antarctica, *Polar Biology*, *18*, 319–324, 1997.

Langhorne, P. J., V. A. Squire, C. Fox, and T. G. Haskell, Break-up of sea ice by ocean waves, *Annals of Glaciology*, *27*, 438–442, 1998.

Langhorne, P. J., V. A. Squire, C. Fox, and T. G. Haskell, Lifetime estimation for a land-fast ice sheet subjected to ocean swell, *Annals of Glaciology*, *33*, 333–338, 2001.

Lefebvre, W., and H. Goosse, An analysis of the atmospheric processes driving the large-scale winter sea ice variability in the Southern Ocean, *Journal of Geophysical Research (Oceans)*, *113*, 2004–2018, doi:10.1029/2006JC004032, 2008.

Lei, R., Z. Li, B. Cheng, Z. Zhang, and P. Heil, Annual cycle of landfast sea ice in Prydz Bay, East Antarctica, *Journal of Geophysical Research (Oceans)*, *115*, 2006, doi:10.1029/2008JC005223, 2010.

Lemke, P., J. Ren, R. B. Alley, I. Allison, J. Carrasco, G. Flato, Y. Fujii, G. Kaser, P. Mote, and T. Thomas, R. H. Zhang, Observations: Changes in Snow, Ice and Frozen Ground, Climate Change 2007: The Physical Science Basis, in *Fourth Assessment Report of the Intergovernmental Panel on Climate Change*, edited by Observations: Changes in Snow, Ice and Frozen Ground, Climate Change 2007: The Physical Science Basis., Cambridge University Press, Cambridge, United Kingdom and New York, NY, USA, 2007.

Li, W., K. Stamnes, H. Eide, and R. Spurr, Bidirectional reflectance distribution function of snow: corrections for the Lambertian assumption in remote sensing applications, *Optical Engineering*, *46*(6), doi:10.1117/1.2746334, 2007.

Lieser, J. L., A Numerical Model for Short-term Sea Ice Forecasting in the Arctic, *Reports on Polar and Marine Research 485*, Alfred Wegener Institute for Polar and Marine Research, Columbusstraße, D-27568 Bremerhaven, Germany, 93 pp., 2004.

Lindsay, R. W., and D. A. Rothrock, Arctic sea ice albedo from AVHRR, *Journal of Climate*, *7*, 1737–1749, 1994.

Liu, J., J. A. Curry, and D. G. Martinson, Interpretation of recent Antarctic sea ice variability, *Geophysical Research Letters*, *31*, doi:10.1029/2003GL018732, 2004a.

Liu, Y., J. R. Key, R. A. Frey, S. A. Ackerman, and W. P. Menzel, Nighttime polar cloud detection with MODIS, *Remote Sensing of Environment*, *92*, 191–194, 2004b.

Lubin, D., and R. A. Massom, *Polar Remote Sensing Volume I: Atmosphere and Oceans*, Praxis-Springer, Chichester and Berlin, 759 pp., 2006.

Lubin, D., and E. Morrow, Evaluation of an AVHRR cloud detection and classification method over the central Arctic Ocean., *Journal of Applied Meteorology*, *37*, 166–183, 1998.

Luo, Y., A. P. Trishchenko, K. V. Khlopenkov, and W. M. Park, Scene identification and clear-sky compositing algorithms for generating North America coverage at 250m spatial resolution from MODIS land channels, in *Earth Observing Systems XII. Proceedings of the Society of Photo-Optical Instrumentation Engineers*, vol. 6677, edited by J. J. Butler and J. Xiong, doi:10.1117/12.739507, 2007.

Lythe, M., A. Hauser, and G. Wendler, Classification of sea ice types in the Ross Sea, Antarctica from SAR and AVHRR imagery, *International Journal of Remote Sensing*, *20*(15), 3073–3085, 1999.

Mae, S., T. Yamanouchi, and Y. Fujii, Remote sensing of fast ice in Lützowholmbukta, East Antarctica, using satellite NOAA-7, 8 and aircraft, *Annals of Glaciology*, *9*, 251–251, 1987.

Mahoney, A., H. Eicken, A. Graves, L. Shapiro, and P. Cotter, Landfast sea ice extent and variability in the Alaskan Arctic derived from SAR imagery, in *Proceedings of the IEEE International Geoscience and Remote Sensing Symposium (IGARSS) 2004*, vol. 3, pp. 2146–2149, 2004.

Mahoney, A., H. Eicken, L. Shapiro, and A. Graves, Defining and locating the

seaward landfast ice edge in northern Alaska, in *Proceedings of the International Conference on Port and Ocean Engineering under Arctic Conditions*, vol. 3, pp. 991–1001, 2005.

Mahoney, A., H. Eicken, A. G. Gaylord, and L. Shapiro, Alaska landfast sea ice: Links with bathymetry and atmospheric circulation, *Journal of Geophysical Research (Oceans)*, *112*, 2001, 2007a.

Mahoney, A., H. Eicken, and L. Shapiro, How fast is landfast sea ice? A study of the attachment and detachment of nearshore ice at Barrow, Alaska, *Cold Regions Science and Technology*, *47*, 233–255, 2007b.

Maksym, T., and M. O. Jeffries, A one-dimensional percolation model of flooding and snow ice formation on Antarctic sea ice, *Journal of Geophysical Research*, *105*, 26,313–26,332, doi:10.1029/2000JC900130, 2000.

Marshall, G. J., Trends in the Southern Annular Mode from observations and reanalyses, *Journal of Climate*, *16*, 4134–4143, 2003.

Martin, S., Polynyas, in *Encyclopedia of Ocean Sciences*, edited by J. H. Steele, K. K. Turekian, and S. A. Thorpe, pp. 2241–2247, Academic Press, London, 2001.

Maslanik, J., T. Agnew, M. Drinkwater, W. Emery, C. Fowler, R. Kwok, and A. Liu, Summary of ice-motion mapping using passive microwave data, *Tech. Rep. 8*, National Snow and Ice Data Centre, Boulder, Colorado, 1998.

Massom, R. A., Recent iceberg calving events in the Ninnis Glacier region, East Antarctica, *Antarctic Science*, *15 (2)*, 303–313, 2003.

Massom, R. A., and D. Lubin, *Polar Remote Sensing Volume II: Ice Sheets*, Praxis-Springer, Chichester and Berlin, 2006.

Massom, R. A., and S. E. Stammerjohn, Antarctic sea ice change and variability - Physical and ecological implications, *Polar Science*, *4*, 149–186, 2010.

Massom, R. A., P. T. Harris, K. J. Michael, and M. J. Potter, The distribution and formative processes of latent-heat polynyas in East Antarctica, *Annals of Glaciology*, *27*, 420–426, 1998.

Massom, R. A., H. Eicken, C. Haas, M. O. Jeffries, M. R. Drinkwater, M. Sturm, A. P. Worby, X. Wu, V. I. Lytle, S. Ushio, K. Morris, P. A. Reid, S. G. Warren, and I. Allison, Snow on Antarctic sea ice, *Reviews of Geophysics*, *39*, 413–445, 2001a.

Massom, R. A., K. L. Hill, V. I. Lytle, A. P. Worby, M. J. Paget, and I. Allison, Effects of regional fast-ice and iceberg distributions on the behaviour of the Mertz Glacier polynya, East Antarctica, *Annals of Glaciology*, *33*, 391–398, 2001b.

Massom, R. A., K. Jacka, M. J. Pook, C. Fowler, N. Adams, and N. Bindoff, An anomalous late-season change in the regional sea ice regime in the vicinity of the Mertz Glacier Polynya, East Antarctica, *Journal of Geophysical Research (Oceans)*, *108*, 3212–3226, doi:10.1029/2002JC001354, 2003.

Massom, R. A., S. E. Stammerjohn, R. C. Smith, M. J. Pook, R. A. Iannuzzi, N. Adams, D. G. Martinson, M. Vernet, W. R. Fraser, L. B. Quetin, R. M. Ross, Y. Massom, and H. R. Krouse, Extreme anomalous atmospheric circulation in the West Antarctic Peninsula region in Austral spring and summer 2001/02, and its profound impact on sea ice and biota, *Journal of Climate*, *19*, 3544–3571, 2006a.

Massom, R. A., A. Worby, V. Lytle, T. Markus, I. Allison, T. Scambos, H. Enomoto, K. Tateyama, T. Haran, J. C. Comiso, A. Pfaffling, T. Tamura, A. Muto, P. Kanagaratnam, B. Giles, N. Young, G. Hyland, and E. Key, ARISE (Antarctic Remote

Ice Sensing Experiment) in the East 2003: validation of satellite-derived sea-ice data products, *Annals of Glaciology*, *44*, 288–296, 2006b.

Massom, R. A., K. Hill, C. Barbraud, N. Adams, A. Ancel, L. Emmerson, and M. Pook, Fast ice distribution in Adélie Land, East Antarctica: Interannual variability and implications for Emperor penguins (*Aptenodytes forsteri*), *Marine Ecology Progress Series*, *374*, 243–257, 2009.

Massom, R. A., A. B. Giles, H. A. Fricker, R. Warner, B. Legrésy, G. Hyland, N. Young, and A. D. Fraser, Examining the interaction between multi-year landfast sea ice and the Mertz Glacier Tongue, East Antarctica; Another factor in ice sheet stability?, *Journal of Geophysical Research (Oceans)*, *115*, C12,027, doi: 10.1029/2009JC006083, 2010a.

Massom, R. A., P. Reid, S. Stammerjohn, and S. Barreira, Antarctica: Sea ice extent and concentration, in *State of The Climate in 2008*, vol. 91, edited by D. S. Arndt, M. O. Baringer, and M. R. Johnson, pp. S131–S133, Bulletin of the American Meteorological Society, 2010b.

McMinn, A., C. Ashworth, and K. Ryan, *In situ* net primary productivity of an Antarctic fast ice bottom algal community, *Aquatic Microbial Ecology*, *21*, 177–185, 2000.

Meijers, A. J. S., A. Klocker, N. L. Bindoff, G. D. Williams, and S. J. Marsland, The circulation and water masses of the Antarctic shelf and continental slope between 30 and 80° E, *Deep-Sea Research II*, *57*, 723–737, 2010.

Mélice, J., J. R. E. Lutjeharms, H. Goosse, T. Fichefet, and C. J. C. Reason, Evidence for the Antarctic Circumpolar Wave in the sub-Antarctic during the past 50 years, *Geophysical Research Letters*, *32*, doi:10.1029/2005GL023361, 2005.

Miller, R. L., G. A. Schmidt, and D. T. Shindell, Forced annular variations in the 20th century Intergovernmental Panel on Climate Change Fourth Assessment Report models, *Journal of Geophysical Research (Atmospheres)*, *111*, doi: 10.1029/2005JD006323, 2006.

Mo, K. C., and M. Ghil, Statistics and dynamics of persistent anomalies, *Journal of Atmospheric Sciences*, *44*, 877–902, 1987.

Mo, K. C., and G. H. White, Teleconnections in the Southern Hemisphere, *Monthly Weather Review*, *113*, 1985.

Morris, K., S. Li, and M. Jeffries, Meso- and micro-scale sea-ice motion in the East Siberian Sea as determined from ERS-1 SAR data, *Journal of Glaciology*, *45*, 370–383, 1999.

Murphy, E. J., A. Clarke, C. Symon, and J. J. Priddle, Temporal variation in Antarctic sea-ice: Analysis of a long term fast-ice record from the South Orkney Islands, *Deep-Sea Research I*, *42 (7)*, 1045–1062, 1995.

Nicholls, N., Commentary and analysis: The insignificance of significance testing, *Bulletin of the American Meteorological Society*, *82*, 981–986, 2001.

NIMA, World Geodetic System 1984: Its Definition and Relationships with Local Geodetic Systems, *Third edition, amendment 1 TR8350.2*, National Imagery and Mapping Agency, Bethesda, Maryland, 2000.

Ninnis, R. M., W. J. Emery, and M. J. Collins, Automated extraction of pack ice motion from Advanced Very High Resolution Radiometer imagery, *Journal of Geohpysical Research*, *91*, 10,725–10,734, 1986.

Nishihama, M., R. Wolfe, D. Solomon, F. Patt, J. Blanchette, A. Fleig, and E. Masuoka, MODIS Level 1A Earth Location Algorithm Theoretical Basis Document,

Tech. Rep. Version 3.0, Hughes STX, General Science Corporation, University of Maryland and NASA/Goddard Spaceflight Center, 1997.

Nunes Vaz, R., and G. Lennon, Physical oceanography of the Prydz Bay region of Antarctic waters, *Deep-Sea Research I*, *43*, 603–641, doi:10.1016/0967-0637(96)00028-3, 1996.

Ohshima, K. I., T. Kawamura, T. Takizawa, S. Ushio, and T. Miyakawa, Current variability under landfast sea ice in Lützow-Holm Bay, Antarctica, *Journal of Geohpysical Research*, *105*, 17,121–17,132, doi:10.1029/2000JC900080, 2000.

Ohshima, K. I., T. Tamura, Y. Fukamachi, and S. Aoki, Sea ice production in the polynya and the associated bottom water formation off the Cape Darnley, East Antarctica, in *9th International Conference on Southern Hemisphere Meteorology and Oceanography*, 2009.

Oliver, C., and S. Quegan, *Undestanding Synthetic Aperture Radar Images*, 481 pp., Artech House, Boston and London, 1998.

Parkinson, C. L., Aqua: An Earth-observing satellite mission to examine water and other climate variables, *IEEE Transactions on Geoscience and Remote Sensing*, *41*, 173–183, doi:10.1109/TGRS.2002.808319, 2003.

Peixóto, J. P., and A. H. Oort, *Physics of Climate*, 520 pp., American Institute of Physics, New York, 1992.

Perlwitz, J., S. Pawson, R. L. Fogt, J. E. Nielsen, and W. D. Neff, Impact of stratospheric ozone hole recovery on Antarctic climate, *Geophysical Research Letters*, *35*, doi:10.1029/2008GL033317, 2008.

Perovich, D., The decreasing summer Arctic sea ice cover and the ice albedo

feedback, *IOP Conference Series: Earth and Environmental Science*, *6*(6), doi: 10.1088/1755-1307/6/6/062010, 2009.

Perovich, D. K., J. A. Richter-Menge, K. F. Jones, and B. Light, Sunlight, water, and ice: Extreme Arctic sea ice melt during the summer of 2007, *Geophysical Research Letters*, *35*, doi:10.1029/2008GL034007, 2008.

Platzman, G. W., The Rossby Wave, *Quarterly Journal of the Royal Meteorological Society*, *94*, 225–248, doi:10.1002/qj.49709440102, 1968.

Pringle, D. J., H. Eicken, H. J. Trodahl, and L. G. E. Backstrom, Thermal conductivity of landfast Antarctic and Arctic sea ice, *Journal of Geophysical Research (Oceans)*, *112*, doi:10.1029/2006JC003641, 2007.

Purdie, C. R., P. J. Langhorne, G. H. Leonard, and T. G. Haskell, Growth of first-year landfast Antarctic sea ice determined from winter temperature measurements, *Annals of Glaciology*, *44*, 170–176, 2006.

Qu, J. J., W. Gao, M. Kafatos, R. E. Murphy, and V. V. Salomonson (Eds.), *Earth Science Satellite Remote Sensing, Volume 1: Science and Instruments*, 418 pp., Springer/Tsinghua University Press, Beijing, 2006.

Raphael, M. N., A zonal wave 3 index for the Southern Hemisphere, *Geophysical Research Letters*, *31*, doi:10.1029/2004GL020365, 2004.

Raphael, M. N., The influence of atmospheric zonal wave three on Antarctic sea ice variability, *Journal of Geophysical Research (Atmospheres)*, *112*, doi: 10.1029/2006JD007852, 2007.

Reijnders, P. J. H., J. Plötz, J. Zegers, and M. Gräfe, Breeding biology of Weddell seals (*Leptonychotes weddellii*) at Drescher Inlet, Riiser Larsen Ice Shelf, Antarctica, *Polar Biology*, *10*, 301–306, 1990.

Riggs, G., and D. A. Hall, Reduction of cloud obscuration in the MODIS snow data product, in *Proceedings of the 60th Annual Eastern Snow Conference*, vol. 60, pp. 205–222, 2003.

Rintoul, S. R., On the Origin and Influence of Adélie Land Bottom Water, in *Ocean, Ice and the Atmosphere: Interactions at the Antarctic Continental Margin. Antarctic Research Series, 75*, edited by S. Jacobs and R. Weiss, pp. 151–171, American Geophysical Union, Washington, D.C., 1998.

Rouse, J. W., Jr., R. H. Haas, J. A. Schell, and D. W. Deering, Monitoring vegetation systems in the Great Plains with ERTS, in *Proceedings of the Third ERTS-1 Symposium*, edited by S. C. Freden, E. P. Mercanti, and M. A. Becker, pp. 309–317, NASA Goddard Space Flight Center, Greenbelt, Maryland, 1974.

Scambos, T., C. Hulbe, and M. Fahnestock, Climate-induced ice shelf disintegration in the Antarctic Peninsula, in *Antarctic Peninsula Climate Variability: Historical and Paleoenvironmental Perspectives, Antarctic Research Series*, vol. 79, edited by E. Domack, A. Leventer, A. Burnett, R. Bindschadler, P. Convey, and M. Kirby, pp. 79–92, AGU, Washington, D.C., 2003.

Scambos, T., T. Haran, M. Fahnestock, T. Painter, and J. Bohlander, MODIS-based Mosaic of Antarctica (MOA) data sets: Continent-wide surface morphology and snow grain size, *Remote Sensing of Environment*, *111*, 242–257, 2007.

Simmonds, I., Modes of atmospheric variability over the Southern Ocean, *Journal of Geophysical Research (Oceans)*, *108*, 8078–8107, doi:10.1029/2000JC000542, 2003.

Simmonds, I., and T. H. Jacka, Relationships between the interannual variability of Antarctic sea ice and the Southern Oscillation, *Journal of Climate*, *8*, 637–648, 1995.

Simmonds, I., and D. A. Jones, The mean structure and temporal variability of the Semi-annual Oscillation in the southern extra-tropics, *International Journal of Climatology*, *18*, 473–504, 1998.

Simmonds, I., and K. Keay, Variability of Southern Hemisphere extratropical cyclone behavior, 1958-97., *Journal of Climate*, *13*, 550–561, 2000.

Simmonds, I., and J. C. King, Global and hemispheric climate variations affecting the Southern Ocean, *Antarctic Science*, *16*(4), 401–413, 2004.

Smith, I. J., P. J. Langhorne, T. G. Haskell, H. J. Trodahl, R. Frew, and M. R. Vennell, Platelet ice and the land-fast sea ice of McMurdo Sound, Antarctica, *Annals of Glaciology*, *33*, 21–27, 2001.

Smith, W. H. F., and D. Sandwell, Global seafloor topography from satellite altimetry and ship depth soundings, *Science*, *277*, 1956–1962, (version 11.1 updated 2008), 1997.

Spinhirne, J. D., S. P. Palm, D. L. Hlavka, W. D. Hart, and A. Mahesh, Global and polar cloud cover from the Geoscience Laser Altimeter System, observations and implications, *AGU Fall Meeting Abstracts*, Abstract number 21B-04, 2004.

Spinhirne, J. D., S. P. Palm, and W. D. Hart, Antarctica cloud cover for October 2003 from GLAS satellite lidar profiling, *Geophysical Research Letters*, *32*, doi: 10.1029/2005GL023782, 2005.

Spreen, G., L. Kaleschke, and G. Heygster, Sea ice remote sensing using AMSR-E 89-GHz channels, *Journal of Geophysical Research (Oceans)*, *113*, doi: 10.1029/2005JC003384, 2008.

Stammerjohn, S. E., D. G. Martinson, R. C. Smith, X. Yuan, and D. Rind, Trends in Antarctic annual sea ice retreat and advance and their relation to El Niño-

Southern Oscillation and Southern Annular Mode variability, *Journal of Geophysical Research (Oceans)*, *113*, doi:10.1029/2007JC004269, 2008.

Steig, E., D. P. Schneider, S. D. Rutherford, M. E. Mann, J. C. Comiso, and D. T. Shindell, Warming of the Antarctic ice-sheet surface since the 1957 International Geophysical Year, *Nature*, *457*, 2009.

Stringer, W. J., S. A. Barrett, and L. K. Schreurs, *Nearshore Ice Conditions and Hazards in the Beaufort, Chukchi and Bering Seas*, Geophysical Institute, University of Alaska, Fairbanks, 1980.

Stroeve, J. C., and A. W. Nolin, New methods to infer snow albedo from the MISR instrument with applications to the Greenland Ice Sheet, *IEEE Transactions on Geoscience and Remote Sensing*, *40*, 1616–1625, doi:10.1109/TGRS.2002.801144, 2002.

Swadling, K. M., A. D. McPhee, and A. McMinn, Spatial distribution of copepods in fast ice of eastern Antarctica, *Polar Bioscience*, *13*, 55–65, 2000.

Tamura, T., K. I. Ohshima, and S. Nihashi, Mapping of sea ice production for Antarctic coastal polynyas, *Geophysical Research Letters*, *35*, 7606, doi:10.1029/2007GL032903, 2008.

Tang, S., D. Qin, J. Ren, J. Kang, and Z. Li, Structure, salinity and isotopic composition of multi-year landfast sea ice in Nella Fjord, Antarctica, *Cold Regions Science and Technology*, *49*, 170–177, 2007.

Timmermann, R., A. Le Brocq, T. Deen, E. Domack, P. Dutrieux, B. K. Galton-Fenzi, H. Hellmer, A. Humbert, D. Jansen, A. Jenkins, A. Lambrecht, K. Makinson, F. Niederjasper, F. Nitsche, O. A. Nøst, L. H. Smedsrud, and W. Smith, A consistent dataset of Antarctic ice shelf topography, cavity geometry, and

global ocean bathymetry, *Earth System Science Data Discussions*, *3*(2), doi: 10.5194/essdd-3-231-2010, 2010.

Tison, J. L., R. D. Lorrain, A. Bouzette, M. Dini, A. Bondesan, and M. Stiévenard, Linking landfast sea ice variability to marine ice accretion at Hells Gate Ice Shelf, Ross Sea, in *Antarctic Sea Ice: Physical Processes, Interactions and Variability*, edited by M. Lizotte and K. Arrigo, pp. 375–407, (AGU Antarctic Research Series No. 74). American Geophysical Union, Washington, DC, 1998.

Troup, A. J., The 'Southern Oscillation', *Quarterly Journal of the Royal Meteorological Society*, *91*, 490–506, doi:10.1002/qj.49709139009, 1965.

Turner, J., The El Niño-Southern Oscillation and Antarctica, *International Journal of Climatology*, *24*, 1–31, doi:10.1002/joc.965, 2004.

Turner, J., S. R. Colwell, G. J. Marshall, T. A. Lachlan-Cope, A. M. Carleton, P. D. Jones, V. Lagun, P. A. Reid, and S. Iagovkina, Antarctic climate change during the last 50 years, *International Journal of Climatology*, *25*, 279–294, doi: 10.1002/joc.1130, 2005.

Turner, J., R. A. Bindschadler, P. Convey, G. Di Prisco, E. Fahrbach, J. Gutt, D. A. Hodgson, P. A. Mayewski, and C. P. Summerhayes (Eds.), *Antarctic Climate Change and the Environment*, Victorie Press, Cambridge, 2009.

Ulaby, F. T., R. K. Moore, and A. K. Fung, *Microwave Remote Sensing: Active and Passive, Vol. I - Microwave Remote Sensing Fundamentals and Radiometry*, 456 pp., Addison-Wesley Publishing Company, 1981.

Ushio, S., Factors affecting fast-ice break-up frequency in Lützow-Holm Bay, Antarctica, *Annals of Glaciology*, *44*, 177–182, 2006.

Ushio, S., Land-fast ice variation during the past five decades - Lützow-Holm Bay, Antarctica, *Ice and Climate News*, *11*, 13–14, 2008.

Uto, S., H. Shimoda, and S. Ushio, Characteristics of sea-ice thickness and snow-depth distributions of the summer landfast ice in Lützow-Holm Bay, East Antarctica, *Annals of Glaciology*, *44*, 281–287, 2006.

van Loon, H., The half-yearly oscillations in middle and high southern latitudes and the coreless winter, *Journal of Atmospheric Sciences*, *24*, 472–486, 1967.

van Loon, H., and R. L. Jenne, The Zonal Harmonic Standing Waves in the Southern Hemisphere, *Journal of Geophysical Research*, *77*, 992–1003, doi: 10.1029/JC077i006p00992, 1972.

Vaughan, D. G., G. J. Marshall, W. M. Connolley, C. Parkinson, R. Mulvaney, D. A. Hodgson, J. C. King, C. J. Pudsey, and J. Turner, Recent rapid regional climate warming on the Antarctic Peninsula, *Climate Change*, *60*, 243–274, 2003.

Venegas, S. A., The Antarctic Circumpolar Wave: A combination of two signals?, *Journal of Climate*, *16*, 2509–2525, 2003.

Wadhams, P., *The Seasonal Ice Zone*, 825-991 pp., Plenum Press, New York, 1986.

Waple, A. M., and R. C. Schnell, The Poles - The Antarctic: Sea ice extent and concentration, in *State of The Climate in 2002*, vol. 84, edited by A. Arguez, pp. S29–S30, Bulletin of the American Meteorological Society, 2003.

Welch, R. M., S. K. Sengupta, A. K. Goroch, P. Rabindra, N. Rangaraj, and M. S. Navar, Polar cloud and surface classification using AVHRR imagery: An intercomparison of methods., *Journal of Applied Meteorology*, *31*, 405–420, 1992.

Werninghaus, R., TerraSAR-X mission, in *Society of Photo-Optical Instrumentation*

Engineers (SPIE) Conference Series, vol. 5236, edited by F. Posa, pp. 9–16, doi: 10.1117/12.511500, 2004.

White, W. B., and R. G. Peterson, An Antarctic circumpolar wave in surface pressure, wind, temperature and sea-ice extent, *Nature*, *380*, 699–702, doi: 10.1038/380699a0, 1996.

White, W. B., S. Chen, and R. G. Peterson, The Antarctic Circumpolar Wave: A beta effect in ocean atmosphere coupling over the Southern Ocean, *Journal of Physical Oceanography*, *28*, 2345–2361, 1998.

Wienecke, B. C., and G. Robertson, Foraging space of emperor penguins *Aptenodytes forsteri* in Antarctic shelf waters in winter, *Marine Ecology Progress Series*, *159*, 249–263, 1997.

Williams, G. D., N. L. Bindoff, S. J. Marsland, and S. R. Rintoul, Formation and export of dense shelf water from the Adélie Depression, East Antarctica, *Journal of Geophysical Research (Oceans)*, *113*, 4039, doi:10.1029/2007JC004346, 2008.

Williams, R. N., W. G. Rees, and N. W. Young, A technique for the identification and analysis of icebergs in synthetic aperture radar images of Antarctica, *International Journal of Remote Sensing*, *20*, 3183–3199, doi:10.1080/014311699211697, 1999.

World Meteorological Organisation, WMO Sea-Ice Nomenclature. Terminology, Codes and Illustrated Glossary, *Tech. Rep. 259*, Geneva Secretariat of the World Meterological Organization, 1970.

Xue, Y., and R. W. Reynolds, Global oceans: Sea surface temperatures in 2008, in *State of The Climate in 2008*, vol. 91, edited by D. S. Arndt, M. O. Baringer, and

M. R. Johnson, pp. S47–S49, Bulletin of the American Meteorological Society, 2010.

Yamanouchi, T., and K. Seko, *Antarctica from NOAA Satellites: Clouds, Ice and Snow*, 91 pp., National Institute of Polar Research, Tokyo, 1992.

Yang, Z., J. Li, W. P. Menzel, and R. A. Frey, Destriping for MODIS data via wavelet shrinkage, in *Applications with Weather Satellites*, vol. 4895, edited by W. P. Menzel, W.-J. Zhang, J. Le Marshall, and M. Tokuno, pp. 187–199, Society of Photographic Instrumentation Engineers, Bellingham, Washington, 2003.

Young, N., B. Legrésy, R. Coleman, and R. A. Massom, Mertz Glacier Tongue unhinged by giant iceberg, *Australian Antarctic Magazine*, *18*, 19, 2010.

Yuan, X., ENSO-related impacts on Antarctic sea ice: A synthesis of phenomenon and mechanisms, *Antarctic Science*, *16*(4), 415–425, 2004.

Yuan, X., and C. Li, Climate modes in southern high latitudes and their impacts on Antarctic sea ice, *Journal of Geophysical Research (Oceans)*, *113*, doi: 10.1029/2006JC004067, 2008.

Zandbergen, R., J. M. Dow, M. R. Merino, R. Píriz, and F. Martínez Fadrique, ERS-1 and ERS-2 Tandem Mission: Orbit determination, prediction and maintenance, *Advances in Space Research*, *19*, 1649–1653, doi:10.1016/S0273-1177(97)00319-0, 1997.

Zink, M., C. Buck, J. L. Suchail, R. Torres, A. Bellini, J. Closa, and Y. L. Desnos, The radar imaging instrument and its applications: ASAR, *ESA Bulletin*, *106*, 46–55, 2001.

Zwally, H. J., J. C. Comiso, C. L. Parkinson, D. J. Cavalieri, and P. Gloersen, Vari-

ability of Antarctic sea ice 1979-1998, *Journal of Geophysical Research (Oceans)*, *107*, 3041–3059, 2002.